PEPTIDE DRUGS AGAINST ANTIBIOTIC RESISTANT BACTERIA

by

Begüm Alaybeyoğlu

B.S., Chemical Engineering, Middle East Technical University, 2010

M.S., Chemical Engineering, Boğaziçi University, 2012

Submitted to the Institute for Graduate Studies in
Science and Engineering in partial fulfillment of
the requirements for the degree of
Doctor of Philosophy

Graduate Program in Chemical Engineering

Boğaziçi University

2017

PEPTIDE DRUGS AGAINST ANTIBIOTIC RESISTANT BACTERIA

APPROVED BY:

Assoc. Prof. Elif Özkırımlı Ölmez (Thesis Supervisor)	.....
Prof. Berna Sarıyar Akbulut	.....
Prof. Kutlu Ülgen	.....
Prof. Işıl Aksan Kurnaz	.....
Assist. Prof. Nihat Alpagu Sayar	.....

DATE OF APPROVAL: 17.07.2017

ACKNOWLEDGEMENTS

I would like to express my sincere thanks to my thesis supervisor Assoc. Prof. Elif Özkırımlı Ölmez, and my thesis committee Prof. Berna Sarıyar Akbulut and Prof. Kutlu Ülgen. Their motivation and understanding helped me throughout my studies and improved my work.

I am very grateful to my defense jury members Prof. Işıl Aksan Kurnaz and Assist. Prof. Nihat Alpagu Sayar for spending time on my thesis and their valuable recommendations.

I wish to express my gratitude to Assoc. Prof. Arzu Çelik, Assist. Prof. İbrahim Yaman, and Dr. Bilge Gedik Uluocak, who deserve special thanks for their guidance and help throughout my experimental studies.

I would like to express my very great appreciation to my family for their endless support. They have always been proud of me and respected my choices even at times when I was in doubt.

I would like to thank all the ARGE staff for their kind support and help during these busy and challenging years. I would like to thank all the former and current members of KB407, and especially Ayşe Eren who made the difficult times easier on both of us.

Finally, I should express my very special thanks to my dearest friends Serhat Erşahin, Özgür Yaşar Çağlar, Erge Akbaş, and Ece Mutlu for always being there for me.

ABSTRACT

PEPTIDE DRUGS AGAINST ANTIBIOTIC RESISTANT BACTERIA

Membrane active peptides have found great interest as drug candidates due to their unique mode of action and availability in nature. In the past 20 years, beta-lactamase-mediated antibiotic resistance has become a lethal issue with the widespread of antibiotic cleaving beta-lactamase enzyme due to the misuse of beta-lactam type antibiotics. In this context, antimicrobial peptides are promising broad-spectrum alternatives to conventional antibiotics in the era of evolving bacterial resistance. In an effort to propose peptide drugs against antibiotic resistance, the understanding of how peptide drugs take action is essential. Here, the goal was to propose novel peptide antimicrobials that can efficiently inhibit periplasmic beta-lactamase and internalize into bacteria. For this aim, the cell-penetrating peptide pVEC and its first five residues (LLIIL) deleted variant del5 pVEC, were analyzed using molecular dynamics simulations to gain insights about the mechanism and free energy of the lipid bilayer translocation, and the contribution of the LLIIL residues to this peptide's uptake. Motivated by the pVEC sequence and the studies on pVEC emphasizing the importance of its LLIIL residues to the uptake of the peptide, the approach was to build chimeric sequences, by combining the LLIIL residues of pVEC with the beta-lactamase inhibitory peptides to facilitate their uptake. Our results show that the addition of LLIIL to the beta-lactamase inhibitory peptides increase their membrane permeabilizing potential. Interestingly, the addition of this short stretch of hydrophobic residues also modified the inhibitory peptides such that they acquired antimicrobial property. The results suggest that addition of the hydrophobic LLIIL residues to the peptide N-terminus may offer a promising strategy to design novel antimicrobial peptides in the battle against antibiotic resistance.

ÖZET

ANTİBİYOTİK DİRENÇLİ BAKTERİLER İÇİN İLAÇ TASARIMI

Membran aktif peptitler, doğadaki bulunma şekilleri ve benzersiz mekanizmaları nedeniyle ilaç adayları olarak büyük ilgi görmüştür. Son 20 yılda, beta-laktamaza bağlı gelişen antibiyotik direnci, beta-laktam tipi antibiyotiklerin kötüye kullanımı nedeniyle yaygınlaşan beta-laktamaz enzimini yüzünden ölümcül bir sorun haline gelmiştir. Bu bağlamda, antimikrobiyel peptitler, gittikçe artan antibiyotik direnci evresinde geleneksel antibiyotiklere geniş spektrum alternatifleri vaat etmektedir. Peptit temelli ilaçları antibiyotik direncine karşı önermek ve kullanmak amacıyla, peptit ilaçlarının nasıl harekete geçtiğini anlamak çok önemlidir. Buradaki amaç, periplazmik beta-laktamazı etkili bir şekilde inhibe edebilen ve bakteri hücrelerine girebilen yeni antimikrobiyel peptitler önermektir. Bu amaçla, hücre içine girebilen pVEC peptidi ve ilk beş kalıntısının (LLIIL) silinmesi ile elde edilen del5 pVEC, moleküler dinamik simülasyonları kullanılarak analiz edilmiş, çift katmanlı lipitten geçiş mekanizmaları ve serbest enerjileri ile LLIIL kalıntılarının geçiş mekanizmasına katkısı incelenmiştir. pVEC sekansından ve LLIIL kalıntılarının pVEC peptidinin hücre içine alınmasındaki önemini vurgulayan çalışmalardan yola çıkarak geliştirdiğimiz yaklaşımla, pVEC peptidinin LLIIL kalıntılarını beta-laktamaz inhibitörü peptitlerle birleştirerek yeni diziler oluşturulmuştur. Sonuçlarımız, LLIIL kalıntılarının beta-laktamaz inhibitörü peptitlere eklenmesinin peptitlerin membran geçirgenliğini arttırıcı potansiyelini yükselttiğini göstermektedir. İlginç bir şekilde, bu hidrofobik kalıntıların ilavesi, inhibitör peptitleri antimikrobiyel özellik kazanmaları doğrultusunda modifiye etmiştir. Sonuçlar, hidrofobik LLIIL kalıntılarının peptit N-terminaline eklenmesinin, antibiyotik direncine karşı savaşta yeni antimikrobiyel peptitler tasarlamak için umut verici bir strateji sunabileceğini düşündürmektedir.

TABLE OF CONTENTS

ACKNOWLEDGEMENTS iii
ABSTRACT iv
ÖZET v
LIST OF FIGURES xii
LIST OF TABLES xxxii
LIST OF SYMBOLS xxxiii
LIST OF ACRONYMS/ABBREVIATIONS xxxiv
1. INTRODUCTION 1
2. THEORETICAL BACKGROUND 3
2.1. Membrane Active Peptides 3
2.1.1. Antimicrobial Peptides (AMPs) 3
2.1.1.1. Antimicrobial Peptide Melittin 4
2.1.2. Cell-Penetrating Peptides (CPPs) 5
2.1.2.1. Cell-penetrating Peptide pVEC 7
2.1.3. Analysis of Membrane Active Peptides by Computational Methods 8
2.1.4. Visualization of Membrane Active Peptides by Microscopy Techniques 11
2.2. Beta-Lactam Antibiotics and Beta-Lactamase Mediated Resistance . . 13
2.2.1. Beta-Lactam Antibiotics 13
2.2.2. Beta-Lactamases 14
2.2.3. Beta-Lactamase Inhibitors and the Beta-Lactamase Inhibitor Protein (BLIP) 15
2.2.3.1. Beta-Lactamase Inhibitor Protein (BLIP) 15
3. MATERIAL AND METHODS 17
3.1. Membrane Translocation Simulations and Analysis 17
3.1.1. Preparation and Equilibration of the Simulations Systems . . . 17
3.1.1.1. Peptides Used in the Study 17
3.1.1.2. Equilibration of Peptides in Water Box 17
3.1.1.3. Preparation and Equilibration of the POPE Lipid Bilayer 19

3.1.1.4. Preparation and Equilibration of the Peptide-Lipid Systems 21
3.1.2. Steered Molecular Dynamics of Peptide Translocation 22
3.1.3. Stretching Simulations of pVEC 24
3.1.4. Umbrella Sampling and Replica Exchange Umbrella Sampling . 25
3.1.5. Potential of Mean Force (PMF) Calculations 27
3.1.6. Application of Dimensionality Reduction Algorithms 28
3.1.6.1. Principal Component Analysis (PCA) 28
3.1.6.2. Isometric Feature Mapping (ISOMAP) 29
3.2. In-vitro Enzyme Kinetics 29
3.3. Measurement of Drug Effects on Bacterial Growth 30
3.3.1. Bacterial Strains and Growth Conditions 30
3.3.2. Drugs Used in the Study 30
3.3.3. Determination of Antibacterial Activity and Viable Cell Count in 2 mL Cultures 33
3.3.4. Determination of Minimal Inhibitory Concentration, and Number of Colony Forming Units 34
3.4. Visualization of Drug Effects on Bacteria 38
3.4.1. Time-lapse Microscopy Using Agarose Pads and Cover Glass Chambers 38
3.4.2. Direct Measurement of Cell Viability and Membrane Permeability 39
3.4.3. Visualization of Drug Effects on Cell Surface and Structure . . . 42
3.4.4. Visualization of Peptide Uptake Using Fluorescence Microscopy 44
3.4.5. Live Cell Imaging with Microfluidic Systems 46
3.4.5.1. Testing of the Reaction Chips with Beads 47
3.4.5.2. Testing of the Reaction Chips with Bacteria 47
3.4.5.3. Bacterial Uptake of Fluorescein Amine in Reaction Chips 48
3.4.5.4. Bacterial Uptake of BacLight Bacterial Viability Kit in Reaction Chips 49
3.4.5.5. Bacterial Uptake of pVEC and P4 Peptides in Reaction Chips 50

3.5. Drug Effects in Mammalian Cell Culture 51
3.5.1. Drug Effects on HeLa Cells 51
3.5.2. Measurement of Cytotoxicity Using XTT Proliferation Assay . . 52
3.5.3. Measurement of Cytotoxicity Using Cell Counter and Trypan Blue Dye 53
4. RESULTS AND DISCUSSION 56
4.1. Membrane Translocation Simulations of Membrane Active Peptides . . 56
4.1.1. SMD Simulations of Membrane Translocation of Beta-Lactamase Inhibitory Peptides 56
4.1.2. SMD Simulations of Membrane Translocation of pVEC and its Mutants 64
4.1.2.1. SMD Simulation of Membrane Translocation of wild-type pVEC 64
4.1.2.2. SMD Simulation of Membrane Translocation of pVEC-1 68
4.1.2.3. SMD Simulation of Membrane Translocation of pVEC-2 71
4.1.2.4. SMD Simulation of Membrane Translocation of pVEC-9 77
4.1.2.5. SMD Simulation of Membrane Translocation of pVEC-11 81
4.1.2.6. Comparison of Membrane Translocation of pVEC and the Mutants 86
4.1.3. Equilibration of the pVEC and del5 pVEC Peptides 92
4.1.4. SMD Simulations of pVEC and del5 pVEC Peptides 93
4.1.5. Stretching Simulations of pVEC 95
4.1.6. Umbrella Sampling Simulations of Membrane Translocation . . 98
4.1.6.1. PMF Calculation for pVEC Membrane Translocation . 98
4.1.6.2. PMF Calculation for del5 pVEC Membrane Translocation 99
4.1.6.3. Comparison of the PMF profiles 100
4.1.7. Replica Exchange Umbrella Sampling Simulations of Peptide Translocation 102
4.1.7.1. PMF Calculation for the Membrane Translocation of pVEC 103

4.1.7.2. PMF Calculation for the Membrane Translocation of del5 pVEC . . . 106
4.1.7.3. Comparison of the PMF Profiles . . . 109
4.1.8. Analysis of Simulation Trajectories by Dimensionality Reduction Algorithms . . . 110
4.1.8.1. PCA and ISOMAP Applications on Stretching Simulation of pVEC . . . 111
4.1.8.2. PCA and ISOMAP Applications on Translocation Simulations . . . 112
4.2. In-vitro Enzyme Kinetics of Beta-lactamase Inhibitory Peptides . . . 117
4.3. Effect of Drugs on Growth of Bacterial Cells . . . 119
4.3.1. Effect of DMSO on Bacterial Growth . . . 119
4.3.2. Effect of Melittin on Bacterial Growth . . . 121
4.3.3. Effect of Ampicillin on Bacterial Growth . . . 128
4.3.4. Effect of Potassium Clavulanate on Bacterial Growth . . . 131
4.3.5. Effect of pVEC and del5 pVEC Peptides on Bacterial Growth . 134
4.3.6. Effect of P1 and P2 Peptides on Bacterial Growth . . . 136
4.3.7. Effect of P2r Peptide on Bacterial Growth . . . 138
4.3.8. Effect of P3A Peptide on Bacterial Growth . . . 143
4.3.9. Effect of P3 Peptide on Bacterial Growth . . . 145
4.3.10. Effect of P4 Peptide on Bacterial Growth . . . 148
4.3.11. Comparison of the Antibacterial Activity of Drugs . . . 155
4.3.12. Drug Synergy Tests . . . 158
4.4. Visualization of Drug Effects on Bacteria . . . 161
4.4.1. Visualization of Membrane Permeability and Bacterial Viability 161
4.4.1.1. Visualization of P1 Effects on Cells Using Time-Lapse Microscopy . . . 161
4.4.1.2. Bacterial Viability Tests with wild-type and Antibiotic Resistant Cells . . . 162
4.4.1.3. Effect of Melittin on Bacterial Viability . . . 165
4.4.1.4. Effect of Ampicillin on Bacterial Viability . . . 165

4.4.1.5. Effect of Potassium Clavulanate on Bacterial Viability 168
4.4.1.6. Effect of Potassium Clavulanate & Ampicillin on Bacterial Viability 169
4.4.1.7. Effect of pVEC and del5 pVEC peptides on Bacterial Bacterial Viability 170
4.4.1.8. Effect of P2 Peptide on Bacterial Viability 172
4.4.1.9. Effect of P2r Peptide on Bacterial Viability 172
4.4.1.10. Effect of P3A Peptide on Bacterial Viability 175
4.4.1.11. Effect of P3 Peptide on Bacterial Viability 176
4.4.1.12. Effect of P4 Peptide on Bacterial Viability 177
4.4.2. Visualization of Drug Effects on Bacteria Using Scanning Electron Microscopy 182
4.4.2.1. Visualization of Bacteria Using Scanning Electron Microscopy 182
4.4.2.2. Visualization of DMSO Effects on Cell Surface 183
4.4.2.3. Visualization of Melittin Effects on Cell Surface 184
4.4.2.4. Visualization of Ampicillin Effects on Cell Surface . . . 186
4.4.2.5. Visualization of Potassium Clavulanate Effects on Cell Surface 188
4.4.2.6. Visualization of Potassium Clavulanate & Ampicillin Effects on Cell Surface 189
4.4.2.7. Visualization of pVEC and del5 pVEC Peptide Effects on Cell Surface 191
4.4.2.8. Visualization of P2r Peptide Effects on Cell Surface . . 193
4.4.2.9. Visualization of P4 Peptide Effects on Cell Surface . . 194
4.4.3. Visualization of Peptide Uptake 196
4.4.3.1. Visualization of P1 and P2 Uptake Using Confocal Microscopy 197
4.4.3.2. Visualization of pVEC Uptake 198
4.4.3.3. Visualization of P4 Uptake 199
4.4.4. Live Cell Imaging with Microfluidic Systems 201

4.4.4.1. Reaction Chip Test Using Beads 201
4.4.4.2. Bacterial Growth in the Reaction Chip 201
4.4.4.3. Bacterial Uptake of Fluorescein Amine 203
4.4.4.4. Bacterial Uptake of the Bacterial Viability Kit 204
4.4.4.5. Bacterial Uptake of pVEC Peptide 207
4.4.4.6. Bacterial Uptake of P4 Peptide 209
4.5. Drugs Effects in Mammalian Cell Culture 211
4.5.1. Effect of P1 on HeLa Cells 211
4.5.2. Measurement of Drug Cytotoxicity Using XTT Assay 212
4.5.3. Measurement of Drug Cytotoxicity Using Cell Counter and Trypan Blue 216
5. CONCLUSIONS AND RECOMMENDATIONS 221
REFERENCES 224

LIST OF FIGURES

Figure 3.1. Solvated CHARMM-GUI POPE bilayer system. The initial assembly (a) and the final system (b) after the 6 cycles of equilibration and 25 ns of production run. 20

Figure 3.2. Simulation systems of del5 pVEC (a) and pVEC (b) before membrane translocation simulations. Peptides are shown as ribbons, lipid tails in silver lines, P heads in blue spheres, and Na^+ and Cl^- are as yellow and cyan spheres, respectively. 22

Figure 3.3. Snapshots taken from pVEC-1 SMD simulation. When the peptide is above the membrane (left), fully embedded in the membrane (center), and after the peptide exits the membrane (right). 23

Figure 3.4. The protocol diagram for determination of minimal inhibitory concentration (MIC) and number of colony forming units (CFUs). . . 35

Figure 3.5. CFU counts of the sample at $OD_{600} = 0.2$ (Sample 1), when Sample 1 is diluted 1:100 (Sample 2) and when Sample 1 is diluted 1:500 (Sample 3). 37

Figure 3.6. The protocol diagram for bacterial viability experiments. 41

Figure 3.7. Sample preparation for visualization of cell viability and membrane permeability using fluorescence microscopy. (a) The culture samples are adsorbed on the agar support surface, (a) then coverslip is placed on top of the support. 42

Figure 3.8. The protocol diagram of sample preparation for SEM imaging. . . 44

Figure 3.9. Schematic of the reaction chamber chips that are used in the experiments. 47

Figure 3.10. Water and viability dye solution tubings were connected, and their outlet was connected to the culture tubing (left). The outlet of latter connector was connected to the chip via a Male Mini Luer fluid connector (right). 50

Figure 4.1. Initial and final structures of P1 peptide. Initial structures were assigned as either beta-hairpin or extended chain. Final structures were obtained after minimization and equilibration in water. . . . 56

Figure 4.2. Initial and final structures of P1 peptide in the peptide-lipid-water system. 57

Figure 4.3. Initial and final structures of P2 peptide. Initial structures were assigned as either beta-hairpin or extended chain. Final structures were obtained after minimization and equilibration in water. . . . 58

Figure 4.4. Interaction energy (top) and force (bottom) profiles of each P1 (left) and P2 (right) SMD simulation. 59

Figure 4.5. Average interaction energy (left) and force (right) profiles of P1 (top) and P2 (bottom) SMD simulations. 60

Figure 4.6. Electrostatic energy profiles of P1 (top left), and P2 (top right), and snapshots from the simulation trajectories of P1 and P2. . . . 61

Figure 4.7. (a) Order parameters of the bilayer palmitoyl (top), and oleyl (bottom) carbon atoms in the presence or absence of the peptides. (b) Order parameters of C2 (top), C8 (center) and C16 (bottom) carbon atoms in the presence of P1 or P2. 62

Figure 4.8. Number of hydrogen bonds formed over 40 ns simulation time for P1 (a) and 45 ns simulation time for P2 (b). The hydrogen bonds formed between the LLIIL tail of P2 and the lipid are highlighted in yellow (b). 63

Figure 4.9. (a) Number of water molecules that penetrate into the membrane during translocation of wild-type pVEC with respect to the z coordinate of the SMD atom. (b) Snapshots of the trajectory taken at the corresponding time points labeled in a. 65

Figure 4.10. Force applied on wt-pVEC peptide during the simulation with respect to the z coordinate of the SMD atom. 66

Figure 4.11. Interaction energy between the wt-pVEC peptide and the membrane with respect to the z coordinate of the SMD atom. 66

Figure 4.12. Snapshots corresponding to the stages observed in the interaction energy profile of the wt-pVEC with the membrane. Water molecules are not shown for clarity. 68

Figure 4.13. (a) Number of water molecules that penetrate into the membrane during translocation of pVEC-1 with respect to the z coordinate of the SMD atom. (b) Snapshots of the trajectory taken at the corresponding time points labeled in a. 69

Figure 4.14. Force applied on the pVEC-1 peptide during the simulation with respect to the z coordinate of the SMD atom. 70

Figure 4.15. Interaction energy between the pVEC-1 peptide and the membrane with respect to the z coordinate of the SMD atom. 71

Figure 4.16. Snapshots corresponding to the stages observed in the interaction energy profile of the pVEC-1 peptide with the membrane. Water molecules are not shown for clarity. 72

Figure 4.17. (a) Number of water molecules that penetrate into the membrane during translocation of pVEC-2 with respect to the z coordinate of the SMD atom. (b) Snapshots of the trajectory taken at the corresponding time points labeled in a. 73

Figure 4.18. Force applied on the pVEC-2 peptide during the simulation with respect to the z coordinate of the SMD atom. 74

Figure 4.19. Interaction energy between the pVEC-2 peptide and the membrane with respect to the z coordinate of the SMD atom. 75

Figure 4.20. Snapshots corresponding to the stages observed in the interaction energy profile of the pVEC-2 peptide with the membrane. Water molecules are not shown for clarity. 76

Figure 4.21. (a) Number of water molecules that penetrate into the membrane during translocation of pVEC-9 with respect to the z coordinate of the SMD atom. (b) Snapshots of the trajectory taken at the corresponding time points labeled in a. 78

Figure 4.22. Force applied on the pVEC-9 peptide during the simulation with respect to the z coordinate of the SMD atom. 79

Figure 4.23. Interaction, electrostatic and Van der Waals energy profiles energy between the pVEC-9 peptide and the membrane with respect to the z coordinate of the SMD atom. 80

Figure 4.24. Snapshots corresponding to the stages observed in the interaction energy profile of the pVEC-9 peptide with the membrane. Water molecules are not shown for clarity. 81

Figure 4.25. (a) Number of water molecules that penetrate into the membrane during translocation of pVEC-11 with respect to the z coordinate of the SMD atom. (b) Snapshots of the trajectory taken at the corresponding time points labeled in a. 82

Figure 4.26. Force applied on the pVEC-11 peptide during the simulation with respect to the z coordinate of the SMD atom. 84

Figure 4.27. Interaction, electrostatic and Van der Waals energy profiles energy between the pVEC-11 peptide and the membrane with respect to the z coordinate of the SMD atom. 85

Figure 4.28. Snapshots corresponding to the stages observed in the interaction energy profile of the pVEC-11 peptide with the membrane. Water molecules are not shown for clarity. 86

Figure 4.29. Number of water molecules that penetrate into the membrane during simulations with wt-pVEC (black), pVEC-1 (green), pVEC-11 (blue), pVEC-2 (red) or pVEC-9 (purple) with respect to the z coordinate of the SMD atom. 87

Figure 4.30. Water pore formation during the translocation of the pVEC peptides. 87

Figure 4.31. Force profiles of wt-pVEC (black), pVEC-1 (green), pVEC-11 (blue), pVEC-2 (red) and pVEC-9 (purple) with respect to the z coordinate of the SMD atom. 88

Figure 4.32. Interaction, electrostatic and van der Waals energy profiles of wt-pVEC (black), pVEC-1 (green), pVEC-11 (blue), pVEC-2 (red) and pVEC-9 (purple) with respect to the z coordinate of the SMD atom. 89

Figure 4.33. Work done on the peptide during the translocation of wt-pVEC (black), pVEC-1 (green), pVEC-11 (blue), pVEC-2 (red) and pVEC-9 (purple) with respect to the z coordinate of the SMD atom. . . . 90

Figure 4.34. Order parameters calculated for the membrane in the presence of wt-pVEC (black triangles), pVEC-1 (green dots), pVEC-2 (red asterisks), pVEC-11 (blue circles) or pVEC-9 (purple asterisks) and in the absence peptides (squares). 91

Figure 4.35. Equilibration of pVEC peptides. (a) RMSD profiles of pVEC (red) and del5 pVEC (blue) peptides during the simulations. (b) Initial peptide conformations, and conformations extracted after 40 ns, 65 ns and 86 ns of equilibration. 92

Figure 4.36. Analysis of the SMD simulations of pVEC (black), del5 pVEC (red) peptides translocating the POPE bilayer. 94

Figure 4.37. Stretching of wild-type pVEC. (a) Initial structure with an end-to-end distance of 27.7 Å, (b) after 2 ns the distance is increased to 40.28 Å, (c) at the end of the simulation the distance was 56.47 Å. 95

Figure 4.38. Stretching of pVEC using the collective variables module. The change in energy (top) and radius of gyration (bottom) are plotted for the whole simulation. 96

Figure 4.39. Stretching of pVEC using SMD. The change of end-to-end distance and force applied are plotted with respect to the simulation time. Force applied and work done are also plotted with respect to the end-to-end distance of the peptide. 97

Figure 4.40. Stretching of pVEC (red) in comparison with its membrane translocation (black). 98

Figure 4.41. Histograms of z-distance between the SMD atom and the lipid bilayer for each umbrella window. 99

Figure 4.42. The potential of mean force for the membrane translocation of pVEC peptide as a function of the z-distance between the center of mass of the bilayer and the peptide N-terminus. 100

Figure 4.43. The potential of mean force for the membrane translocation of del5 pVEC peptide as a function of the z-distance between the center of mass of the bilayer and the peptide N-terminus. 101

Figure 4.44. Comparison of the PMF profiles for the membrane translocation of pVEC and del5 pVEC peptides. 102

Figure 4.45. Comparison of 4 pVEC REUS simulations with 1 Å or 2 Å replica spacing. PMF (a) and accepted exchange percentage (b) between replicas are plotted as a function of the z-distance of the peptide center of mass lipid center. 104

Figure 4.46. REUS simulations for the membrane translocation of pVEC peptide. PMF (a) and accepted exchange percentage between replicas (b) plotted as a function of the peptide-lipid distance corresponding to each replica. 105

Figure 4.47. Comparison of del5 pVEC REUS simulations with 1 Å and 2 Å replica spacing. PMF (a) and accepted exchange percentage (b) between replicas are plotted as a function of the z-distance of the peptide center of mass lipid center. 107

Figure 4.48. REUS simulations for the membrane translocation of del5 pVEC peptide. PMF (a) and accepted exchange percentage between replicas (b) plotted as a function of the peptide-lipid distance corresponding to each replica. 108

Figure 4.49. Comparison of the PMF profiles generated from REUS simulations of pVEC (black) and del5 pVEC (red) translocating the POPE bilayer. 110

Figure 4.50. PCA (a) and ISOMAP (b) projections of the pVEC stretching simulation. (c) First principal component (PC1) and (d) first ISOMAP dimension (DIM1) are plotted with respect to the end-to-end distance. 112

Figure 4.51. PCA applied on the membrane translocation simulation of pVEC. First two principal components are shown with z-coordinate (a) and force (b) color-coding. PC1 is plotted with respect to the z-coordinate (c) and radius of gyration(d). 113

Figure 4.52. Comparison of PCA results for four different pVEC systems; (a) wt-pVEC, (b) retro-pVEC, (c) scr-pVEC, (d) del5 pVEC. Data is color-coded with respect to z coordinate of the SMD atom. 114

Figure 4.53. ISOMAP applied on the membrane translocation simulation of pVEC. First three dimensions are shown with z-coordinate (a,b) color-coding. DIM1 is plotted with respect to the z-coordinate (c) and radius of gyration(d). 116

Figure 4.54. Comparison of ISOMAP results for four different pVEC systems; (a) wt-pVEC, (b) retro-pVEC, (c) scr-pVEC, and (d) del5 pVEC. Data points are color-coded with respect to z coordinate of the SMD atom. 117

Figure 4.55. Growth curves of *E. coli* K12 (left) and *E. coli* K12 pUC18 (right) cultures for 20 hours of incubation. Bacteria at standard inoculum (top) and high inoculum (bottom) dose were treated with different DMSO concentrations. 120

Figure 4.56. The photograph of the plate after incubation of 20 hours (left) and the plate setup used in the experiment (right). 121

Figure 4.57. Absorbance measurement (at 600 nm) of all samples for each row (rows A-H) of the microplate. 122

Figure 4.58. The photograph of the plate after incubation of 20 hours (left) and the plate setup used in the experiment (right). 123

Figure 4.59. Absorbance measurement (at 600 nm) of all samples for each row (rows A-H) of the microplate. 124

Figure 4.60. Growth curve of *E. coli* K12 pUC18 cultures treated with different melittin concentrations for 20 hours. Control curves are the average of each set and plotted with the standard error of the mean. . . . 125

Figure 4.61. Growth curves of *E. coli* K12 (left) and *E. coli* K12 pUC18 (right) cultures for 20 hours of incubation. Bacteria at standard inoculum (top) and high inoculum (bottom) dose were treated with different melittin concentrations. 127

Figure 4.62. Number of colony forming units (A) in antibiotic resistant *E. coli* K12 pUC18 and (B) in wild-type *E. coli* K12 cultures after 2 hours of incubation with sub-MIC and MIC of melittin compared with the control samples. 128

Figure 4.63. Growth curves of *E. coli* K12 (left) and *E. coli* K12 pUC18 (right) cultures for 20 hours of incubation. Bacteria at standard inoculum (top) and high inoculum (bottom) dose were treated with different ampicillin concentrations. 129

Figure 4.64. Number of colony forming units (top) in antibiotic resistant *E. coli* K12 pUC18 and (bottom) in wild-type *E. coli* K12 cultures after 2 hours of incubation with sub-MIC and MIC of ampicillin compared with the control samples. 130

Figure 4.65. Growth curves of *E. coli* K12 (left) and *E. coli* K12 pUC18 (right) cultures for 20 hours of incubation. Bacteria at standard inoculum (top) and high inoculum (bottom) dose were treated with different PC concentrations. 132

Figure 4.66. Number of colony forming units (top) in antibiotic resistant *E. coli* K12 pUC18 and (bottom) in wild-type *E. coli* K12 cultures after 2 hours of incubation with sub-MIC and MIC of (PC) compared with the control samples. 133

Figure 4.67. Growth curves of *E. coli* K12 (left) and *E. coli* K12 pUC18 (right) cultures for 20 hours of incubation. Bacteria at standard inoculum (top) and high inoculum (bottom) dose were treated with different peptide concentrations. 134

Figure 4.68. Growth curves of *E. coli* K12 (left) and *E. coli* K12 pUC18 (right) cultures for 20 hours of incubation. Bacteria at standard inoculum (top) and high inoculum (bottom) dose were treated with different peptide concentrations. 135

Figure 4.69. Number of colony forming units in wild-type *E. coli* K12 cultures after 2 hours of incubation with sub-MIC and MIC of pVEC, and 500 μM del5 pVEC compared with the control samples. 136

Figure 4.70. Growth profiles (left) and colony forming units (right) in the presence of 100 μM peptide (circles) or in the absence of peptide (stars) for *E. coli* K12 pUC18 or *E. coli* K12 cells treated with P1 or P2. 0 hour indicates the time of peptide addition. 137

Figure 4.71. The microplate setup used in the experiment. 139

Figure 4.72. Growth curves of the P2r peptide treated cultures and control samples for the first 2 hours of incubation (top), for 4 hours of incubation (middle), and for 20 hours of incubation (bottom). 140

Figure 4.73. Comparison of CFU counts for the P2r treated and control samples in *E. coli* K12 pUC18 cultures after incubation for 2 or 4 hours. The average counts are shown for the control sample CFUs. 141

Figure 4.74. Growth curves of bacteria at $7x10^6$ CFU/mL cell density (left) and at $7x10^5$ CFU/mL cell density (right) treated with different P2r peptide concentrations. 141

Figure 4.75. Comparison of CFU counts for the P2r treated and control samples in *E. coli* K12 cultures after incubation for 2 or 4 hours. The average counts are shown for the control sample CFUs. 142

Figure 4.76. The microplate setup used in the experiment. 143

Figure 4.77. Growth curves of the P3A peptide treated cultures and control samples for the first 2 hours of incubation (top), for 4 hours of incubation (middle), and for 20 hours of incubation (bottom). . . 144

Figure 4.78. Comparison of CFU counts for the P3A treated and control samples in *E. coli* K12 pUC18 cultures after incubation for 2 or 4 hours. The average counts are shown for the control sample CFUs. 145

Figure 4.79. Growth curves of *E. coli* K12 (left) and *E. coli* K12 pUC18 (right) cultures for 20 hours of incubation. Bacteria at standard inoculum (top) and high inoculum (bottom) dose were treated with different P3 peptide concentrations. 146

Figure 4.80. Number of colony forming units (top) in antibiotic resistant *E. coli* K12 pUC18 and (bottom) in wild-type *E. coli* K12 cultures after 2 hours of incubation with 500 μM of P3 peptide compared with the control samples. 147

Figure 4.81. The microplate setup used in the experiment. 148

Figure 4.82. Growth curves of the P4 peptide treated and control samples for the first 2 hours of incubation (top), and for 4 hours of incubation (bottom). 149

Figure 4.83. Comparison of CFU counts for the P4 treated and control samples in *E. coli* K12 pUC18 cultures after incubation for 2 or 4 hours. The average counts are shown for the control sample CFUs. 150

Figure 4.84. Growth curves of *E. coli* K12 pUC18 bacteria at $7x10^6$ CFU/mL cell density (left) and at $7x10^5$ CFU/mL cell density (right) treated with treated with different P4 peptide concentrations. 150

Figure 4.85. The microplate setup used in the experiment. 151

Figure 4.86. Comparison of CFU counts for the P4 treated and control *E. coli* K12 cultures after incubation for 2, 4, and 20 hours. The average counts are shown for the control sample CFUs. 152

Figure 4.87. Growth curves of *E. coli* K12 (left) and *E. coli* K12 pUC18 (right) cultures for 20 hours of incubation. Bacteria at standard inoculum (top) and high inoculum (bottom) dose were treated with different P4 peptide concentrations. 153

Figure 4.88. Number of colony forming units (top) in antibiotic resistant *E. coli* K12 pUC18 and (bottom) in wild-type *E. coli* K12 cultures after 2 hours of incubation with sub-MIC and MIC of P4 peptide compared with the control samples. 154

Figure 4.89. Growth curves of *E. coli* K12 pUC18 cultures for 20 hours of incubation. Bacteria at standard inoculation cell density (left) and high inoculation cell density (right) were treated with different concentrations of drug combinations. 160

Figure 4.90. Time-lapse imaging of cells incubated with P1. Within a recording time of approximately 3.5 hours, 4-5 cell cycles were observed. . . 162

Figure 4.91. Snapshots of antibiotic resistant cells, green and red fluorescence overlaid (top), green fluorescence (middle-left), red fluorescence (middle-right), and their counts (bottom). 163

Figure 4.92. Snapshots of wild-type bacteria incubated with ampicillin for 1 hour. Green and red fluorescence overlaid (top), green fluorescence (middle-left), red fluorescence (middle-right), and their counts (bottom). 164

Figure 4.93. Fluorescence microscopy images of *E. coli* K12 (left) and *E. coli* K12 pUC18 (right) cells treated with sub-MIC and MIC of melittin, compared with the control samples (top). 166

Figure 4.94. Fluorescence microscopy images of *E. coli* K12 (left) and *E. coli* K12 pUC18 (right) cells treated with sub-MIC and MIC of ampicillin, compared with the control samples (top). 167

Figure 4.95. Fluorescence microscopy images of *E. coli* K12 (left) and *E. coli* K12 pUC18 (right) cells treated with sub-MIC and MIC of potassium clavulanate, compared with the control samples (top). 168

Figure 4.96. Fluorescence microscopy images of *E. coli* K12 pUC18 cells treated with sub-MIC/2 and sub-MIC of potassium clavulanate (PC) & ampicillin combination, compared with the control sample (top). . 170

Figure 4.97. Fluorescence microscopy images of control samples and *E. coli* K12 cells treated with pVEC or del5 pVEC peptides. Cells were incubated with SYTO9 and PI nucleic acid dyes before imaging. . . . 171

Figure 4.98. Microscopy images of *E. coli* K12 pUC18 cells that were either incubated with buffer solution (left) or 100 μM P2 peptide (right) for four hours. Images captured using green and red microscopy filters were overlaid. 173

Figure 4.99. Microscopy images of antibiotic resistant *E. coli* K12 pUC18 cultures that were either incubated with buffer solution (top) or with 100 μM P2r peptide (center) or with 200 μM P2r peptide (bottom) for four hours. 174

Figure 4.100. Microscopy images of antibiotic resistant (left) and wild-type (right) cultures that were either incubated with buffer solution (top) or with 100 μM P2r peptide (center) or with 200 μM P2r peptide (bottom) for four hours. 175

Figure 4.101. Microscopy images of antibiotic resistant *E. coli* K12 pUC18 cultures that were either incubated with buffer solution (top) or with 100 μM P3A peptide (bottom) for two (left) or four (right) hours. 176

Figure 4.102. Fluorescence microscopy images of *E. coli* K12 (left) and *E. coli* K12 pUC18 (right) cells treated with 500 μM of P3 peptide, compared with the control samples (top). 177

Figure 4.103. Microscopy images of antibiotic resistant *E. coli* K12 pUC18 cultures that were either incubated with buffer solution (D3) or with 20 μM (C1), 40 μM (C2), 80 μM (C3) P4 peptide for four hours. . 178

Figure 4.104. Microscopy images of *E. coli* K12 pUC18 cells, either incubated with buffer solution (left) or with 80 μM P4 peptide (right) for two hours, either without agar supports (top), or with agar gel supports (bottom). 179

Figure 4.105. Microscopy images of antibiotic resistant cells that were either incubated with buffer solution (top) or with 80 μM P4 peptide (center) or with 160 μM P4 peptide (bottom) for two (left) or four (right) hours. 180

Figure 4.106. Fluorescence microscopy images of *E. coli* K12 (left) and *E. coli* K12 pUC18 (right) cells treated with sub-MIC and MIC of P4 peptide, compared with the control samples (top). 181

Figure 4.107. SEM images of *E. coli* K12 pUC18 cells. (A) Cells captured at 2000X, and (B) 8000X magnification. (C) At 10000X magnification cell surface can be observed, (D) a less crowded area captured at 10000X magnification. 183

Figure 4.108. SEM images of control samples treated with water (A, B), and DMSO treated *E. coli* K12 pUC18 (C, E) and *E. coli* K12 (D, F) cells. 184

Figure 4.109. SEM images of *E. coli* K12 pUC18 (C and E) or *E. coli* K12 (D, F, and G) cells treated with different concentrations of melittin in comparison with the control samples (A and B). Images are captured with 8000X magnification. 185

Figure 4.110. SEM images of control samples (top row) and ampicillin treated *E. coli* K12 pUC18 (left column) and *E. coli* K12 (right column) cells. 187

Figure 4.111. SEM images of control samples (A, B) and potassium clavulanate treated *E. coli* K12 pUC18 (C, E) and *E. coli* K12 (D, F) cells. . . 189

Figure 4.112. SEM images of control sample (A) and *E. coli* K12 pUC18 cells treated with different concentrations of the potassium clavulanate (PC) and ampicillin (Amp) combination (B, C). 190

Figure 4.113. SEM images of control samples (top row) and *E. coli* K12 cells treated with pVEC (left column) or del5 pVEC (right column) peptides. 192

Figure 4.114. SEM images of *E. coli* K12 pUC18 (C) or *E. coli* K12 (D) cells treated with 100 μM P2r peptide in comparison with the untreated cells (A and B). Images are captured with 8000X magnification. . 193

Figure 4.115. SEM images of *E. coli* K12 pUC18 (C) or *E. coli* K12 (D) cells treated with 80 μM P4 peptide in comparison with the untreated cells (A and B). Images are captured with 8000X magnification. . 194

Figure 4.116. SEM images of control samples (top row) and P4 peptide treated *E. coli* K12 pUC18 (left column) and *E. coli* K12 (right column) cells. 196

Figure 4.117. Captures of cells 4 hours after incubation with (a, b) P1 or (c, d) P2. (a) and (c) are the phase microscopy, (b) and (d) are the fluorescence microscopy images. 197

Figure 4.118. Visualization of pVEC uptake after 30 minutes (top row), 90 minutes (middle row), and 180 minutes (bottom row) of incubation time, under brightfield (left) and UV with FITC filter (right). . . . 199

Figure 4.119. Visualization of P4 uptake after 30 minutes (top row), 90 minutes (middle row), and 180 minutes (bottom row) of incubation time, under brightfield (left) and under UV with FITC filter (right). . . 200

Figure 4.120. Microscopy images of the chip test with beads. After bead loading (i), distilled water was pumped. Images were captured from the same spot after (ii) 1 hour, (iii) 2 hours, (iv) 3 hours, (v) 4 hours, and (vi) after 5 hours. 202

Figure 4.121. Microscopy images of bacterial growth captured at 60X zoom. After cell loading (i), only LB medium was pumped. Images were captured from the same spot every 15 minutes (ii-xi) in total experiment duration of 2.5 hours. 203

Figure 4.122. Microscopy images of the chip at the end of the experiment. At the end of 2.5 hours (left) the chamber was filled with bacteria, and (right) the outlet well had a much lower concentration of bacteria swept away by the flow. 204

Figure 4.123. Microscopy images of bacterial uptake of fluorescein amine. After cell loading, fluorescein amine was perfused (i) for 1 hour. Images were captured from the same spot every 15 min (ii-iv). After 1.5 hours (vii), only LB medium was pumped. 205

Figure 4.124. Microscopy images of bacterial viability dye uptake. After cell loading, viability dye was perfused. After 30 minutes of incubation time (i), images were captured from the same spot every 30 minutes. . . 206

Figure 4.125. Microscopy images of pVEC uptake. After cell loading, pVEC was perfused. After 30 minutes of incubation time, images were captured from the same spot every 30 minutes. 208

Figure 4.126. Microscopy images of P4 uptake. After cell loading, P4 solution pump was switched on, and images were captured from the same spot every 30 minutes under brightfield (left column) and UV with FITC filter (right column). 210

Figure 4.127. Snapshots of cells in PBS added medium on days 1 (left), 3 (middle) and 6 (right). 211

Figure 4.128. Snapshots of cells in amp and PBS added medium on days 1 (left), 3 (middle) and 6 (right). 212

Figure 4.129. Snapshots of cells in P1 and amp added medium on days 1 (left), 3 (middle) and 6 (right). 212

Figure 4.130. Plate layout used in the cytotoxicity experiment (top). Plate photograph after 3 hours of incubation with the cell proliferation assay (bottom). 213

Figure 4.131. Percent viability of HK-2 cultures treated with (top) melittin or potassium clavulanate, and (bottom) treated with ampicillin with respect to the nontreated cultures. Nontreated cultures are assumed to be 100% viable. 214

Figure 4.132. Percent viability of HK-2 cultures treated with different concentrations of ampicillin, pVEC peptide or P4 peptide with respect to the nontreated cultures. Nontreated cultures are assumed to be 100% viable. 215

Figure 4.133. Microscopy images of HK-2 cells upon 24 hour treatment with melittin, potassium clavulanate, ampicillin, pVEC, and P4 peptide in comparison with the nontreated cells. 218

Figure 4.134. Percent viability of HK-2 cultures treated with MIC of melittin, ampicillin, potassium clavulanate, pVEC, and P4 peptide with respect to the nontreated cultures. 219

LIST OF TABLES

Table 3.1. Peptides used in the membrane translocation simulations. 18

Table 3.2. Drugs used in the study. 32

Table 3.3. OD_{600} measurements and plate counts of the sample at OD_{600} = 0.20 (Sample 1), when Sample 1 is diluted 1:100 (Sample 2) and when Sample 1 is diluted 1:500 (Sample 3). 36

Table 4.1. R-TEM-1 beta-lactamase inhibition in the presence and absence of P1. 118

Table 4.2. Minimal inhibitory concentration of each drug against antibiotic resistant *E. coli* K12 pUC18 and wild-type *E. coli* K12 bacteria at standard and high inoculum doses. 156

LIST OF SYMBOLS

D	Geodesics matrix
G	Neighbourhood graph
m	Sample mean
S	Covariance matrix
t_n	Data vector
x_n	Reduced representation of vector t_n
Å	Angstrom
Cα	Carbon alpha
ϵ	Distance cutoff
ϕ	Dihedral angle
ψ	Dihedral angle

LIST OF ACRONYMS/ABBREVIATIONS

AFM	Atomic Force Microscopy
AMP(s)	Antimicrobial Peptide(s) *or* Ampicillin
BLIP	Beta-lactamase Inhibitor Protein
CFU(s)	Colony forming unit(s)
Colvar(s)	Collective variable(s)
CPP(s)	Cell-penetrating Peptide(s)
EM	Electron Microscopy
HDP(s)	Host Defense Peptide(s)
ISOMAP	Isometric Feature Mapping
MD	Molecular Dynamics
MDS	Multidimensional Scaling
MIC	Minimal Inhibitory Concentration
PBP(s)	Penicillin-binding Protein(s)
PC	Potassium Clavulanate
PCA	Principal Component Analysis
PI	Propidium Iodide
PMF	Potential of Mean Force
PTD(s)	Protein Transduction Domain(s)
REUS	Replica Exchange Umbrella Sampling
SEM	Scanning Electron Microscopy
SMD	Steered Molecular Dynamics
US	Umbrella Sampling
VdW	Van der Waals
VMD	Visual Molecular Dynamics
WHAM	Weighted Histogram Analysis Method

1. INTRODUCTION

Passive diffusion through lipid membranes is a common mechanism for drug uptake into to the cells, but many drug candidates are disregarded as they fail to go through the membrane due to low membrane permeability [1]. Much effort has been made to develop drug carriers that can cross the membranes and transport biologically active cargo into cells. One of the biggest breakthroughs in this field is the discovery of cell-penetrating peptides (CPPs) [2, 3] that can be efficiently internalized into cells and used as carriers for intracellular delivery of bioactive molecules [4]. This ability of CPPs and their low toxicity make them promising potential delivery vectors. Recently, the design of chimeric peptides by combining parts of several peptides or proteins have been favored, since the resulting peptides carry the properties of the original sequences, and may be even more efficient than the original sequence in some cases [5].

Antibiotic resistance is a worldwide health problem and has become one of the leading causes of death in the past 20 years [6]. Bacteria are able to develop drug resistance in different mechanisms, but the production of the antibiotic inactivating beta-lactamase enzyme is the endemic mechanism of antibiotic resistance [7–9]. Successful combination therapies of beta-lactam antibiotics with beta-lactamase inhibitors have been clinically used, but beta-lactamases have evolved inhibitor resistant mutations for these therapies as well [10]. Due to the increase in the diversity of target proteins as a result of selective pressure and evolutionary process, design of novel inhibitors is still an area of intense research. Guiding this field, the beta-lactamase-beta-lactamase inhibitor protein (BLIP) complex is an attractive model both for beta-lactamase inhibitor design [11] and the study of protein-protein interactions [12].

In my previous MSc. Thesis studies, it was aimed to investigate the translocation mechanism of the cell-penetrating peptide pVEC (LLIILRRRIRKQAHAHSK) and to analyze it on a residue basis in order to identify critical residues for bacterial uptake. Wild-type and mutant pVEC peptides were chosen to be studied using steered molecular dynamics (SMD) simulations. The peptide transport was observed to occur in three

main stages and residues contributing to the interaction of pVEC with the lipid bilayer was investigated. In the experimental part of the study, the effect of two novel BLIP based peptides and a known beta-lactamase inhibitor peptide on growth of antibiotic resistant *E. coli* K12 pUC18 cells was examined. Modified BLIP based peptide was taken into the cells, as revealed by microscopy and incubation with this peptide led to cell death. The studies showed that inclusion of the five hydrophobic residues at the N-terminus enhanced the uptake potential of the inhibitory peptide.

In this study, peptide drugs will be discussed in two different points of view. In the first part, the aim is to study the cell-penetrating peptide pVEC and its variants, in order to gain insights about its membrane translocation. For this aim, computational studies on pVEC and its variants were carried out. While molecular dynamics simulations on pVEC provide information at the molecular level, the simulations of mutations and deletions on this peptide also delivered perceptions on molecular interactions that contribute to this peptide's penetration and translocation ability. Application of dimensionality reduction algorithms on molecular dynamics data was carried out as an innovative approach to analyze big data using only statistics methodology instead of physical and visual analysis of biological systems. In the second part of the study, the aim is to discover novel peptide antimicrobials that are not only periplasmic beta-lactamase inhibitors, but also can penetrate into bacteria. Inspired by the studies on the cell-penetrating peptide pVEC emphasizing the importance of its N-terminal residues (LLIIL) to the uptake of the peptide, our approach was to build a chimera. To build the chimeric peptides, beta-lactamase inhibitory peptides were combined with the hydrophobic pVEC residues (LLIIL) in the N-terminus. All proposed peptides were then tested for their antibacterial activity, membrane permeabilizing potential and their effects on cell surface. Peptides were also tested for mammalian cytotoxicity and their activity were compared to other drugs such as the antimicrobial peptide melittin, beta-lactam antibiotic ampicillin and beta-lactamase inhibitor potassium clavulanate. Finally, a live-cell imaging study was carried out with selected peptides to investigate their bacterial uptake using microfluidic chips. The methods used and results reported in this thesis promise potential toward the design of novel antimicrobials and it can hopefully guide future peptide-based drug design efforts.

2. THEORETICAL BACKGROUND

2.1. Membrane Active Peptides

Biological membranes are physical barriers with complex dynamic structures that consist of arrangements of phospholipids [13]. This physical barrier separates intracellular regions from extracellular environment to protect the cell, thus maintain membrane protein stability and function [14]. The hydrocarbon chains of the phospholipids are isolated from the aqueous phase to form a sheet-like nonpolar core region that is unfavorable to all polar and charged species [13, 14] including peptides, proteins and nucleic acids. Only ions and small molecules can readily be transported across membranes through specific channels and transporters upon stimulation with ligands [4]. One of the biggest breakthroughs in this field is the discovery of cell-penetrating peptides (CPPs) [2, 3] or protein transduction domains (PTDs) that can be efficiently internalized into cells and used as carriers for intracellular delivery of bioactive molecules [4]. Another group of peptides; antimicrobial peptides (AMPs), have multiple functions [15], but mainly bactericidal due to their membrane integrity impairment feature [16].

2.1.1. Antimicrobial Peptides (AMPs)

Antimicrobial peptides (AMPs) or host defense peptides (HDPs) were defined as a group of membrane active peptides considering their ability to kill bacteria, virus, and fungi either through membrane integrity disruption or through cellular function inhibition [17–20]. Even though antimicrobial peptides are evolutionarily ancient, they are widespread in plants and animals, suggesting that they have a fundamental role in the evolution of organisms [17]. The unique mode of action of antimicrobial peptides made them favorable and promising candidates for novel drugs against drug resistance that bacteria, fungi, and viruses may develop [17,21]. The common feature of all AMPs is their strong interactions with the cell membrane, not necessarily causing permanent membrane permeabilization, which enables AMPs to translocate into the cells [21].

AMPs may demonstrate multiple roles, including chemotactic and immunomodulatory functions [15], but their main activity is bactericidal, killing bacteria by perturbing membrane permeability [16]. AMPs take action by binding to the membrane surface below a threshold peptide-to-lipid ratio, but at higher ratios they either facilitate pore formation [22–24] resulting in cell component leakage and cell death [25, 26] or induce membrane disintegration and/or micellization by the so-called carpet mechanism [27].

Moreover, recent studies have shown that the design of chimeric peptides opens a new way of rational engineering of novel antimicrobial peptides with membrane penetration or membrane-disruptive properties. Fusing peptides to Tat11 arginine-rich motif [28], to a stretch of cationic cell-penetrating nona (D-arginine) residues [29], to the antimicrobial peptide ri-melittin [30] or to pVEC [31] results in peptides with high uptake potential.

2.1.1.1. Antimicrobial Peptide Melittin. Melittin, the principal toxic component of venom of the honey bee Apis mellifera [32–34], is a linear cationic, non-selective, amphipathic peptide of 26 amino acids [35, 36]. It exhibits high antimicrobial [33, 36–38] and antiviral activity [36], and cytotoxicity in different types of mammalian [35,39–41], and cancer cells [42].

Melittin has been favored as an antimicrobial due to its low minimal inhibitory concentration values. Melittin was tested against many bacterial strains and the killing doses were reported in the 1.6 - 15.6 μM range for *E. coli*, 0.3 - 1 μM for *Bacillus subtilis*, 0.5 - 3.9 μM for *S. aureus*, and 1 - 7.8 μM for MRSA [33, 35, 38, 43].

Melittin is a helical water-soluble peptide in its monomer or tetramer form [44]. Upon investigation of its membrane disruption mechanism, it was observed that melittin acts like a detergent on the lipid bilayers, as it forms aggregates of tetramers, which penetrate into the phospholipid bilayers to later disrupt them [42, 45, 46]. Scanning-electron and transmission-electron microscopy studies showed that bacteria treated with melittin had irregular cell surface with bleb formation, and upon treatment with

melittin, bacterial inner and outer membrane, and the peptidoglycan layer, were damaged [47]. In other microscopy studies, transient membrane disruption and cytoplasm leakage was observed upon treatment of bacteria with melittin [48], but pore formation occurred at a much reduced level than expected [48].

2.1.2. Cell-Penetrating Peptides (CPPs)

The hydrophilic character of peptides prevents their cellular uptake due to the hydrophobic nature of the cell wall and membranes [49]. Several strategies (such as microinjection, electroporation, liposomes and viral vectors) have been developed in order to circumvent the limitations in peptide uptake. However, all of these strategies have serious drawbacks such as toxicity and low efficiency.

An alternative in the delivery of peptide inhibitors is the use of cell penetrating peptides (CPPs) or protein transduction domains (PTDs), which can translocate the cell membrane and carry cargo into cells [2]. The strategy was inspired from the observation that two intracellular proteins Tat (HIV-1 transcriptional activator protein) [50] and pAntp (Drosophila antennapedia transcription protein) [51] were able to pass through the membrane, and they made delivery of conjugated molecules such as peptides or proteins possible. Protein transduction domains (PTDs), now mostly known as CPPs include all the peptides that are able to translocate through membranes, regardless of the characteristics of the peptides [49].

Cell penetrating peptides (CPPs) are cationic and amphipathic peptides of less than 30 residues derived from natural or unnatural proteins or chimeric sequences [2, 3, 5, 49, 52, 53], and they are able to cross the cell membrane by direct, energy-independent penetration or endocytosis [54]. CPPs, such as TAT [50], penetratin [51], transportan [55], TP10 [56], and pVEC [57] improve cargo delivery into mammalian cells, with favorable delivery and distribution properties in-vivo [58, 59]. Almost every CPP sequence includes positively charged amino acids, and most frequently studied CPPs involve a chain of arginines [5].

Initially, the CPPs classification was made based on the peptide's interaction with the cargo. The CPPs were divided into two main classes; as CPPs that require chemical linkage with the cargo, and the CPPs that involve formation of stable, non-covalent complexes with the cargo. Another classification of CPPs was proposed later, and the classes were defined based on the CPPs structural properties, affinity for phospholipids, and translocation pathways [60]. CPPs were divided into three subgroups according to their secondary structures in the presence of phospholipids. The first subgroup consists of the peptides that display no change in structure (random coil) in different phospholipids, or in different lipid/peptide ratios. The CPPs in the second subgroup adopt beta-structure, and the CPPs in the third subgroup adopt helical conformations [60].

The properties for membrane translocation of CPPs highly depend on their natural secondary structure and especially the secondary structure they adapt when they come in contact with the lipid bilayers. Although CPP-membrane interactions determine the CPPs' uptake efficiency, CPPs are known to be delivery vectors therefore; they must deliver their cargo molecules to the target. In general, when couple to larger molecules, CPPs transport their cargo using endocytosis. The steps of the process are (i) complex formation of the CPP and the cargo, (ii) interaction with the membrane and endosomal uptake, (iii) endosomal escape, (iv) localization [5, 61].

Although structure-activity relationship (SAR) studies and the utilization of endocytotic inhibitors have revealed the uptake mechanism of CPP families to some extent [5, 62–64], a complete and detailed picture of CPP uptake is not yet available. It is more likely that the CPPs follow multiple pathways including direct penetration and endocytotic uptake mediated by clathrin, caveolea and/or other molecules [5]. Although a general scheme for uptake mechanism of CPPs is missing, it is agreed that the initial contact between the CPPs and membrane involves electrostatic interactions. After the initial contact, the cellular uptake is driven by the physical properties of the CPP; the ability to interact with lipids, the type and concentration of the cargo, and the composition of the membrane [5].

In earlier studies, CPPs and CPP conjugates were thought to enter cells by direct penetration through membranes, but these studies were performed using fixed cells [4], in which chemicals used for fixation were shown to affect the internalization of the peptides, which would otherwise be adsorbed on the cell surface [65–67]. Experiments using living unfixed cells showed that endocytosis has a major role in internalization of these peptides under physiological conditions even though direct translocation across membranes and cytosolic distribution of arginine-rich CPPs may still be observed. These results suggest that there are at least two pathways, which are endocytosis and direct translocation, for CPP internalization and direct translocation is highly dependent on concentration [4]. The overall CPP uptake kinetics, specifically the three CPPs M918, TP10 and pVEC was investigated using a quenched fluorescence assay. The study proved that different CPPs might exploit different pathways simultaneously since they observed change in the uptake levels and overall kinetic profile when cells were treated with different endocytosis inhibitors [64].

Even though CPPs were discovered and defined by their cargo carrying and internalization ability [68], they share common structural properties with antimicrobial peptides (AMPs), another group of membrane active peptides. CPPs and AMPs share some physical properties such as a net positive charge, short sequences, and strong interactions with membranes [21,49]. CPPs penetratin, pVEC, TP10, and MAP demonstrate AMP action and they were shown to permeabilize and kill bacteria in infected mammalian cultures at doses that do not damage human cells [21,69–71].

2.1.2.1. Cell-penetrating Peptide pVEC. pVEC is an 18-amino acid-long CPP [57,72], derived from residues 615 - 632 of the murine vascular endothelial-cadherin (VE-cadherin) protein [73], which provide the physical contact between adjacent cells. VE-cadherin protein also participates in the control of vascular permeability and angiogenesis, and has an active role in the information transfer from the outside of the cell [73]. pVEC can carry proteins and oligomers as cargo into human aortic endothelial, brain capillary endothelial, Bowes melanoma, and murine brain endothelial cells [57,72], and can be translocated into gram-negative and gram-positive bacteria and fungi [71].

With the sequence LLIILRRRIRKQAHAHSK, pVEC has a hydrophobic N - terminus, a cationic mid-section and a polar C-terminus, making it an amphipathic molecule. The peptide sequence contains 13 cytosolic amino acids closest to the membrane and 5 amino acids from the C terminus of the transmembrane region of the VE-cadherin protein [57]. Four Arg and two Lys residues in the sequence make the peptide highly positively charged. Alanine scanning has identified the contribution of each residue to peptide's uptake by human Bowes melanoma cells and it was found that mutation of the five N-terminal residues (LLIIL) to L-alanine resulted in 50-75% reduction in cellular uptake [72]. Sequence alignment of VE-cadherin protein from different organisms showed that residues corresponding to Leu1, Leu2, Leu5, Arg6, Arg8 and Lys11 in the pVEC sequence are highly conserved, suggesting that these residues carry functional importance for the full length protein as well [74].

pVEC has a random coil structure in pure water and neutral phospholipids, but it forms a beta-sheet in negatively charged DOPG membranes [60]. However, it conserves its random coil conformation in the presence of neutral phospholipids such as DOPC (dioleoylphosphatidylcholine) or 80/20 mixture of DOPC/DOPG, and in the presence of large unilamellar vesicles composed of 40/40/20 mixture of DOPC/SM/Chol (SM: sphingomyelin, Chol: cholesterol) [60].

Even though pVEC was defined as a cell-penetrating peptide, it was later found out that pVEC has antimicrobial properties as well [71,75]. Upon treatment of bacteria with pVEC, inhibition of bacterial growth was observed at the concentration range of 16-25 μM for *E. coli* cells, at 4 μM for *B. subtilis*, *S. aureus*, and *S. epidermidis* [71,75]. pVEC was also antimicrobial against the yeast *S. cerevisiae* at concentrations higher than 25 μM [71].

2.1.3. Analysis of Membrane Active Peptides by Computational Methods

Molecular dynamics (MD) simulations are commonly used to observe the behavior of the membrane active peptides and the system upon penetration of the peptide into the membrane. The MD simulations of the CPP transportan 10 (tp10) and a POPC

showed that tp10 binds to the POPC membrane in a parallel orientation. Within a 200 ns simulation time, only the hydrophobic side of the peptide was inserted in the membrane [76]. For the investigation of the membrane translocation mechanism of Tat peptide, extensive molecular dynamics simulations were performed with DOPC lipid bilayer. The simulations showed that the penetration of Tat starts with the attraction between the Arg and Lys side chains and the lipid P-heads [77].

Much effort has been spent to develop computational methods for accurate prediction of membrane permeability and partition free energy calculations for peptide-membrane systems. However, MD simulations are not yet used for high-throughput permeability predictions, due to their high computational cost. The permeability, which is the partitioning of the solute into the membrane, can be quantified by the potential of mean force (PMF) for solute translocation across the membrane. PMF calculations of membrane permeation MD simulations require a physical model; defined by the force fields, the size of the system, simulation parameters, a reaction coordinate for quantification along the simulation pathway, and sufficient conformational sampling of both the order parameter and orthogonal degrees of freedom [1]. Since peptide translocation events are on the order of minutes [53,61,78], it is not possible to observe them within the time frame of equilibrium MD simulations, which are limited to observing events on the order of 10 to 100 ns [53, 79]. The time limitation in conventional MD simulations has been overcome by using other methods such as coarse grained simulations [80], replica exchange simulations [81], free energy perturbation [82] or other non-equilibrium MD simulations such as metadynamics, umbrella sampling or SMD simulations [74, 77, 83, 84] to study peptide adsorption or translocation through the lipid bilayer.

Simulations with peptide-membrane systems showed that some residues contribute to peptide translocation more significantly than the others. Ile and Leu, the most hydrophobic residues, prefer to be in the bilayer core, having free energy values around -20 kJ/mol at the bilayer center [85]. Previous reports suggested the critical involvement of cationic residues during peptide adsorption on the membrane [86]. Arginine, a common residue of many antimicrobial [87] and cell-penetrating pep-

tides [61, 65, 88, 89], which has a free energy of +60 kJ/mol at the bilayer center, was shown to be stabilized by the presence of a surrounding water droplet [85,90] and arginine rich peptides, such as Tat, were shown to form a channel in which the protonation/deprotonation of the fatty acids in the bilayer contribute to uptake of this peptide [77]. For CPPs that contain multiple arginine residues, such as Tat [52,65,77,89] and nona-arginine [88,91,92], multiple arginines were strictly required for their translocation through the membrane. These multiple arginines were found to be taking advantage of the formation of a water defect when located in the bilayer core [85,90,93]. Moreover it was shown that the energetic cost of additional charges is lower than when there is a single arginine at the center of the bilayer [90], which could be overcome by the simultaneous transfer of three or four Leu residues [85,93]. This does not necessarily suggest that the peptide LLLRRR would actively cross the membrane, but a peptide with similar composition could cross the membrane at a low energetic cost [90].

Steered molecular dynamics (SMD) is a computational time-effective approach to study biomolecular processes such as binding - unbinding events, and their elastic properties. SMD methodology has the advantage inducing relatively large conformational changes on ns time scales, which are hardly accessible with conventional MD. SMD simulations apply a time- dependent artificial force to pull the systems along a certain pathway, and mimic atomic force microscopy (AFM) experiments, which permits comparison of simulated and experimental force-extension profiles [94]. The application of SMD simulations was shown to be suitable for investigating the interactions that govern the membrane affinity processes of small molecules and peptides [95].

Molecular dynamics trajectories provide a sampling of configurations that researches wish to characterize. Given a set of configurations along a process, the aim is to find a low-dimensional embedding, which conserves the underlying manifold, but may also help to characterize a simulation quantitatively. In practice, dimensionality reduction is the search of this embedding with a set of coordinates that provide considerable variation in data, while other coordinates could be eliminated to characterize the whole process [96]. The classical techniques for dimensionality reduction, such as principal component analysis (PCA) and multidimensional scaling (MDS), are simple

and efficient to compute, and able to discover the true structure of data lying under the high-dimensional input space. However, data sets containing nonlinear structures are not accessible by PCA and MDS. In this context, ISOMAP approach builds on classical MDS, preserving the intrinsic geometry and the geodesic distance between neighboring data points, which guarantees the recovering of the true dimensionality of nonlinear data [97].

Different dimensionality reduction algorithms were used to characterize folding/unfolding simulations, molecular motion and protein flexibility. High dimensional data from protein folding landscape of a src homology 3 (SH3) coarse-grained protein model was analyzed to find clusters in data with nonlinear dimensionality reduction methods ISOMAP and Scalable ISOMAP (ScIMAP). The projected folding free- energy landscape successfully identified the transition-state of the reaction [96]. In another study, a new algorithm DPES-ScIMAP was proposed for the analysis of molecular motion based on ScIMAP algorithm [98]. The diffusion map algorithm is another nonlinear dimensionality reduction technique applied to molecular simulations of n-alkane chains, and the folding pathways of an antimicrobial peptide [99].

2.1.4. Visualization of Membrane Active Peptides by Microscopy Techniques

A common and relatively old technique to observe single cells is light/fluorescence microscopy in combination with staining and/or sectioning. Even though the resolution of light or fluorescence microscopy is usually not enough to reveal detailed cell structures, they can be used for initial identification and detection of bacteria, give information about the cellular morphology, and the reaction of the cells against drugs or fluorescent labeled peptides.

Fluorescence microscopy experiments with two CPPs; pVEC and penetratin, in four different mammalian cell lines showed that the concentration of pVEC was highest in the murine brain endothelial cells. As a result, pVEC was determined to be a potent carrier peptide due to its efficient and rapid penetration characteristic into the

cells [57]. The usage of SYTOX Green as a cytotoxicity indicator dye under fluorescence microscopy showed that the CPP TP10 caused rapid permeabilization of S. aureus, and the CPP pVEC permeabilizes M. smegmatis cells, while both CPPs were harmless to mammalian HeLa cells [69]. The interaction kinetics of a melittin derivative was studied using time-lapse fluorescence microscopy, to show that melittin caused membrane pore formation in synthetic membranes and membrane disruption in bacteria [48].

Another important approach in observation of single cells is electron microscopy (EM). The electron microscopes are at least 400 times higher in resolution compared to optical microscopes, and they can reveal detailed structures of the cell surface or the inside of the cells.

The effect of two cationic amphiphilic AMPs; gramicidin S and PGLa, on cell envelope of bacteria was studied using scanning electron microscopy (SEM) [100]. The study showed that *E. coli* cells were shorter after treatment with the AMPs, and blisters and bubbles formed on surface of the cells [100]. In other studies investigating the effect of novel or well-established AMPs on membrane integrity and surface structure, the common observations were change of cell surface smoothness, decrease in surface stiffness, formation of micelles and 'blebs' related to local destabilizations or total cell surface rupture [47, 101–103].

The majority of experiments with cells are performed after removal of the cells from their natural environment in a time dependent manner. Under these conditions cells are exposed to synthetic environments, which lack biochemical and mechanical interactions with the extracellular matrix, and direct cell-cell contacts with the neighboring cells that vary in time and space [104]. Unfortunately most experimental conditions are poor mimics of the natural environment; thus microfluidic systems may provide an alternative approach to monitor live cells in their natural environment. Microfluidic systems are small platforms with a typical length scale of one hundred nanometers to several hundreds of micrometers, consisting of channel systems connected to liquid reservoirs by liquid connectors. Even though the initial goal of microfluidics was to reduce sample consumption [105], lab-on-a-chip technology has successfully provided

portable, fast, controllable and reproducible operations [106] for biological processes such as drug screening [105], cell counting [104, 106–108], enzymatic assays, and even DNA extraction from bacteria [109].

2.2. Beta-Lactam Antibiotics and Beta-Lactamase Mediated Resistance

2.2.1. Beta-Lactam Antibiotics

The history of the discovery of beta-lactam antibiotics began with the study of Alexander Fleming in 1921, when he discovered lysozyme. The lysozyme enzyme was shown to dissolve the cell wall and kill bacteria, which led to the discovery of penicillin [110]. Later, the work at the Northern Regional Research Laboratory revealed that different strains, culture conditions and media resulted in the production of different penicillin compounds, all of them containing a beta-lactam ring [110]. Benzylpenicillin, or Penicillin G, was the first beta-lactam antibiotic that went into clinical trials. Today, beta-lactam antibiotics is a large family containing penicillin derivatives, monobactams, and carbapenems, whic share the the structural feature of a highly reactive four-member ring, called the beta-lactam ring [8].

As antimicrobial therapy provided prevention of some infections, the availability and success of antibiotics resulted in overconfidence. In 1929, Alexander Fleming focused on resistance to penicillin as a potential problem, but the therapeutic feature of penicillin overshadowed the resistance issue. Thus, it was known from the beginning that bacteria have the ability to eliminate antibiotics. Over the years, antibiotic resistance issues have drawn increased attention [110].

Beta-lactam antibiotics are rendered inactive by bacteria in three primary mechanisms of resistance; production of beta-lactamase enyzme, alteration of antibiotic target, and blocking the antibiotic's way to the target by efflux pumps [7].

2.2.2. Beta-Lactamases

The production of beta-lactamase enzymes is the most common and effective mechanism of bacterial resistance to beta-lactam antibiotics. Beta-lactamases, found widely dispersed amongst Gram-positive and Gram-negative bacteria, degrade the beta-lactam ring rendering antimicrobials ineffective [111]. Beta-lactamase enzymes (EC 3.5.2.6) were first identified in *Staphylococcus aureus* strains in the late 1940s, before the clinical trials with penicillin have started [111]. These enzymes are especially important in Gram-negative bacteria, since beta-lactamases prevent a natural protection from the antibiotics and therefore they constitute the major defense mechanism of these organisms. The beta-lactamase can easily spread during the transfer of genes by plasmids or transposons between microbes. Once the enzyme is expressed in an organism, it is secreted into the periplasmic space, bound to the cytoplasmic membrane or excreted [110].

Beta-lactamases were categorized based on sequence similarity (Ambler classes A through D) [112] or according to their substrate and inhibitor profiles (Bush-Jacoby-Medeiros Groups 1 through 4) [113]. In a recent study, a beta-lactamase network was built, in which the proteins were represented as nodes and were connected by edges with a weight depending on the number of shared identical or similar ligands. The use of ligand sharing information to cluster proteins resulted in classification of proteins based on both sequence and functional similarity [114].

Nevertheless, beta-lactamase evolution and identification of new beta-lactamases has continued and resistance trends have changed greatly over the last 15 years [115]. Over 1000 identified beta-lactamases are reported in literature. Class A, the most abundant beta-lactamases with more than 550 enzymes, includes over 40 variants of TEM and SHV enzyme families. Class D (group 2d) and class C (group 1) beta-lactamases represent the most rapidly growing (130%) classes of enzymes since 2005. It is expected that the number of unique beta-lactamases will increase to represent natural homologs of common enzymes that may have no selective advantage [113].

2.2.3. Beta-Lactamase Inhibitors and the Beta-Lactamase Inhibitor Protein (BLIP)

Approaches have been suggested to overcome beta-lactamase-mediated antibiotic resistance. The usage of extended-spectrum cephalosporins that cannot be hydrolyzed by beta-lactamases was one of the approaches. Another approach to overcome antibiotic resistance was the co-administration of a beta-lactamase inhibitor; such as clavulanic acid or sulbactam, with a beta-lactam antibiotic, such as ampicillin or amoxicillin [116]. The disadvantage of both approaches is that they apply selective pressure for mutations, which either result in beta-lactamases that can cleave extended-spectrum antibiotics or that cannot be inhibited by beta-lactamase inhibitors anymore [11]. At the time when the beta-lactamase inhibitor tazobactam was introduced (in 1993) in combination with piperacillin, most of the known plasmid-encoded beta-lactamases belonged to class A, which could almost all be inhibited by tazobactam. However, today more and more gram-negative pathogens have resistance against the piperacillin-tazobactam combination [117].

Clavulanic acid, or clavulanate is one of the most studied beta-lactamase inhibitors [118]. Even though it was suggested as a combination drug with an antibiotic, clavulanate alone displays limited antibacterial activity [118, 119], and it has been suggested that it may influence the activity of beta-lactam antibiotics by mechanisms other than the inhibition of beta-lactamase enzyme [120]. Clavulanate can bind to penicillin-binding proteins (PBPs) as other beta-lactams do, which may be the reason of the enhancement of antimicrobial activity [120]. Clavulanate, when combined with penicillin, was found to reduce the penicillin killing doses by up to 4-5 folds, which was explained by the synergetic effect of two drugs binding to PBPs [121].

2.2.3.1. Beta-Lactamase Inhibitor Protein (BLIP). The discovery of beta-lactamase inhibitor protein (BLIP) has led to intense research toward elucidation of the beta-lactamase-BLIP interactions and beta-lactamase inhibition mechanism. The natural, 165-amino-acid protein is produced by Streptomyces clavuligerus, which also produces

beta-lactam antibiotics such as cephamycins, and a beta-lactamase inhibitor, clavulanic acid [122–125].

BLIP is able to bind and inhibit class A beta-lactamases with K_i values of 1 - 3 μM, and specifically inhibits TEM-1 with a K_i of 0.5 nM [124], but it does not efficiently bind to class B, C or D beta-lactamases [11].

TEM-1 beta-lactamase structure has two domains, of which the substrate binding site is located at the interface [126,127]. In the TEM-1-BLIP complex (PDB Id: 1JTG), the Ala46-Tyr51 loop of BLIP blocks the beta-lactamase active site [128, 129]. The major contact residues between BLIP and TEM-1 beta-lactamase were determined as BLIP 41 to 50 residues [11]. Moreover, Y53A mutation was found to be as critical as the D49A mutation, which results in 40-fold decrease in the BLIP binding affinity [12, 123, 130].

Motivated by these findings on the TEM-1 - BLIP interface, BLIP based peptide inhibitor design has been an ongoing research effort. The peptide based on the A46-Y51 region of BLIP was reported to inhibit beta-lactamase with a K_i value around 500 μM [11]. Furthermore, phage display studies were used to identify peptides, such as RRHGHYY or Pep90 (YHFLWGP), with higher affinity for beta-lactamase [131–134].

3. MATERIAL AND METHODS

3.1. Membrane Translocation Simulations and Analysis

Steered molecular dynamics (SMD) simulations on two beta-lactamase inhibitory peptides, the cell-penetrating peptide pVEC, and its five derivatives, translocating the POPE lipid bilayer were performed in an effort to elucidate the mechanism whereby the peptides cross the POPE lipid bilayer.

3.1.1. Preparation and Equilibration of the Simulations Systems

3.1.1.1. Peptides Used in the Study. The beta-lactamase inhibitory peptides (P1 and P2), the cell-penetrating peptide pVEC, and its five derivatives (del5 pVEC, pVEC-1, pVEC-2, pVEC-9, pVEC-11) were used to study the lipid bilayer translocation of these peptides (Table 3.1). Beta-lactamase inhibitory peptide P1 is based on the 45-53 residues of the beta-lactamase inhibitory protein (BLIP) [129, 131]. P2 was designed as a chimeric peptide to include P1 with the addition of five N-terminal pVEC residues (LLIIL). The cell-penetrating peptide pVEC [57, 72] and pVEC with first five residues (LLIIL) deleted derivative; del5 pVEC were used for comparison and investigation of the effect of its N-terminus. Four pVEC mutants with either increased or decreases antibacterial activity were also used on order to investigate the effect of mutations on the membrane translocation of these peptides.

3.1.1.2. Equilibration of Peptides in Water Box. For the POPE translocation simulations of beta-lactamase inhibitory peptides P1 and P2, the P1 and P2 peptides were first built and energy minimized. The coordinates for the peptides P1 and P2 were either based on the structure of 45-53 residues of the reference beta-lactamase inhibitory protein (BLIP, PDB ID: 1jtg) structure [129, 131] or they were assigned as an extended chain (ϕ=-180° and ψ=180°, or random coil) using the psfgen plugin in the Visual Molecular Dynamics (VMD) package [135]. The initial coordinates of

Table 3.1. Peptides used in the membrane translocation simulations.

Peptide	**Description**	**Sequence**
P1	BLIP 45-53 region	HAAGDYYAY
P2	BLIP 45-53 region with N-terminal pVEC residues	LLIILHAAGDYYAY
pVEC	cell-penetrating peptide	LLIILRRRIRKQAHAHSK
del5 pVEC	pVEC with first 5 residues deleted	RRRIRKQAHAHSK
pVEC-1	pVEC with A13R mutation (improved activity)	LLIILRRRIRKQRHAHSK
pVEC-2	pVEC with H16L mutation (decreased activity)	LLIILRRRIRKQAHALSK
pVEC-9	pVEC with R6L, K11R mutations (improved activity)	LLIILLRRIRRQAHAHSK
pVEC-11	pVEC with R6L, H14R, H16R mutations (improved activity)	LLIILLRRIRKQARARSK

P1 (HAAGDYYAY) based on the 45-53 residues of BLIP forms a beta-hairpin. The coordinates for the LLIIL residues in P2 (LLIILHAAGDYYAY) were assigned as an extended chain. The time step was 2 fs and the coordinates were stored every 0.5 ps to create the simulation trajectories. Peptides placed into a water box (10 Å x 10 Å x 10 Å) were energy minimized for 1000 steps and equilibrated for 2 ns of MD simulations with constraints on peptide atoms and for 2 ns without any constraints. Simulations were performed using NAMD molecular dynamics package [136, 137] with CHARMM27 [138] force-field parameters.

For the POPE translocation simulations of pVEC and its mutants, pVEC, pVEC-1, pVEC-2, pVEC-9, and pVEC-11 peptides were first built and energy minimized. The initial coordinates of the peptides were assigned randomly using the psfgen plugin in the VMD package. Wild-type pVEC and its mutants, pVEC-1, pVEC-2, pVEC-9, and pVEC-11 were studied (Table 3.1). The peptides were randomly placed into a water

box (10 Å x 10 Å x 10 Å). The water-peptide system was minimized for 1000 steps and equilibrated for 2 ns with constraints on peptide atoms. The constraints were then removed and the system was equilibrated for 2 ns further. Simulations were performed using NAMD molecular dynamics package with CHARMM27 force-field parameters.

For the comparison of membrane translocation of pVEC and del5 pVEC, and in order to investigate the effect of LLILL residues on the bilayer translocation, peptides pVEC and del5 pVEC were first built and energy minimized. The initial coordinates of the peptides pVEC (LLIILRRRIRKQAHAHSK) and del5 pVEC (RRRIRKQAHAHSK) (Table 3.1) were assigned as extended chain (ϕ=-180° and ψ=180°) and were prepared using the Molefacture plugin in the VMD package. The initial structures were built using the psfgen plugin in the VMD package with CHARMM36 topology [138–140]. Extended chain conformations of pVEC and del5 pVEC were each placed into a water box by adding a layer of water molecules 12 Å in each direction from the peptide atom with the largest coordinate in that direction. Water molecules within 2.8 Å of the peptides were removed. The water-peptide systems were energy minimized for 1000 steps and equilibrated for 2 ns with constraints on peptide atoms. The constraints were then removed and the system was equilibrated for 100 ns further. Simulations were performed at constant temperature and pressure, 310 K and 1 atm, using NAMD package with CHARMM36 force-field parameters [138–140]. The time step was 2 fs and the coordinates were stored every 0.5 ps to create the simulation trajectories.

3.1.1.3. Preparation and Equilibration of the POPE Lipid Bilayer. In all membrane translocation simulations, the 128-lipid membrane was selected as POPE (1-Palmitoyl-2-oleoyl-sn-glycero-3-phosphoethanolamine), which was used to mimic the inner leaflet of the outer membrane of *E. coli* [141, 142].

For the membrane translocation simulations of beta-lactamase inhibitory peptides P1 and P2, and the membrane translocation simulations of pVEC and its mutants (pVEC, pVEC-1, pVEC-2, pVEC-9, and pVEC-11), the 128-lipid POPE bilayer was

prepared using the Membrane Builder plugin of VMD. The membrane was solvated with TIP3P water molecules 60 Å in positive and negative z-directions. After solvation, the water-membrane system was equilibrated for 0.5 ns with constraints on the membrane and for 0.5 ns without any constraints.

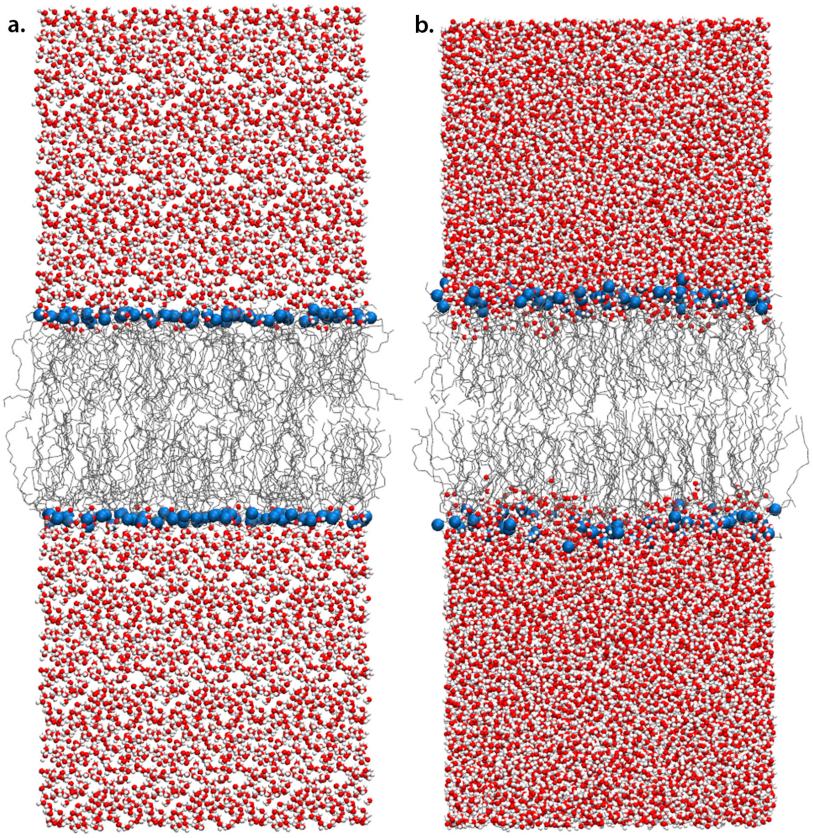

Figure 3.1. Solvated CHARMM-GUI POPE bilayer system. The initial assembly (a) and the final system (b) after the 6 cycles of equilibration and 25 ns of production run.

For the comparison of membrane translocation of pVEC and del5 pVEC peptides, the CHARMM-GUI Membrane Builder [143–145] was used to generate the membrane coordinates of the POPE bilayer and to generate the NAMD input files to be used in the equilibration simulations of this bilayer. The membrane was solvated with a layer of 60 Å TIP3P water molecules on either side (Figure 3.1a). No ions were added to the systems during the preparation of the water-lipid system, since POPE bilayer is neutral. The NAMD input files were used to minimize and equilibrate the water-lipid

system in six equilibration cycles. The first cycle involves 10,000 steps of minimization and 25,000 steps of equilibration at 310 K with a time step of 1 fs. The system is equilibrated at a total of 6 cycles following each other, where the force constant of the restraints on the lipid bilayer is slowly decreased at each step. Simulations were carried out with CHARMM36 force-field parameters [138,139,146]. A final production run was performed for 25 ns without any restraints on the system and the final coordinates were used in the membrane translocation simulations of the peptides (Figure 3.1b). The van der Waals interactions were smoothly switched off at 12 Å by a forced-based switching function. Long-range electrostatic interactions were calculated using the particle-mesh Ewald (PME) method.

3.1.1.4. Preparation and Equilibration of the Peptide-Lipid Systems. In all membrane translocation simulations, each previously equilibrated peptide conformation was extracted from the equilibration simulations and was placed into the water layer above the membrane manually, such that the minimum distance between the peptide atoms and the lipid head group phosphate atoms was 10 Å.

As the peptide was placed in the water layer above the lipid bilayer, the water molecules within 2.8 Å of the peptide atoms were removed. Counter ions (Na^+ and Cl^-) were added to neutralize the whole system and to set the final ion concentration to 0.15 M using the Autoionize plugin of the VMD package (Figure 3.2).

Each simulation system consisting of over 55,000 atoms was minimized for 5000 steps and equilibrated for 0.5 ns with constraints on peptide atoms and for 0.5 ns without any constraints. Equilibration simulations were performed at constant temperature and pressure, (300 K or) 310 K and 1 atm, using NAMD package with CHARMM27 [138] or CHARMM36 [138, 140, 146] force-field parameters.

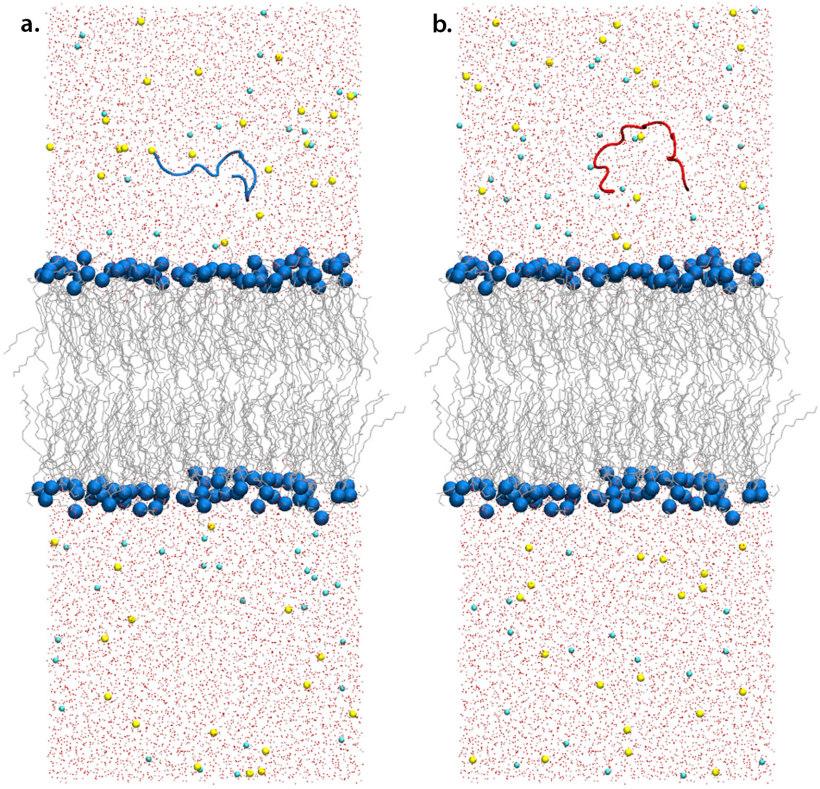

Figure 3.2. Simulation systems of del5 pVEC (a) and pVEC (b) before membrane translocation simulations. Peptides are shown as ribbons, lipid tails in silver lines, P heads in blue spheres, and Na^+ and Cl^- are as yellow and cyan spheres, respectively.

3.1.2. Steered Molecular Dynamics of Peptide Translocation

For the membrane translocation simulations of beta-lactamase inhibitory peptides P1 and P2, and the membrane translocation simulations of pVEC and its mutants (pVEC, pVEC-1, pVEC-2, pVEC-9, and pVEC-11), steered molecular dynamics (SMD) simulations [137] were performed by applying force on the N terminal Cα atom (SMD atom) of the peptide in the negative z-direction to move the peptide from one side of the membrane to the other (Figure 3.3). Peptide is shown as ribbon (red), lipids in lines (gray), membrane P-heads in VdW representation (purple), and water molecules are shown in CPK representation (blue) in Figure 3.3. Constraints were applied on the P-heads of the lipid bilayer only in z-direction and allowing the P-heads to move freely in x- and y- directions to allow the formation of a pore with minimal

membrane disruption. The spring constant was 10 kcal/mol/Å^2 and the velocity of pulling was 0.0000050 Å/timestep (2.50 Å/ns with a timestep of 2.0 fs). Simulations were performed at constant temperature and pressure, 300 K and 1 atm, using NAMD molecular dynamics package with CHARMM27 force-field parameters. The simulations were performed at constant temperature and pressure, 300 K and 1 atm respectively, for a simulation time of 40-50 ns. Simulations with P1 and P2 were repeated three times (for 40 ns each) and the results were averaged for analysis.

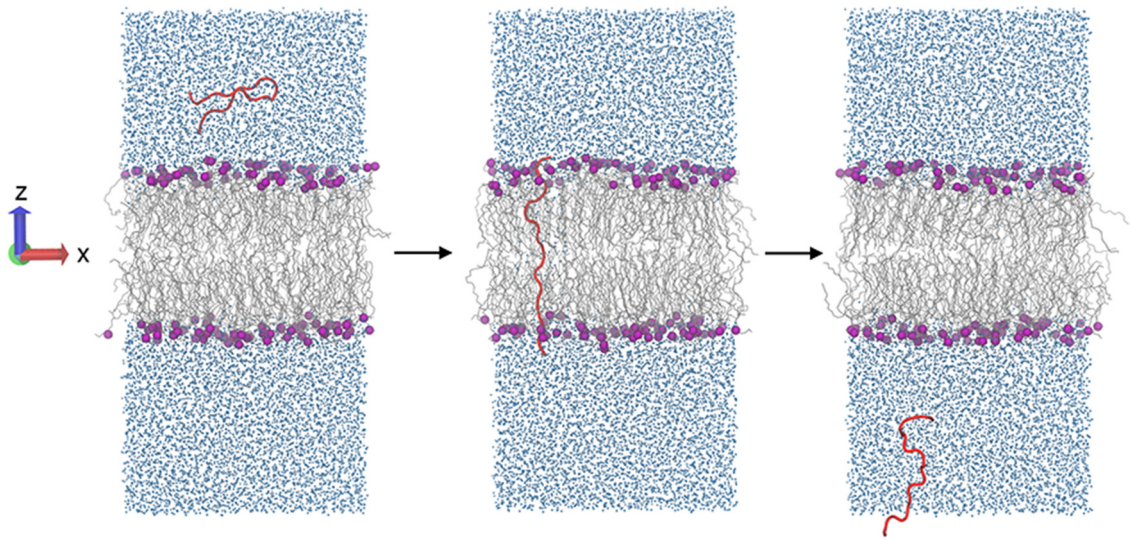

Figure 3.3. Snapshots taken from pVEC-1 SMD simulation. When the peptide is above the membrane (left), fully embedded in the membrane (center), and after the peptide exits the membrane (right).

For the comparison of membrane translocation of pVEC and del5 pVEC peptides, the simulations were carried out by applying force on the center of mass of the peptide in the z-direction to move the peptide from one side of the membrane to the other. For these simulations, the center of mass of the lipid bilayer was constrained in z-direction using the collective variables (colvars) module of NAMD package [147], while it was free to move in x- and y-directions allowing a possible change in the thickness of the bilayer upon peptide insertion. The spring constant was set to 10 kcal/mol/Å^2 and the velocity of pulling was set to 0.0000020 Å/timestep corresponding to 1.0 Å/ns, which is 2.5 times slower than the velocity used in our previous studies [74].

The translocation of the peptides across the POPE bilayer was monitored by calculating interaction energy between the peptide and the lipid bilayer, force applied on the peptide, work done to pull the peptide through the bilayer, number of water molecules that entered the lipid bilayer, and change in membrane thickness during translocation of the peptides. The work performed in the pulling simulations was calculated by taking the integral of the force profile with respect to simulation timestep.

The order parameters were computed with respect to the membrane normal axis using the equation; order parameter (where) is the angle between a vector along the acyl chain methylene/methyl hydrogens and the membrane normal axis. An order parameter of 1 indicates full order and that chains reside along the bilayer normal; whereas, an order parameter of -0.5 indicates that chains are perpendicular to the normal [148]. The carbon numbers increase when it is away from the lipid head group and closer to the bilayer core. Larger order parameters for a carbon atom correlate with lower fluctuations throughout the simulation and hence more order.

3.1.3. Stretching Simulations of pVEC

A simulation system of wild-type pVEC in a water box was prepared and the peptide was stretched. The initial structure, with an end-to-end distance of 27.7 Å, is the same with the one that was used in the SMD simulations of membrane translocation of pVEC. In the SMD simulations, peptide reaches its most extended conformation, where it is embedded in the lipid bilayer, with an end-to-end distance around 57 Å.

For the stretching of pVEC, two different methods were applied. In the first simulation, the harmonic restraint (with a force constant of 5 kcal/mol) was applied on the end-to-end distance and in the course of a 10 ns MD simulation; this distance was increased from 27.7 Å to 56.47 Å. Collective variables (colvars) module of NAMD [147] was used for defining the colvar end-to-end distance and to apply the harmonic bias on it.

In the second stretching simulation, the peptide was stretched for 6,000,000 steps (12 ns simulation time) by fixing the Cα atom of the Leu1 residue and pulling the Cα atom of Lys18 with a velocity of 0.0000050 Å/timestep (2.50 Å/ns with a timestep of 2.0 fs). The peptide was stretched from an end-to-end distance of 27.7 to 57 Å. The change in the end-to-end distance, change in the radius of gyration, force applied on the peptide and work done throughout the simulation were calculated.

3.1.4. Umbrella Sampling and Replica Exchange Umbrella Sampling

In umbrella sampling method [149] the system of interest is simulated in the presence of an artificial biasing potential that is introduced to enhance the sampling in the neighborhood of a selected value of the reaction coordinate. In order to achieve this, a reaction coordinate has to be selected and then it has to be divided into a desired number of windows where each window is sampled locally. The biasing potential restrains the variations in the reaction coordinate into a small range around some prescribed value (window center), helping to achieve a more efficient configurational sampling in the region. For each window that is sampled locally, the probability distributions are calculated to plot the histograms of the reaction coordinate around the window center in each window. The key to achieving sufficient sampling is that all neighbor histograms should overlap at around 20-30 percent to ensure that every point on the reaction coordinate is visited.

We have previously investigated the membrane translocation of pVEC (LLIIL-RRRIRKQAHAHSK) and del5 pVEC (RRRIRKQAHAHSK) using SMD simulations, in which the peptide-lipid interactions were studied in detail to determine the specific regions of the peptide that may contribute to the cellular uptake [74]. The previous SMD simulation was carried out by pulling the peptide from its N-terminus through the 128-lipid POPE bilayer, with constraints on the P-heads only in the z-direction, to mimic the membrane translocation of the pVEC peptides. Using these previous simulations, the reaction coordinate was selected as the distance (in z-direction) between the SMD atom (Cα atom of the Leu1 residue for pVEC and Cα atom of the Arg1 residue for del5 pVEC) and the center of the lipid bilayer. The distance between the

SMD atom and the lipid bilayer projected on z-axis was calculated for the whole SMD trajectory. The reaction coordinate was then divided into equally spaced windows that were simulated locally and independent from each other. In order to achieve the local sampling, collective variables (colvars) module was used for NAMD simulations [147]. The colvars module enables to define a variable that will be biased, calculated or driven to a target value during a MD simulation. In each window, the collective variable was defined as the distance between the SMD atom and the lipid bilayer (projected on z-axis). A harmonic bias (with a force constant of 1.0 kcal/mol) was applied on this variable to make sure that the collective variable stays in the window and oscillates around its center (initial) value.

The umbrella sampling (US) simulations for the membrane translocation of pVEC were carried out using 57 independent windows, in which the initial structures were extracted from the SMD simulation. Each window was first minimized and then simulated for 2 ns with harmonic bias on the z-distance between the peptide N-terminus and the lipid bilayer center. Similarly, for the umbrella sampling simulations for the membrane translocation of del5 pVEC, 51 independent windows, in which the initial coordinates were extracted from the SMD simulation, were first minimized and then equilibrated for 2 ns with harmonic bias on the z-distance between the peptide N-terminus and the lipid bilayer center. After the simulations were completed, the distance variable calculated in each step of the last 1 ns of each window was used (first 1 ns of each window is considered as equilibration and is not used) to plot the histograms of the collective variable.

The replica exchange umbrella sampling (REUS) method differs from the conventional umbrella sampling (US) methodology by allowing the system to attempt an exchange of parameters between neighboring windows [150]. By doing this, each replica may sample different states, which may otherwise be thermodynamically inaccessible due to high-energy barriers along the reaction coordinate. This is possible only by running simultaneous simulations, so that each replica can communicate with its neighbors. The common replica exchange methodology [150] applied in MD simulations allows temperature exchange; where the system is simulated at different temperatures

and swapping between those temperatures is allowed at every exchange attempt. For our simulations, instead of temperature exchange, we used Hamiltonian exchange [151], in which the Hamiltonian to be exchanged was the US harmonic potential. The key to achieve sufficient sampling in REUS simulations is that replicas should exchange around 30-40 percent to assure that every point on the reaction coordinate is visited.

In this study, using the SMD simulations carried out for the membrane translocation of pVEC and del5 pVEC peptides, the reaction coordinate of our system was selected as the distance (in z-direction) between the peptide center of mass and the center of the lipid bilayer. The SMD simulations were carried out by pulling the peptide from its center of mass through the CHARMM-GUI 128-lipid POPE bilayer, which was constrained on its center of mass only in the z-direction. The distance between the peptide and the lipid bilayer projected onto the z-axis was calculated for the whole SMD trajectory. The selected reaction coordinate was then divided into equally spaced (2 Å or 1 Å) replicas and snapshots corresponding to each window were extracted from the SMD simulations to be used as the initial coordinates of the REUS simulations. In order to achieve local sampling, collective variables (colvars) module was used for the simulations [147]. In each replica, the collective variable was defined as the center of mass distance between the peptide and the lipid bilayer (projected on z-axis). A harmonic bias (with a force constant of 1.0 kcal/mol) was applied on this variable to make sure that the collective variable oscillates around its center (initial) value. Replica exchange was enabled by allowing the neighboring replicas to attempt exchange every 1000 steps. The output files (.traj files) of the colvars module were used to generate the PMF. Accepted exchange attempts were also calculated for each replica to make sure that the neighbors are close enough to each other, to allow enhanced sampling.

3.1.5. Potential of Mean Force (PMF) Calculations

In order to determine the potential of mean force (PMF) [152] for the translocation of peptides along some defined reaction coordinate, umbrella sampling (US) and replica exchange umbrella sampling (REUS) simulations were carried out.

For the US and REUS simulations of pVEC and del5 pVEC, the probability distribution of each window/replica is calculated to plot the histograms along the reaction coordinate around the window center. After the histograms are computed, the weighted histogram analysis method (WHAM) is used to calculate the PMF. WHAM [153,154] recombines the unbiased histograms to get the total probability distribution, which is calculated as a linear combination of the unbiased probability distributions [155]. The WHAM approach has been routinely used to calculate the PMF along a reaction coordinate for over 20 years. It has also been compared to other weighting methods and the weighted histogram analysis method was found to be the most reliable approach [152].

3.1.6. Application of Dimensionality Reduction Algorithms

The aim in this part of the study was to use the dimensionality reduction techniques principal component analysis (PCA) and isometric feature mapping (ISOMAP) to define a low dimensional embedding that could be used to characterize the membrane translocation of the cell-penetrating peptide pVEC, and its derivatives. Steered molecular dynamics (SMD) simulation trajectories (.dcd files) were used as the source of data. The trajectory files contain the conformations of the peptides, in which, each trajectory yields 3x18 dimensions (x, y, z Cartesian coordinates) for N conformations (frames), a total of Nx54 data matrix.

3.1.6.1. Principal Component Analysis (PCA). The most common definition of PCA is that, for a set of observed d-dimensional data vectors, $\{t_n\}$, $n\epsilon\{1...N\}$, the q principal axes w_j, $j\epsilon\{1...q\}$, are those orthonormal axes onto which the retained variance under projection is maximal. It can be shown that the vectors w are given by the q dominant eigenvectors (i.e. those with the largest associated eigenvalues) of the sample covariance matrix $S = \Sigma n(t_n - m)(t_n - m)/N$ such that $S_{wj} = \lambda_j w_j$ and where m is the sample mean. The vector $x_n = W^T (t_n - m)$, where $W = (w_1, ... , w_q)$, is thus a q-dimensional reduced representation of the observed vector t_n.

3.1.6.2. Isometric Feature Mapping (ISOMAP). The isometric feature mapping approach builds on classical Multi Dimensional Scaling (MDS) algorithm, but seeks to preserve the intrinsic geometry of the data, as captured in the geodesic manifold distances between all pairs of data points. It is guaranteed asymptotically to recover the true dimensionality and geometric structure of a strictly larger class of nonlinear manifolds [97]. The complete ISOMAP, algorithm has three steps:

- Build a neighborhood graph, G. For each point, find the set of points that are nearest neighbors on the manifold using the distance measure $d(x_i, x_j)$. The typical approach is to select the k nearest neighbors to every point. Alternatively, a distance cutoff, ϵ, can be introduced, and all pairs of points closer than ϵ are considered nearest neighbors.
- Compute the geodesics. The geodesics are approximated as the shortest paths on G for all pairs of points. Construct a matrix D where D_{ij} is the shortest path between x_i and x_j.
- Compute the low-dimensional embedding. Use Multidimensional Scaling (MDS) on the matrix D of estimated geodesic distances computed in step 2). This produces coordinates for each point that best preserve the geodesic distances. These coordinates, when plotted as Euclidean coordinates, have the effect of unrolling the non-linear surface.

3.2. In-vitro Enzyme Kinetics

Beta-lactamase activity was measured by monitoring the hydrolysis of the chromogenic substrate CENTA [156] (by continuous recording of the change in absorbance at 405 nm) by periplasmic R-TEM-1 beta-lactamase, which was extracted from *E. coli* K12 pUC18 cells by osmotic shock procedure.

For the determination of Km value for CENTA, five assays with different substrate concentrations (in the final concentration range of 35-120 μM) were carried out in a total volume of 1 mL in 50 mM potassium phosphate buffer (pH 7.0) with final enzyme concentration of 36.33 nM at room temperature.

For inhibition studies, P1 peptide (HAAGDYYAY) at a final concentration of 100 μM was added to the enzyme-buffer mixture. The K_m and V_{max} (and K_i for the inhibition) values were calculated using the initial rate measurements with application of linear least squares algorithm ($R^2 > 0.9$) on the Hanes-Woolf plot, a linear transformation and a graphical representation of the Michaelis-Menten equation.

3.3. Measurement of Drug Effects on Bacterial Growth

3.3.1. Bacterial Strains and Growth Conditions

The experiments were performed with the *Escherichia coli* K12 strain. Cells were obtained from previously prepared laboratory stocks. Beta-lactamase expression was obtained from pUC18 plasmid carrying the gene for RTEM-1. pUC18 plasmid vector was also obtained from laboratory stocks.

In all of the experiments, the cells were cultured in LB medium and plated in LB-agar medium. LB medium was prepared by dissolving 10 g peptone, 5 g yeast extract, and 10 g NaCl in 1 L demineralized water and further sterilized by autoclaving at 1 atm and 121 °C for 15 minutes. LB-agar medium was prepared by dissolving 10 g peptone, 5 g yeast extract, 10 g NaCl, and 15 g agar in 1 L demineralized water and further sterilized by autoclaving at 1 atm and 121 °C for 15 minutes.

3.3.2. Drugs Used in the Study

Dimethyl sulfoxide (DMSO), potassium clavulanate (VETRANAL, analytical standard), ampicillin (ROAMP ROCHE), and melittin from honey bee venom (M2272, equal or larger than 85% purity) were purchased from Sigma-Aldrich. Peptides pVEC, del5 pVEC, P1, P2, P2r, P3A, P3, and P4 were purchased from Thermo Fisher Scientific Inc. with given sequence in Table 3.2.

Ampicillin and potassium clavulanate were dissolved in sterile demineralized water to a final concentration of 400 mg/mL and 1 mM, respectively and filter sterilized

prior to aliquoting. 100 μl of drug aliquots were prepared and stored at -20 °C.

First stock solution of melittin was prepared in DMSO-PBS buffer mixture (0.375% DMSO) at a final concentration of 1 mM. The second stock of melittin was dissolved in sterile demineralized water to a final concentration of 1 mM. 50 μl of peptide aliquots were prepared and stored at -20 °C.

pVEC and del5 pVEC were first dissolved in the minimum possible volume of DMSO and then diluted to 5 mM final concentration (final DMSO concentration was 1%) with sterile demineralized water. 50 μl of peptide aliquots were prepared and stored at -20 °C.

P1 was dissolved in sterile 50 mM K^+PO_4 buffer (pH 7.0) solution to a final concentration of 1 mM. 100 μl of peptide aliquots were prepared and stored at -20 °C.

P2 was first dissolved in the minimum possible volume of DMSO and then diluted to a final concentration of 1 mM with sterile 50 mM K^+PO_4 buffer (pH 7.0) solution. The final peptide solution had 20% (v/v) DMSO, and 100 μl of peptide aliquots were stored at -20 °C.

P2r and P3A were first dissolved in the minimum possible volume of 50% (v/v) DMSO/water solution and then diluted to 1 mM peptide concentration with water. The final stock solutions of P2r and P3A had 3.69% and 2.303% DMSO, respectively. 100 μl of peptide aliquots were prepared and stored at -20 °C.

P3 was dissolved in sterile demineralized water to a final concentration of 5 mM. 50 μl of peptide aliquots were prepared and stored at -20 °C.

First stock of P4 was first dissolved in the minimum possible volume of 50% (v/v) DMSO/buffer solution and then diluted to 1 mM peptide concentration with PBS. The final stock solution had 4.75% DMSO, and 100 μl of peptide aliquots were stored at -20 °C. The second stock of P4 was first dissolved in the minimum possible volume of

Table 3.2. Drugs used in the study.

Drug	**Description**	**Sequence**
DMSO	lipid membrane permeabilizer molecule	-
Melittin	antimicrobial peptide from honey bee venom	GIGAVLKVLTTGLPALISWIKRKRQQ-NH_2
Ampicillin	beta-lactam antibiotic	-
Potassium Clavulanate	beta-lactamase inhibitor molecule	-
pVEC	cell-penetrating peptide	LLIILRRRIRKQAHAHSK-NH_2
del5 pVEC	pVEC with first 5 residues deleted	RRRIRKQAHAHSK-NH_2
P1	BLIP 45-53 region	HAAGDYYAY-NH2
P2	BLIP 45-53 with N-terminal pVEC residues	LLIILHAAGDYYAY-NH_2
P2r	BLIP 45-53 with N-terminal pVEC residues and RRR linker region	LLIILHAAGDYYAY-NH_2
P3A	beta-lactamase inhibitory peptide	RRGHYYA-NH_2
P3	beta-lactamase inhibitory peptide	RRGHYY-NH_2
P4	beta-lactamase inhibitory peptide with N-terminal pVEC residues	LLIILRRGHYY-NH_2

DMSO and then diluted to a final concentration of 5 mM with sterile demineralized water. The final stock solution had 4% DMSO, and 50 μl of peptide aliquots were stored at -20 °C.

3.3.3. Determination of Antibacterial Activity and Viable Cell Count in 2 mL Cultures

In order to determine the effect of the beta-lactamase inhibitory peptides P1 (HAAGDYYAY) and P2 (LLIILHAAGDYYAY) on wild-type *E. coli* K12 and antibiotic resistant *E. coli* K12 pUC18 cells, a preculture in 2 mL LB medium (supplemented with 0.1 mg/mL ampicillin for *E. coli* K12 pUC18 cultures) from -80 °C bacteria stock was prepared and incubated at 37 °C and 180 rpm overnight (16 hours). Next morning, fresh LB (2 mL in a tube, supplemented with 0.1 mg/mL ampicillin for *E. coli* K12 pUC18 cultures) was inoculated with preculture and incubated at 37 °C and 180 rpm until OD_{600} reached 0.2. Cultures in early logarithmic growth phase ($OD_{600} = 0.2$) were treated with peptides P1 or P2 at a final concentration of 100 μM. Equal volume of buffer was added to the control set of P1 (HAAGDYYAY) and equal volume of 20% (v/v) DMSO - buffer mixture was added to the control set of P2 (LLIILHAAGDYYAY) in order to eliminate any possible DMSO and/or buffer effect on the cell growth. All of the experiments were repeated three times and the average of duplicate plate counts at each time point for three repetitions of each experiment were plotted with standard error.

Optical densities of *E. coli* cells were measured every hour at a wavelength of 600 nm using a spectrophotometer in order to determine the growth profile of *E. coli* cultures. LB medium was used for both the blank and diluting the samples to keep the spectroscopic readings within the reliable range of 0.2 to 0.8. Culture samples were plated to compare the number of colony forming units of the control cultures and cultures treated with the peptides. For a ten-fold dilution, 100 μl of the bacterial sample taken at the desired time interval was transferred into a centrifuge tube containing 900 μl of fresh LB medium and vortexed to homogenize. This procedure was repeated many times until the desired dilution is achieved. Finally, 1 mL of culture with the desired dilution was deposited in a sterile Petri dish and LB-agar was poured into Petri dishes. The sample and the liquid agar were mixed gently by moving the plates through an eight-shaped path. The plates were left to cool and then incubated overnight at 37 °C. The colonies were counted to determine the colony forming units (CFUs) in Petri

dishes. Average values from plates were calculated and reported.

3.3.4. Determination of Minimal Inhibitory Concentration, and Number of Colony Forming Units

The general minimal inhibitory concentration (MIC) determination protocol used frequently in literature suggests a low bacterial inoculum dose at the beginning of the experiments ($2x10^4$ to 10^5 CFU/mL) [157]. On the other hand, in order to visualize bacterial viability and membrane damage induced by the peptides using fluorescence microscopy and SEM imaging techniques, the cell density has to be sufficiently high (10^8-10^{10} CFU/mL) [100]. Since the determination of minimal inhibitory concentration of drugs is highly dependent on the inoculation cell density, MIC determination experiments were carried out both at high and standard inoculum doses. The measurement of colony forming units (CFUs), and visualization experiments were carried out at high inoculation cell density of bacteria.

The general protocol used for MIC determination experiments at standard and/or high inoculation cell density, followed by the measurement of number of colony forming units (CFUs) is as follows (Figure 3.4):

- Prepare a preculture in 15 mL (in a flask) LB medium (supplemented with 0.1 mg/mL ampicillin for *E. coli* K12 pUC18 cultures) from -80 °C bacteria stock and incubate at 37 °C and 180 rpm overnight (16 hours).
- Inoculate fresh LB (15 mL in a flask, supplemented with 0.1 mg/mL ampicillin for *E. coli* K12 pUC18 cultures) with 100-150 μL of preculture in the morning and incubate at 37 °C and 180 rpm until OD_{600} reaches 0.7.
- Inoculate fresh LB (15 mL in a flask, supplemented with 0.1 mg/mL ampicillin for *E. coli* K12 pUC18 cultures) with 100-150 μL of the culture and incubate at 37 °C and 180 rpm until OD_{600} reaches 0.2.
- Prepare drug/peptide solutions by adding 200 μL of the highest concentration to be tested to the well on the far right of each row and add 100 μL water/buffer solution to the other wells.

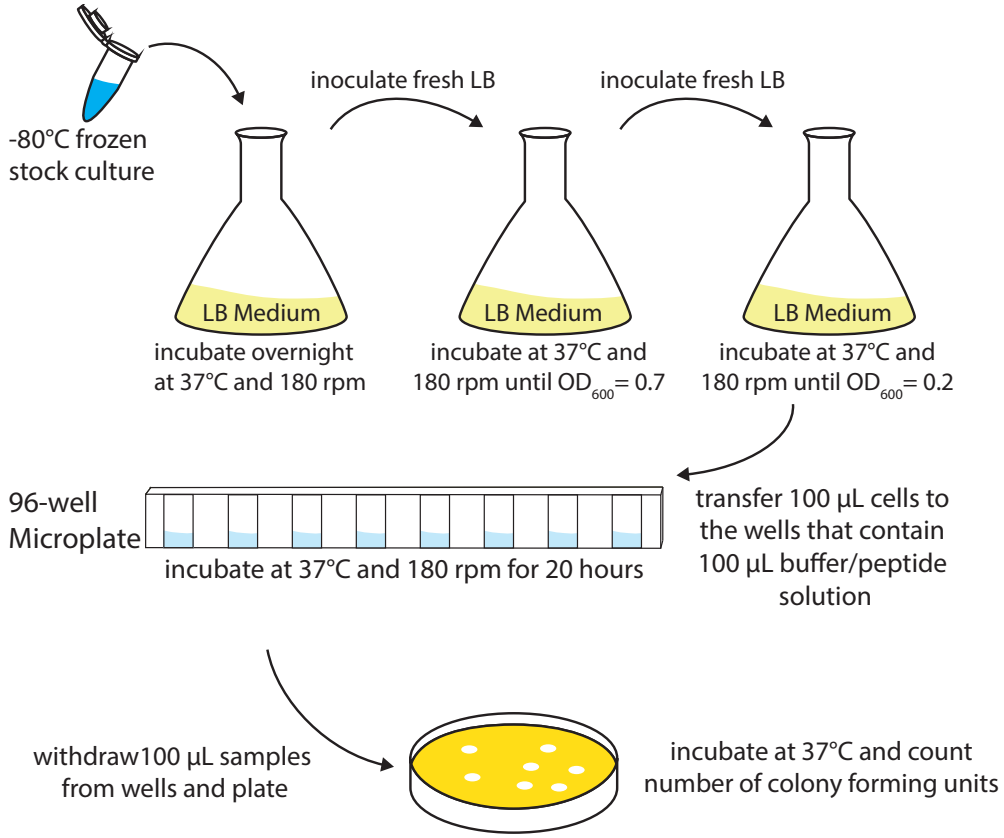

Figure 3.4. The protocol diagram for determination of minimal inhibitory concentration (MIC) and number of colony forming units (CFUs).

- Start performing 2-fold serial dilutions by first withdrawing 100 μL of the highest drug/peptide concentration and pipetting it to the next well on the left that has 100 μL water/buffer solution.
- Continue performing 2-fold serial dilutions by mixing thoroughly and withdrawing 100 μL of drug/peptide and adding it to the next well on the left until you reach column #1. Discard 100 μL of the diluted drug/peptide solution in the last well on the far left.
- To carry out the experiment at standard inoculum dose (2x10^4 to 10^5 CFU/mL), dilute the culture at OD_{600} = 0.2 by 1:500 for *E. coli* K12 pUC18 cultures and 1:600 for *E. coli* K12 cultures.
- Add 100 μL of the diluted cultures to the wells that have 100 μL drug/peptide solutions at 2-fold concentrations.

- To carry out the experiment at high inoculum dose (10^7-10^8 CFU/mL), add 100 μL of the culture at OD_{600} = 0.2 to the wells that have 100 μL drug/peptide solutions at 2-fold concentrations.
- For CFU measurements, incubate the microplate at 37 °C and 180 rpm orbital shaking for 2 (and/or 4, and/or 20) hours and withdraw 100 μL of selected culture samples at the end of incubation.
- Dilute the samples in 10-fold serial dilutions and plate in Agar-LB to count the number of colony forming units after incubation at 37 °C for up to 24 hours.
- For MIC determination at standard and high inoculum doses, incubate the microplate for 20 hours, while taking OD_{600} measurements at every 5 minutes.
- After 20 hours of incubation, the MIC value is determined as the lowest drug concentration at which no growth is observed.

In order to determine the inoculum dose at the beginning of the experiments and to make sure that the initial cell counts are in the desired range, CFUs of the cultures were measured before each MIC determination experiment. The following protocol is carried out in each experiment and results for only one experiment are given below.

Table 3.3. OD_{600} measurements and plate counts of the sample at OD_{600} = 0.20 (Sample 1), when Sample 1 is diluted 1:100 (Sample 2) and when Sample 1 is diluted 1:500 (Sample 3).

Sample	**OD_{600}**		**CFU/mL**				
	Measured	Calculated	10^3 dilution	10^4 dilution	10^5 dilution	10^6 dilution	10^7 dilution
1	0.2	-				83	8
						42	10
2	-	0.002		49	8		
				53	8		
3	-	0.0004	107	13			
			113	8			

Samples from the culture at OD_{600} = 0.2 and diluted cultures (dilution of 1:100 or 1:500 in this example, for *E. coli* K12 pUC18 cells) were withdrawn. Using 10-fold serial dilutions in LB medium, samples were plated on LB-Agar plates and the number of colony forming units in each sample was counted. It was observed that the number of CFUs were in the order of $6x10^7$ for the culture at OD_{600} = 0.2, and in the order of $5x10^5$ and $1x10^5$ for the cultures diluted 1:100 and 1:500, respectively (Table 3.3 and Figure 3.5).

Considering the reported inoculum doses in the literature, the inoculum dose where the *E. coli* K12 pUC18 culture at OD_{600} = 0.2 was diluted 1:500 was considered suitable for the experiments that are carried out at standard inoculation cell density. Similarly, 1:600 dilution of the *E. coli* K12 culture at OD_{600} = 0.2 was considered suitable for the experiments carried out at standard inoculation cell density. For the experiments carried out at high inoculation cell density, the cultures at OD_{600} = 0.2 were added directly to the microplate wells.

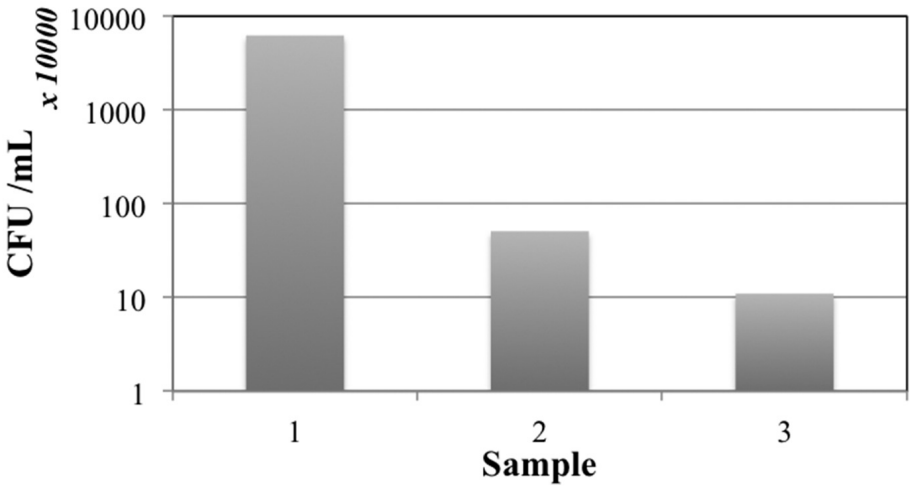

Figure 3.5. CFU counts of the sample at OD_{600} = 0.2 (Sample 1), when Sample 1 is diluted 1:100 (Sample 2) and when Sample 1 is diluted 1:500 (Sample 3).

3.4. Visualization of Drug Effects on Bacteria

3.4.1. Time-lapse Microscopy Using Agarose Pads and Cover Glass Chambers

The growth of antibiotic resistant *E. coli* K12 pUC18 cells and the effect of beta-lactamase inhibitory peptide P1 (HAAGDYYAY) on cell growth were observed using time-lapse microscopy. For these experiments, M9 minimal medium was used instead of LB medium for imaging purposes. A preculture in 2 mL M9 medium (supplemented with 0.1 mg/mL ampicillin) from -80 °C bacteria stock was prepared and incubated at 37 °C and 180 rpm overnight (16 hours). Next morning, fresh M9 medium (2 mL in a tube, supplemented with 0.1 mg/mL ampicillin) was inoculated with preculture and incubated at 37 °C and 180 rpm until OD_{600} reached 0.1. Cultures in early logarithmic growth phase ($OD_{600} = 0.1$) were used for imaging the bacterial growth or for treatment with P1 peptide.

The first time-lapse experiment was carried out under confocal microscopy with untreated cells pipetted on agarose pads. The details of the protocol were described in literature previously [158]. Agarose pads were prepared by adding 1.5% (wt/volume) low-melt agarose (0.15 g) in 10 mL M9 medium and dissolved by microwaving and vortexing. After a few minutes of cooling, 1 mL agarose was pipetted onto a 22-mm^2 cover glass slide. Immediately after pipetting, another cover glass was placed on top to create an agarose sandwich in between the two slides. The pads were kept at room temperature for 1 hour to solidify. After the agarose pads were ready, the bacteria was seeded onto the pads, allowed to settle for 15-20 minutes and time-lapse microscopy were started after placing of the cover glass on top. This setup was tested several times and even after 5-6 hours of imaging, cell growth was not observed.

Later, inverted microscope was set up for time-lapse imaging and a chamber of microscopy glasses (22-mm^2) stuck together with Vaseline at the edges was prepared. Similar to the experiments carried out with agarose pads, cultures in early logarithmic growth phase ($OD_{600} = 0.1$) were used for this experiment, and 20X diluted *E. coli*

K12 pUC18 culture was pipetted into the chamber. Using this setup, movies were recorded using untreated cells, cells incubated with antibiotic or P1 peptide. In all of the movies, cell growth was observed similarly in terms of number of division cycles and duration of each cell division cycle. Magnification of 40X was found appropriate for stable focus and single cell observation.

3.4.2. Direct Measurement of Cell Viability and Membrane Permeability

The general protocol used for determination of antibacterial effect of drugs and visualization of the change in bacterial viability is as follows (Figure 3.6):

- Prepare a preculture in 15 mL (in a flask) LB medium (supplemented with 0.1 mg/mL ampicillin for *E. coli* K12 pUC18 cultures) from -80 °C bacteria stock and incubate at 37 °C and 180 rpm overnight (16 hours).
- Inoculate fresh LB (15 mL in a flask, supplemented with 0.1 mg/mL ampicillin for *E. coli* K12 pUC18 cultures) with 100-150 μL of preculture in the morning and incubate at 37 °C and 180 rpm until OD_{600} reaches 0.7.
- Inoculate fresh LB (15 mL in a flask, supplemented with 0.1 mg/mL ampicillin for *E. coli* K12 pUC18 cultures) with 100-150 μL of the culture and incubate at 37 °C and 180 rpm until OD_{600} reaches 0.2.
- Prepare drug/peptide solutions by adding 200 μL of the highest concentration to be tested to the well on the far right of each row and add 100 μL water/buffer solution to the other wells.
- Start performing 2-fold serial dilutions by first withdrawing 100 μL of the highest drug/peptide concentration and pipetting it to the next well on the left that has 100 μL water/buffer solution.
- Continue performing 2-fold serial dilutions by mixing thoroughly and withdrawing 100 μL of drug/peptide and adding it to the next well on the left until you reach column #1. Discard 100 μL of the diluted drug/peptide solution in the last well on the far left.

- Add 100 μL of the culture at $OD_{600} = 0.2$ to the wells that have 100 μL drug or peptide solutions at 2-fold concentrations.
- Incubate the microplate at 37 °C and 180 rpm orbital shaking for 2 (and/or 4) hours (continue to incubate the microplate for up to 20 hours for minimal inhibitory concentration determination).
- Withdraw 75-100 μL of sample cultures at the end of 2 or 4 hours of incubation.
- The withdrawn cultures should have the number of colony forming units (CFU) of around 10^8 CFU/mL according to the manual of the bacterial viability kit (LIVE/DEAD BacLight Bacterial Viability Kit) [159].
- Dilute the withdrawn culture samples in 500 μL of 0.85% NaCl solution and centrifuge for 10 minutes at 10000 rpm.
- Remove the supernatant and dissolve the pellet in 500 μL of 0.85% NaCl solution. Repeat this washing step three times.
- Bring the viability kit (stored at -20 °C) to room temperature and prepare a mixture of dyes (Component A SYTO 9, 1.67 mM / Propidium iodide, 1.67 mM and Component B SYTO 9, 1.67 mM / Propidium iodide, 18.3 mM) with equal amount of both components. SYTO9 is able to dye all nucleic acids independent from the viability of the cell. On the other hand, PI is able to penetrate into the damaged cells only and dyes the nucleic acids as well. The emissions of two dyes are observed at different wavelengths and upon staining with PI the SYTO9 signal is decreased. Therefore, the viable cells are observed as green, while the cells that have membrane damage are considered dead and observed as red.
- Dissolve the recovered pellet in 500 μL of 0.85% NaCl solution and incubate with 1.5 μL of the dye mixture for 15 minutes at room temperature.
- Observe 2.5 μL of culture sample that was incubated with dye mixture under the Nikon Eclipse E200-LED fluorescence microscope with both FITC and TexasRed filters.

The initial experiments with the bacterial viability kit were carried out by visualizing 2.5 μL sample cultures (incubated with bacterial viability kit) that were pipetted directly in between the microscopy glasses. Since the aim is to observe the viability, a

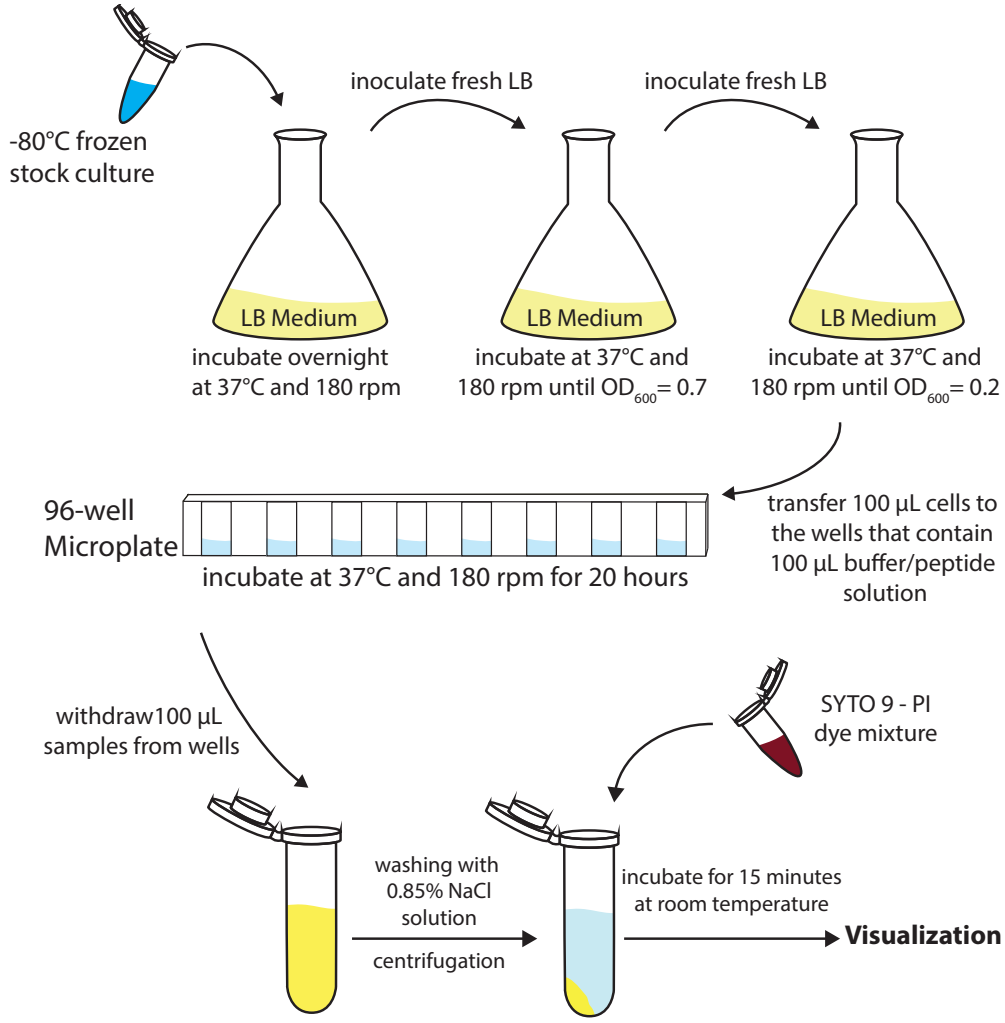

Figure 3.6. The protocol diagram for bacterial viability experiments.

visualization method that does not involve fixation of bacteria was considered suitable, which actually resulted in bacteria that were still mobile during visualization under microscopy. Moreover, it was observed that the number of cells was too low for easy quantitative visual analysis of change in viability. Therefore, instead of visual analysis, the microscopy images were analyzed using ImageJ software and the number of live or dead cells in each image was counted. Even though the live/dead cell ratio comparison is possible for detection of change in bacterial viability, the results were not considered reliable due to the mobility of cells during imaging and the low cell number observed in each image. The sample preparation protocol was later modified and involved an additional step. In order to decrease the mobility of the bacteria and

to gather the cells together, a gel support was prepared. Agar was dissolved in water (15 g/L) and sterilized by autoclaving. The agar-water solution was kept at 55-60 °C to prevent thickening, and 500 μL melted agar was pipetted onto the microscopy glass. The coverslip was placed onto the melted agar to form a sandwich and it was left to cool down. The coverslip was then removed and 2.5 μL of the dye incubated cell culture was pipetted as a drop onto the gel support and left to be adsorbed on the surface (Figure 3.7a). After the sample is adsorbed on the gel surface, a clean coverslip is placed on the gel support (Figure 3.7b).

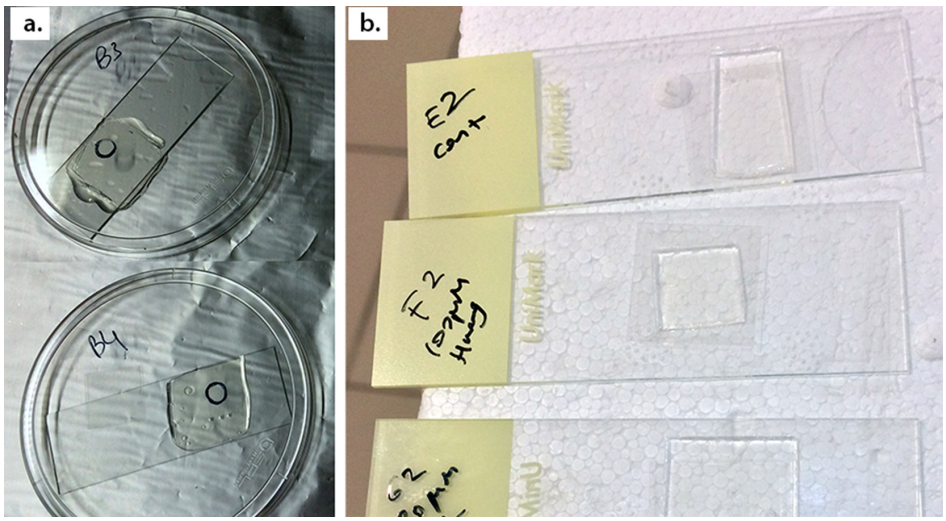

Figure 3.7. Sample preparation for visualization of cell viability and membrane permeability using fluorescence microscopy. (a) The culture samples are adsorbed on the agar support surface, (a) then coverslip is placed on top of the support.

3.4.3. Visualization of Drug Effects on Cell Surface and Structure

Scanning electron microscopy (SEM) was used for high-resolution imaging of the protuberances on the bacterial cell envelope. The general protocol used for preparation of samples for SEM imaging is described below (Figure 3.8):

- Prepare a preculture in 15 mL (in a flask) LB medium (supplemented with 0.1 mg/mL ampicillin for *E. coli* K12 pUC18 cultures) from -80 °C bacteria stock and incubate at 37 °C and 180 rpm overnight (16 hours).

- Inoculate fresh LB (15 mL in a flask, supplemented with 0.1 mg/mL ampicillin for *E. coli* K12 pUC18 cultures) with 100-150 μL of preculture in the morning and incubate at 37 °C and 180 rpm until OD_{600} reaches 0.7.
- Inoculate fresh LB (15 mL in a flask, supplemented with 0.1 mg/mL ampicillin for *E. coli* K12 pUC18 cultures) with 100-150 μL of the culture and incubate at 37 °C and 180 rpm until OD_{600} reaches 0.2.
- Prepare drug/peptide solutions by adding 200 μL of the highest concentration to be tested to the well on the far right of each row and add 100 μL water/buffer solution to the other wells.
- Start performing 2-fold serial dilutions by first withdrawing 100 μL of the highest drug/peptide concentration and pipetting it to the next well on the left that has 100 μL water/buffer solution.
- Continue performing 2-fold serial dilutions by mixing thoroughly and withdrawing 100 μL of drug/peptide and adding it to the next well on the left until you reach column #1. Discard 100 μL of the diluted drug/peptide solution in the last well on the far left.
- Add 100 μL of the culture at $OD_{600} = 0.2$ to the wells that have 100 μL drug or peptide solutions at 2-fold concentrations.
- Incubate the microplate at 37 °C and 180 rpm orbital shaking for 2 hours (continue to incubate the microplate for up to 20 hours for minimal inhibitory concentration determination).
- Withdraw 25-30 μL of culture samples from the selected wells of the microplate and pipette on 0.22 μm pore-sized nitrocellulose membrane filters.
- After the filters have absorbed the samples, float the filters on 2% glutaraldehyde/water (or glutaraldehyde/PBS buffer) solution for 1.5 hours.
- After the fixation step, wash the filters with water (or PBS buffer at pH=7.0 if the glutaraldehyde solution was prepared in buffer).
- Perform dehydration in ethanol series by floating the filters on 30%, 50%, 70% and 90% ethanol-water solutions each for 10 minutes.
- Finally, float the filters on absolute ethanol for 1 hour.
- Leave the filters to air-dry overnight in an empty sterile petri dish.

- The next day, cut small pieces from the filters and coat with Platinum prior to SEM imaging.
- Place the coated filters in the vacuum chamber and capture images in high vacuum mode with 5.0 kV accelerating voltage, 3.0 spot size, working distance around 10 mm, and different magnifications, typically 2000x and 8000x.

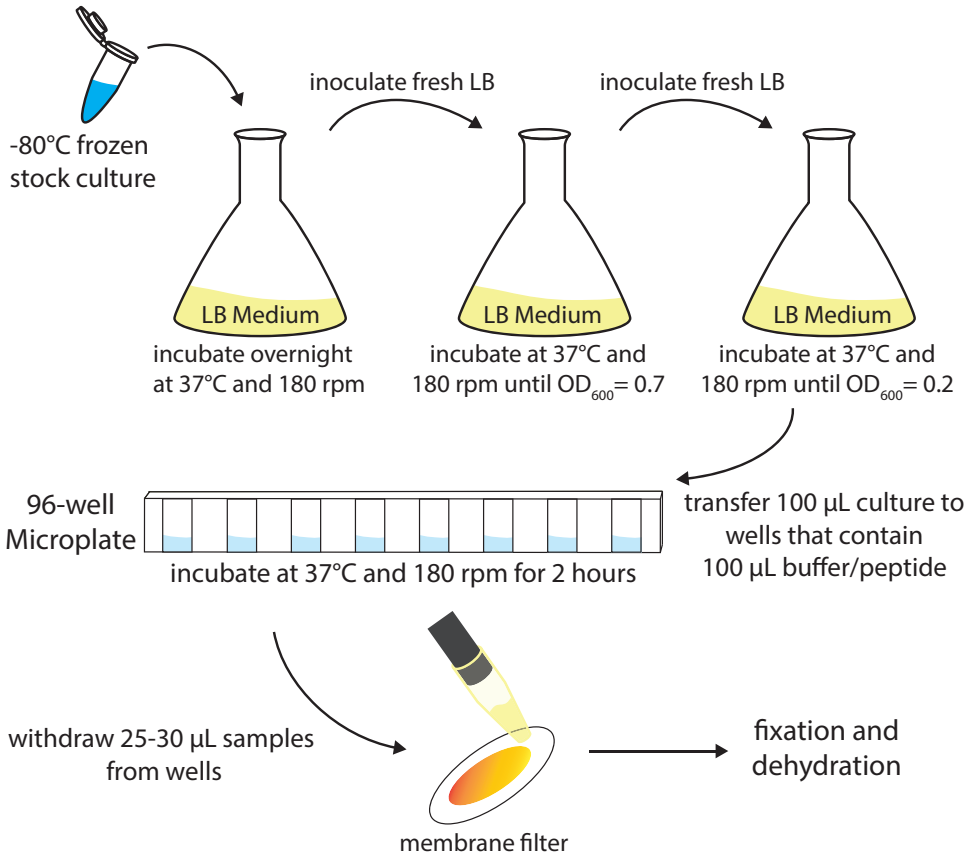

Figure 3.8. The protocol diagram of sample preparation for SEM imaging.

3.4.4. Visualization of Peptide Uptake Using Fluorescence Microscopy

The initial tests of bacterial uptake of peptides were carried out with fluorescein labeled P1 (5-Fluorescein-NH-HAAGDYYAY- $CONH_2$) and fluorescein labeled P2 (5/6-Fluorescein-NH-LLIILHAAGDYYAY- $CONH_2$) peptides. The peptides were delivered as powder in glassware and they were maintained at -20 °C. They were both dissolved in 50 mM K^+PO_4 buffer (pH=7.0) to a concentration of 1 mM and then aliquoted. After aliquoting, the stocks were kept at -20 °C.

A preculture of *E. coli* K12 pUC18 cells in 2 mL LB medium (supplemented with 0.1 mg/mL ampicillin) from -80 °C bacteria stock was prepared and incubated at 37 °C and 180 rpm overnight (16 hours). Next morning, fresh LB (2 mL in a tube, supplemented with 0.1 mg/mL ampicillin) was inoculated with preculture and incubated at 37 °C and 180 rpm until OD_{600} reached 0.2. Cultures in early logarithmic growth phase ($OD_{600} = 0.2$) were treated with peptides P1 or P2 at a final concentration of 100 μM. After 4 hours of incubation with the peptides, 1 mL of *E. coli* K12 pUC18 culture samples were centrifuged and washed with buffer solution twice. The pellets were then recovered and dissolved in buffer solution again to dilute the samples with respect to the recorded OD_{600} of the sample. 2.5 μL samples were observed using a confocal microscope under phase contrast and UV with FITC filter.

The protocol used for preparation of samples for peptide uptake imaging was later modified. Since the usage of microplates and microplate reader decreases the amount of materials to be used, the sample preparation for the uptake experiments of labeled pVEC and labeled P4 peptides were carried out using a microplate in smaller volume. The labeled pVEC (H-LLIILRRRIRKQAHAHSKK(HF488)-NH_2) and labeled P4 (H-LLIILRRGHYYK(HF488)-NH_2) peptides were delivered as powder in glassware and they were maintained at -20 °C. They were first dissolved in the minimum possible volume of DMSO and then diluted to 5 mM peptide concentration with water. The final stock solutions of labeled pVEC and labeled P4 peptides had 2% and 4% DMSO, respectively. 50 μL of peptide aliquots were prepared and stored at -20 °C.

The protocol used for visualization of bacterial uptake of pVEC and P4 peptides is described below:

- Prepare a preculture of wild-type *E. coli* K12 cells in 15 mL (in a flask) LB medium from -80 °C bacteria stock and incubate at 37 °C and 180 rpm overnight (16 hours).
- Inoculate fresh LB (15 mL in a flask) with 100-150 μL of preculture in the morning and incubate at 37 °C and 180 rpm until OD_{600} reaches 0.7.

- Inoculate fresh LB (15 mL in a flask) with 100-150 μL of the culture and incubate at 37 °C and 180 rpm until OD_{600} reaches 0.2.
- Prepare peptide solutions by adding 200 μL of the highest concentration to be tested to the well on the far right of each row and add 100 μL water to the other wells.
- Start performing 2-fold serial dilutions by first withdrawing 100 μL of the highest peptide concentration and pipetting it to the next well on the left that has 100 μL water.
- Continue performing 2-fold serial dilutions by mixing thoroughly and withdrawing 100 μL of peptide and adding it to the next well on the left until you reach column #1. Discard 100 μL of the diluted peptide solution in the last well on the far left.
- Add 100 μL of the culture at $OD_{600} = 0.2$ to the wells that contain 100 μL peptide solutions at 2-fold concentrations.
- Incubate the microplate at 37 °C and 180 rpm orbital shaking.
- Withdraw 200 μL of culture samples from the selected wells of the microplate at the end of 30, 90, and 180 minutes of incubation time.
- Centrifuge the samples for 10 minutes at 10000 rpm.
- Remove the supernatant and dissolve the pellet in 100 μL of sterile demi-water. Repeat this washing step three times.
- Dissolve the final pellet in 100 μL of sterile demi-water and observe 2.5 μL of the washed culture sample under the Nikon Eclipse Ti-E inverted microscope under brightfield and UV with FITC filter.

3.4.5. Live Cell Imaging with Microfluidic Systems

Hydrophilized, Zeonor reaction chamber chips of 10 μL volume; with 500 μm chamber depth and 188 μl lid thickness (Figure 3.9) were purchased from Microfluidic ChipShop GmbH. Silicon tubings (with inner diameter of 0.5 mm and outer diameter of 2.5 mm) were used to feed liquids from each syringe placed at a peristaltic syringe pump. Opaque and Thermoplastic Elastomer (TPE) Male Mini Luer fluid connectors were used in the experiments to connect the silicone tubings to the chip inlet.

All experiments were carried out at room temperature and chips were continuously monitored using Nikon Eclipse Ti-E inverted microscope. Wild-type *E. coli* K12 cells were used in all experiments with bacteria and LB medium was used as broth media.

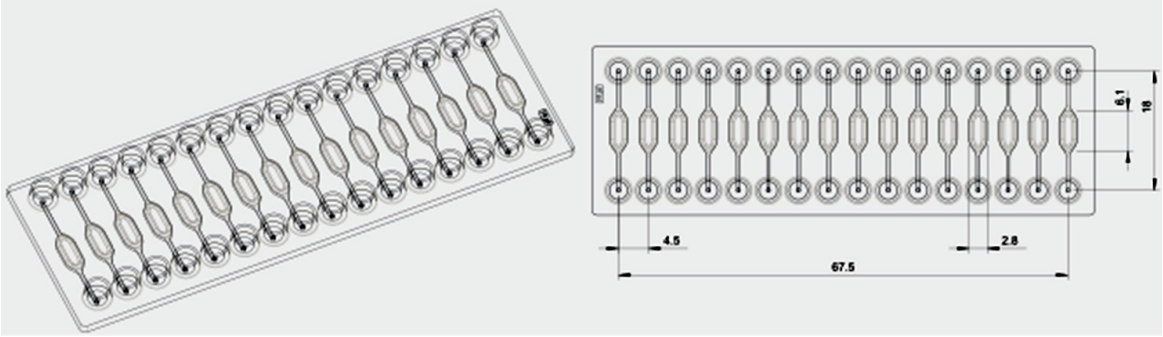

Figure 3.9. Schematic of the reaction chamber chips that are used in the experiments.

3.4.5.1. Testing of the Reaction Chips with Beads. The channel was first perfused with distilled water at a rate of 1 μL/min and the flow in the chamber was monitored to observe that the channel was filled in around 40 minutes. After perfusion with distilled water, the beads (with a diameter of 2 μm) were perfused into the chamber through the microfluidic inlet channel at a rate of 0.2 μL/min, and the chamber was continuously monitored. The inlet bead flow was stopped and distilled water (at a rate of 0.2 μL/min) was perfused again into the channel to see if the beads were able to stay in the chamber rather then being swept by the water flow.

3.4.5.2. Testing of the Reaction Chips with Bacteria. The growth experiments were performed with wild-type *Escherichia coli* K12 cells. The pre-culture was prepared from a single colony of wild type *E. coli* in 15 mL Luria-Bertani (LB) medium (per liter: 10 g tryptone, 5 g yeast extract, 10 g NaCl) and cells were grown overnight at 37 °C and 180 rpm. This pre-culture was used to inoculate 15 mL fresh LB medium at 1:100 dilution and the inoculum was incubated at 37 °C and 180 rpm until the OD_{600} was 0.2 (early logarithmic phase). In μL/min) without bacteria, and then switched to a broth media with cultured bacteria (at OD_{600} of 0.2). In the first attempts, many

problems were faced during this switching between the LB medium and culture tubings. Bubbling in the chambers and increased pressure leading to purging of chamber contents were some of the major problems. To overcome these problems, a Y-shaped capillary connector was introduced between the tubings of LB medium and bacterial culture. By using this connector, the need of unplugging and re-plugging the tubings to the inlet of the channel was eliminated.

After the first perfusion of the chamber with LB medium, LB syringe pump was switched off and bacterial culture pump was switched on. After a short period of pumping the culture at a rate of 0.1 μL/min, the flow was stopped for a short period to allow the bacteria to settle down. After the immobilization period, the flow of plain LB medium was turned on. The chamber was monitored continuously and images from the same spot were captured every 15 minutes starting from the time point when the cells were loaded in the chamber.

3.4.5.3. Bacterial Uptake of Fluorescein Amine in Reaction Chips. Experiments were performed with wild-type *Escherichia coli* K12 cells. The pre-culture was prepared from a single colony of wild type *E. coli* in 15 mL LB medium and cells were grown overnight at 37 °C and 180 rpm. This pre-culture was used to inoculate 15 mL fresh LB medium at 1:100 dilution and the inoculum was incubated at 37 °C and 180 rpm until the OD_{600} was 0.1. The culture at OD_{600} = 0.1 was then diluted 1:2 and kept in +4 °C prior to perfusion into the chip.

In this experiment, two Y-shaped capillary connectors between the tubings of LB medium, bacterial culture, and fluorescein amine (600 μM, in water) were introduced. The chamber was first perfused with plain LB medium (1 μL/min) without bacteria, and then a broth media with cultured bacteria (at OD_{600} of around 0.05) was fed to the channel. After a short period of pumping the culture at a rate of 0.1 μL/min, sterile LB medium was reintroduced (at a rate of 0.1 μL/min) for 1 hour to allow the bacteria to slowly settle down and to sweep the excess amount of mobile bacteria. After 1 hour, fluorescein amine was perfused at a rate of 0.1 μL/min for a total volume

of 10 μL. After perfusion of fluorescein amine, washing with LB medium (at a rate of 0.1 μL/min) was carried out. The chamber was monitored continuously and images from the same spot were captured every 15 minutes starting from the time point when fluorescein amine was perfused. Fluorescence microscopy images (overlaid on bright field) were captured using the FITC filter.

3.4.5.4. Bacterial Uptake of BacLight Bacterial Viability Kit in Reaction Chips. Nucleic acid dyes, such as SYTO9 and PI, may bind to the nucleic acids or other components in rich growth media, which may in turn reduce or abolish the dye uptake into the cells. For the experiments with the viability kit, as described in Section 3.4.2, the experimental procedure involved a centrifugation and washing step of the cells to remove the growth medium completely, as it was suggested in the viability kit manual [159]. The preliminary chip experiment with this bacterial viability kit involved perfusion of LB medium followed by the perfusion of the viability dye solution. The viability dye uptake into bacteria (data not shown) was not observed, but a high amount of background fluorescence was observed continuously, possibly due to binding of the dyes to the media components. Therefore, an additional centrifugation and washing steps were introduced for the cells, and LB medium usage in the chip was omitted. Instead, sterile demi-water was used as the washing and perfusion liquid in the chip.

The experiment was performed with wild-type *Escherichia coli* K12 cells. The pre-culture was prepared from a single colony of wild type *E. coli* in 15 mL LB medium and cells were grown overnight at 37 °C and 180 rpm. This pre-culture was used to inoculate 15 mL fresh LB medium at 1:100 dilution and the inoculum was incubated at 37 °C and 180 rpm until the OD_{600} was 0.2. 4 mL of this culture was centrifuged at 10,000 rpm for 10 minutes and the supernatant was removed. The pellet was dissolved in sterile water and centrifuged again at 10,000 rpm for 5 minutes. By repeating this last step twice, the cells were washed and growth media traces were removed. 4 mL of the washed culture at OD_{600} = 0.2 was then diluted 1:2 and kept in +4 °C prior to perfusion into the chip. Two Y-shaped capillary connectors were used between the tubings of water, bacterial culture, and bacterial viability dye solution (3 μL dye

mixture of equal amounts of Component A and Component B in 500 μL water) (Figure 3.10). The chamber was first perfused with water (1 mL/hour) without bacteria, and then with cultured bacteria (at OD_{600} of around 0.1). After pumping the culture at a rate of 0.2 μL/min for 30 minutes, the culture pump was switched off and the dye solution pump was switched on (at a rate of 0.3 μL/min). After waiting for about 30 minutes, the chamber was monitored continuously while still feeding viability dye solution, and images from the same spot were captured every 30 minutes. Fluorescence microscopy images were captured using the FITC (for SYTO9 signal) and Texas Red (for PI signal) filters.

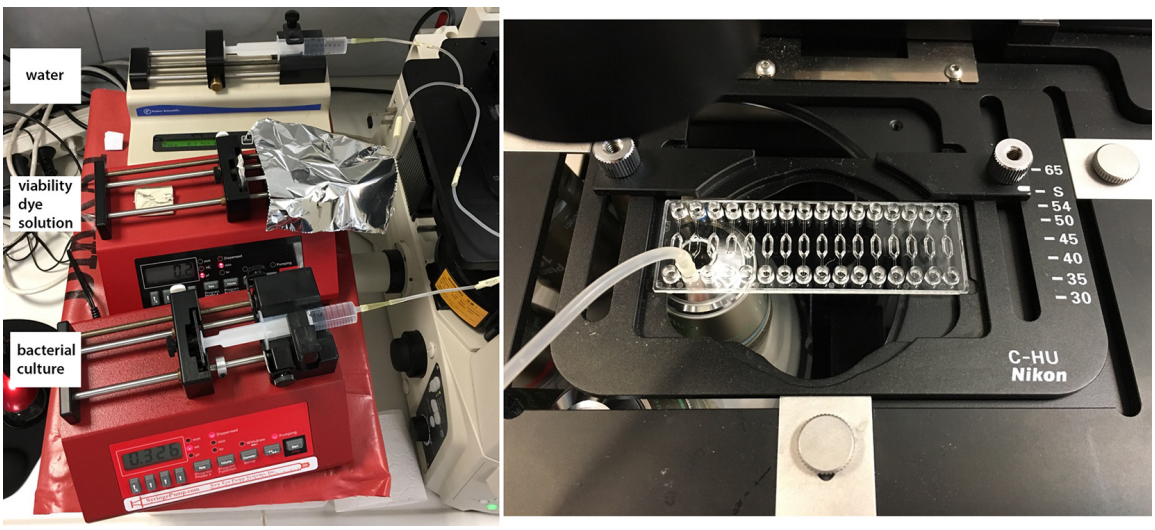

Figure 3.10. Water and viability dye solution tubings were connected, and their outlet was connected to the culture tubing (left). The outlet of latter connector was connected to the chip via a Male Mini Luer fluid connector (right).

3.4.5.5. Bacterial Uptake of pVEC and P4 Peptides in Reaction Chips. Experiments were performed with wild-type *Escherichia coli* K12 cells. The pre-culture was prepared from a single colony of wild type *E. coli* in 15 mL LB medium and cells were grown overnight at 37 °C and 180 rpm. This pre-culture was used to inoculate 15 mL fresh LB medium at 1:100 dilution and the inoculum was incubated at 37 °C and 180 rpm until the OD_{600} was 0.2. 4 mL of this culture was centrifuged at 10,000 rpm for 10 minutes and the supernatant was removed. The pellet was dissolved in sterile water and centrifuged again at 10,000 rpm for 5 minutes. By repeating this last step twice,

the cells were washed and growth media traces were removed. 4 mL of the washed culture at OD_{600} = 0.2 was then diluted 1:2 and kept in +4 °C prior to perfusion into the chip. Two Y-shaped capillary connectors were used between the tubings of water, bacterial culture, and pVEC or P4 solutions (250 μM in DMSO-water mixture).

The chamber was first perfused with water (1 mL/hour) without bacteria, and then with cultured bacteria (at OD_{600} of around 0.1). After pumping the culture at a rate of 0.2 μL/min for 30 minutes, the culture pump was switched off and the peptide solution pump was switched on (at a rate of 0.3 μL/min). For the uptake experiment with pVEC peptide, continuous chamber monitoring was started after 30 minutes of incubation with the peptide. After 1 hour of feeding pVEC solution, the peptide pump was switched off and washing with sterile water was carried out. For the uptake experiment with P4 peptide, continuous chamber monitoring was started immediately when the P4 solution pump was switched on and no further washing of the chamber was carried out. In both experiments images from the same spot in the chamber were captured every 30 minutes. Fluorescence microscopy images were captured using the FITC filter.

3.5. Drug Effects in Mammalian Cell Culture

3.5.1. Drug Effects on HeLa Cells

Previously plated HeLa cells were washed with trypsin to remove them off the plate and then centrifuged to form a pellet. The pellet was dissolved in 1-1.5 mL of DMEM medium and 50 μL of the culture were plated in each of 3 plates. The plates were then filled with 2 mL of DMEM medium.

The next day, DMEM medium was removed from the plates and fresh medium was added. Three different media were prepared; first one was 2 mL DMEM with 200 μL PBS buffer added, second was 2 mL DMEM with 2 μL ampicillin and 200 μL PBS buffer added, and the third one was 2 mL DMEM with 2 μL ampicillin and 200 μL P1 peptide. Microscopy images were taken of the same spot on each plate on the first,

third and sixth days. Hemocytometer was used for counting of number of the HeLa cells in each treated culture.

3.5.2. Measurement of Cytotoxicity Using XTT Proliferation Assay

Tetrazolium salts (MTT, XTT) have been widely used for many years in quantification of viable cells, histochemical localization studies and cell biology assays [160, 161]. The XTT cell proliferation assay was first described [162] as an effective method to quantify cell growth and to measure drug sensitivity in tumor cell lines and can be used in cell proliferation, cytotoxicity, and apoptosis assays [161–163]. The Cell Proliferation Kit II (XTT) contains two reagents, which are XTT labeling reagent (sodium 3- [1-(phenylaminocarbonyl) - 3,4 - tetrazolium] - bis (4-methoxy-6-nitro) benzene sulfonic acid hydrate, dissolved in RPMI 1640 without phenol red) and electron-coupling reagent (ECR) (PMS; (N-methyl dibenzopyrazine methyl sulfate) dissolved in phosphate buffered saline (PBS)). The cell proliferation assay is based on the reduction of colorless or slightly yellow tetrazolium salt (XTT) to form an orange formazan dye by cells with metabolic activity. The accuracy and sensitivity of an XTT assay is greatly improved by the usage of PMS since it helps the reduction of XTT by picking up electrons at the cell surface.

The general protocol used for measurement of drug cytotoxicity with XTT assay is described below:

- Bring frozen HK-2 (human kidney cell) stock to 37 °C and centrifuge to recover the cells.
- Dissolve the pellet in Dulbecco's Modified Eagle Medium: Nutrient Mixture F-12 (DMEM/F12) and add 5000 cells per 100 μL (5x10^4 cells/mL) to each well of 96-wells TPP plate.
- Incubate the microplate overnight at 37 °C under a humidified, 5% CO2 atmosphere.
- The next day, cells are adherent to the plate and remove the medium from all wells.

- Supplement DMEM/F12 media with selected drugs to a desired final concentration and add 100 μL of supplemented media to selected wells.
- Prepare control samples to include the same amount of water with the drug treated samples, non-treated samples to include DMEM/F12 media (100 μL) without any drug. Prepare blank wells to have only DMEM/F12 media (100 μL) without any cells. All samples should be prepared as triplicates.
- Incubate the plate overnight (20-24 hours) at 37 °C under a humidified, 5% CO2 atmosphere.
- The next day, bring the frozen XTT Assay reagents to room temperature and mix 4 mL XTT with 80 μL ECR.
- Add 100 μL of this mixture to all wells and incubate the plate further for 3 hours at 37 °C under a humidified, 5% CO2 atmosphere.
- After 3 hours of incubation, measure the absorbance for each well at 490 and 650 nm wavelengths.
- Subtract the absorbance values measured at 650 nm from the ones measured at 450 nm. Subtract the blank absorbance values from all measurements of wells that had HK-2 cells. Since non-treated samples are considered to be 100% viable, normalize the absorbance measurements of other wells with respect to non-treated samples.

3.5.3. Measurement of Cytotoxicity Using Cell Counter and Trypan Blue Dye

The XTT assay measures metabolic activity of a culture, therefore the assay results could indicate either the change in the number of cells or the change in the metabolic activity of each cell. Considering this, the number of viable cells upon treatment with drugs could also be measured by using a cell counter and trypan blue dye. Trypan blue is a viability dye that can penetrate into cells with damaged membranes and it does not alter the viability of the cells [164–166].

The general protocol used for measurement of drug cytotoxicity with cell counter and trypan blue dye is described below:

- Bring frozen HK-2 (human kidney cell) stock to 37 °C and centrifuge to recover the cells.
- Dissolve the pellet in Dulbecco's Modified Eagle Medium: Nutrient Mixture F-12 (DMEM/F12) and add 2 mL HK-2 culture ($5x10^4$ cells/mL) to each well of 6-well TPP plate.
- Incubate the microplate overnight at 37 °C under a humidified, 5% CO2 atmosphere.
- The next day, cells are adherent to the plate and remove the medium from all wells (except one well, which will be the nontreated sample).
- Supplement DMEM/F12 media with selected drugs to a desired final concentration and add 2 mL of supplemented media to selected wells.
- Prepare control (blank) samples to include the same amount of water (or DMSO-water mixture) with the drug treated samples.
- Incubate the plate overnight (20-24 hours) at 37 °C under a humidified, 5% CO2 atmosphere.
- The next day, capture microscopy images for all treatments and the nontreated sample for comparison of the drug effects.
- Before using the cell counter, withdraw the medium from each well and pipette in separate falcons.
- Add 1 mL PBS buffer to each well to wash and then withdraw again to be pipetted in each falcon.
- To wash off the adherent cells in each well, add 250 μL trypsin to each well and incubate the plates at 37 °C under a humidified, 5% CO2 atmosphere for around 5 minutes.
- After 5 minutes, check each well under microscopy to see if the cells are round-shaped and moving around upon shaking the plate.
- If the adherent cells are removed off the wells, add 500 μL PBS to each well and withdraw contents from each well to pipette in falcons.
- Centrifuge each falcon at 2000 rpm for 2 minutes, remove the supernatant and dissolve the pellets in 1 or 2 mL PBS.
- Mix 10 μL trypan blue with each 10 μL dissolved pellet sample to dye the cells.

- Get 10 μL of dyed cell suspension and pipette into the microscopy glass to place into the cell counter.

4. RESULTS AND DISCUSSION

4.1. Membrane Translocation Simulations of Membrane Active Peptides

4.1.1. SMD Simulations of Membrane Translocation of Beta-Lactamase Inhibitory Peptides

The molecular mechanism by which the beta-lactamase inhibitory peptides move through the membrane was examined by steered molecular dynamics (SMD) simulations. The results given in this section can also be found in the manuscript published in the Journal of Peptide Science entitled 'A Novel Chimeric Peptide with Antimicrobial Activity' by Begum Alaybeyoglu, Berna Sariyar Akbulut and Elif Ozkirimli.

In order to investigate the effect of initial peptide conformations on the translocation mechanism, the coordinates for the peptides P1 and P2 were either based on BLIP 45-53 residues or they were assigned as extended chain.

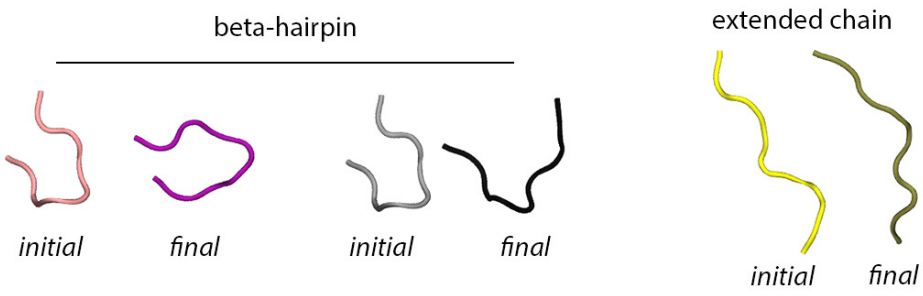

Figure 4.1. Initial and final structures of P1 peptide. Initial structures were assigned as either beta-hairpin or extended chain. Final structures were obtained after minimization and equilibration in water.

In the simulations of P1, the beta-hairpin (formed by H bonding between residues Gly4, Asp5, Tyr6) was maintained during the equilibration of the peptide in water (Figure 4.1). On the other hand, when the initial structure was assigned as an extended

chain, the equilibrated peptide became more compact after the equilibration simulation in the peptide-lipid-water system, as it got closer to the membrane, and a beta-hairpin formed by residues Gly4, Asp5, and Tyr6 (Figure 4.2). When two initial structures were compared, it was observed that the extended chain initial structure changed as the peptide made the initial contact with the P-heads, resembling the structure observed with the beta-hairpin initial structure of P1.

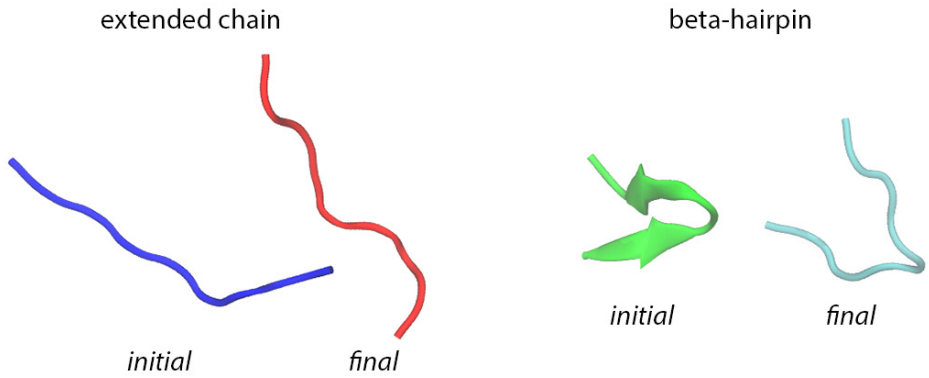

Figure 4.2. Initial and final structures of P1 peptide in the peptide-lipid-water system.

Similarly, for P2, the peptide assumed a more compact form whether the starting structure is an extended chain or a beta-hairpin. The hairpin formed by Gly9, Asp10, and Tyr11 residues of P2 in the initial beta-hairpin structure was maintained after equilibration of the peptide with beta-hairpin initial conformation and the same hairpin formed after equilibration of the extended chain structure (Figure 4.3).

Interestingly, the peptide conformations in the lipid bilayer during the SMD simulations were very similar for P1 and P2. These observations of the calculated SMD trajectories suggested that the initial structure assignment does not change the translocation pathway and interactions with the membrane. For all cases, the peptides moved through the bilayer as a single chain, penetrating the bilayer like a needle.

In order to investigate the membrane translocation dynamics of P1 and P2 peptides, and the contribution of the LLIIL stretch, SMD simulation for both peptides were carried out multiple times with the POPE lipid bilayer. Each simulation was first

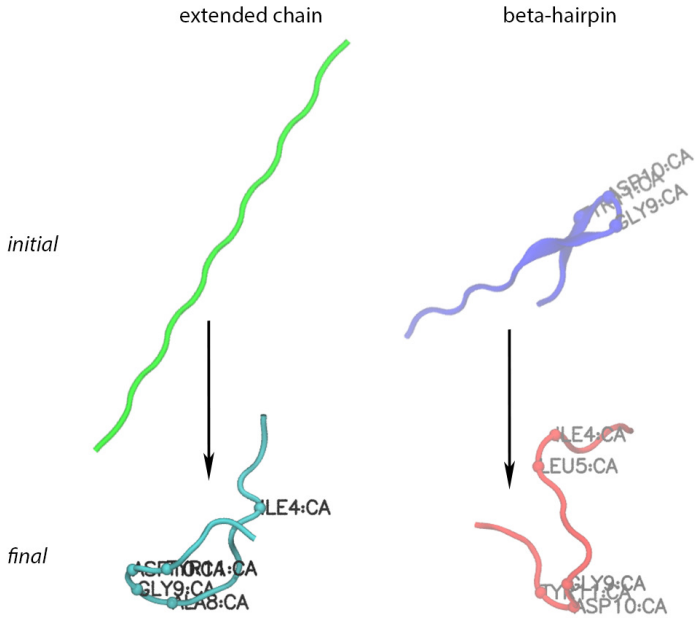

Figure 4.3. Initial and final structures of P2 peptide. Initial structures were assigned as either beta-hairpin or extended chain. Final structures were obtained after minimization and equilibration in water.

analyzed separately (Figure 4.4), and average profiles were calculated for P1 and P2 simulations (Figure 4.5).

The modification of P1 (addition of LLIIL) increased the hydrophobicity of the peptide; hence P2 was expected to have increased interactions with the membrane lipids. Even though the averaged interaction energy profiles for both peptides are similar in trend and magnitude (Figure 4.4 and Figure 4.5) and do not reveal any distinct stages of the transport process, the electrostatic energy between the peptide and the lipid suggests that transport occurs in four stages at electrostatic energy values of -40, -100, -40 and -60 kcal/mol. For P1, electrostatic energy was -40 kcal/mol only between z values of 40 to 30 Å, but for P2, the electrostatic energy was -40 kcal/mol between z values of 40 to 10 Å (Figure 4.6). This stage (i) corresponds to the initial interactions of the peptides with the membrane and P2 has increased interactions due to its hydrophobic N-terminus. The electrostatic energy increases to -60 kcal/mol and it is conserved until the SMD atom reaches the membrane core. At this stage P2 is

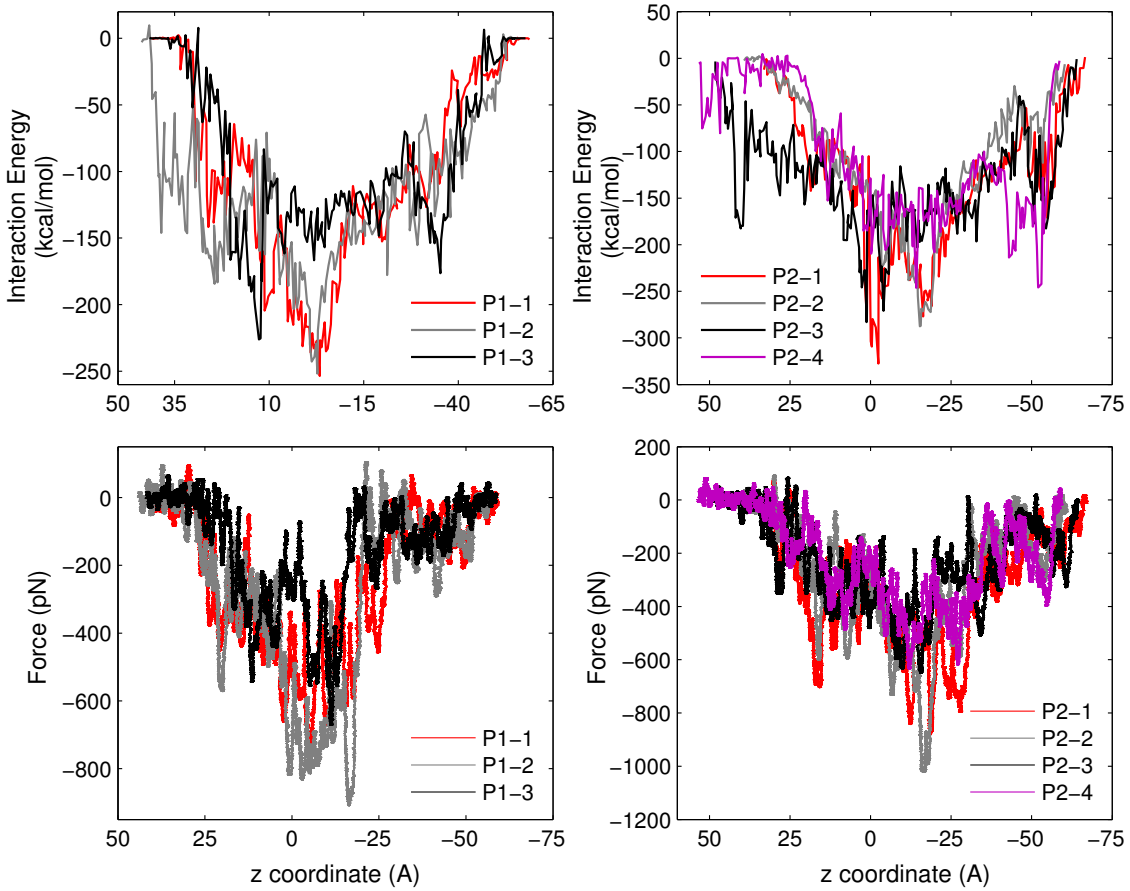

Figure 4.4. Interaction energy (top) and force (bottom) profiles of each P1 (left) and P2 (right) SMD simulation.

in contact with the membrane closely and reaches a more compact state compared to its initial structure (Figure 4.6). This behavior of P2 resembles that of antimicrobial peptides, which are usually found to adapt a horizontal orientation during their initial contact with the membranes.

The initial interactions of P1, on the other hand, increase almost linearly as the peptide penetrates into the bilayer with no plateau in interaction energy (Figure 4.4 and Figure 4.5). The maximum values of electrostatic energies reached by P1 and P2 are similar in magnitude but the driving forces of the interactions are different. Electrostatic energy of P1 reaches its maximum values at stage (ii) as the peptide

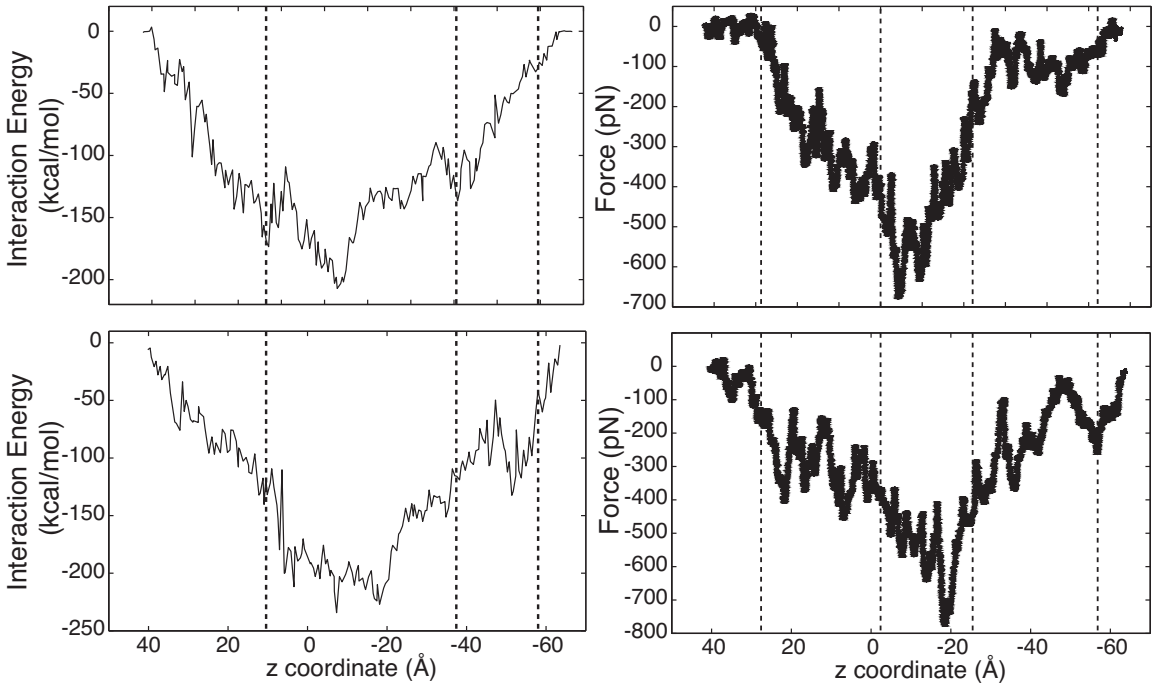

Figure 4.5. Average interaction energy (left) and force (right) profiles of P1 (top) and P2 (bottom) SMD simulations.

N-terminus penetrates and starts embedding itself in the lipid bilayer (Figure 4.6). On the other hand, the electrostatic energy of P2 reaches its maximum when the hydrophobic N-terminus reaches the bilayer core and this value is conserved until the N-terminus exits the bilayer. Indeed, when the electrostatic interaction energy values are calculated on a residue basis, the strongest interactions occur between Asp, C-terminus Tyr (Asp5 and Tyr9 for P1, Asp10 and Tyr14 for P2) residues and phosphate groups for both P1 and P2. His1 residue of P1 is one of the major contributors to electrostatic interactions, whereas in the case of P2, His6 residue is no longer of importance and Leu1 has become a major electrostatic interaction contributor. Stage (iii) corresponds to the conformations of both peptides fully embedded in the membrane where the van der Waals (VdW) and interaction energy between the peptides and the membrane reach maximum values (Figure 4.6). For both peptides, the electrostatic interaction energy decreases upon exit of N-terminus from the bilayer at stage (iv). The final increase in the electrostatic energy at stage (v) is observed as the C-terminus (YYAY) of both peptides leave the membrane (Figure 4.6). The van der Waals energy between

the lipids and P2 reaches higher values than that with P1 when the peptide is fully embedded in the membrane (between z values of -10 to -30 Å).

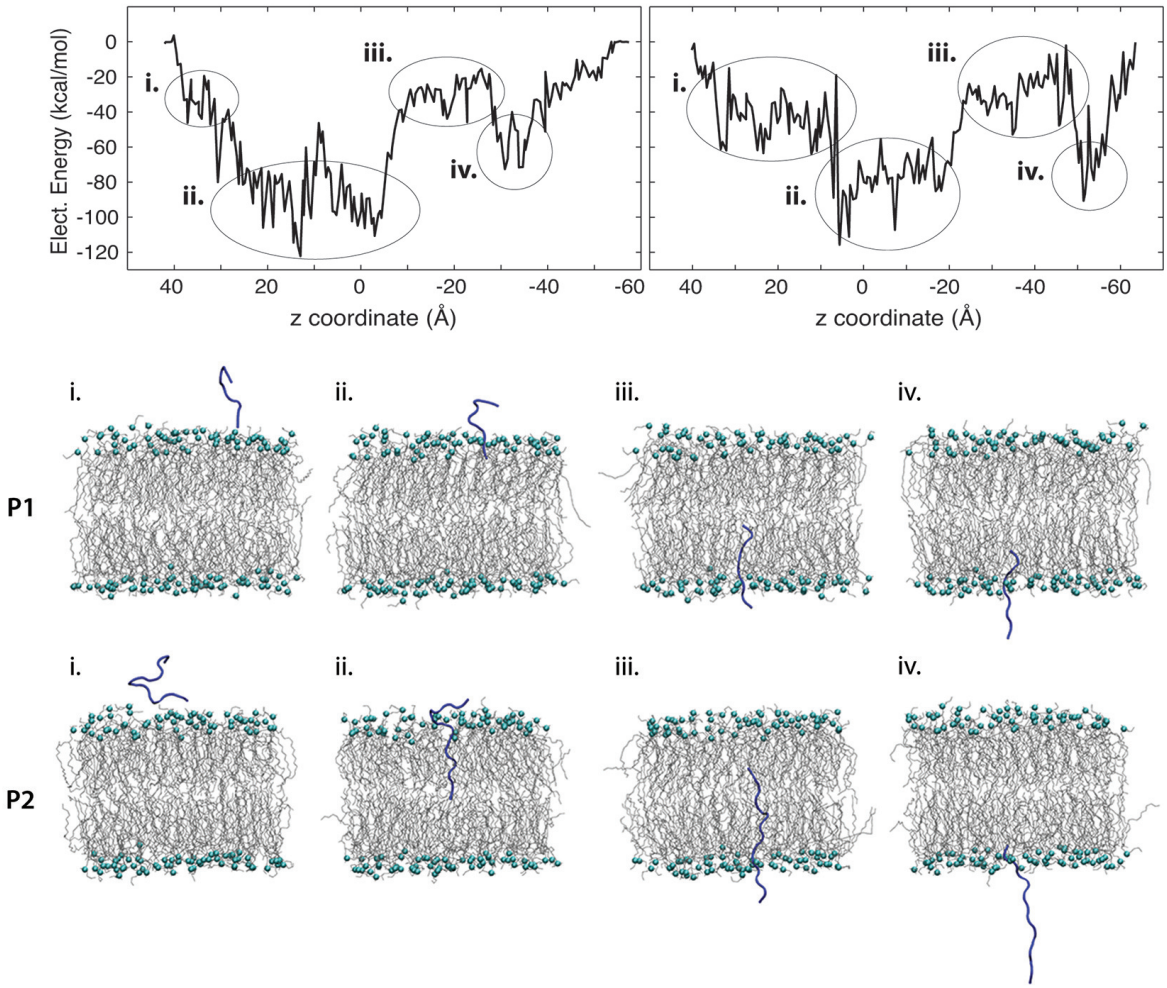

Figure 4.6. Electrostatic energy profiles of P1 (top left), and P2 (top right), and snapshots from the simulation trajectories of P1 and P2.

Lipid tail order parameters measured using deuterium solid-state NMR of deuterium labeled lipids provide information about the order and configuration of the fatty acyl chains. Here, the order of the lipid tails in the presence of the peptides was compared with that in a 20 ns membrane-water MD simulation to determine the effect of peptide penetration (Figure 4.7a). The calculated order parameters were in good agreement with experimentally measured C-D bond order parameters of sn-2 acyl chain at 30 °C for POPE membrane [167]. As expected, the order parameter for the membrane was higher in the absence of the peptides than in the presence of the

peptides. The decrease in order parameter in the presence of the peptides was most significant at the bilayer surface while it can be considered negligible at the bilayer core. As the peptide moved through the bilayer, a pore formed (since the phosphate heads were free to move in the x-y direction) in the membrane plane. Therefore, the increase in disorder was induced by transport of the peptides across the bilayer and the interactions of the peptide with the lipid acyl chains.

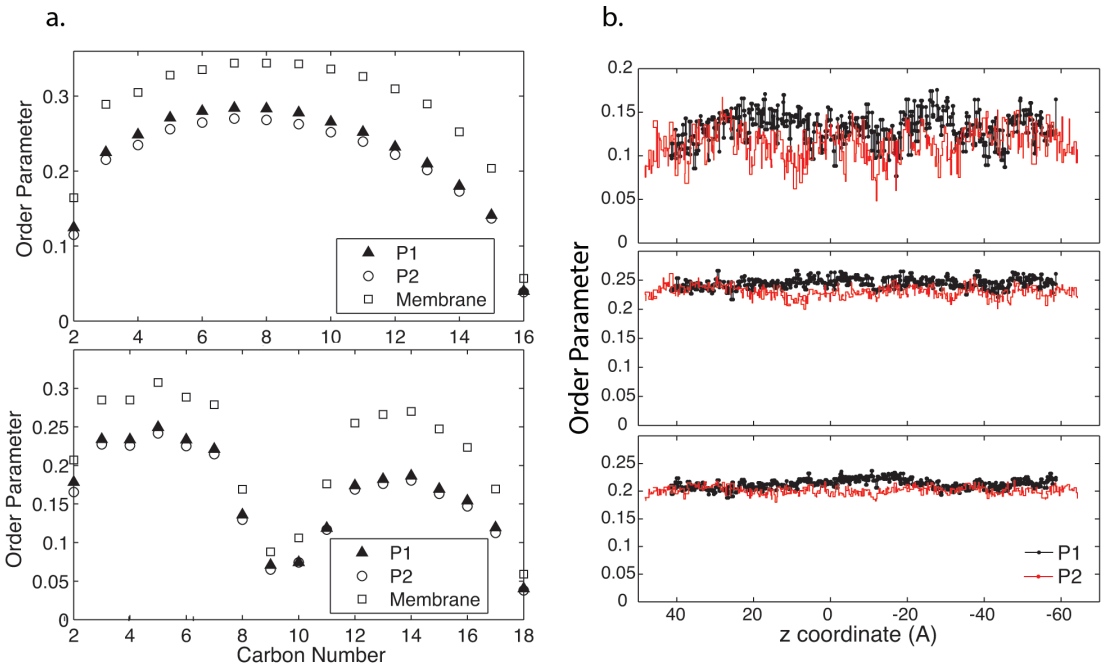

Figure 4.7. (a) Order parameters of the bilayer palmitoyl (top), and oleyl (bottom) carbon atoms in the presence or absence of the peptides. (b) Order parameters of C2 (top), C8 (center) and C16 (bottom) carbon atoms in the presence of P1 or P2.

On average, P2 created slightly higher disorder especially near the lipid head groups (Figure 4.7a) possibly suggesting that the higher hydrophobicity of P2 results in increased interactions with the membrane lipids during initial penetration causing fluctuations of the lipid tails that are closer to the lipid-water interface. While the change in the C8 or C16 carbon order parameters of the palmitoyl tail was negligible, the order parameter of the C2 in the palmitoyl tail fluctuated significantly during the simulations (Figure 4.7b). Such an increase in the disorder of carbons near the membrane surface suggested that the strong interaction with the membrane surface

might have induced pore formation. The results are in agreement with the interaction energy analysis, which showed that the initial penetration into the upper P-heads is an important energy barrier in the uptake of the peptides.

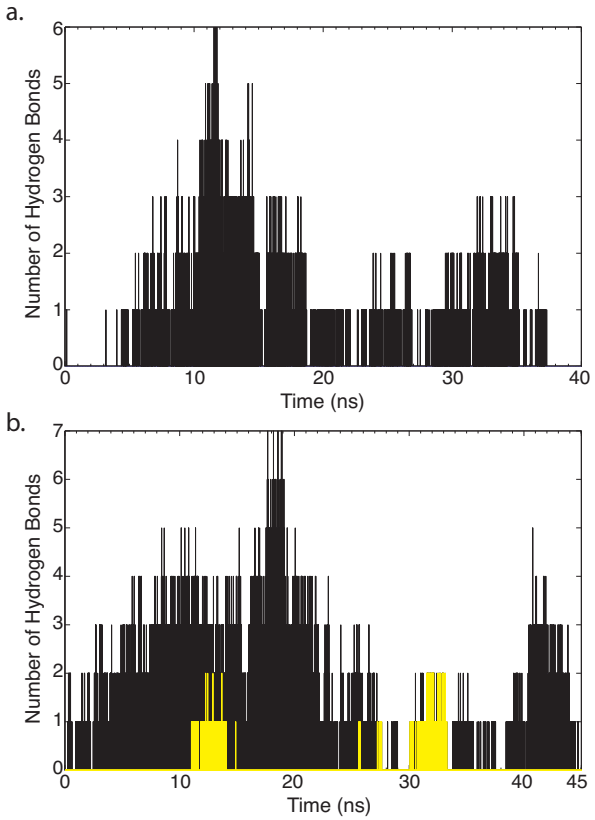

Figure 4.8. Number of hydrogen bonds formed over 40 ns simulation time for P1 (a) and 45 ns simulation time for P2 (b). The hydrogen bonds formed between the LLIIL tail of P2 and the lipid are highlighted in yellow (b).

The hydrogen bonding interactions of the peptides with the lipid bilayer further provides insights on residue-based interactions for each peptide. The hydrogen bonding interactions during the translocation of P2 are present over the entire course of the simulation even though the LLIIL tail is not the major contributor statistically (Figure 1b). The Asp residue (Asp5 in P1 and Asp10 in P2) is found to be the major contributor to the hydrogen bonding of the peptides with 15% occupancy for P1 and 25% occupancy for P2 over the simulation times. Tyr residues are the second major contributors to the hydrogen bonding with 6% occupancy of Tyr6, 2% occupancy of Tyr7, 10% occupancy of Tyr9 for P1 and 11% occupancy of Tyr11, 9% occupancy of Tyr12, 26% occupancy of

Tyr14 for P2 respectively. For P2, the LLIIL tail contributes to the hydrogen bonding interactions with 4% occupancy, which facilitates the peptide lipid interactions.

4.1.2. SMD Simulations of Membrane Translocation of pVEC and its Mutants

In this part of the study, wild type and mutant pVEC peptides with increased or decreased activity were compared using SMD simulations (Table 3.1). Here, SMD simulations on the wild-type pVEC and four mutants were performed in an effort to observe the mechanism whereby the peptides are translocated across the cell membrane.

4.1.2.1. SMD Simulation of Membrane Translocation of wild-type pVEC. Membrane translocation simulation for wild-type pVEC (wt-pVEC or wt) was analyzed for water molecules that enter the lipid bilayer upon pore formation, force applied on the peptide and interactions of the peptide with the lipid bilayer (Figure 4.9). Peptide is shown in cartoon representation (black) and water molecules are represented as blue spheres (Figure 4.9b).

Water molecules start to penetrate into the membrane with the initial penetration of the N-terminus. The number of water molecules reaches a local maximum value of 33 as the N-terminus resides around the membrane core (Figure 4.9). The pore formed by the peptide is larger during the N-terminus insertion, which lets the water molecules to penetrate into the membrane, but as the water molecules are pushed out of the membrane a local minimum value is observed (ii). As the rest of the peptide is inserted, more water molecules penetrate into the membrane and the number of water molecules reaches a global maximum value (around 50) since the peptide is surrounded by water when it is fully embedded in the membrane (iii). Number of water molecules decreases as the peptide leaves the membrane (iv).

The SMD simulations were carried out using constant velocity pulling. Thus, the force applied on the peptide varies throughout the simulations and this variation gives

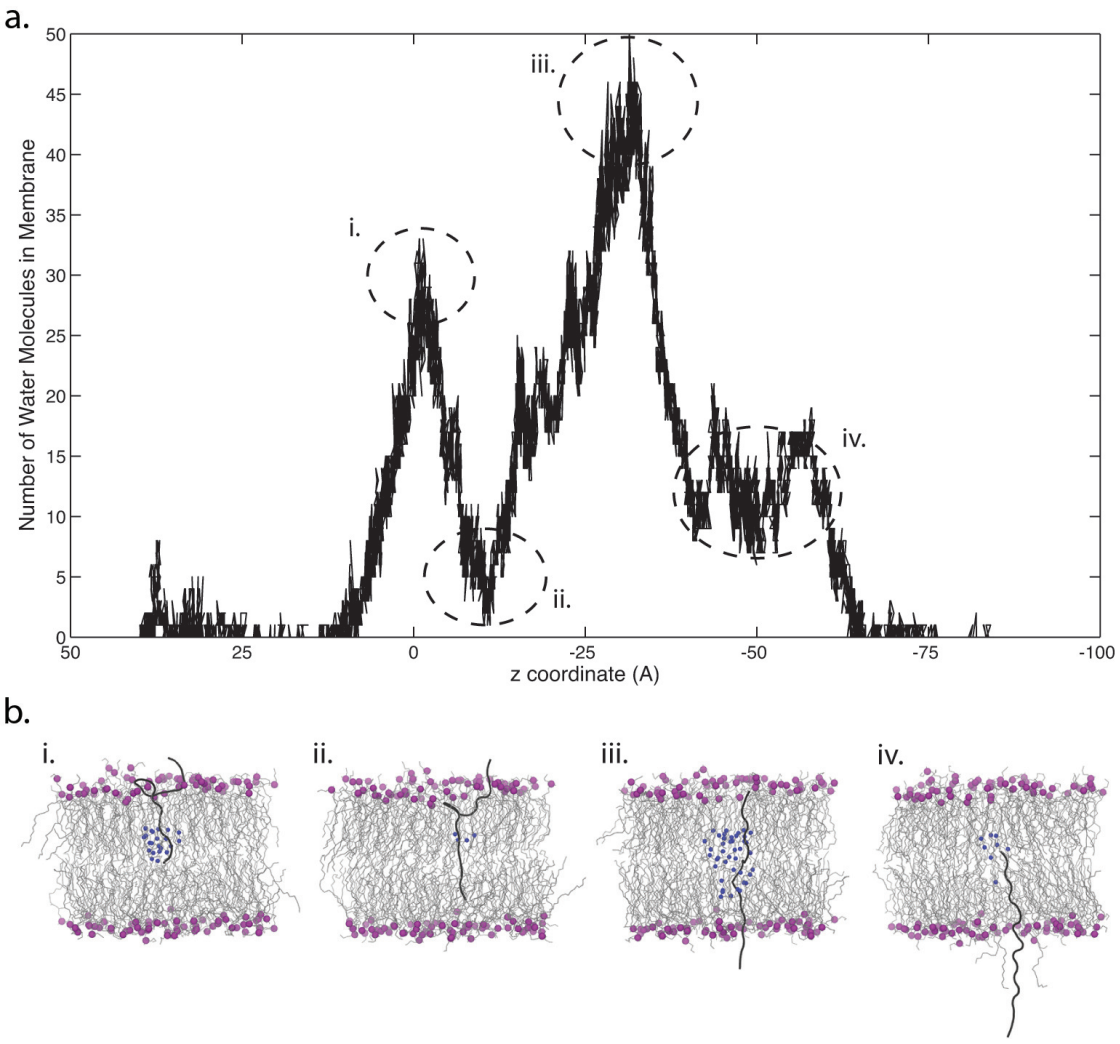

Figure 4.9. (a) Number of water molecules that penetrate into the membrane during translocation of wild-type pVEC with respect to the z coordinate of the SMD atom. (b) Snapshots of the trajectory taken at the corresponding time points labeled in a.

insights on the interactions between the peptide and the membrane. The force profile of wt-pVEC (Figure 4.10) shows that the force applied to pull the peptide through the membrane increases gradually up to a value of 1300 pN until the N-terminus reaches the lower phosphate heads (z=-10). After that barrier, the force fluctuates around the global maximum value until the N-terminus starts to leave the membrane (z=-40). As the N-terminus exits the membrane, the force that was applied decreases gradually and eventually reaches to a value around zero, where the peptide is in water again.

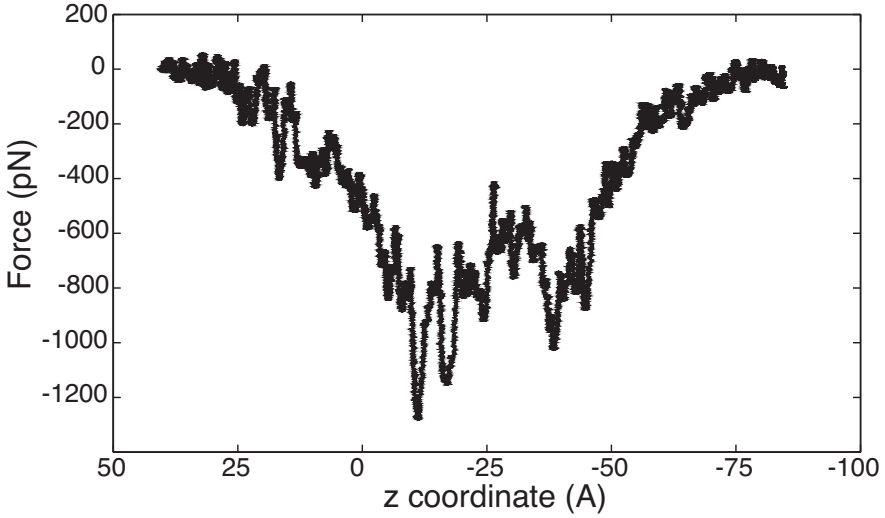

Figure 4.10. Force applied on wt-pVEC peptide during the simulation with respect to the z coordinate of the SMD atom.

The interaction energy profile of wt-pVEC with the lipid bilayer is given in Figure 4.11 with electrostatic and Van der Waals energy profiles. Figure 4.12 shows the snapshots from the simulation corresponding to the points labeled in the interaction energy profile in Figure 4.11.

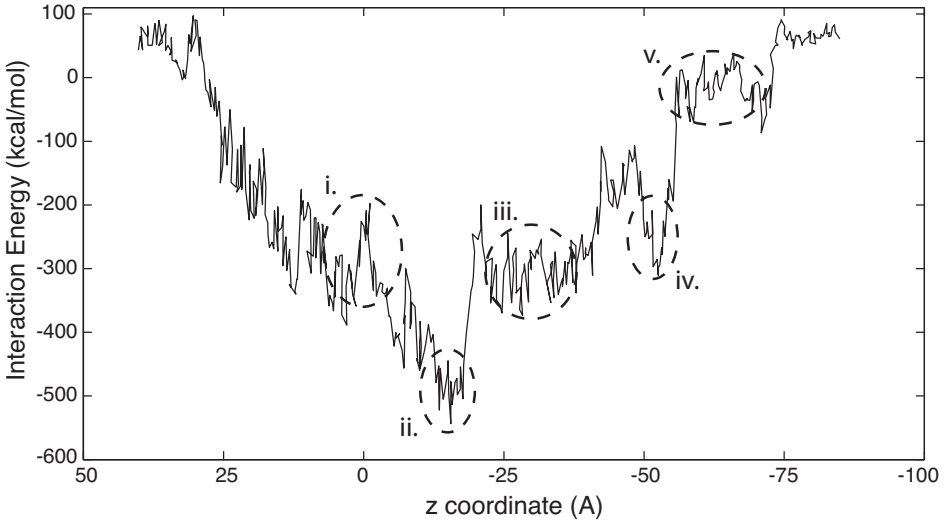

Figure 4.11. Interaction energy between the wt-pVEC peptide and the membrane with respect to the z coordinate of the SMD atom.

The interaction energy for wt-pVEC increases as peptide approaches and eventually penetrates into the membrane and oscillates around a value of -300 kcal/mol when z coordinate of the SMD atom is around zero (Figure 4.11 and Figure 4.12i). At this point, first 6 residues have already penetrated into the membrane and Arg7 resides between the phosphate heads of the upper lipid layer, but residues His14, Ala15 and His16 are also interacting with the membrane as the beta-hairpin loop lays on the surface of the membrane. The interaction energy increases even more as the beta-hairpin loop unfolds and reaches to a maximum value around -550 kcal/mol when z coordinate of the SMD atom is around -15 (Figure 4.11 and Figure 4.12ii). This point also corresponds to the maximum value of electrostatic interactions since the N-terminus is in contact with the lower phosphate atoms while the C-terminus is in contact with the upper phosphate atoms at the same time. As the N-terminus starts to exit from the membrane the interaction energy starts decreasing and oscillates around -300 kcal/mol again when z coordinate of the SMD atom is around -30 (Figure 4.11 and Figure 4.12iii). At this point, residues Ile3, Ile4 and Leu5 start to exit from the membrane and since first 2 residues (Leu1 and Leu2), which contribute highly to the interactions of the peptide with the lipid bilayer, have already left the membrane, the interaction energy reaches a small plateau. After this point, the peptides continues to move out of the membrane and the interaction energy profile decreases abruptly with the exit of the previously unfolded beta-hairpin loop. A sudden increase in the interaction energy profile is observed (around -300 kcal/mol when z coordinate of the SMD atom is around -50) as the exit of the peptide (residues Arg10, Lys11 and Gln12) disturbs the membrane causing some of the lipid tails to hang out and peptide interacts with these lipid tails (Figure 4.11 and Figure 4.12iv). The final plateau is observed with the exit of the C-terminus (residues His14, Ala15 and His16) from the membrane (when z coordinate of the SMD atom is around -60). Although the overall interaction energy between the peptide and membrane decreases, these residues are in contact with the lipid tails hanging out from the membrane causing fluctuations in the interaction energy profile (Figure 4.11 and Figure 4.12v).

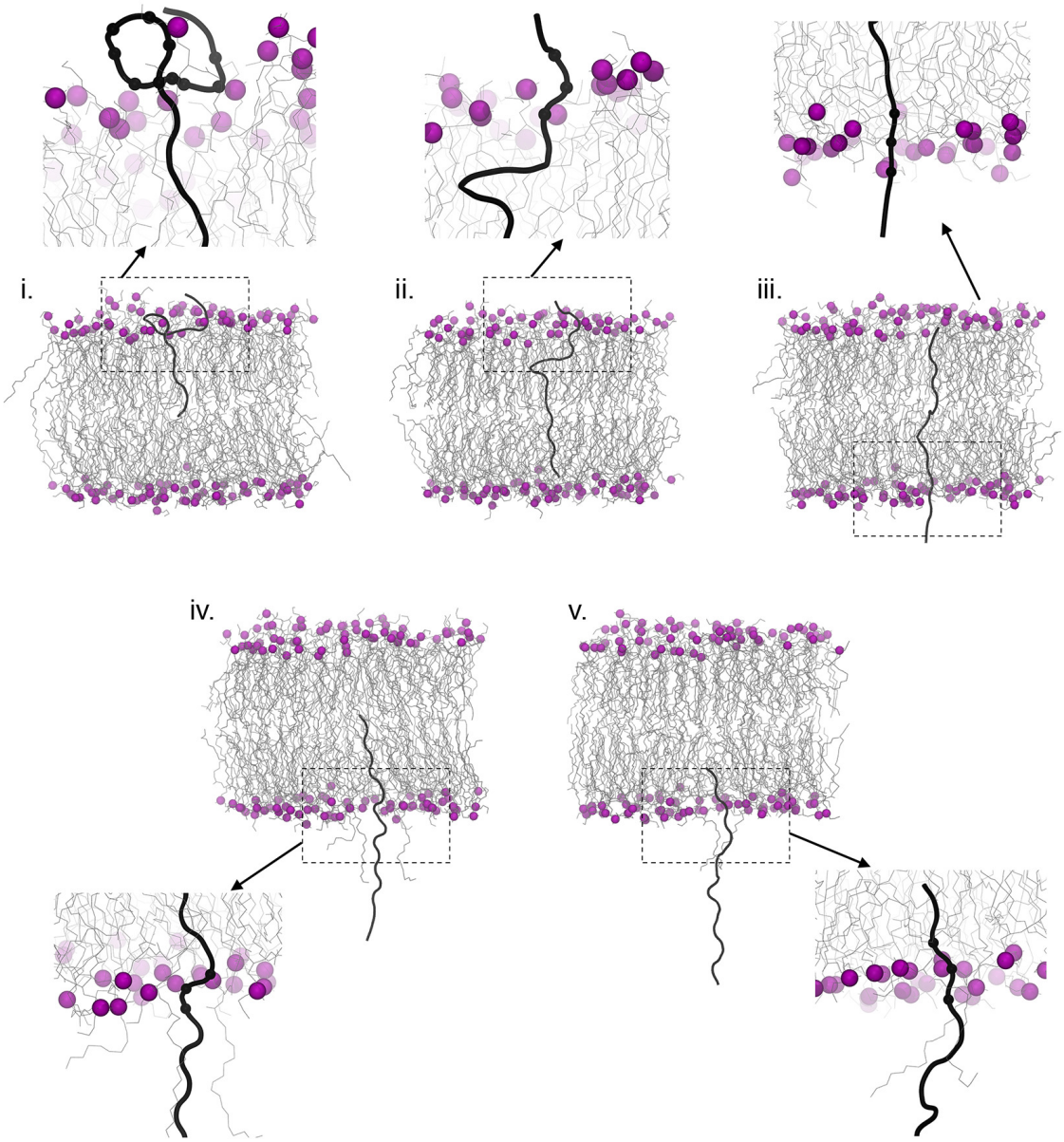

Figure 4.12. Snapshots corresponding to the stages observed in the interaction energy profile of the wt-pVEC with the membrane. Water molecules are not shown for clarity.

4.1.2.2. SMD Simulation of Membrane Translocation of pVEC-1. Similar to that of wt-pVEC simulation, water molecules start to penetrate into the membrane as the N-terminus of pVEC-1 reaches the membrane core (Figure 4.13, z=0). The pore formed by the peptide gets smaller as the peptide unfolds in the membrane and a local minimum value is observed in the number of waters molecules that penetrate into the membrane

(z=-10). As the rest of the peptide is inserted, the number of water molecules reaches a global maximum value (around 55) as the peptide is surrounded by water molecules when it is fully embedded in the membrane (around z=-25). Number of water molecules starts to decrease only when the C-terminus of the peptide leaves the membrane.

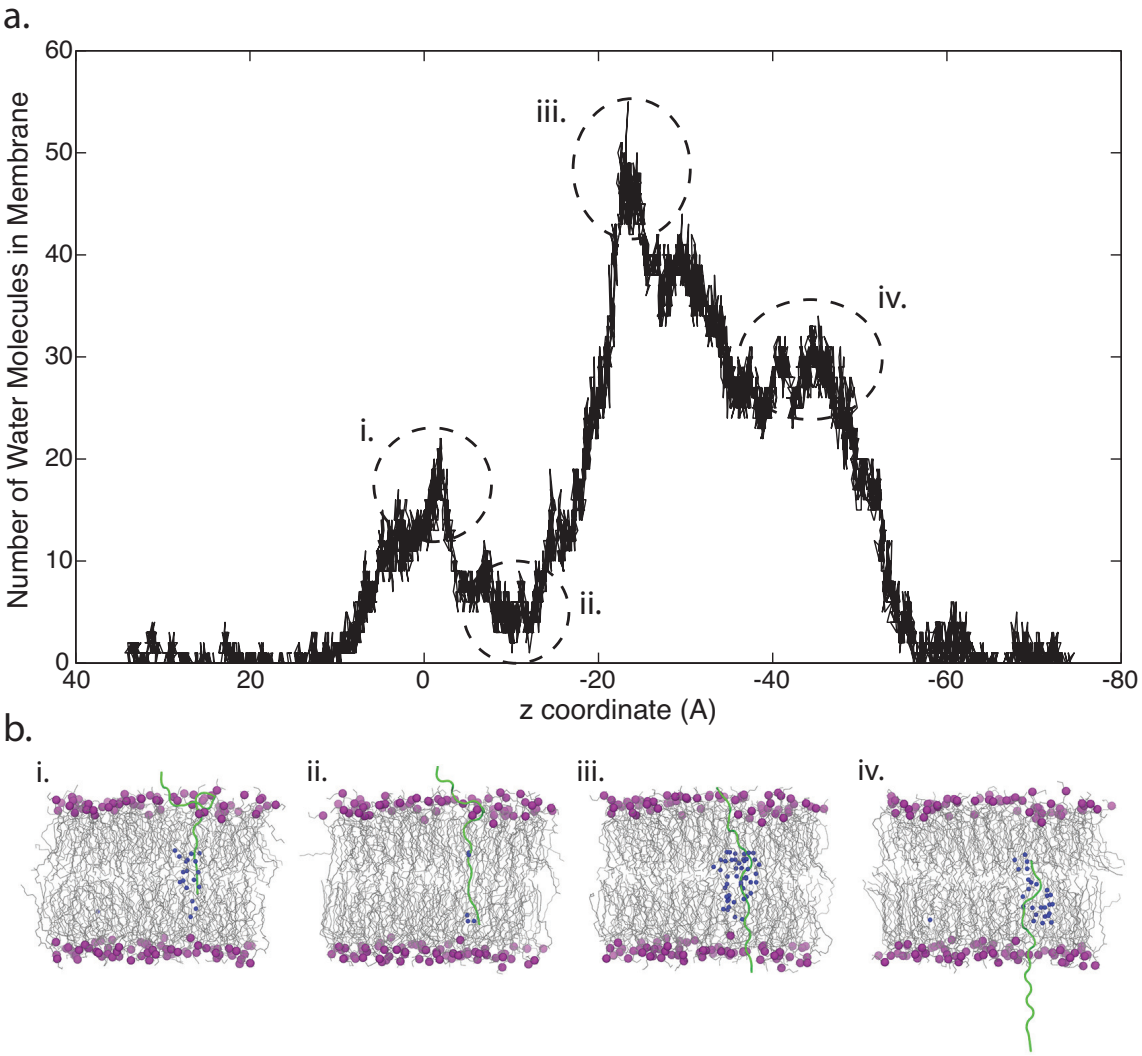

Figure 4.13. (a) Number of water molecules that penetrate into the membrane during translocation of pVEC-1 with respect to the z coordinate of the SMD atom. (b) Snapshots of the trajectory taken at the corresponding time points labeled in a.

The force profile of pVEC-1 (Figure 4.14) shows that the force applied to pull the peptide through the membrane increases gradually up to a value around 1150 pN until the N-terminus is close to the lower layer phosphate heads (z=-10). After that barrier,

the force fluctuates around the global maximum value until the N-terminus starts to leave the membrane (z=-20). As the N-terminus exits the membrane, the force that was applied decreases gradually and eventually reaches to a value around zero, where the peptide is in water again.

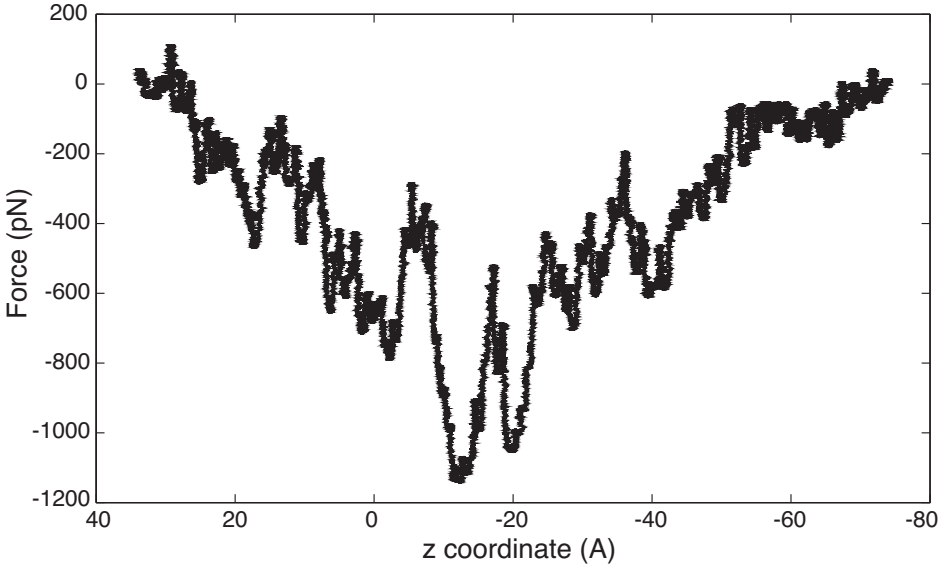

Figure 4.14. Force applied on the pVEC-1 peptide during the simulation with respect to the z coordinate of the SMD atom.

The interaction energy profile of pVEC-1 with the lipid bilayer is given in Figure 4.15. Figure 4.16 shows the snapshots from the simulation corresponding to the points labeled in the interaction energy profile in Figure 4.15.

The interaction energy for pVEC-1 starts increasing as the peptide approaches to the membrane and a local minimum is observed around a value of -200 kcal/mol when z coordinate of the SMD atom is around +19, just after the N-terminus of the peptides penetrates into the membrane (Figure 4.15 and Figure 4.16i). The interaction energy continues increasing as the beta-hairpin loop unfolds and peptide is embedding itself into membrane. The interaction energy reaches to a maximum value around -750 kcal/mol when z coordinate of the SMD atom is around -11 (Figure 4.15 and Figure 4.16ii). This point also corresponds to the maximum value of electrostatic interactions since the N-terminus is in contact with the lower phosphate atoms while the residues

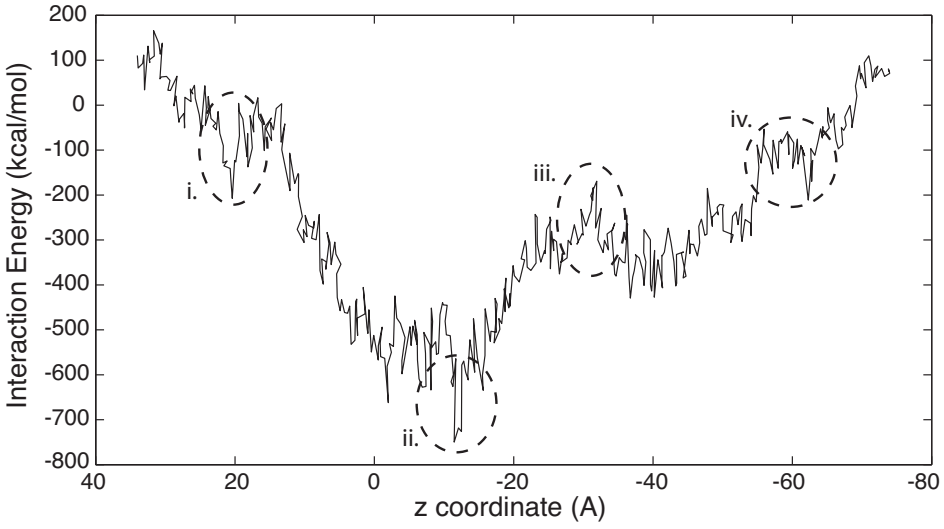

Figure 4.15. Interaction energy between the pVEC-1 peptide and the membrane with respect to the z coordinate of the SMD atom.

Arg10, Lys11, Gln12, Arg13 and His14 are penetrating into the membrane at the same time.

As the N-terminus starts to exit from the membrane the interaction energy starts decreasing and oscillates around -200 kcal/mol again when z coordinate of the SMD atom is around -30 (Figure 4.15 and Figure 4.16iii). At this point, residues Ile3, Ile4 and Leu5 start to exit from the membrane and since first 2 residues (Leu1 and Leu2), which contribute highly to the interactions of the peptide with the lipid bilayer, have already left the membrane, the interaction energy reaches a small plateau. After this point, the peptides continues to move out of the membrane and the interaction energy profile decreases abruptly with the exit of the previously unfolded beta-hairpin loop. The final plateau is observed with the exit of the C-terminus from the membrane when z coordinate of the SMD atom is around -60 (Figure 4.15 and Figure 4.16iv), since these peptides continue to interact with the lipids tails hanging out of the lipid bilayer.

4.1.2.3. SMD Simulation of Membrane Translocation of pVEC-2. Similar to that of wt-pVEC or pVEC-1 simulations, water molecules start to penetrate into the mem-

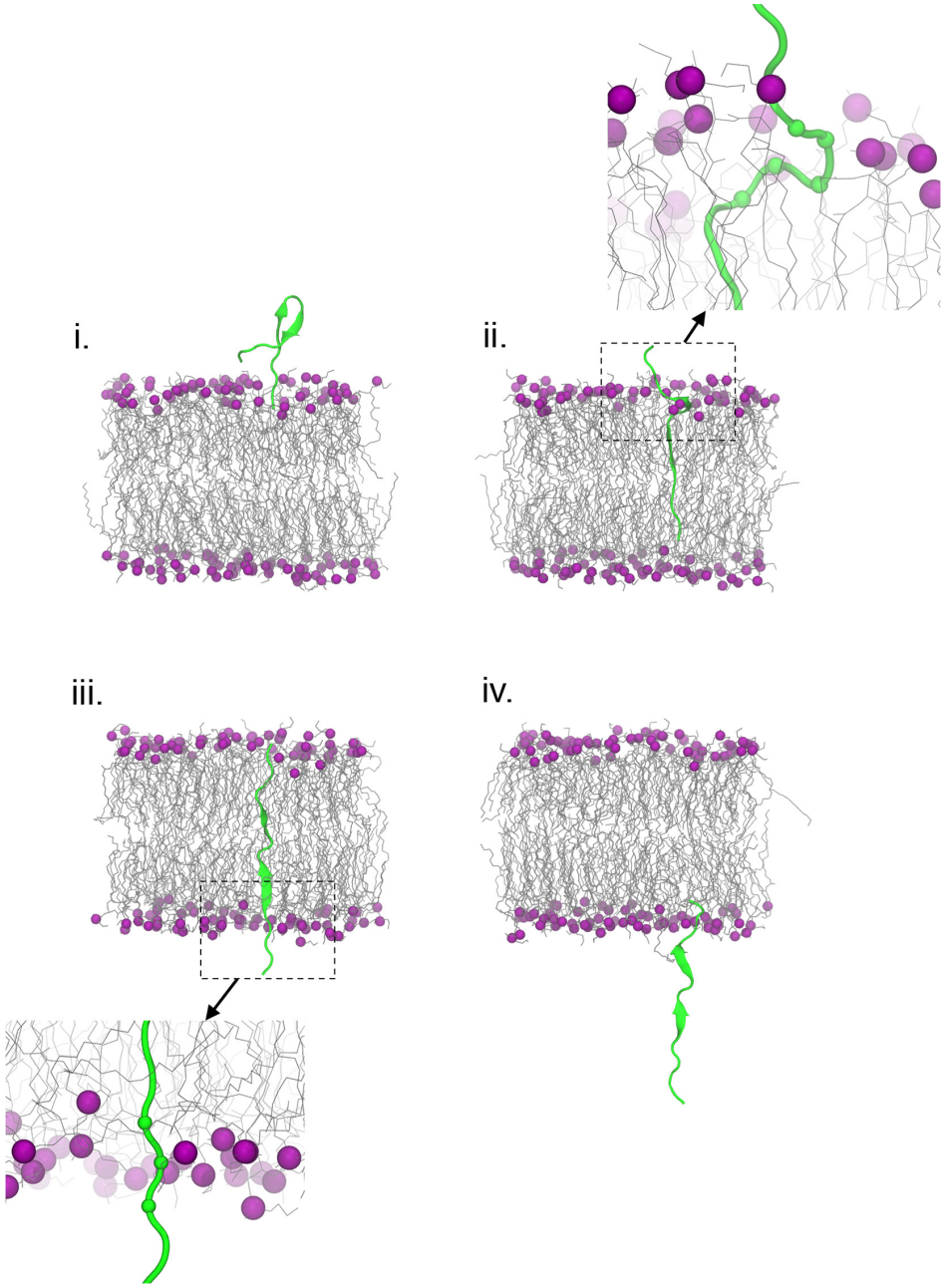

Figure 4.16. Snapshots corresponding to the stages observed in the interaction energy profile of the pVEC-1 peptide with the membrane. Water molecules are not shown for clarity.

brane as the N-terminus of pVEC-2 reaches the membrane core (Figure 4.17, z=0). The pore formed by the peptide gets smaller as the peptide unfolds in the membrane and a local minimum value is observed in the number of waters molecules that penetrate into the membrane (z=-10). As the rest of the peptide is inserted, the number of water

molecules reaches a global maximum value (around 40) as the peptide is surrounded by water molecules when it is fully embedded in the membrane (around z=-30). Number of water molecules decreases as the peptide leaves the membrane.

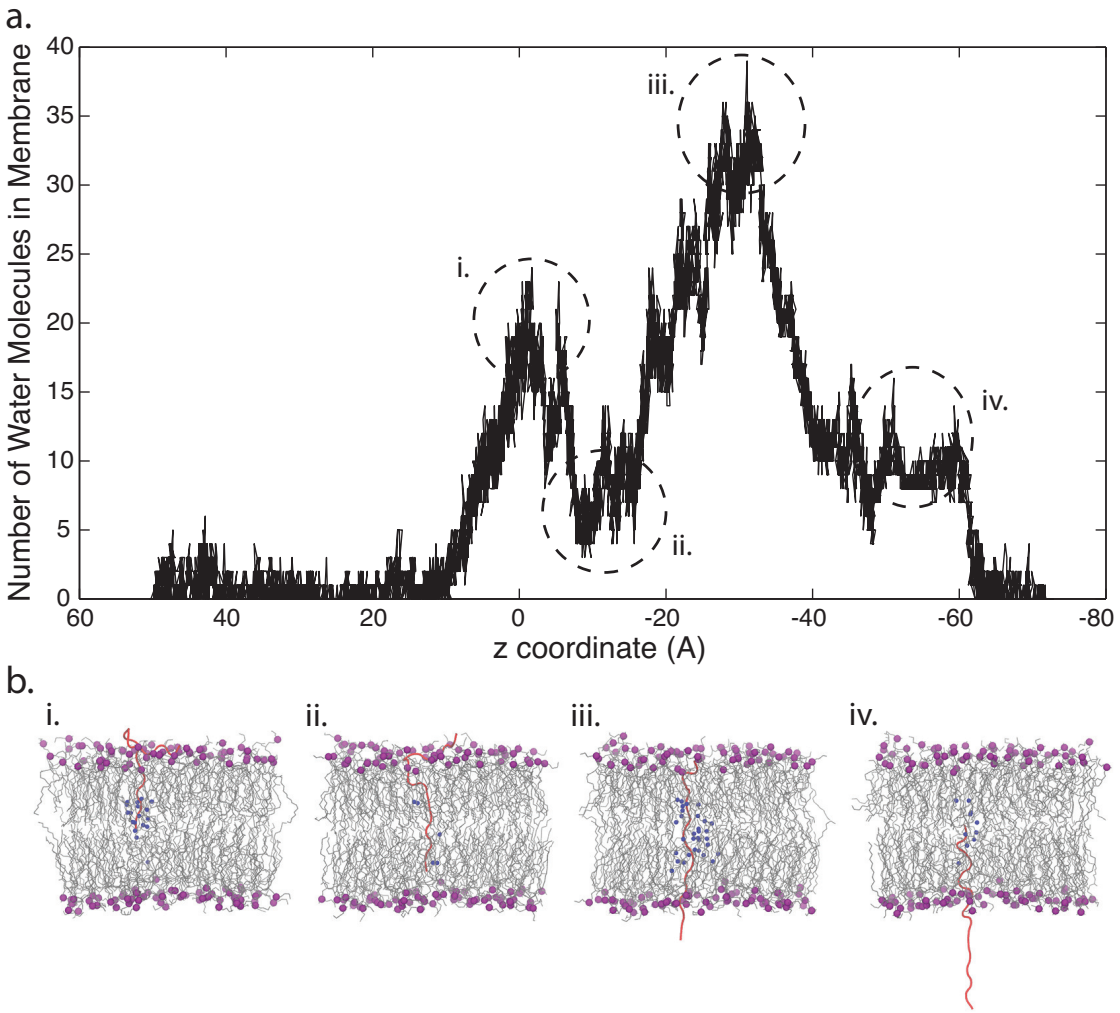

Figure 4.17. (a) Number of water molecules that penetrate into the membrane during translocation of pVEC-2 with respect to the z coordinate of the SMD atom. (b) Snapshots of the trajectory taken at the corresponding time points labeled in a.

The force profile of pVEC-2 (Figure 4.18) shows that the force applied increases gradually up to a value of 900 pN when the N-terminus is around the membrane core (z=0). This maximum force value is smaller in magnitude when compared to that of wt-pVEC and pVEC-1 simulations. After that barrier, the force fluctuates until a new barrier is reached when the N-terminus resides in the lower layer phosphate groups of

the membrane (z=-20). This second barrier observed for pVEC-2 simulation is also smaller in magnitude when compared to that of wt-pVEC and pVEC-1, indicating that the attractive interactions between the peptide and the membrane is weaker. As the peptide exits the membrane, the force applied decreases gradually and eventually reaches to a value around zero.

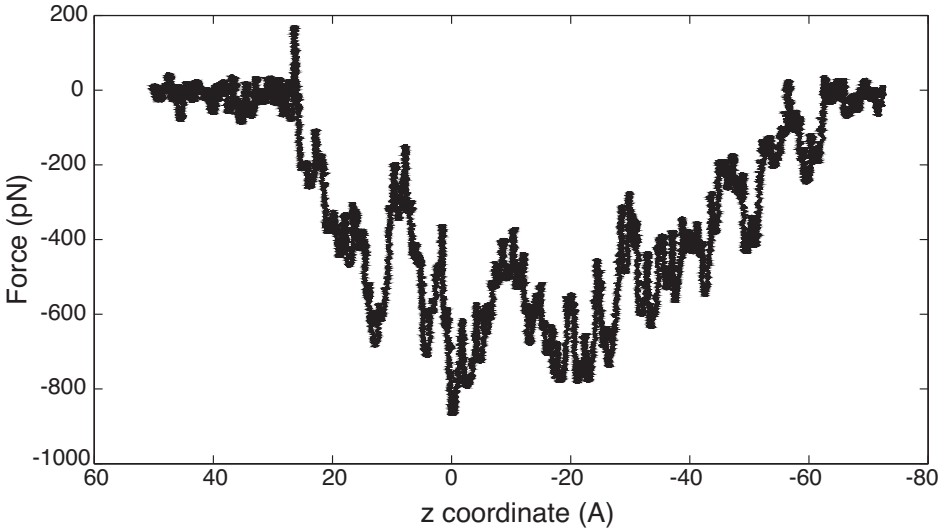

Figure 4.18. Force applied on the pVEC-2 peptide during the simulation with respect to the z coordinate of the SMD atom.

The interaction energy profile of pVEC-2 with the lipid bilayer is given in Figure 4.19. Figure 4.20 shows the snapshots from the simulation corresponding to the points labeled in the interaction energy profile in Figure 4.19.

The interaction energy for pVEC-2 starts increasing as the peptide approaches and eventually penetrates into the membrane. After the initial penetration, oscillations around the first local minimum value of -400 kcal/mol when z coordinate of the SMD atom is around zero (Figure 4.19 and Figure 4.20i) are observed. At this point, first 6 residues have already penetrated into the membrane and Arg7, Arg8 and Ile9 reside between the phosphate heads of the upper lipid layer, but residues His14, Ala15, His16 and Ser17 are also interacting with the membrane as the beta-hairpin loop lays on the surface of the membrane. The interaction energy increases even more as the beta-hairpin loop unfolds and reaches to a maximum value around -500 kcal/mol when z

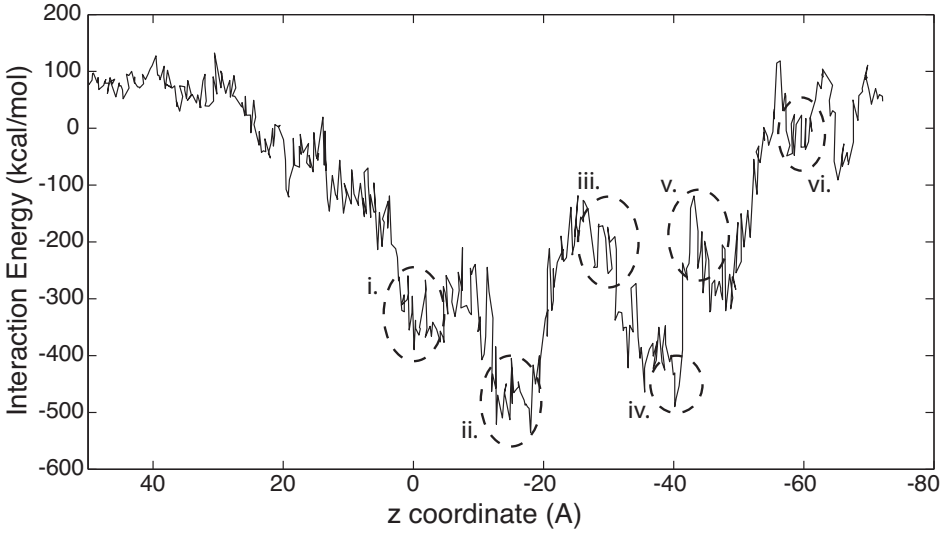

Figure 4.19. Interaction energy between the pVEC-2 peptide and the membrane with respect to the z coordinate of the SMD atom.

coordinate of the SMD atom is around -15 (Figure 4.19 and Figure 4.20ii). This point also corresponds to one of the maximum values of electrostatic interactions since the N-terminus is in contact with the lower phosphate atoms while the C-terminus is in contact with the upper phosphate atoms (residues His14, Ala15, His16 and Ser17 are now penetrating into the membrane) at the same time.

As the N-terminus starts to exit from the membrane the interaction energy starts decreasing and oscillates around -200 kcal/mol again when z coordinate of the SMD atom is around -30 (Figure 4.19 and Figure 4.20iii). At this point, residues Ile3, Ile4 and Leu5 start to exit from the membrane and since first 2 residues (Leu1 and Leu2), which contribute highly to the interactions of the peptide with the lipid bilayer, have already left the membrane, the interaction energy reaches a small plateau. After this point, the peptides continues to move out of the membrane, but a sudden increase in the interaction energy profile is observed (around -450 kcal/mol when z coordinate of the SMD atom is around -40) as residues Arg6, Arg7 and Arg8 reside in between the phosphate groups of the lower layer and the peptide continues to exit from the membrane (Figure 4.19 and Figure 4.20.iv). At this stage, another maximum value of electrostatic interactions is observed. As peptide continues its way out of the membrane

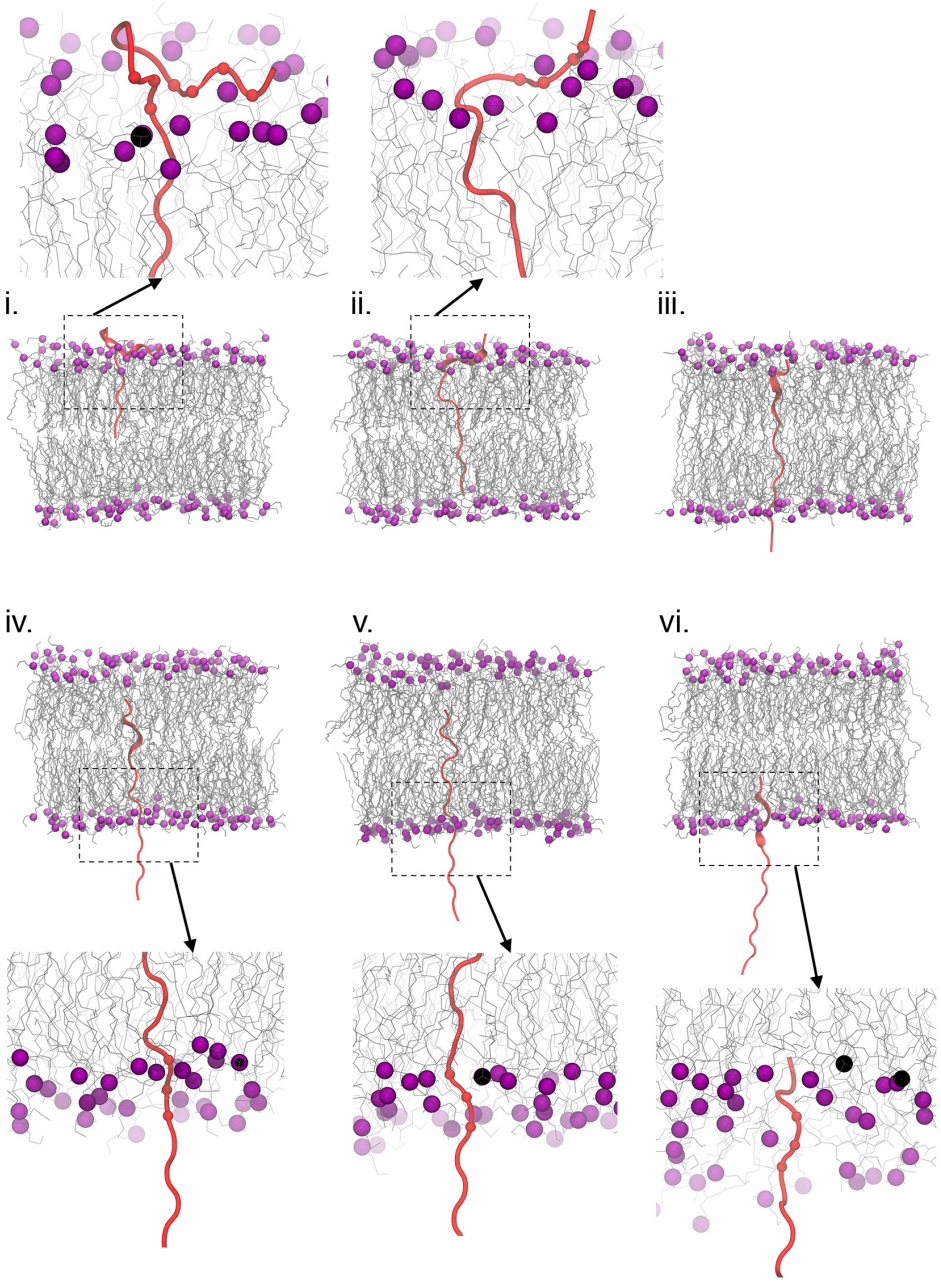

Figure 4.20. Snapshots corresponding to the stages observed in the interaction energy profile of the pVEC-2 peptide with the membrane. Water molecules are not shown for clarity.

an abrupt decrease in the interaction energy profiles is observed just after Arg6 have left the membrane and the residues Arg7, Arg8 and Ile9 reside between the phosphate groups of the lower layer (Figure 4.19 and Figure 4.20v). The final plateau is observed with the exit of the C-terminus (residues Ala13, His14 and Ala15) from the membrane

when z coordinate of the SMD atom is around -60 (Figure 4.19 and Figure 4.20vi).

4.1.2.4. SMD Simulation of Membrane Translocation of pVEC-9. Membrane translocation simulation for pVEC-9 was analyzed for water molecules that enter the lipid bilayer upon pore formation, force applied on the peptide and interactions of the peptide with the lipid bilayer.

Water molecules start to penetrate into the membrane with the initial penetration of the N-terminus (Figure 4.21i). The number of water molecules reaches a local maximum value of 41 as the N-terminus resides around the membrane core (Figure 4.21ii). The pore formed by the peptide is larger during the N-terminus insertion because of the Arg7-Gln12 loop that is conserved during the penetration of these residues. The formation of this pore lets the water molecules to penetrate into the membrane, but as the peptide (Arg7-Gln12 loop) unfolds in the membrane, the water molecules are pushed out and a local minimum value (16 water molecules) is observed (iii). As the rest of the peptide is inserted, more water molecules penetrate into the membrane and the number of water molecules reaches a global maximum value of 98 (iv) since the peptide is surrounded by water when it is fully embedded in the membrane, forming a pore in the lipid bilayer. Number of water molecules start to decrease shortly after the N terminus have left the lipid bilayer and after the whole peptide have left the bilayer the number of water molecules is back to 0 (v).

The force profile of pVEC-9 (Figure 4.22) shows that the peptide is pulled toward the lipid bilayer by atomic interactions, which is observed by the force applied on the peptide in positive direction (around z=+30 to +35). As the peptide N terminus reaches the upper phosphate heads of the bilayer, the force abruptly increases to a value around 1200 pN (Figure 4.22). At this stage, the N terminus penetrates into the bilayer followed by a sudden decrease in the force. The force applied on the peptide gradually increases as the peptide is steered toward the membrane core and reaches up to a value of 1400 pN when the N-terminus reaches the lower phosphate heads (z=-15 to -20). After that barrier, the force fluctuates around the global maximum value until

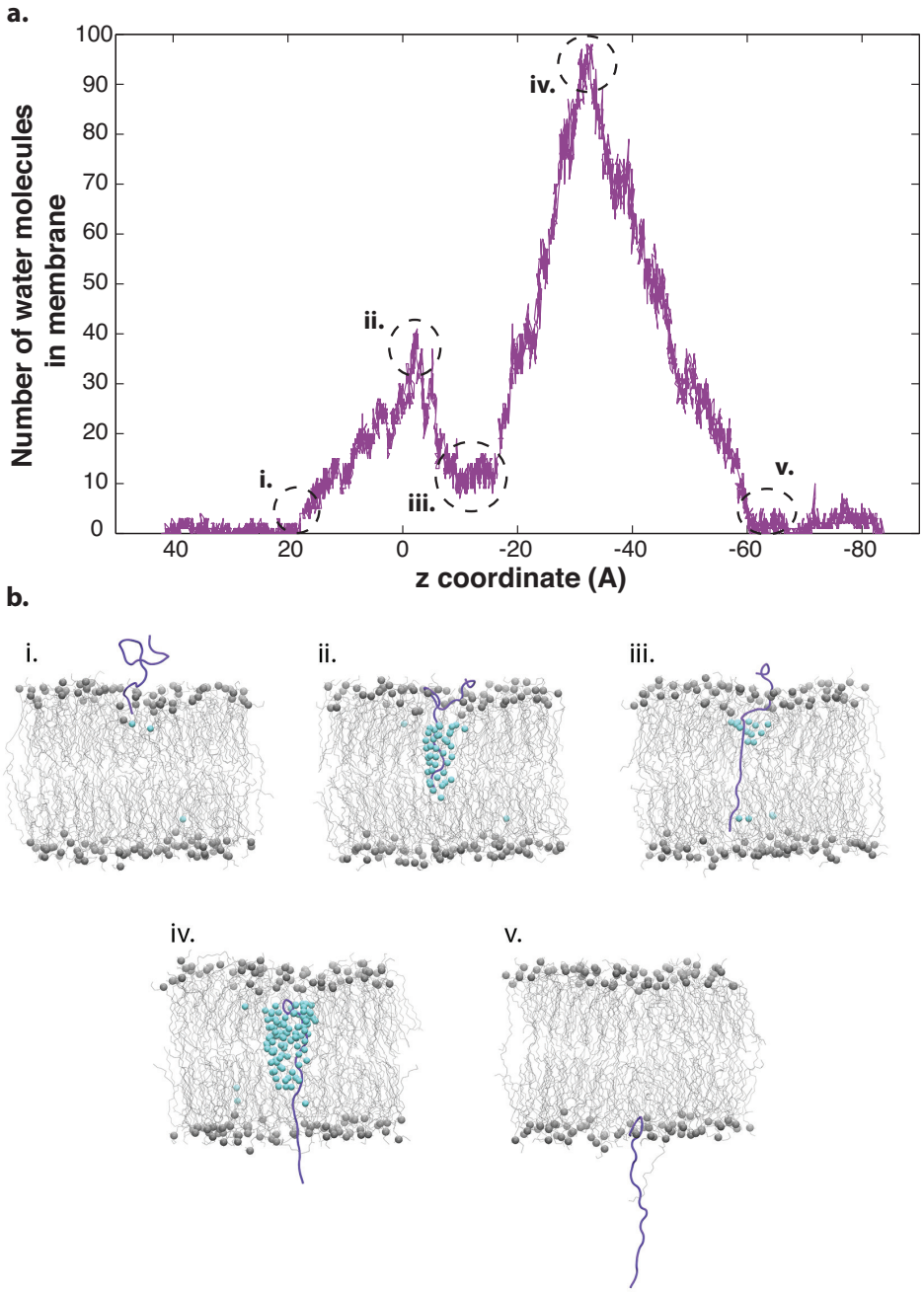

Figure 4.21. (a) Number of water molecules that penetrate into the membrane during translocation of pVEC-9 with respect to the z coordinate of the SMD atom. (b) Snapshots of the trajectory taken at the corresponding time points labeled in a.

the R rich mid section starts to leave the membrane (z=-35). As residues Leu6, Arg7 and Arg8 residues exit the membrane, the force that was applied decreases abruptly (to 400 pN), but since the during the exit (around z =-55) of Arg11 (the mutated

residue) the force increases up to 550 pN. After the Arg11 have left the membrane, the force applied on the peptide decreases and fluctuates around 0 pN until the peptide completely leaves the lipid bilayer.

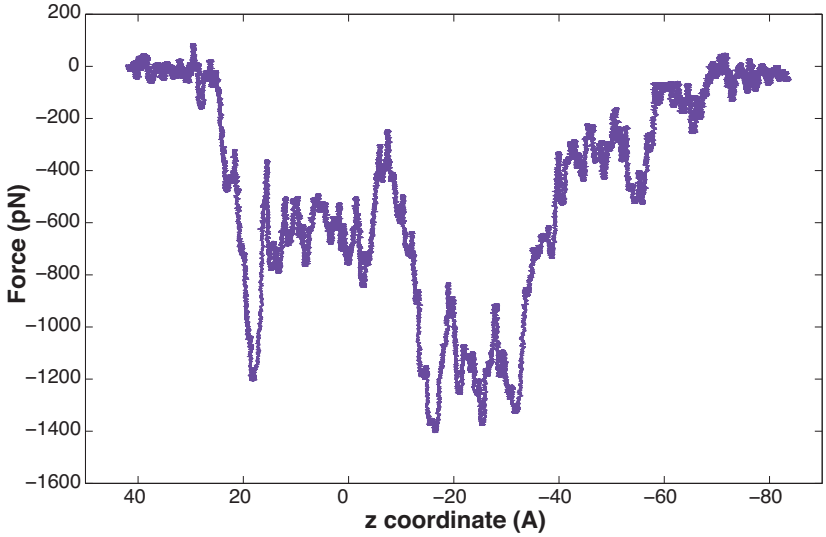

Figure 4.22. Force applied on the pVEC-9 peptide during the simulation with respect to the z coordinate of the SMD atom.

The interaction energy profile of pVEC-9 with the lipid bilayer is given in Figure 4.23 with electrostatic and Van der Waals energy profiles. Figure 4.24 shows the snapshots from the simulation corresponding to the points labeled in the interaction energy profile in Figure 4.23.

The interaction energy for pVEC-9 oscillates around a value of +100 kcal/mol until the peptide terminus touches the upper phosphate heads of the lipid bilayer when the interaction energy is 0 kcal/mol. As the peptide penetrates into the lipid bilayer, the interaction energy starts to decrease (Figure 4.23i and Figure 4.24i), but the peptide forms a loop between residues Arg7 and Gln12, which is adsorbed on the membrane surface and conserved for a long period, until the Gln12 residue penetrates into the bilayer. The interaction energy decreases even more as the Arg7-Gln12 loop starts to unfold and reaches to a maximum value around -600 kcal/mol when z coordinate of the SMD atom is around -20 (Figure 4.23ii and Figure 4.24ii). This point also corresponds to the maximum value of electrostatic and Van der Waals interactions since the N-

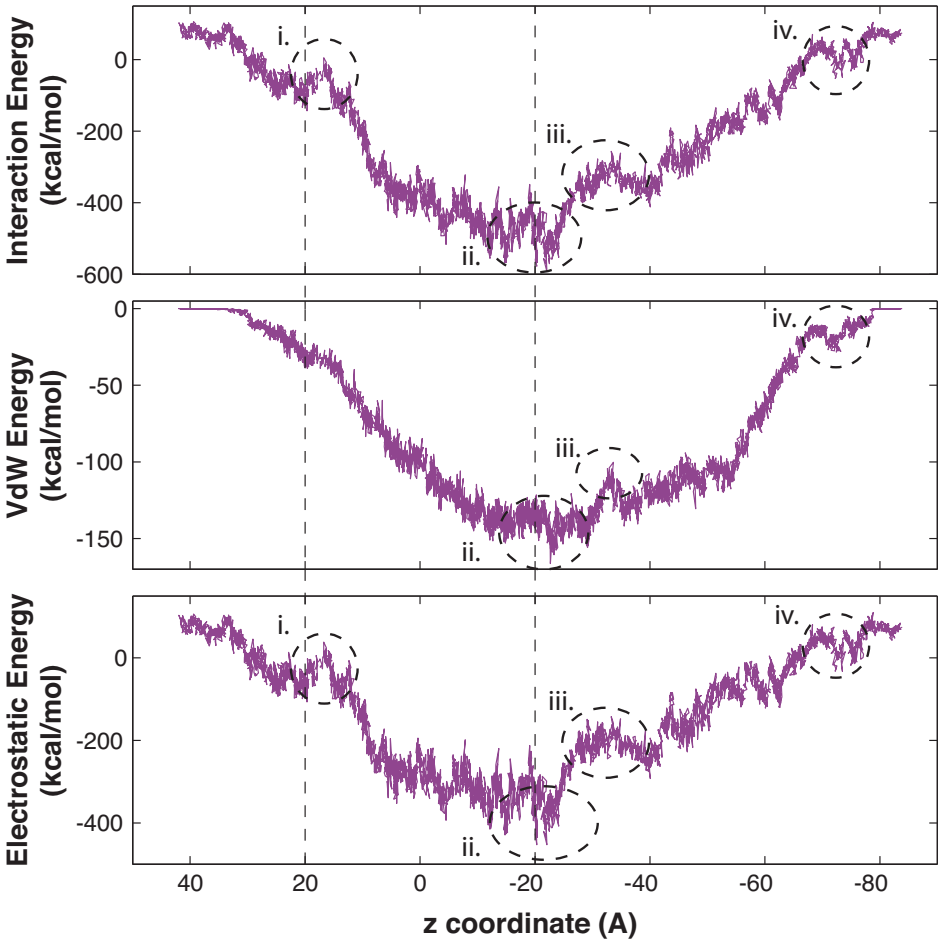

Figure 4.23. Interaction, electrostatic and Van der Waals energy profiles energy between the pVEC-9 peptide and the membrane with respect to the z coordinate of the SMD atom.

terminus is in contact with the lower phosphate layer while the C-terminus is in contact with the upper phosphate layer at the same time. As the N-terminus starts to exit from the membrane the interaction energy increases abruptly and oscillates around -200 kcal/mol when z coordinate of the SMD atom is around -30 (Figure 4.23iii and Figure 4.24iii). At this point, since first 2 residues (Leu1 and Leu2), which contribute highly to the interactions of the peptide with the lipid bilayer, have already left the membrane and the C-terminus have already passed the upper phosphate layer, the interaction energy reaches a small plateau. After this point, the peptide continues to move out of the membrane and the interaction energy increases gradually. The

final plateau is observed with the exit of the C-terminus from the membrane (when z coordinate of the SMD atom is around -70), which disturbs the membrane causing some of the lipid tails to hang out (Figure 4.23iv and Figure 4.24iv). At this point, although the overall interaction energy between the peptide and membrane decreases, the peptide C-terminus is still in contact with the lipid tails hanging out from the membrane for a longer period, causing fluctuations in the interaction energy profile. After the C-terminus loses all contact with the lipid tails, the interaction energy reaches a value around +100 kcal/mol, similar to that in the beginning of the simulations.

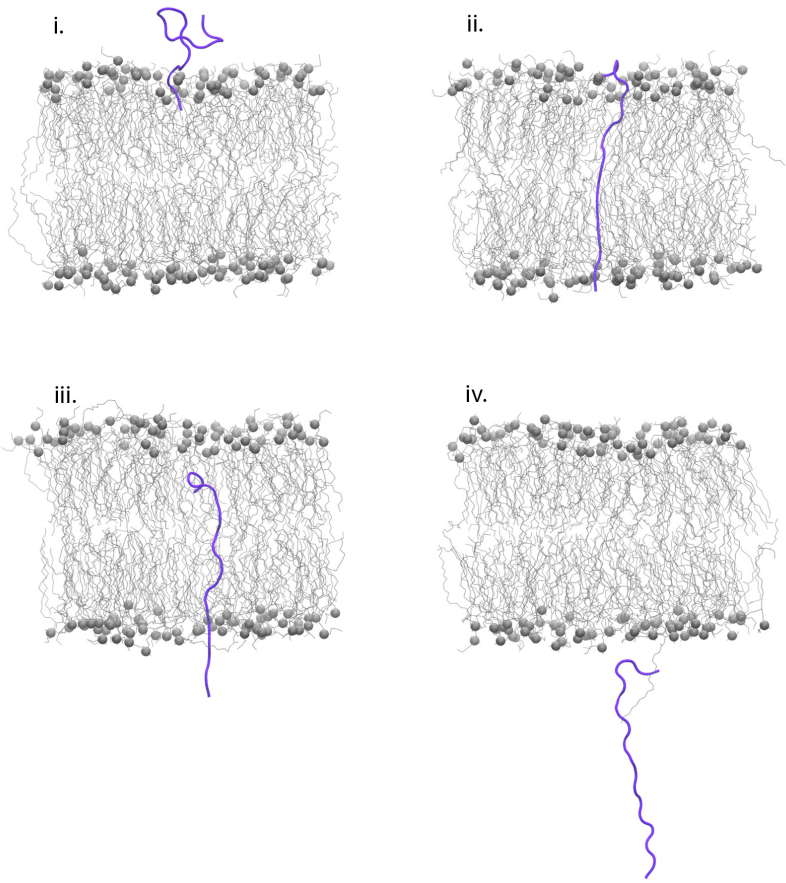

Figure 4.24. Snapshots corresponding to the stages observed in the interaction energy profile of the pVEC-9 peptide with the membrane. Water molecules are not shown for clarity.

4.1.2.5. SMD Simulation of Membrane Translocation of pVEC-11. Membrane translocation simulation for pVEC-11 was analyzed for water molecules that enter the lipid

bilayer upon pore formation, force applied on the peptide and interactions of the peptide with the lipid bilayer.

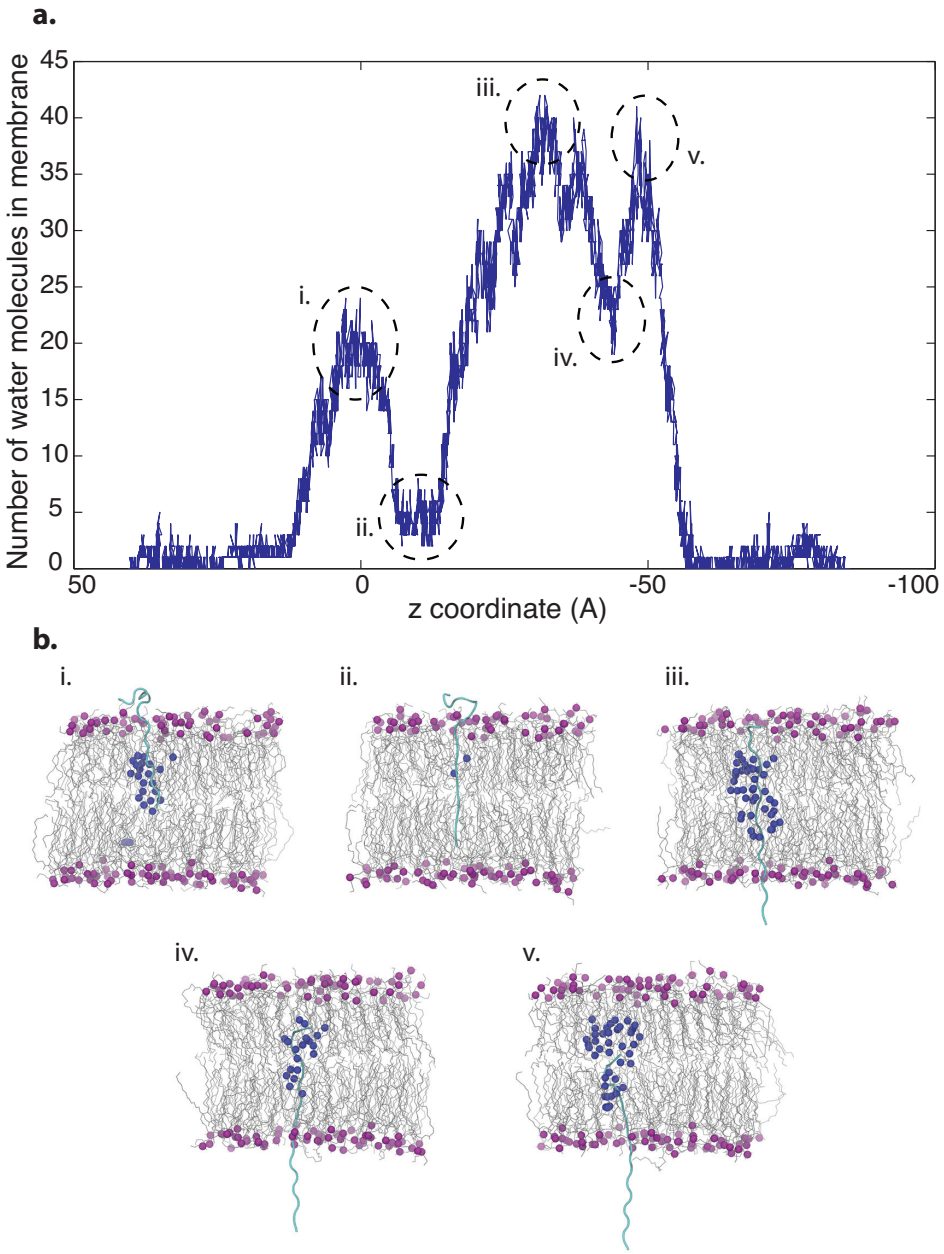

Figure 4.25. (a) Number of water molecules that penetrate into the membrane during translocation of pVEC-11 with respect to the z coordinate of the SMD atom. (b) Snapshots of the trajectory taken at the corresponding time points labeled in a.

Water molecules start to penetrate into the membrane with the initial penetration of the N-terminus. The number of water molecules reaches a local maximum value of

24 as the N-terminus resides around the membrane core (Figure 4.25i). The pore formed by the peptide is larger during the N-terminus insertion, which lets the water molecules to penetrate into the membrane, but as the peptide unfolds in the membrane the water molecules are pushed out and a local minimum value is observed (ii). As the rest of the peptide is inserted, more water molecules penetrate into the membrane and the number of water molecules reaches a global maximum value of 42 since the peptide is surrounded by water when it is fully embedded in the membrane (iii). As the Arg rich mid-section exits, some of the water molecules are pushed out of the membrane (iv). Interestingly, specific to the simulation of pVEC-11, the mutations at the C terminus (H14R and H16R) cause formation of another water pore around the C terminus (third peak in the number of water molecules, Figure 4.25v) as it is pulled toward the membrane core. Number of water molecules start to decrease only after the C terminus passes the membrane core to reach the lower phosphate head of the lipid bilayer.

The force profile of pVEC-11 (Figure 4.26) shows that the peptide is pulled toward the lipid bilayer by atomic interactions, which is observed by the force applied on the peptide in positive direction (between z=+30 and +25). As the peptide N terminus reaches the upper phosphate heads of the bilayer, the force abruptly increases to a value around 800 pN (Figure 4.26). At this stage, the N terminus penetrates into the bilayer followed by a sudden decrease in the force. The force applied on the peptide gradually increases as the peptide is steered toward the membrane core and reaches up to a value of 1000 pN when the N-terminus reaches the lower phosphate heads (z=-15 to -20). After that barrier, the force fluctuates around the global maximum value until the R rich mid section starts to leave the membrane (z=-45). As these residues exit the membrane, the force that was applied decreases abruptly to 0 pN and fluctuates around this value until the peptide completely leaves the lipid bilayer.

The interaction energy profile of pVEC-11 with the lipid bilayer is given in Figure 4.27 with electrostatic and Van der Waals energy profiles. Figure 4.28 shows the snapshots from the simulation corresponding to the points labeled in the interaction energy profile in Figure 4.27.

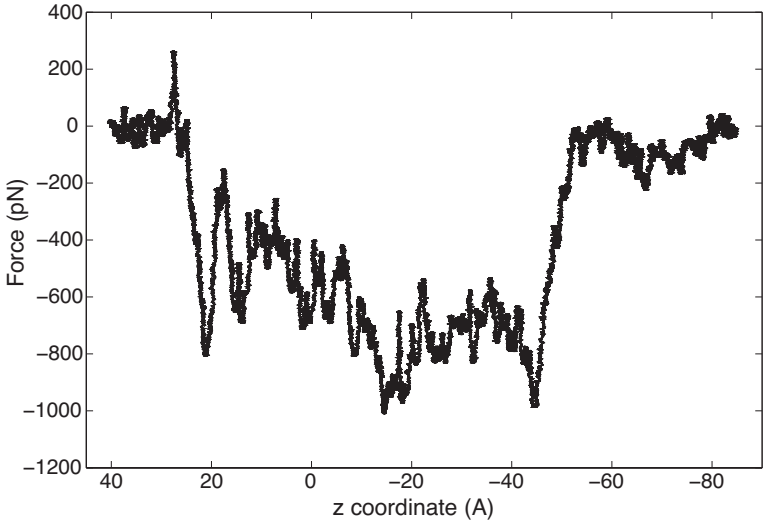

Figure 4.26. Force applied on the pVEC-11 peptide during the simulation with respect to the z coordinate of the SMD atom.

The interaction energy for pVEC-11 oscillates around a value of +100 kcal/mol until the peptide terminus touches the upper phosphate heads of the lipid bilayer when the interaction energy is 0 kcal/mol (Figure 4.27i and Figure 4.28i). The interaction energy decreases gradually and the peptide starts to rotate so that its C terminus is also in contact with the membrane surface even though it is pulled from the N terminus (Figure 4.27ii and Figure 4.28ii). As the peptide penetrates into the lipid bilayer, the interaction energy continues to decrease, but the peptide conserves its T shape by the adsorption of the C terminus on the membrane surface. The interaction energy decreases even more as the beta-hairpin loop unfolds and reaches to a maximum value around -800 kcal/mol when z coordinate of the SMD atom is around -15 (Figure 4.27iii and Figure 4.28iii). This point also corresponds to the maximum value of electrostatic interactions since the N-terminus is in contact with the lower phosphate layer while the C-terminus is in contact with the upper phosphate layer at the same time.

As the N-terminus starts to exit from the membrane the interaction energy starts increasing and oscillates around -400 kcal/mol when z coordinate of the SMD atom is around -30 (Figure 4.27iv and Figure 4.28iv). At this point, residues Ile3, Ile4 and Leu5 start to exit from the membrane and since first 2 residues (Leu1 and Leu2), which

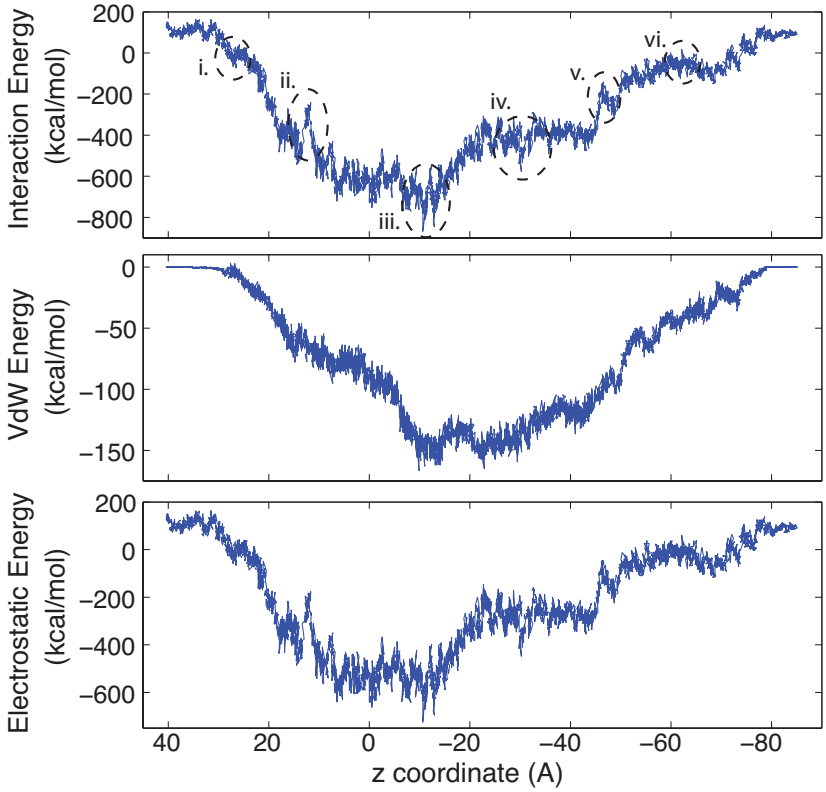

Figure 4.27. Interaction, electrostatic and Van der Waals energy profiles energy between the pVEC-11 peptide and the membrane with respect to the z coordinate of the SMD atom.

contribute highly to the interactions of the peptide with the lipid bilayer, have already left the membrane, the interaction energy reaches a small plateau. After this point, the peptide continues to move out of the membrane and a sudden increase in the interaction energy is observed (around -200 kcal/mol when z coordinate of the SMD atom is around -45) as the exit of the peptide (residues Arg10, Lys11 and Gln12) disturbs the membrane causing some of the lipid tails to hang out (Figure 4.27v and Figure 4.28v). The final plateau is observed with the exit of the C-terminus (residues Arg14, Ala15 and Arg16) from the membrane (when z coordinate of the SMD atom is around -65). Although the overall interaction energy between the peptide and membrane decreases, these residues are in contact with the lower phosphate heads and the lipid tails hanging out from the membrane for a longer period, causing fluctuations in the interaction energy profile (Figure 4.27vi and Figure 4.28vi).

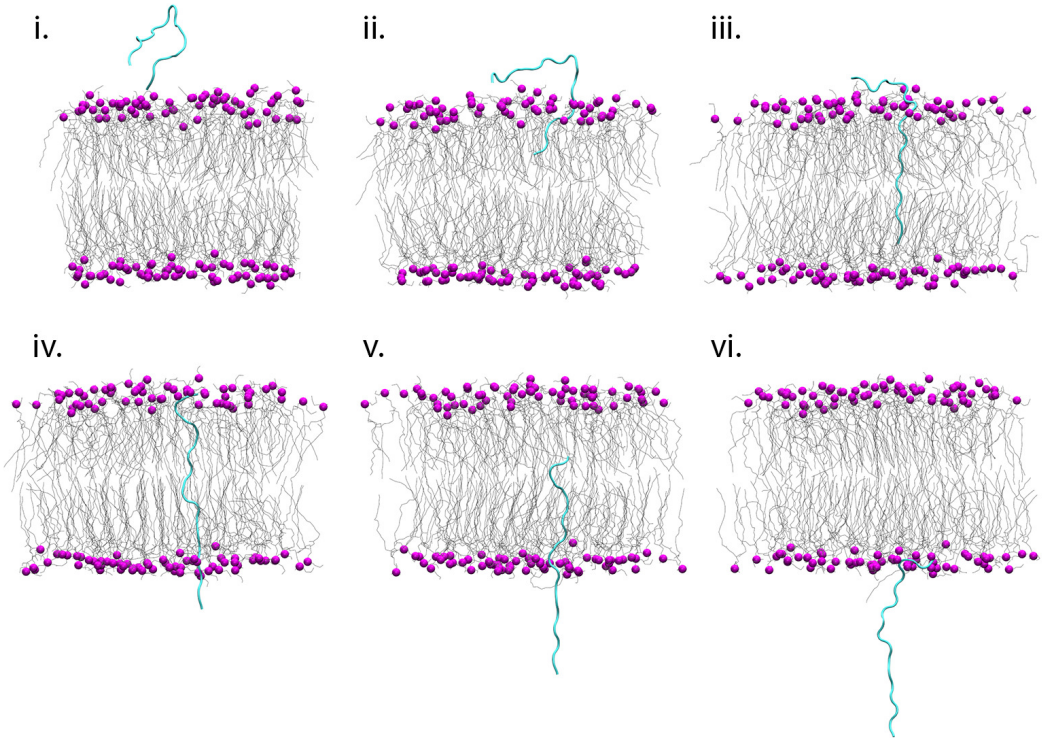

Figure 4.28. Snapshots corresponding to the stages observed in the interaction energy profile of the pVEC-11 peptide with the membrane. Water molecules are not shown for clarity.

4.1.2.6. Comparison of Membrane Translocation of pVEC and the Mutants. The water defect that forms for the five peptides were compared and it was observed that for wilt-type pVEC (wt) and pVEC-2, the number of water molecules increases to 40 and then abruptly drops to 10 while for pVEC-1 and pVEC-11, the number of water molecules is maintained at around 25-50 between z values of -20 to -60 (Figure 4.29). The translocation of pVEC-9 on the other hand, results in a much larger water pore compared to pVEC-1 and pVEC-11, but the water pore is again maintained for longer period of time (between z= -20 to -60). At the maximum value of water molecules, the water pore is continuous from one side of the membrane to the other (Figure 4.30).

The comparison of force profiles showed that (Figure 4.31) the least force in magnitude had to be applied on pVEC-2, which may indicate that the interacting forces are weaker between the peptide and the lipid bilayer. When the interaction energy

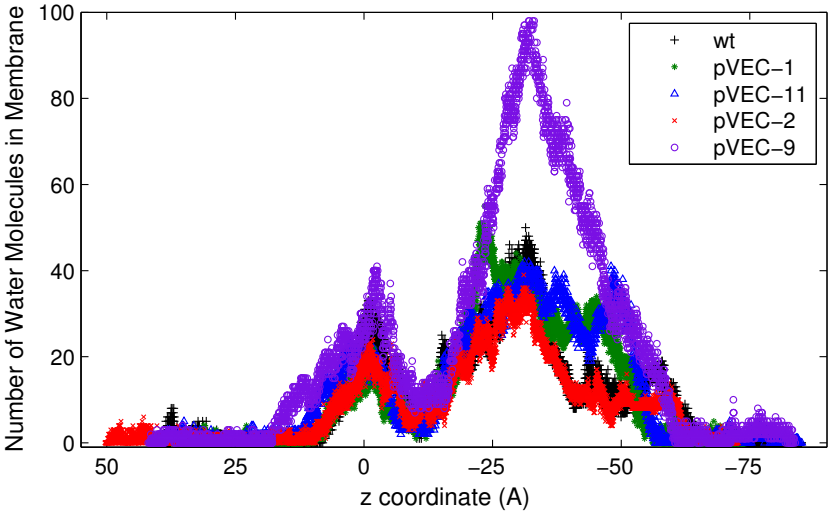

Figure 4.29. Number of water molecules that penetrate into the membrane during simulations with wt-pVEC (black), pVEC-1 (green), pVEC-11 (blue), pVEC-2 (red) or pVEC-9 (purple) with respect to the z coordinate of the SMD atom.

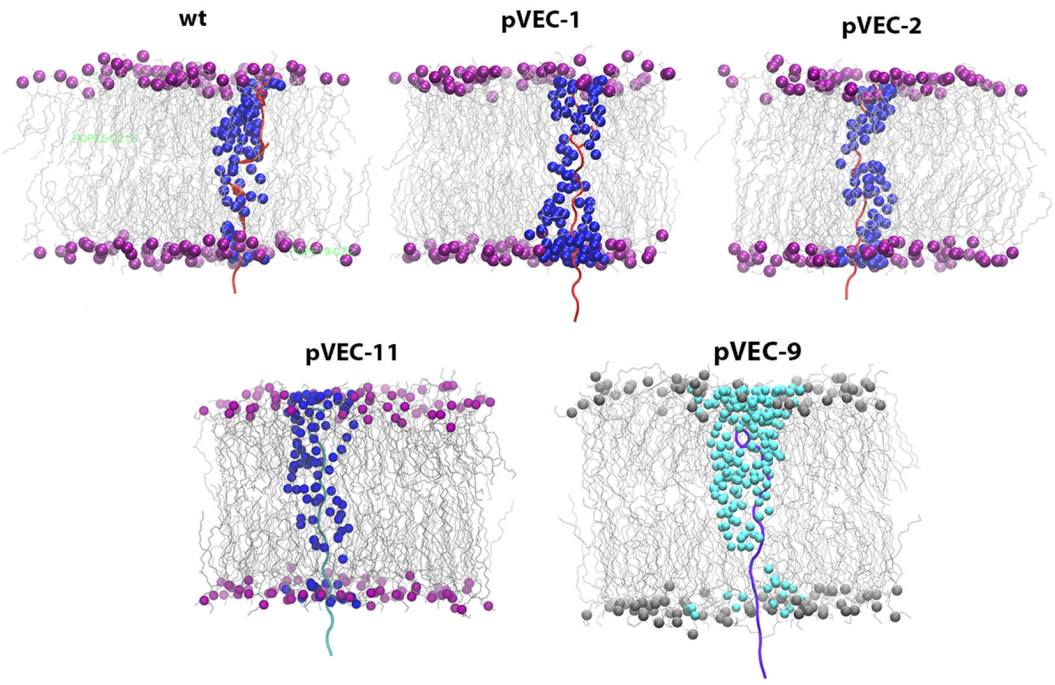

Figure 4.30. Water pore formation during the translocation of the pVEC peptides.

profile of each peptide with the lipid bilayer is compared, it was observed that pVEC-11 made the strongest interactions throughout the simulation (Figure 4.32) mostly due to electrostatic interactions with the phosphate heads.

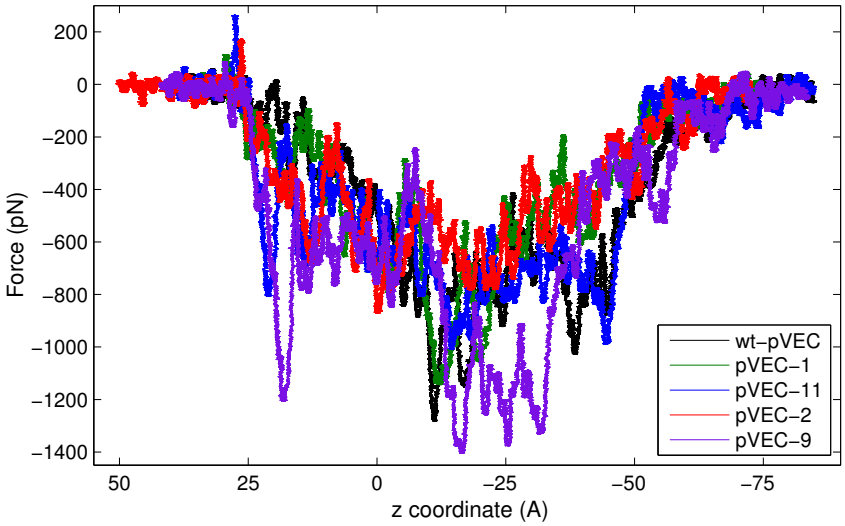

Figure 4.31. Force profiles of wt-pVEC (black), pVEC-1 (green), pVEC-11 (blue), pVEC-2 (red) and pVEC-9 (purple) with respect to the z coordinate of the SMD atom.

On the other hand, the maximum value of force was required for the translocation of pVEC-9, which also results in the highest value of maximum work done (Figure 4.33) during its translocation. Although the maximum force applied and the maximum work done during the translocation simulations corresponds to that of pVEC-9, the interaction energy during its translocation is lower compared to that of pVEC-11 and pVEC-1. We believe that this may be a result of the largest water pore formation, which in turn may block the peptide's interaction with the lipids. The interaction energy and force profiles for pVEC-2 showed a shallow dip compared to wild-type pVEC (wt), pVEC-1, pVEC-9 and especially pVEC-11. This is actually similar to our previous results on scramble pVEC, a pVEC analogue with a decreased uptake value compared to other pVEC analogues. Our previous results suggested that high interaction energy between the cationic stretch and the upper or the lower phosphate

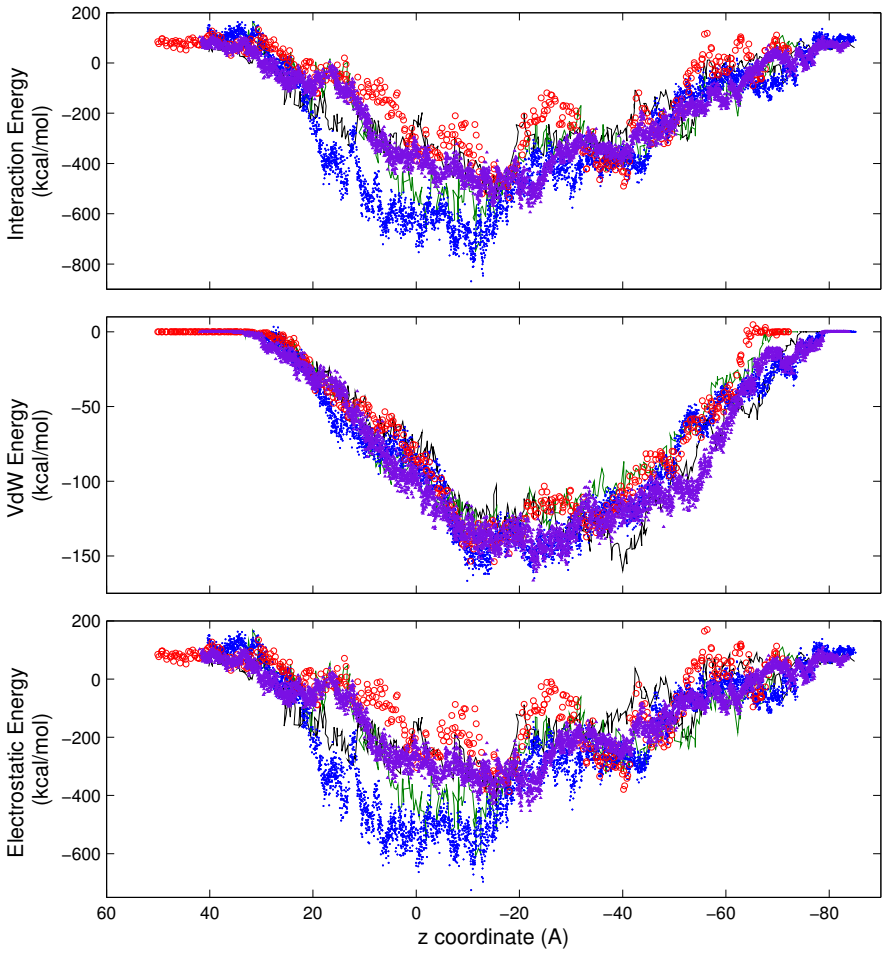

Figure 4.32. Interaction, electrostatic and van der Waals energy profiles of wt-pVEC (black), pVEC-1 (green), pVEC-11 (blue), pVEC-2 (red) and pVEC-9 (purple) with respect to the z coordinate of the SMD atom.

layer may also drive the peptide forward in the SMD direction.

In order to compare the effects of peptides on the membrane, order parameters were calculated for each simulation system. Here, the order of the lipid tails in the presence of the peptides was compared with that in a 20 ns membrane-water MD simulation to determine the effect of peptide penetration.

The results show that, all five peptides have similar disordering effect on the membrane when averaged over the whole simulation time (Figure 4.34). Throughout

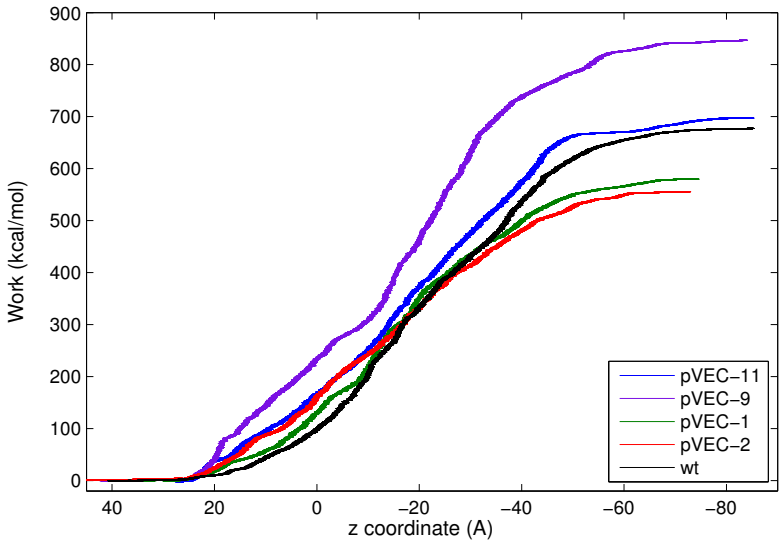

Figure 4.33. Work done on the peptide during the translocation of wt-pVEC (black), pVEC-1 (green), pVEC-11 (blue), pVEC-2 (red) and pVEC-9 (purple) with respect to the z coordinate of the SMD atom.

the SMD simulations, harmonic constraints are applied on the phosphate heads of lipid bilayers in the z direction, and as a result, the thickness of the bilayer stays almost constant. As the peptide moves through the bilayer, a pore forms (because the phosphate heads are free to move in the x-y direction) in the membrane plane. Therefore, the increase in disorder in the presence of peptide is not due to membrane thinning, which cannot be observed with the current simulations, but it is due to the disorder induced by transport of the peptides across the bilayer and the interactions of the peptide with the lipid acyl chains.

The results presented here based on SMD simulations on four pVEC variants suggest that formation of a larger water pore that is maintained for a long period and stronger electrostatic interactions with the membrane are related to an increase in the uptake potential of pVEC peptides. We believe the enhancement of the water pore that is formed during the translocation is facilitating the uptake of pVEC-1, pVEC-11 and pVEC-9.

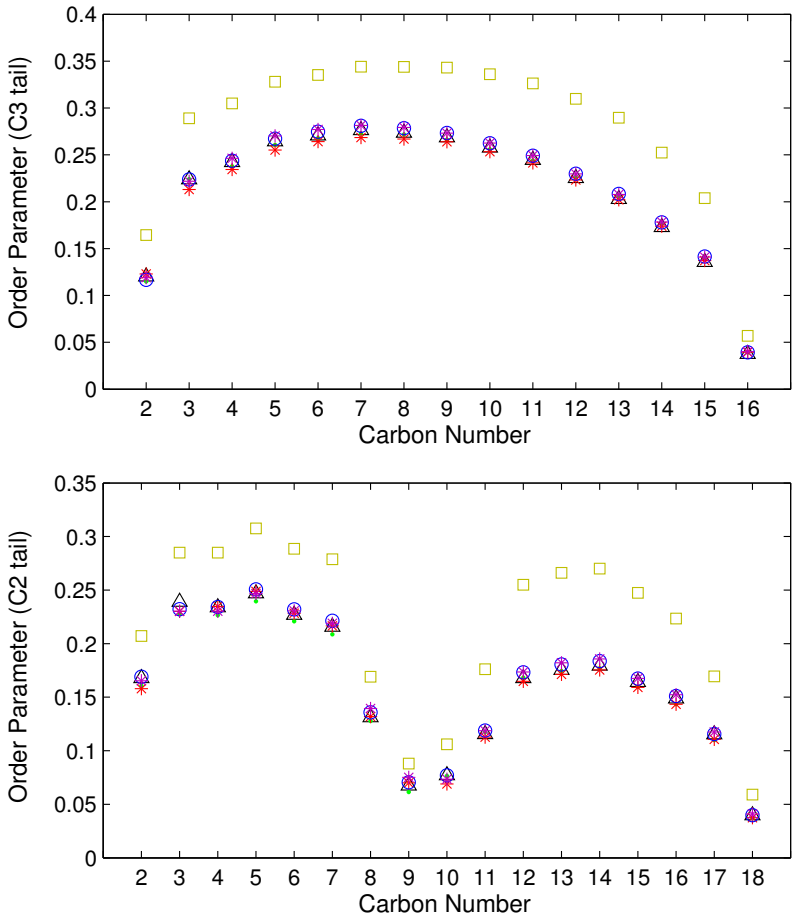

Figure 4.34. Order parameters calculated for the membrane in the presence of wt-pVEC (black triangles), pVEC-1 (green dots), pVEC-2 (red asterisks), pVEC-11 (blue circles) or pVEC-9 (purple asterisks) and in the absence peptides (squares).

Moreover, the comparison of the interactions of each peptide with the lipid bilayer showed that pVEC-11 made the strongest interactions throughout the simulation via mostly the electrostatic interactions with the phosphate heads. The interaction energy and force profiles for pVEC-2 showed a shallow dip profile compared to wild-type pVEC (wt), pVEC-1 and especially pVEC-11, similar to our previous results on scramble pVEC, a pVEC analogue with a much decreased uptake value. The results show that, all five peptides have similar disordering effect on the membrane when averaged over the whole simulation time due to the disorder induced by transport of the peptides across the bilayer and the interactions of the peptide with the lipid acyl chains.

4.1.3. Equilibration of the pVEC and del5 pVEC Peptides

For the SMD simulations of pVEC and del5 pVEC peptides, new simulation systems were prepared. The first step was the equilibration of extended chain conformations of both peptides.

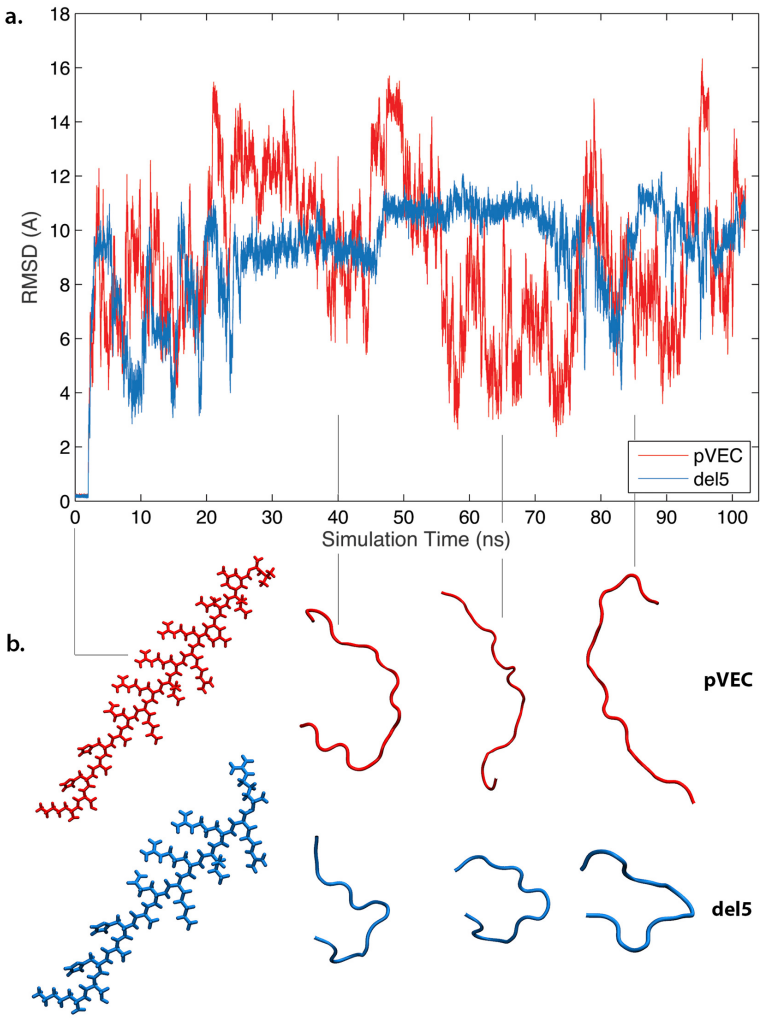

Figure 4.35. Equilibration of pVEC peptides. (a) RMSD profiles of pVEC (red) and del5 pVEC (blue) peptides during the simulations. (b) Initial peptide conformations, and conformations extracted after 40 ns, 65 ns and 86 ns of equilibration.

The simulation trajectories were analyzed and the RMSD for each peptide was calculated by aligning the peptide backbone to the initial structure (Figure 4.35). The del5 pVEC peptide RMSD to the initial coordinates was more stable after 25 ns of

simulation time, whereas pVEC peptide assumes a random coil structure throughout 100 ns of equilibration simulation. Three different conformations for each peptide were extracted from the equilibration simulations of pVEC and del5 pVEC systems at 40 ns, 65 ns and 86 ns simulation time (Figure 4.35) to be used as the initial structures in the SMD simulations of the membrane translocation of these peptides.

4.1.4. SMD Simulations of pVEC and del5 pVEC Peptides

In order to move the peptides from one side of the lipid bilayer to the other, force needs to be applied on the center of mass, in the -z direction to pull the peptides. The force profiles plotted as a function of the z-coordinate of the peptide center of mass (Figure 4.36) are similar for pVEC and del5 pVEC simulations. The force applied on the peptide starts to increase, as the peptide gets closer to the membrane. The force reaches its maximum value when the peptides are in the bilayer core (z around 0 Å). The major difference in the force profile of pVEC and del5 pVEC is that the maximum force applied on the pVEC peptide (around 1100 pN) is higher than that of del5 pVEC (around 600 pN). Moreover, the force applied on pVEC increases abruptly just before the peptide reaches the bilayer core and decreases abruptly after the peptide passes the bilayer core. On the other hand, the force applied on del5 pVEC decreases gradually as the peptide moves toward the lower layer of the membrane. Similar to our observations on the force profiles of pVEC and del5 pVEC systems, the work done (Figure 4.36) to pull the del5 pVEC through the POPE bilayer was much lower (around 300 kcal/mol), when compared to that to pull pVEC (400 kcal/mol).

During the pulling simulations of pVEC and del5 pVEC peptides, no constraints were applied on the phosphate heads of the bilayer. Instead, the translational motion of the bilayer was restrained by constraining the center of mass in the z-direction only. Therefore, the P-heads were free to move and change in the thickness of the membrane was allowed. In both SMD simulations, we observed that upper P-heads started to move toward the bilayer core as the peptide penetrated into the bilayer. As the P-heads moved toward the membrane core, a water pore started to form in both simulations and the membrane thickness increased. The pores were largest when the peptides were

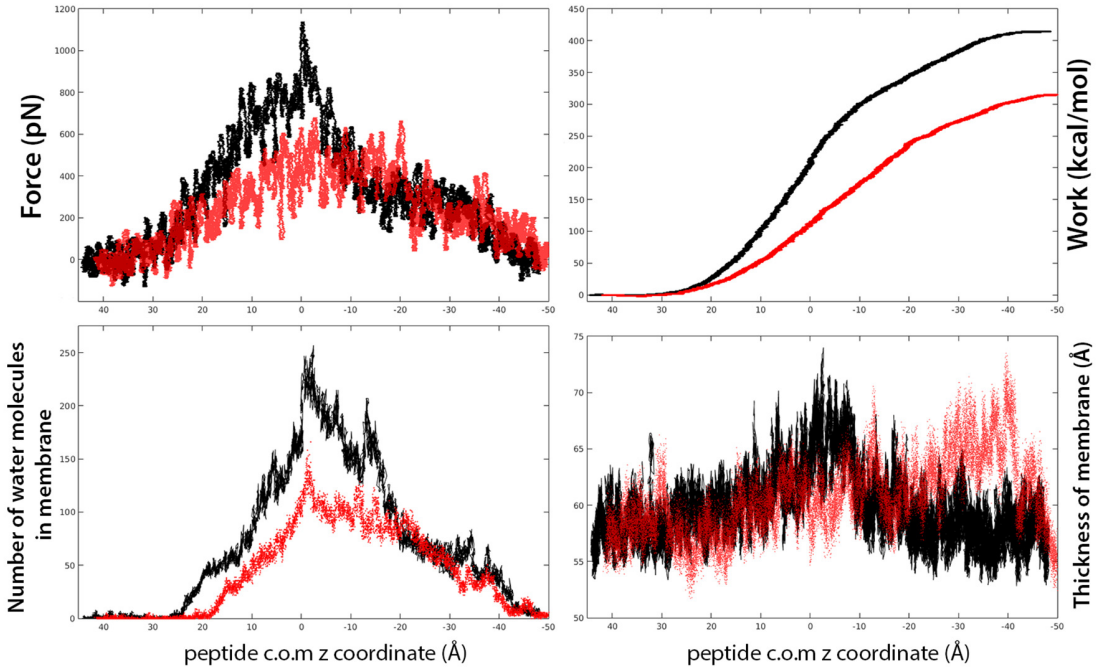

Figure 4.36. Analysis of the SMD simulations of pVEC (black), del5 pVEC (red) peptides translocating the POPE bilayer.

embedded in the lipid bilayer (z around 0 Å). At this stage, the membrane thickness was highest for the pVEC simulation system. A larger pore (around 250 water molecules at maximum) formed in the presence of pVEC when compared to del5 pVEC (around 150 water molecules at maximum) (Figure 4.36). Similar to our observations on the force profiles of both systems, the water pore formed during the translocation of pVEC deformed faster than that in the del5 pVEC simulation. After pVEC passed the bilayer core, the thickness of the membrane started to decrease back to its initial value toward the end of the simulation. The membrane thickness in the del5 pVEC system stayed higher toward the end of the simulation. After the peptide has lost its interaction with the bilayer completely, the membrane thickness decreased back to its initial value (Figure 4.36).

4.1.5. Stretching Simulations of pVEC

A simulation system of wild-type pVEC in a water box was prepared and the peptide was stretched. The initial structure, with an end-to-end distance of 27.7 Å, is the same with the one that was used in the SMD simulations of membrane translocation of pVEC. In the SMD simulations, the peptide unfolds as it translocates through the membrane. In its most extended conformation, where the peptide is embedded in the lipid bilayer, the end-to-end distance is observed to be around 57 Å.

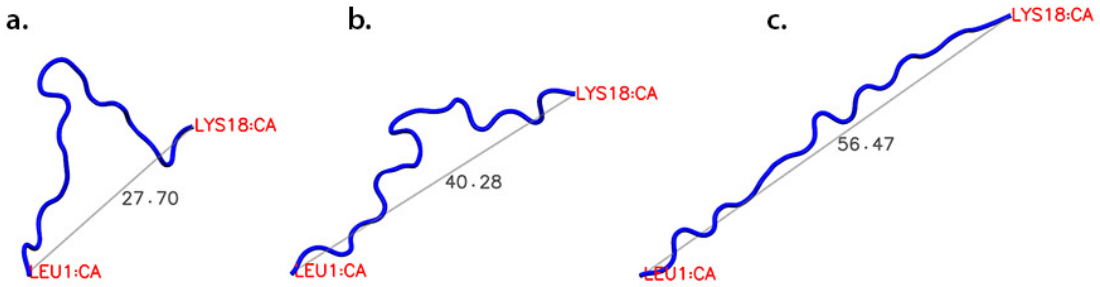

Figure 4.37. Stretching of wild-type pVEC. (a) Initial structure with an end-to-end distance of 27.7 Å, (b) after 2 ns the distance is increased to 40.28 Å, (c) at the end of the simulation the distance was 56.47 Å.

For the stretching of pVEC, two simulations using two different methods were carried out. In the first simulation, a harmonic bias was applied to increase the end-to-end-distance of the peptide from 27.7 Å to 56.47 Å, in the course of a 10 ns MD simulation (Figure 4.37). The change in the radius of gyration, and the change in energy throughout the simulation can be seen in Figure 4.38.

The average interaction and electrostatic energy was around -600 kcal/mol throughout the simulations. It was observed that van der Waals contribution was minor to the total energy. The radius of gyration (rgyr) increased from around 11 Å to 17 Å at the end of the simulation.

In the second stretching simulation, the C_α atom of the Leu1 residue was fixed and the C_α atom of Lys18 was pulled in the opposite direction to increase the end-to-

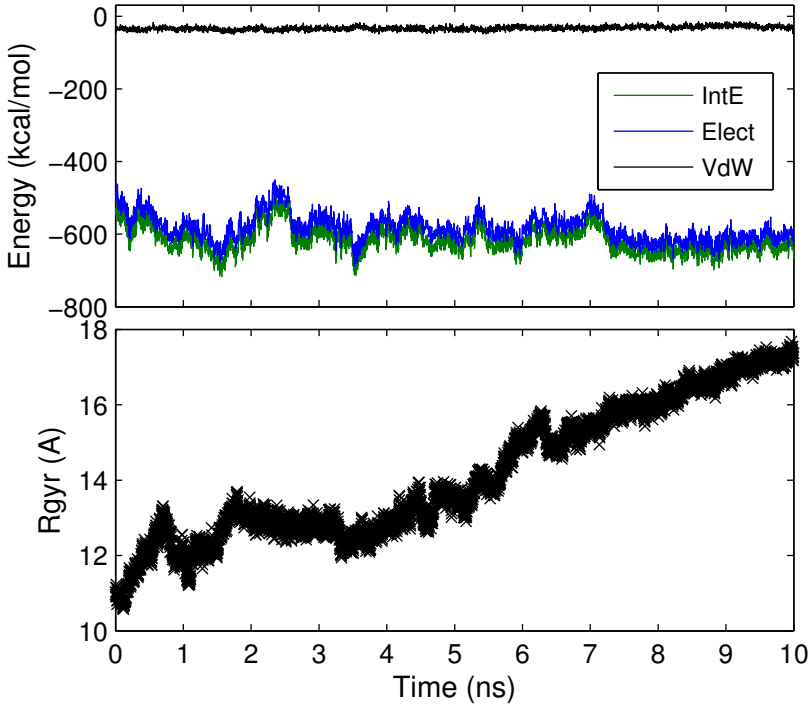

Figure 4.38. Stretching of pVEC using the collective variables module. The change in energy (top) and radius of gyration (bottom) are plotted for the whole simulation.

end-distance in the course of a 12 ns simulation time. The change in the end-to-end distance, force applied on the peptide and work done throughout the simulation can be seen in Figure 4.39.

The end-to-end distance of the peptide increased gradually from 27 Å to 57 Å in a 12 ns simulation time. The force profile with respect to simulation time or end-to-end distance of the peptide, showed some oscillations during the first 8 ns where the end-to-end distance was increased from 27 Å to 45 Å. To increase the distance from 45 Å to 57 Å, the force applied on the peptide abruptly increased to a final value of around 200 pN. In consistent with the force profile, work done gradually increased 5 kcal/mol to extent the peptide to an end-to-end distance of 45 Å. For further extension, the work increased up to 18 kcal/mol.

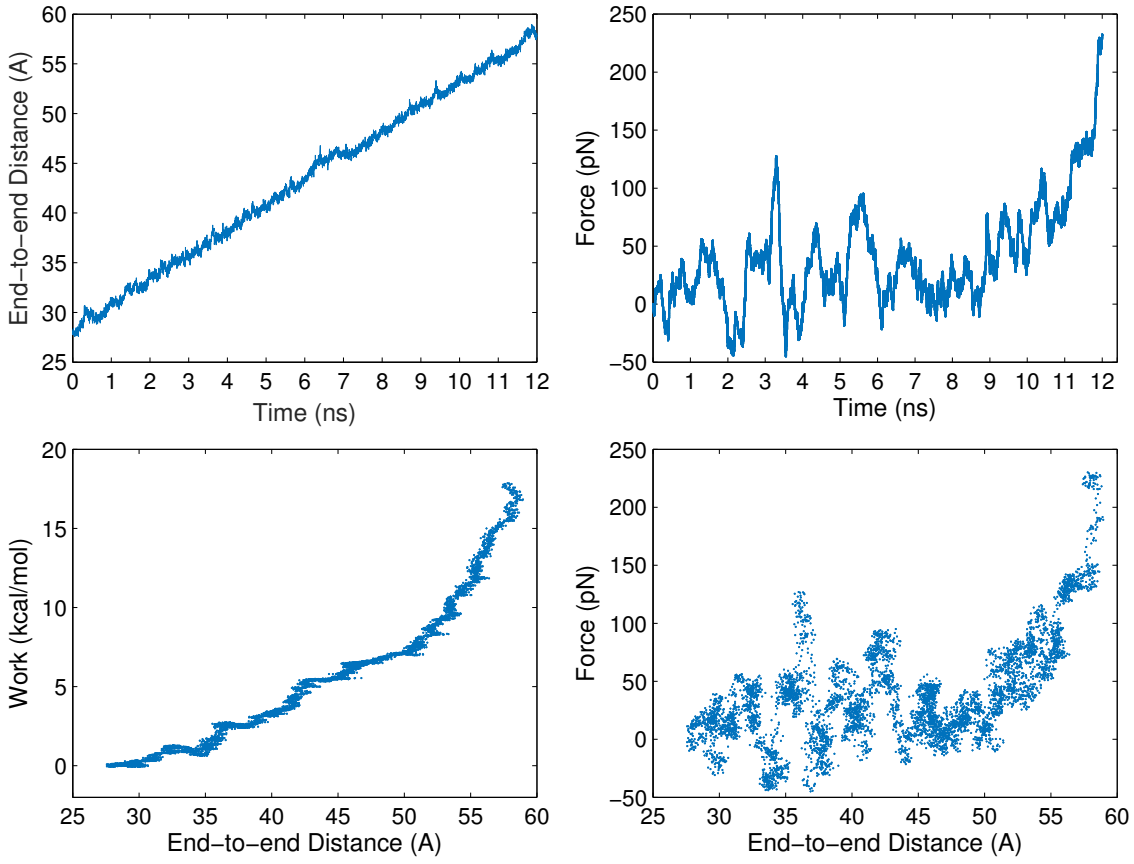

Figure 4.39. Stretching of pVEC using SMD. The change of end-to-end distance and force applied are plotted with respect to the simulation time. Force applied and work done are also plotted with respect to the end-to-end distance of the peptide.

To compare the force applied on the pVEC peptide during stretching and membrane translocation, force and work profiles were plotted together with respect to the radius of gyration of the peptide (Figure 4.40). It was observed that the contribution of peptide stretching to the total force or work was minor when compared to that of membrane translocation. The results suggested that pulling the peptide through a lipid bilayer necessitates a higher amount of force when compared to that of stretching the peptide.

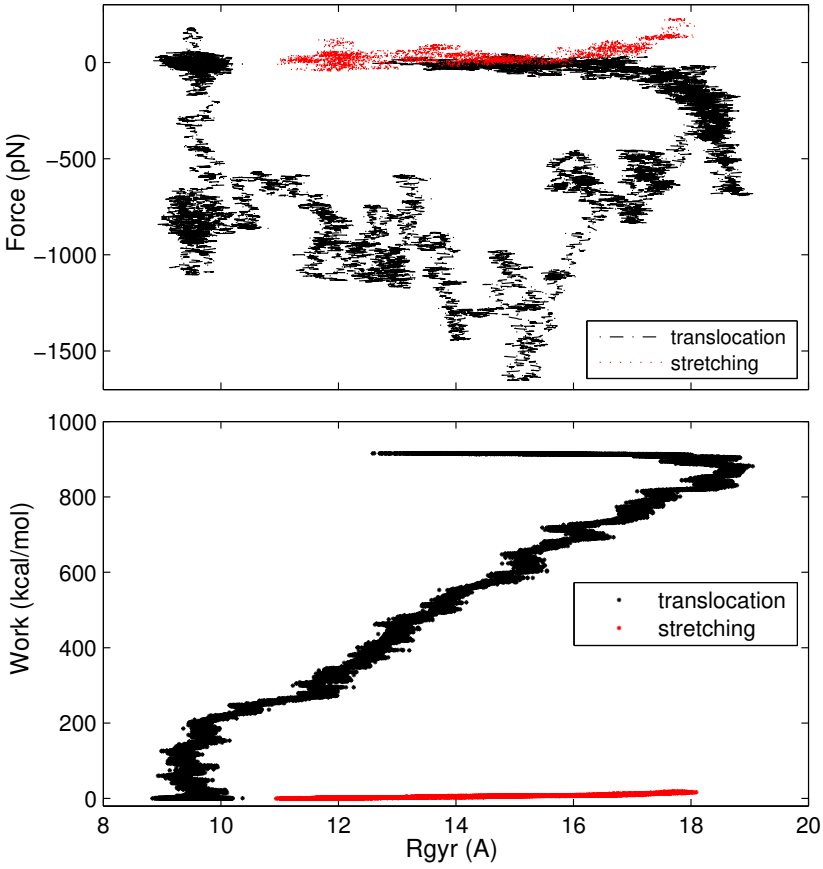

Figure 4.40. Stretching of pVEC (red) in comparison with its membrane translocation (black).

4.1.6. Umbrella Sampling Simulations of Membrane Translocation

4.1.6.1. PMF Calculation for pVEC Membrane Translocation. The umbrella sampling (US) simulations for the membrane translocation of pVEC were carried out using 57 independent windows, in which the initial structures were extracted from the SMD simulation. Each window was first minimized and then simulated for 2 ns. After the simulations were completed, the distance variable calculated in each step of the last 1 ns of each window was used to plot the histograms of the distance variable (Figure 4.41).

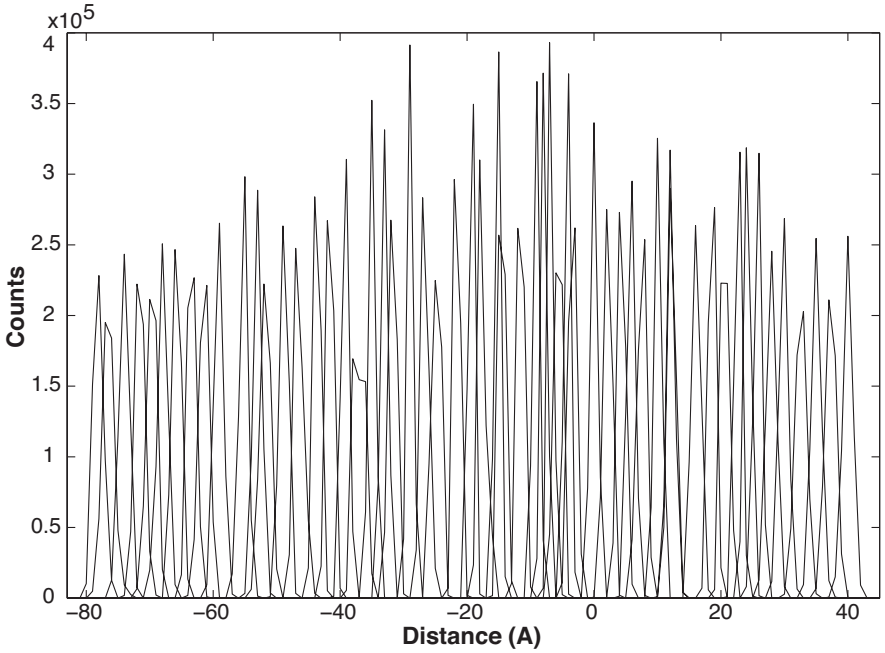

Figure 4.41. Histograms of z-distance between the SMD atom and the lipid bilayer for each umbrella window.

The PMF calculated for the membrane translocation of pVEC shows a barrier of 145 kcal/mol energy to move the peptide from one side of the membrane to the other (Figure 4.42). The system reaches its minimum energy of 0 kcal/mol when the distance between the SMD atom and the membrane is 26.37 Å. At this stage, the peptide is just above the upper phosphate heads of the lipid bilayer and shortly after it penetrates the bilayer. Moreover, since the PMF profile is not symmetric and always positive, the system may possibly be far away from equilibrium, which may be overcome by repeating US simulations with different initial conformations and longer simulations times.

4.1.6.2. PMF Calculation for del5 pVEC Membrane Translocation. The umbrella sampling simulations for the membrane translocation of del5 pVEC was carried out using a similar protocol that was followed for the umbrella sampling simulations of the membrane translocation of pVEC peptide. 51 independent windows, in which the initial coordinates were extracted from the SMD simulation, were first minimized and then

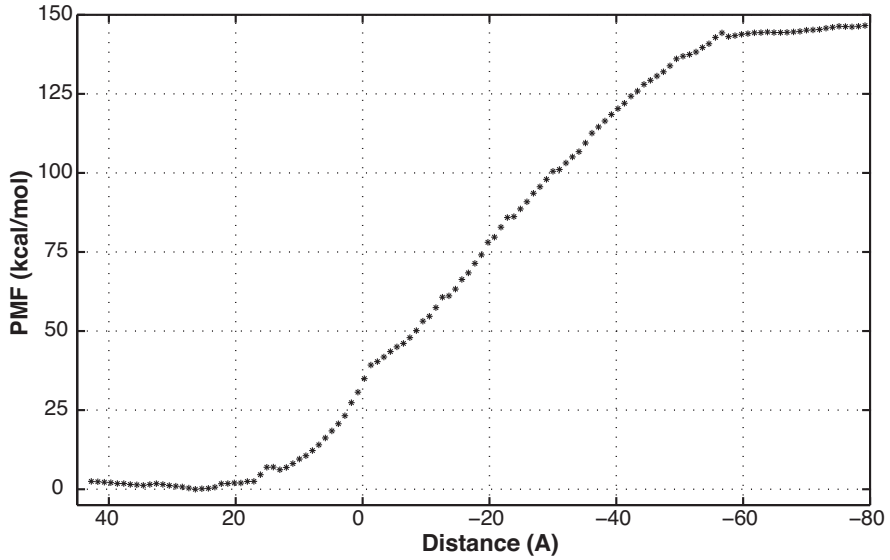

Figure 4.42. The potential of mean force for the membrane translocation of pVEC peptide as a function of the z-distance between the center of mass of the bilayer and the peptide N-terminus.

equilibrated for 2 ns. After the simulations were completed, the distance variable calculated in each step of the last 1 ns of each window was used to plot the histograms of the distance variable. The PMF calculated for the membrane translocation of del5 pVEC shows a free energy difference of -23 kcal/mol energy to move the peptide from one side of the membrane to the other (Figure 4.43). It was also observed that the system reaches its minimum energy of 0 kcal/mol when the distance between the SMD atom and the membrane is 18.5 Å. At this stage, the peptide N-terminus is embedded in the upper phosphate heads of the lipid bilayer and inserts into the bilayer shortly after this stage. The PMF profile was almost symmetric at the plane where the distance variable is -10, suggesting that the system was near equilibrium.

4.1.6.3. Comparison of the PMF profiles. The membrane translocation PMF profiles for pVEC and del5 pVEC peptides was motivated by the structure activity relation studies showing that the uptake of the cell-penetrating peptide pVEC was abolished upon deletion of its N-terminus (LLIIL) [57, 72]. Considering these findings, a lower free energy was expected for the membrane translocation of the pVEC peptide when

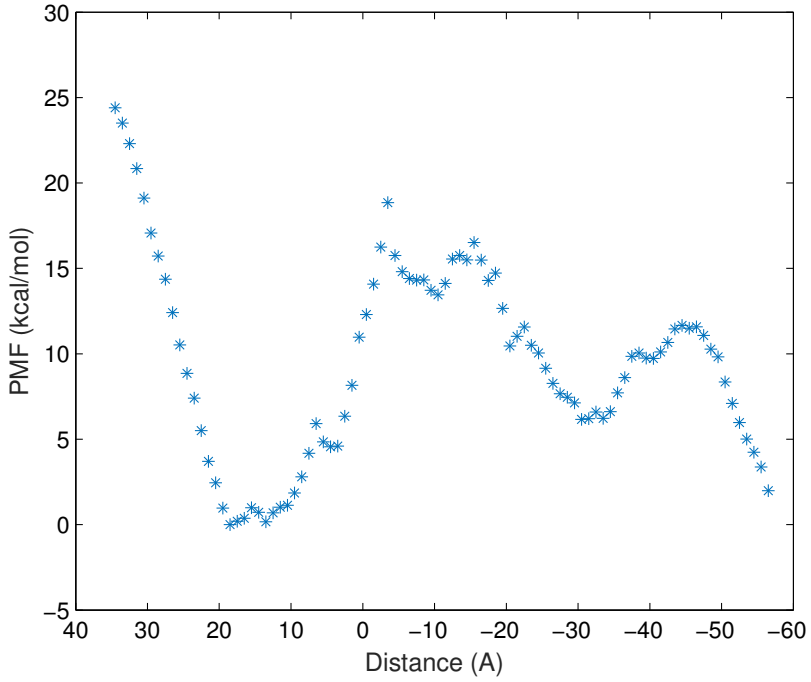

Figure 4.43. The potential of mean force for the membrane translocation of del5 pVEC peptide as a function of the z-distance between the center of mass of the bilayer and the peptide N-terminus.

compared to that of del5 pVEC, suggesting that pVEC translocation would be more favorable.

In our simulations, we have observed that the computed PMF profiles are quite different for pVEC and del5 pVEC systems. For ease of comparison, the initial data points (far left) in the PMF profiles were considered as the initial states, where the peptide is not interacting with the membrane. The whole PMF profiles were translated by assigning the initial states a PMF value of 0 kcal/mol (Figure 4.44). It was observed that the PMF profile of pVEC peptide is almost always positive throughout the reaction coordinate suggesting the translocation is unfavorable. On the contrary, the PMF profile of del5 pVEC system was found to be lower than that of pVEC, a result that was not expected (Figure 4.44).

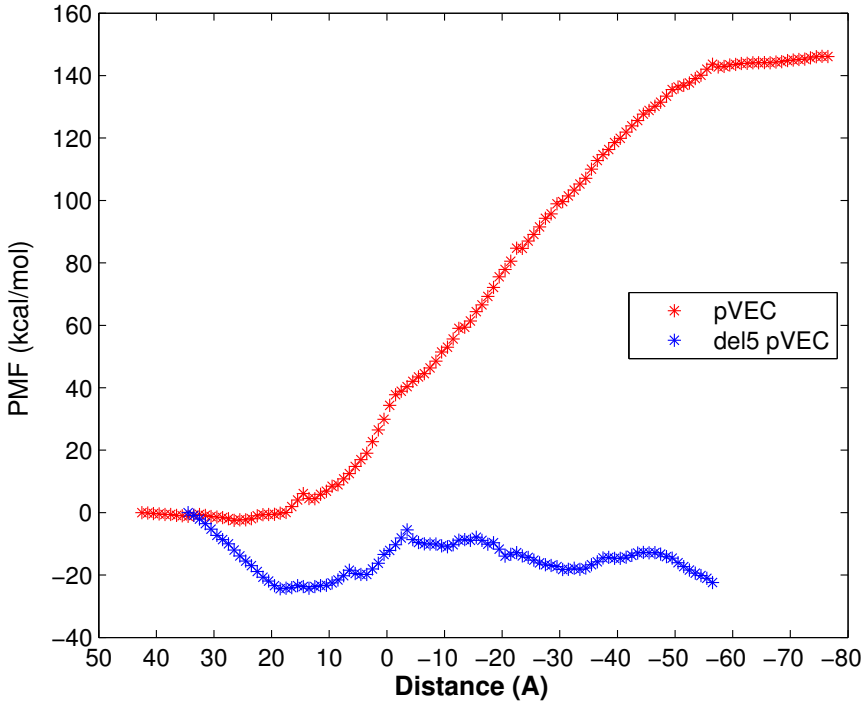

Figure 4.44. Comparison of the PMF profiles for the membrane translocation of pVEC and del5 pVEC peptides.

A characteristic feature in free energy calculations of bilayer systems is that the PMF profile is symmetric around the bilayer center and the convergence to equilibrium can be tested by checking the symmetry of these PMF profiles [90, 152, 168]. The expected symmetric PMF profile was not observed for the pVEC system, but the del5 pVEC PMF curve was almost symmetric (Figure 4.44). These results suggest that del5 pVEC simulations were near equilibrium when compared to pVEC simulations, which may be the reason of the lower PMF curve obtained for the del5 pVEC system.

4.1.7. Replica Exchange Umbrella Sampling Simulations of Peptide Translocation

We have previously investigated the membrane translocation of pVEC (LLIIL-RRRIRKQAHAHSK) and del5 pVEC (RRRIRKQAHAHSK) using steered molecular dynamics (SMD) simulations, in which the peptide-lipid interactions were studied in

detail to determine the specific regions of the peptide that may contribute to cellular uptake [74]. The previous SMD simulations were carried out by pulling the peptide from its N-terminus through the 128-lipid POPE bilayer, which was constrained on its P heads only in the z-direction. In this study, the SMD simulations were carried out by pulling the peptide from its center of mass with a smaller velocity, through the CHARMM-GUI 128-lipid POPE bilayer, which was constrained on its center of mass only in the z-direction. Using these SMD simulations, the reaction coordinate of our system was selected as the distance (in z-direction) between the peptide center of mass and the center of the lipid bilayer. The selected reaction coordinate was then divided into equally spaced (2 Å or 1 Å) replicas and snapshots corresponding to each window were extracted from the SMD simulations to be used as the initial coordinates of the replica exchange umbrella sampling (REUS) simulations.

4.1.7.1. PMF Calculation for the Membrane Translocation of pVEC. For the REUS simulations of pVEC translocation across the membrane, the z-distance between the peptide center of mass and lipid bilayer center of mass was selected as the reaction coordinate. The 40 - 18 Å range of the reaction coordinate was divided into 12 replicas with 2 Å spacing. The initial structures were extracted from the previous pVEC SMD simulation. Simulations were carried out for 5 ns per replica and then were extended to 10 ns per replica.

The PMF generated from the first 5 ns (per replica) of the REUS simulations (Figure 4.45a, red circles) indicates an energy barrier of around 14 kcal/mol to move the pVEC peptide from the water layer (42 Å distance from the bilayer center) into the POPE bilayer (17.5 Å distance from the bilayer center). The PMF reaches its minimum value (close to 0) at around 35.5 Å, which corresponds to a state where the peptide is not interacting with the membrane. After extending the simulations to 10 ns (per replica), no major change in the PMF was observed (Figure 4.45a, orange circles). Although the PMF was slightly lower in the 30 Å - 25 Å range, it started to diverge from the PMF generated from the first 5 ns in the 22 Å - 17 Å range. The exchange rates calculated for the 10 ns (per replica) REUS simulations with 2 Å replica

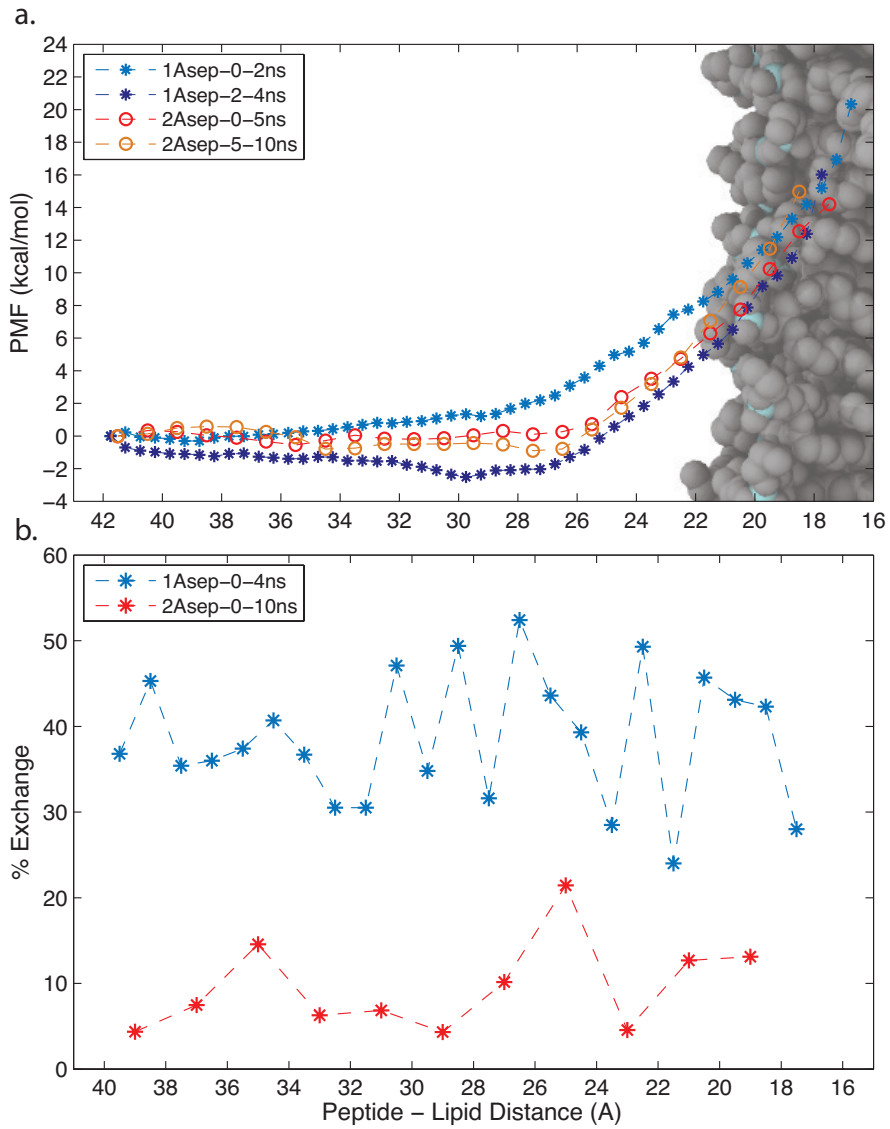

Figure 4.45. Comparison of 4 pVEC REUS simulations with 1 Å or 2 Å replica spacing. PMF (a) and accepted exchange percentage (b) between replicas are plotted as a function of the z-distance of the peptide center of mass lipid center.

spacing indicate that the average exchange percentage was around 10% (Figure 4.45b, red). This average exchange rate is lower than the recommended rates [151], which are around 30-40%. Especially, the exchange rates of replicas corresponding to the states with peptide-lipid distance of 39 Å, 29 Å, and 23 Å were around 5%, which did not increase even after 10 ns (per window) simulation time. These results suggested that 2 Å replica spacing is wide to achieve efficient exchange between replicas.

The REUS simulations for the membrane translocation of pVEC were then carried out by dividing the 40 Å - 17 Å range of the reaction coordinate into 24 replicas with 1 Å spacing. The results of the initial runs with 1 Å spacing are given in comparison with 2 Å spacing in Figure 4.45.

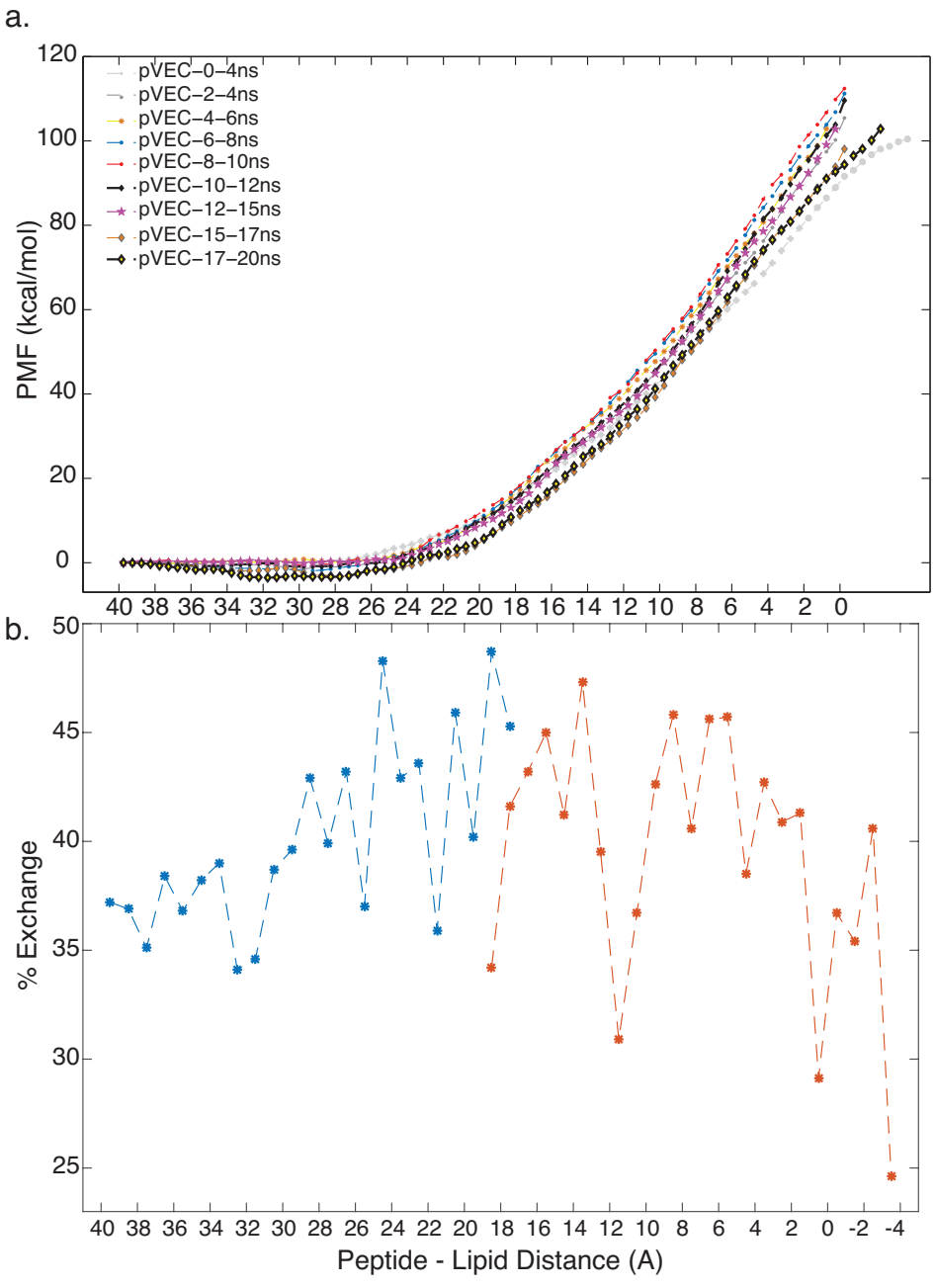

Figure 4.46. REUS simulations for the membrane translocation of pVEC peptide. PMF (a) and accepted exchange percentage between replicas (b) plotted as a function of the peptide-lipid distance corresponding to each replica.

The PMF generated from each 2 ns (per replica) of the REUS simulations (Figure 4.46a) indicates an energy barrier of around 100-120 kcal/mol to move the pVEC peptide from the water layer (40 Å distance from the bilayer center) into the POPE bilayer core (0 Å distance from the bilayer center). The PMF reaches its minimum value (around -3 kcal/mol) at around 31 Å, which corresponds to a state where the peptide is not interacting with the membrane. Throughout each 2 ns of simulation in the first 10 ns (Figure 4.46a), the PMF increased indicating that the simulation is far from equilibrium. On the other hand, throughout the last 5 ns (per replica) of the simulations (Figure 4.46a) a decrease in the PMF was observed, suggesting a convergence to equilibration. Using the last 3 ns of the simulation data, the final PMF was calculated as 94 kcal/mol (Figure 4.46a, black-yellow diamonds). The exchange rates calculated for the all 20 ns (per replica) simulations indicate that the average exchange percentage was around 40% (Figure 4.46b).

4.1.7.2. PMF Calculation for the Membrane Translocation of del5 pVEC. The REUS simulations for the membrane translocation of del5 pVEC were also tested by dividing the 40 Å - 18 Å range of the reaction coordinate (z-distance between center of mass of peptide and center of mass of lipid bilayer) into 12 replicas with 2 Å spacing. The initial structures were extracted from the previous del5 pVEC SMD simulation. Harmonic bias with a force constant of 1.0 kcal/mol was applied on the peptide-lipid z-distance to achieve local sampling. Simulations were carried out for 5 ns (per replica) simulation time.

The PMF generated from the first 5 ns (per replica) of the REUS simulations (Figure 4.47a) indicates an energy barrier of around 9 kcal/mol to move the del5 pVEC peptide from the water layer (42 Å distance from the bilayer center) into the POPE bilayer (17.5 Å distance from the bilayer center). The PMF is at its minimum value of -3 kcal/mol at around 28.5 Å, which corresponds to a state where the peptide is not interacting with the membrane. The exchange rates calculated for the 5 ns (per replica) REUS simulations with 2 Å replica spacing indicate that the average exchange percentage was less than 10% (Figure 4.46b). This average exchange rate is lower

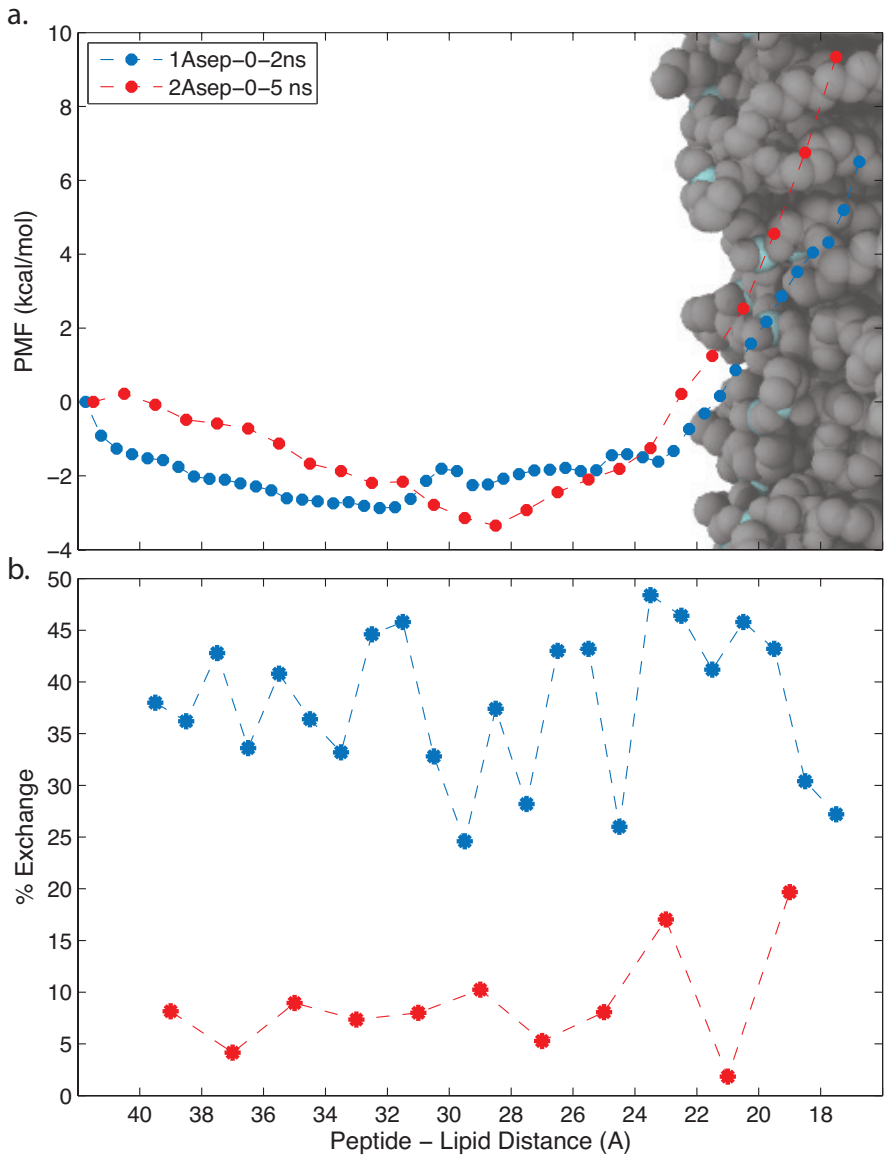

Figure 4.47. Comparison of del5 pVEC REUS simulations with 1 Å and 2 Å replica spacing. PMF (a) and accepted exchange percentage (b) between replicas are plotted as a function of the z-distance of the peptide center of mass lipid center.

than the recommended rates, which are around 30-40%. Especially, the exchange rates of replicas corresponding to the states with peptide-lipid distance of 37 Å, and 21 Å were less than 5%, which seemed unlikely to exceed 30% by extending the simulations. These results suggested that 2 Å replica spacing is wide for the del5 pVEC simulation system to achieve efficient exchange between replicas.

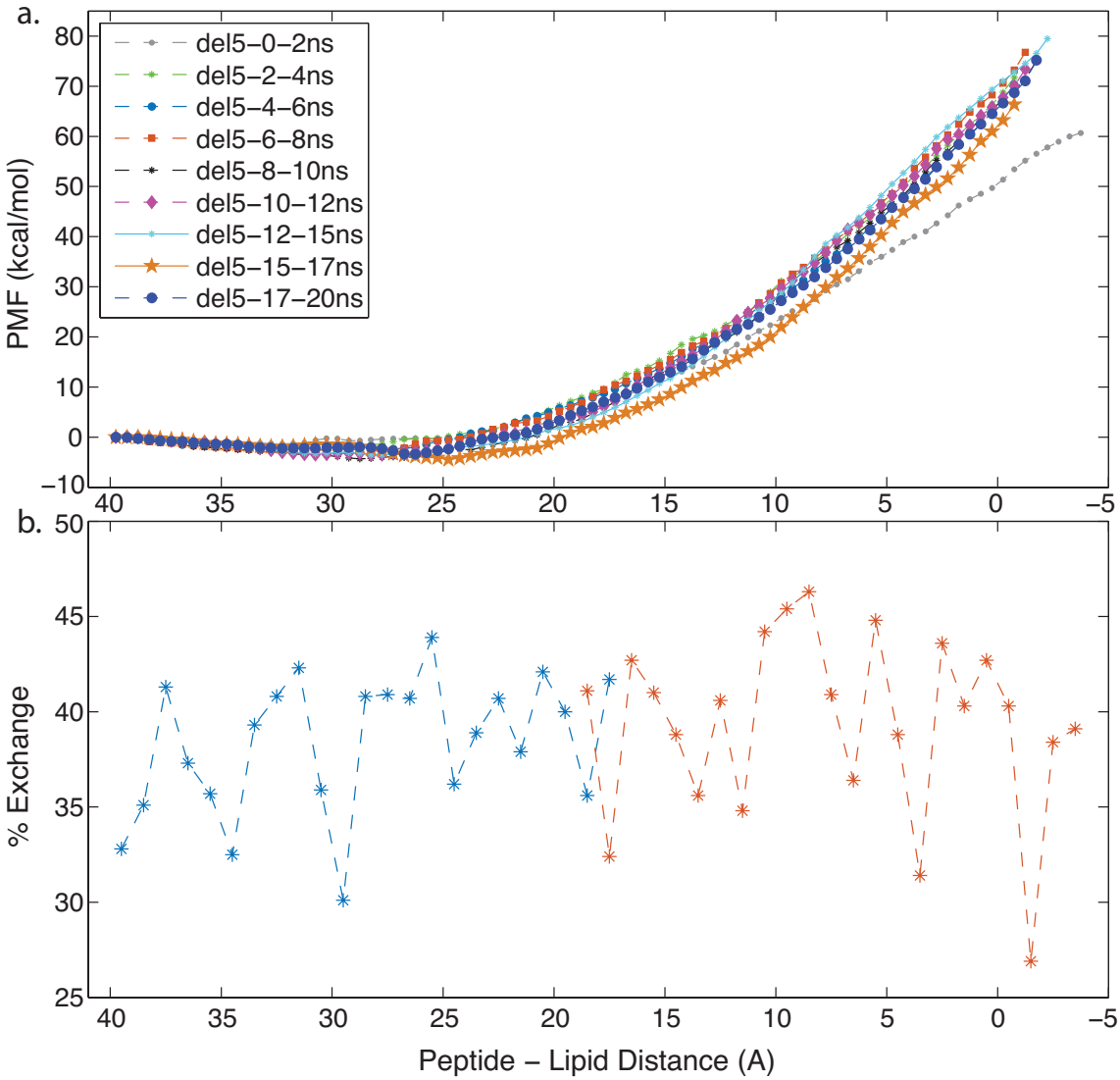

Figure 4.48. REUS simulations for the membrane translocation of del5 pVEC peptide. PMF (a) and accepted exchange percentage between replicas (b) plotted as a function of the peptide-lipid distance corresponding to each replica.

The REUS simulations for the membrane translocation of del5 pVEC were then carried out by dividing the 40 Å - 17 Å range of the reaction coordinate into 24 replicas with 1 Å spacing. The results of the initial runs with 1 Å spacing are given in comparison with 2 Å spacing in Figure 4.47.

The PMF generated from each 2 ns (per replica) of the REUS simulations with (Figure 4.48a) indicates an energy barrier of around 70-80 kcal/mol to move the del5

pVEC peptide from the water layer (40 Å distance from the bilayer center) into the POPE bilayer core (0 Å distance from the bilayer center). The PMF reaches its minimum value (around -5 kcal/mol) at around 28 Å, which corresponds to a state where the peptide is not interacting with the membrane. Using the last 3 ns (per replica) of the simulation data, the final PMF is calculated as 65 kcal/mol (Figure 4.48a, dark blue). The exchange rates calculated for the all 20 ns (per replica) REUS simulations indicate that the average exchange percentage was around 40% (Figure 4.48b).

4.1.7.3. Comparison of the PMF Profiles. We focused on the calculation the membrane translocation PMF profiles for pVEC and del5 pVEC peptides based on the results of the structure activity relation studies that showed the uptake of the cell-penetrating peptide pVEC was abolished upon deletion of its hydrophobic N-terminus (LLIIL) [57, 72]. Considering these findings, if the simulation pathway is realistic, a lower free energy should be observed for the membrane translocation of pVEC peptide when compared to that of del5 pVEC peptide, suggesting that pVEC translocation would be more favorable.

However, our calculations suggest that the PMF trends are similar for pVEC and del5 pVEC systems. The PMF profile generated from the last 3 ns simulations of pVEC is always positive throughout the reaction coordinate and the energetic cost of carrying pVEC into the bilayer core is around 94 kcal/mol, suggesting the translocation is unfavorable. The PMF profile generated from the last 3 ns simulations of del5 pVEC system was found to be lower than that of pVEC with a free energy around 65 kcal/mol and the increase in the profile after del5 pVEC penetrates into the bilayer was much lower than that for pVEC. These results suggest that del5 pVEC translocates into the POPE bilayer at a lower energetic cost.

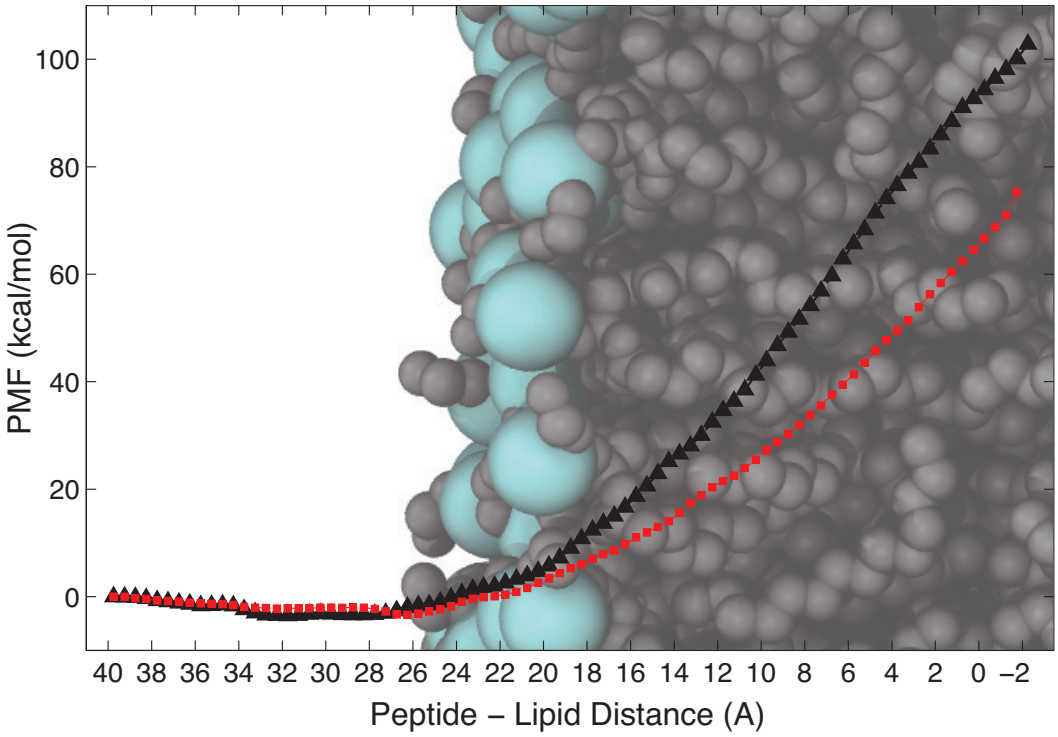

Figure 4.49. Comparison of the PMF profiles generated from REUS simulations of pVEC (black) and del5 pVEC (red) translocating the POPE bilayer.

4.1.8. Analysis of Simulation Trajectories by Dimensionality Reduction Algorithms

The data sets of molecular configurations produced by simulations could be analyzed in order to extract the important features of the system motion. Given a sample of configurations, finding a low-dimensional embedding such that the shape of the underlying manifold is preserved, is the principal of any dimensionality reduction problem. The aim is to define a low-dimensional embedding that could be used quantitatively to characterize a simulation [96].

The molecular dynamics simulation trajectories were analyzed using dimensionality reduction techniques PCA and ISOMAP [97] to interpret the underlying manifold. Before applying the dimensionality reduction algorithms on the complex membrane translocation simulations, a simpler system, the stretching of pVEC was analyzed.

4.1.8.1. PCA and ISOMAP Applications on Stretching Simulation of pVEC. For the application of PCA algorithm on the stretching of pVEC, the peptide trajectory was aligned (with respect to backbone, reference frame is the initial structure) and alpha-carbon atom coordinates of the aligned peptide in every 10,000 simulation step (every 20 ps) was used as data set. The percent variance explained by the first two components was calculated as 82% (67.22% for the first and 15.1% for the second component).

The simulation data projected on the first two PCs (PC1 and PC2) are color-coded with respect to the end-to-end distance of the peptide (Figure 4.50a). The data projected on the first two principal components (PC1 and PC2) shows a disordered profile (Figure 4.50a) even though the first component (PC1) is related to the increase in the end-to-end distance of the peptide (color-coding blue to red). This was expected since the highest variance corresponds to PC1 (67.22%) and can be verified by plotting the distance with respect to the data mapped on PC1 (Figure 4.50c), which yields an almost linear profile. On the other hand, plotting the data mapped on PC2 does not show any structure when plotted against any physical variable in the simulation system.

For the application of the ISOMAP algorithm, the Cartesian coordinates of C_α atoms of each residue at every 2000 simulation step (every 4 ps) of the aligned peptide trajectory were used as the data set. Variations for the first 2 dimensions were calculated for different values of k, and the best k value was chosen to be 5, which yields the highest variation in the data. At this k value, the total variation of the data in the first 2 ISOMAP dimensions (DIM1 and DIM2) was calculated as 99.72%, of which 99.5% is already explained by the first ISOMAP dimension (DIM1).

The simulation data projected on the first two DIMs (DIM1 and DIM2) are color-coded with respect to the end-to-end distance of the peptide (Figure 4.50b).The data projected on the first two dimensions (DIM1 and DIM2) shows a structured profile (Figure 4.50b) and with further investigation, it can be suggested that application of the ISOMAP algorithm enables the identification of abrupt structural changes. Since the first dimension (DIM 1) already represents most of the data, further investigation

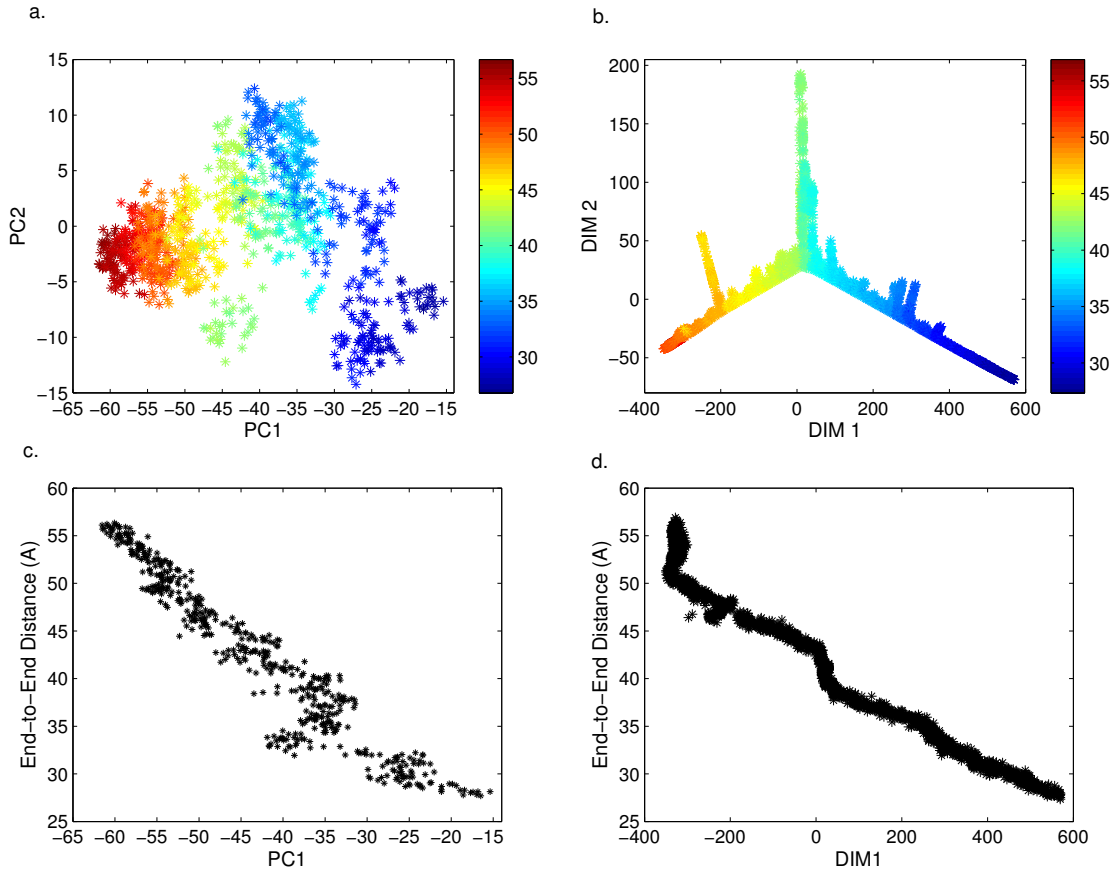

Figure 4.50. PCA (a) and ISOMAP (b) projections of the pVEC stretching simulation. (c) First principal component (PC1) and (d) first ISOMAP dimension (DIM1) are plotted with respect to the end-to-end distance.

for the physical characterization of DIM 1 should be carried out. When the distance between the SMD atom and the lipid bilayer is plotted against the data projected on DIM 1 (Figure 4.50d), it is observed that DIM 1 not only contains the information on the increase of the distance, but also gives information about the abrupt structural changes (such as rotations) indicated by the jumps between data points. On the other hand, DIM 2, by itself represents a negligible amount of data, but the projection on DIM 2 is harder to characterize.

4.1.8.2. PCA and ISOMAP Applications on Translocation Simulations. The simulation systems of 4 different pVEC derivative peptides (wt-pVEC, retro-pVEC, scrambled-

pVEC and del5 pVEC) translocating the POPE lipid bilayer were analyzed. The simulations analyzed here were previously carried out and explained in detail in another study [74].

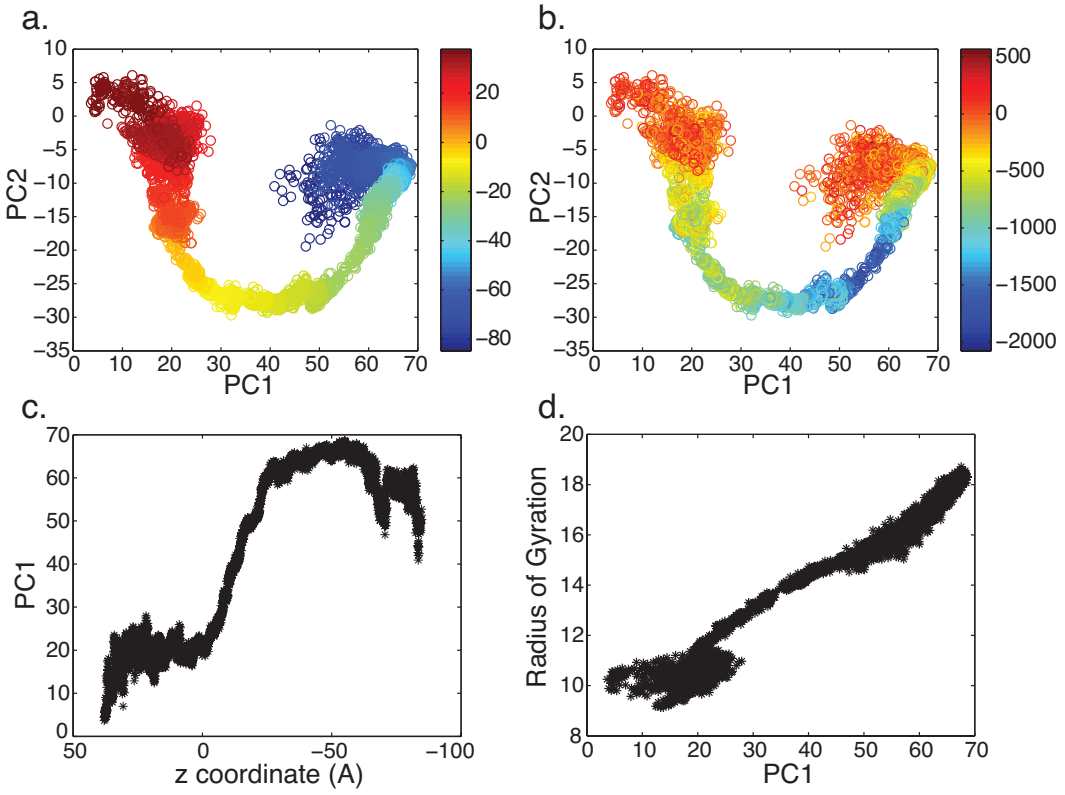

Figure 4.51. PCA applied on the membrane translocation simulation of pVEC. First two principal components are shown with z-coordinate (a) and force (b) color-coding. PC1 is plotted with respect to the z-coordinate (c) and radius of gyration(d).

For the application of PCA algorithm, the peptide trajectories were aligned (with respect to backbone, reference frame is the initial structure) and C_α atom coordinates of each aligned peptide were used as data sets. The results of the PCA for the wt-pVEC system are given below as an example. Figure 4.51 shows the principal components and first principal component (PC1) plotted against second principal component (PC2) with z coordinate (Figure 4.51a), and force color-coding (Figure 4.51b). The z-coordinate coloring scheme represents the simulation trajectory starting from dark red (beginning of the simulation) to dark blue (end of the simulation). The accumulated data points of dark red and dark blue colors represent the motion of the peptide

in water layer above the membrane (before initial penetration) and the motion of the peptide in water layer below the membrane (after peptide exit from the membrane) respectively. When the peptide is in the membrane (between z values 20 to 40 Å), data points tend to follow a clearly observable U shape. In order to determine what PC1 corresponds to in the simulation, PC1 is plotted against both z-coordinate of the SMD atom (Figure 4.51c) and radius of gyration Figure 4.51d). It was observed that PC1 versus radius of gyration plot was almost linear, which shows that the algorithm defines PC1 as the radius of gyration for the simulation system.

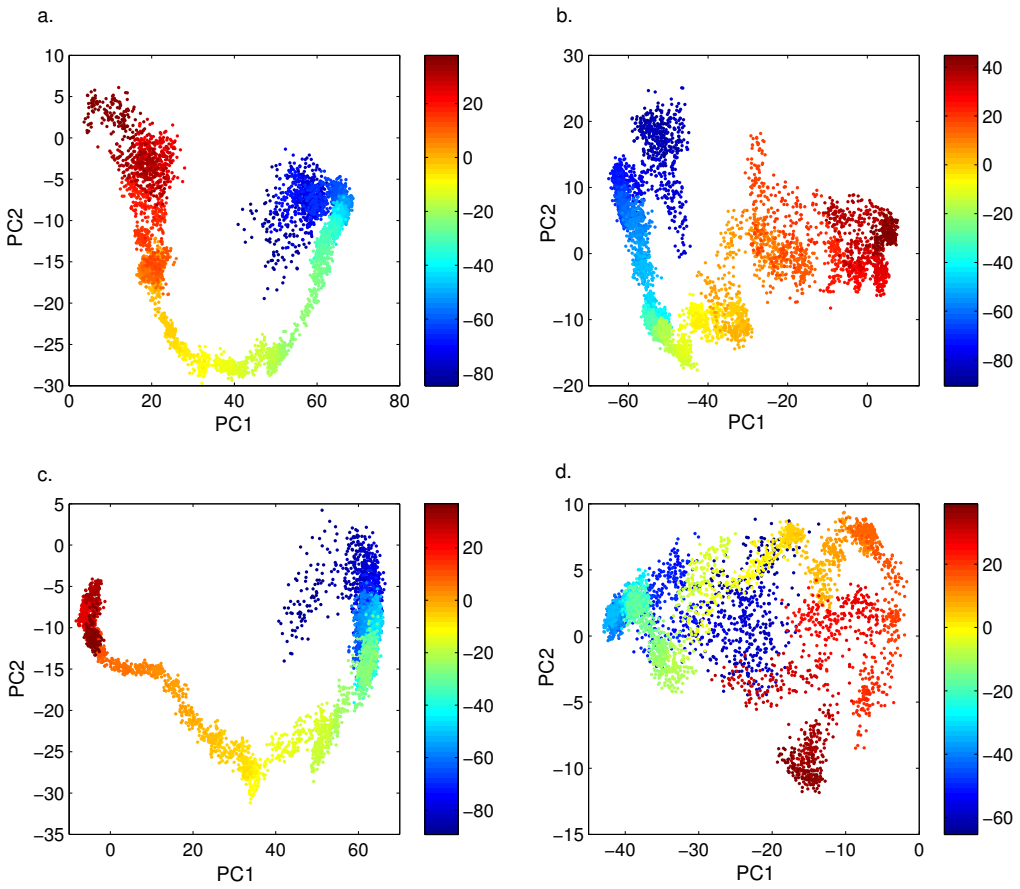

Figure 4.52. Comparison of PCA results for four different pVEC systems; (a) wt-pVEC, (b) retro-pVEC, (c) scr-pVEC, (d) del5 pVEC. Data is color-coded with respect to z coordinate of the SMD atom.

The application of PCA on the SMD simulations of pVEC derivatives showed that PC1 is always defined as the radius of gyration independent from the peptide used in the

simulation. On the other hand, the three modes of translocation (before penetration, in membrane and after exit) observed in the PCA results for the wt-pVEC system are detectable for the scrambled-pVEC (Figure 4.52c) simulation whereas they can hardly be specified for retro-pVEC (Figure 4.52b). Also, there is no detectable structure for the simulation of del5 pVEC system (Figure 4.52d). These major differences may give idea about the importance of the LLIIL residues in the translocation mechanism, since deletion of these residues changes the underlying manifold.

For the application of ISOMAP algorithm, the peptide trajectories were aligned (backbone) with respect to the initial structure and C_α atom coordinates of each aligned peptide are used as data sets. Variation for the first two dimensions were calculated for different values of k and the best k value was selected such that it results in the highest variation (for first two dimensions) for the ISOMAP projection for each system.

The results of the ISOMAP projection for the wt-pVEC system are given below as an example. Figure 4.53 shows the first three dimensions (DIM1, DIM2, DIM3) detected by ISOMAP algorithm and they were plotted with respect to each other. The coloring scheme represents the simulation trajectory starting from dark red (beginning of the simulation) to dark blue (end of the simulation). The first two dimensions of ISOMAP plotted with respect to each other (DIM1 versus DIM2), different from PCA, shows the data spread out as the peptide penetrates into the membrane and it unfolds. In order to determine what DIM1 corresponds to in the simulation, DIM1 is plotted against both radius of gyration and z coordinate of the SMD atom (Figure 4.53). DIM1 versus z coordinate of the SMD plot was almost linear (Figure 4.53c), which shows that the algorithm defines DIM1 and the main motion as the change in z coordinate of the SMD atom for the simulation system. The advantage and the reason of preference for the usage of ISOMAP algorithm was that it is a nonlinear dimensionality reduction algorithm, which uses neighborhood relations of data points and thus keeps track of the motion as a continuous process instead of handling the data points separately.

The application of ISOMAP on the SMD simulations of pVEC derivatives showed that DIM1 is defined either as the z coordinate of the SMD atom or as the combination

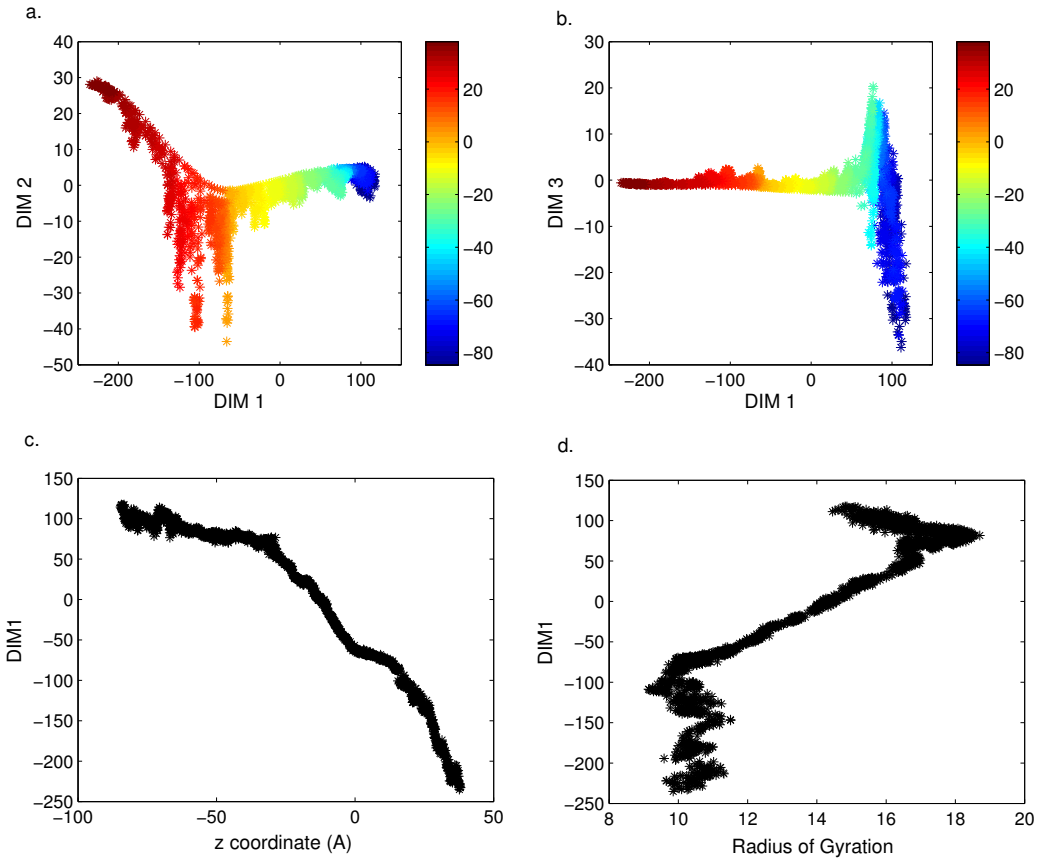

Figure 4.53. ISOMAP applied on the membrane translocation simulation of pVEC. First three dimensions are shown with z-coordinate (a,b) color-coding. DIM1 is plotted with respect to the z-coordinate (c) and radius of gyration(d).

of the z coordinate of the SMD atom and the radius of gyration of the peptide. The ISOMAP projection of retro-pVEC was very similar to that of wt-pVEC (Figure 4.54b). On the other hand, the projection of scrambled-pVEC (scr-pVEC) simulation showed a different manifold especially toward the end of the simulations (blue to dark blue colored data points), where the peptide fluctuates and takes a lot of time to exit the membrane (Figure 4.54c). The most different manifold was the projection of del5 pVEC system (Figure 4.54d), similar to the case in PCA. As mentioned earlier, the major differences in manifolds may give idea about the importance of the LLIIL residues in the translocation mechanism, since deletion of these residues (del5 pVEC) changes the underlying manifold abruptly.

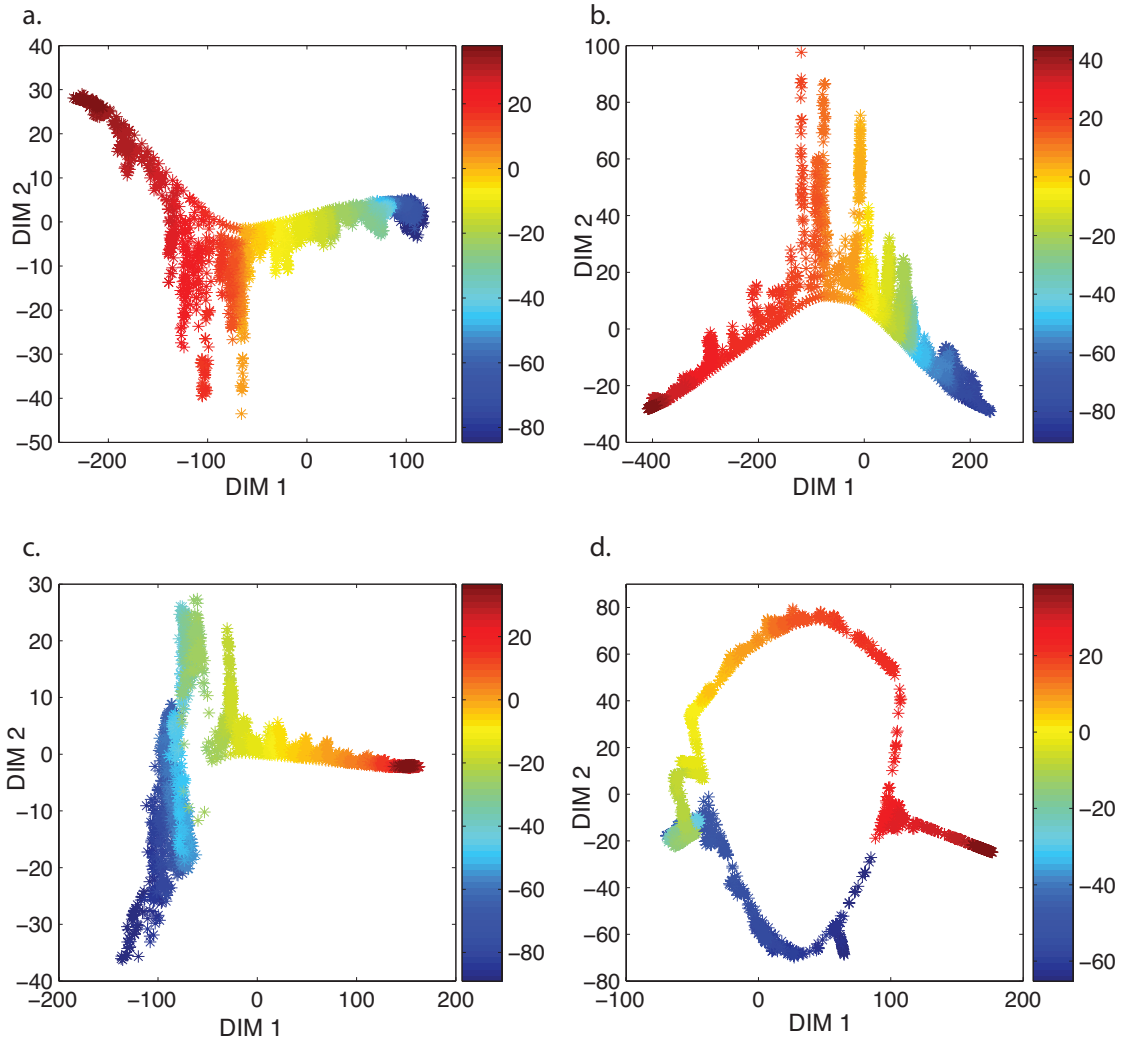

Figure 4.54. Comparison of ISOMAP results for four different pVEC systems; (a) wt-pVEC, (b) retro-pVEC, (c) scr-pVEC, and (d) del5 pVEC. Data points are color-coded with respect to z coordinate of the SMD atom.

4.2. In-vitro Enzyme Kinetics of Beta-lactamase Inhibitory Peptides

In order to investigate the binding and inhibition of beta-lactamase enzyme by the proposed inhibitory peptides, in-vitro enzyme kinetics experiments were carried out. The results given in this section can also be found in the manuscript published in the Journal of Peptide Science entitled 'A Novel Chimeric Peptide with Antimicrobial Activity' by Begum Alaybeyoglu, Berna Sariyar Akbulut and Elif Ozkirimli.

Enzyme kinetics experiments carried out with TEM-1 beta-lactamase and its substrate CENTA resulted in K_m and k_{cat} values of 70 μM and 110 s^{-1}, respectively, for a final enzyme concentration of 11.2 nM with the initial rate measurements method. In an independent study, the K_i value for the peptide based on the 46-51 loop of BLIP was reported as 500 μM [11]. Here, the enzyme kinetics experiments were carried out with R-TEM-1 beta-lactamase purified from beta-lactamase expressing bacteria and with the substrate CENTA. The effect of P1 addition and beta-lactamase inhibition with P1 was investigated accordingly. Table summarizes the kinetic constants obtained with CENTA and R-TEM-1 beta-lactamase in the presence and absence of P1.

Table 4.1. R-TEM-1 beta-lactamase inhibition in the presence and absence of P1.

	CENTA	**P1**
[Enzyme] (nM)	36.33	36.33
[CENTA] (μM)	35-120	35-120
[P1] (μM)	-	100
V_{max} (μM/min)	5125	5231
K_m (μM)	55.02	93.88
k_{cat} (s^{-1})	2351	929
K_i (μM)	-	58.6

The kinetic constants K_m and V_{max} obtained for CENTA hydrolysis with R-TEM-1 beta-lactamase were calculated as 55.02 μM and 5125 μM/min, respectively for a final enzyme concentration of 36.33 nM. Upon addition of P1, V_{max} did not change (5231 μM/min), while K_m value increased to 93.88 μM showing that P1 is a competitive inhibitor of R-TEM-1 beta-lactamase with a K_i value of 58.6 μM. In comparison, the K_i for the peptide based on 46-51 loop of BLIP was 500 μM, suggesting that extension of this previously identified peptide to include His45 and Tyr53 results in tighter binding and improved inhibition.

4.3. Effect of Drugs on Growth of Bacterial Cells

The aim in this part of the study was to design chimeric peptides that can penetrate into bacteria to reach and inhibit the target beta-lactamase enzyme. With this aim, two BLIP-based beta-lactamase inhibitory peptides, HAAGDYYAY [84] and RRGHYY [131,132] were tested and further modified to enhance their bacterial uptake. The modification approach involved the addition of the five N-terminal residues (LLIIL) of the cell-penetrating peptide pVEC to the N-terminus of the peptides to design a chimera that combines the key fragments of an inhibitor protein and a cell-penetrating peptide. The chimeric peptide LLIILHAAGDYYAY [84] was further modified with addition of three arginine residues as a linker region (LLIILRRRHAAGDYYAY) to increase the peptide solubility. All peptides were tested for their antimicrobial activity on wild-type and antibiotic resistant *E. coli* strains, and their antimicrobial activity was compared with antimicrobial actions of a lipid membrane permeabilizer DMSO, a well-established antimicrobial peptide melittin [35, 36], a beta-lactam antibiotic ampicillin [169], a known beta-lactamase inhibitor potassium clavulanate [118, 120, 121], and the cell-penetrating peptide pVEC [57, 72]. Moreover, pVEC and its variant del5 pVEC, which does not include the N-terminal hydrophobic residues (LLIIL) was compared in terms of their antimicrobial action, in order to investigate the significance of the LLIIL stretch on the antimicrobial action and membrane permeabilization potential of the cell-penetrating peptide pVEC.

4.3.1. Effect of DMSO on Bacterial Growth

In order to determine the effect of lipid membrane permeabilizer DMSO on wild-type *E. coli* K12 and antibiotic resistant *E. coli* K12 pUC18 cells, cultures at standard and high inoculation cell density were treated with different DMSO concentrations in the 0.39% - 50% range. The control samples were treated with water only for comparison.

After 20 hours of incubation of the DMSO treated and control cultures, visible growth was observed in control cultures at both standard and high inoculation density

of *E. coli* K12 and *E. coli* K12 pUC18 cells. On the other hand, visible growth was not observed in the cultures treated with 12.5% DMSO or more at standard inoculation density of both *E. coli* K12 and *E. coli* K12 pUC18 cells. At high inoculation density of both *E. coli* K12 and *E. coli* K12 pUC18 cells, visible growth was not observed in the cultures treated with 25% DMSO or more.

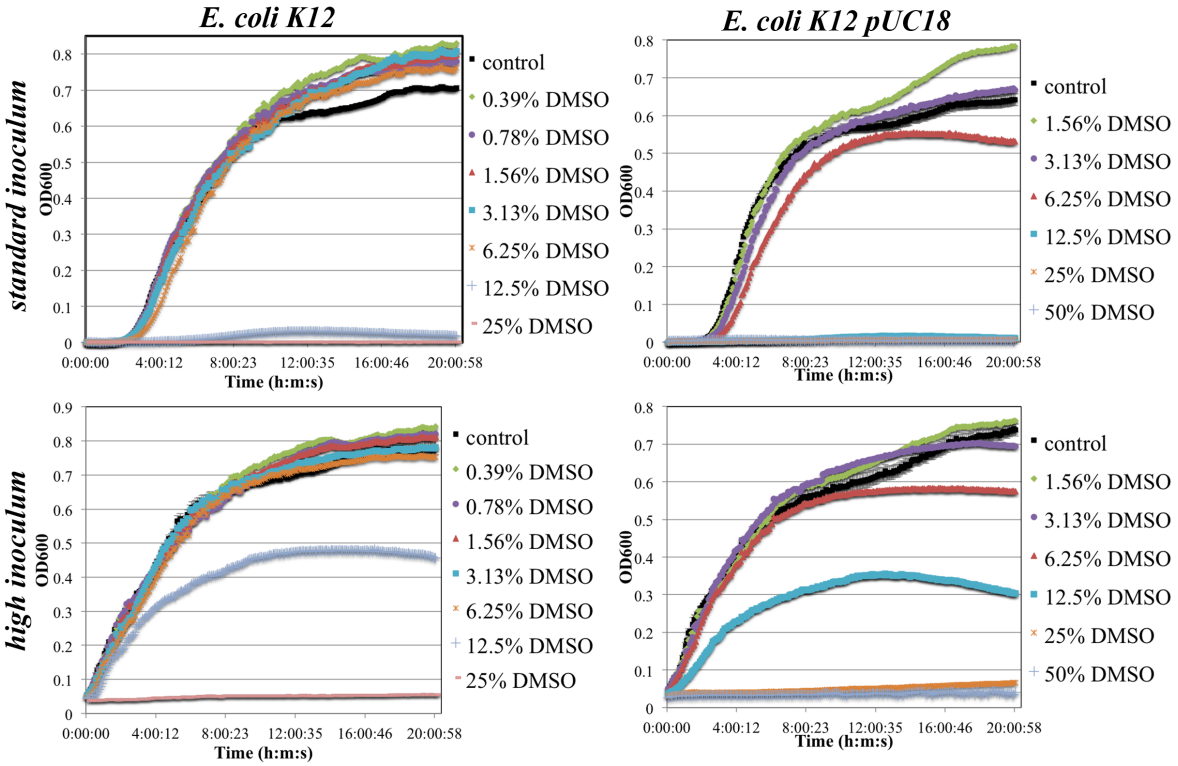

Figure 4.55. Growth curves of *E. coli* K12 (left) and *E. coli* K12 pUC18 (right) cultures for 20 hours of incubation. Bacteria at standard inoculum (top) and high inoculum (bottom) dose were treated with different DMSO concentrations.

Growth curves of each DMSO treated culture and control cultures are given in (Figure 4.55). Even though the MIC for DMSO was determined as 25% at high inoculation density and 12.5% at standard inoculation density of both *E. coli* strains, it was observed that 6.25% DMSO or higher concentrations also inhibit the growth of *E. coli* K12 pUC18 cells effectively (Figure 4.55). At 3.13% or lower DMSO concentrations, cell growth profile was similar to that of the control samples. A similar observation was made for wild-type *E. coli* K12 cells. 12.5% DMSO or higher concentrations also inhibit the growth of *E. coli* K12 cells effectively, and at 6.25% or lower

DMSO concentrations, cell growth profile was similar to that of the control samples (Figure 4.55). The results suggest that wild-type *E. coli* K12 cells can tolerate higher DMSO concentrations when compared to the antibiotic resistant *E. coli* K12 pUC18 cells.

4.3.2. Effect of Melittin on Bacterial Growth

The initial experiments with melittin were carried out with antibiotic resistant *E. coli* K12 pUC18 cells. In order to determine the minimal inhibitory concentration of melittin on *E. coli* K12 pUC18 cells at high inoculation cell density, 100 μL of cell culture (at OD_{600} = 0.2) was added to each well containing different concentrations of melittin (or melittin free) solutions, and the plate (Figure 4.56) was placed in the microplate reader for incubation of 20 hours at 37 °C and 180 rpm orbital shaking.

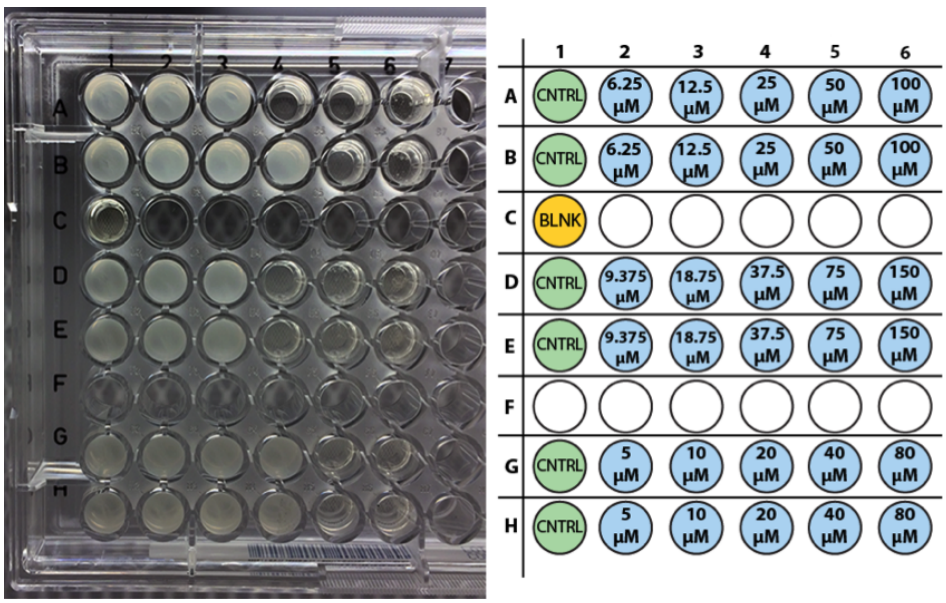

Figure 4.56. The photograph of the plate after incubation of 20 hours (left) and the plate setup used in the experiment (right).

After 20 hours of incubation, there was no visible growth (Figure 4.56) in any wells in columns 5 and 6, in wells D4, E4 (at 37.5 μM melittin concentration) and A4 (which is one replicate of two samples treated with 25 μM of melittin). Assuming there were not any experimental errors, 25 μM concentration is the determined MIC

for melittin on *E. coli* K12 pUC18 cells. The OD_{600} of each sample was monitored for 20 hours (Figure 4.57).

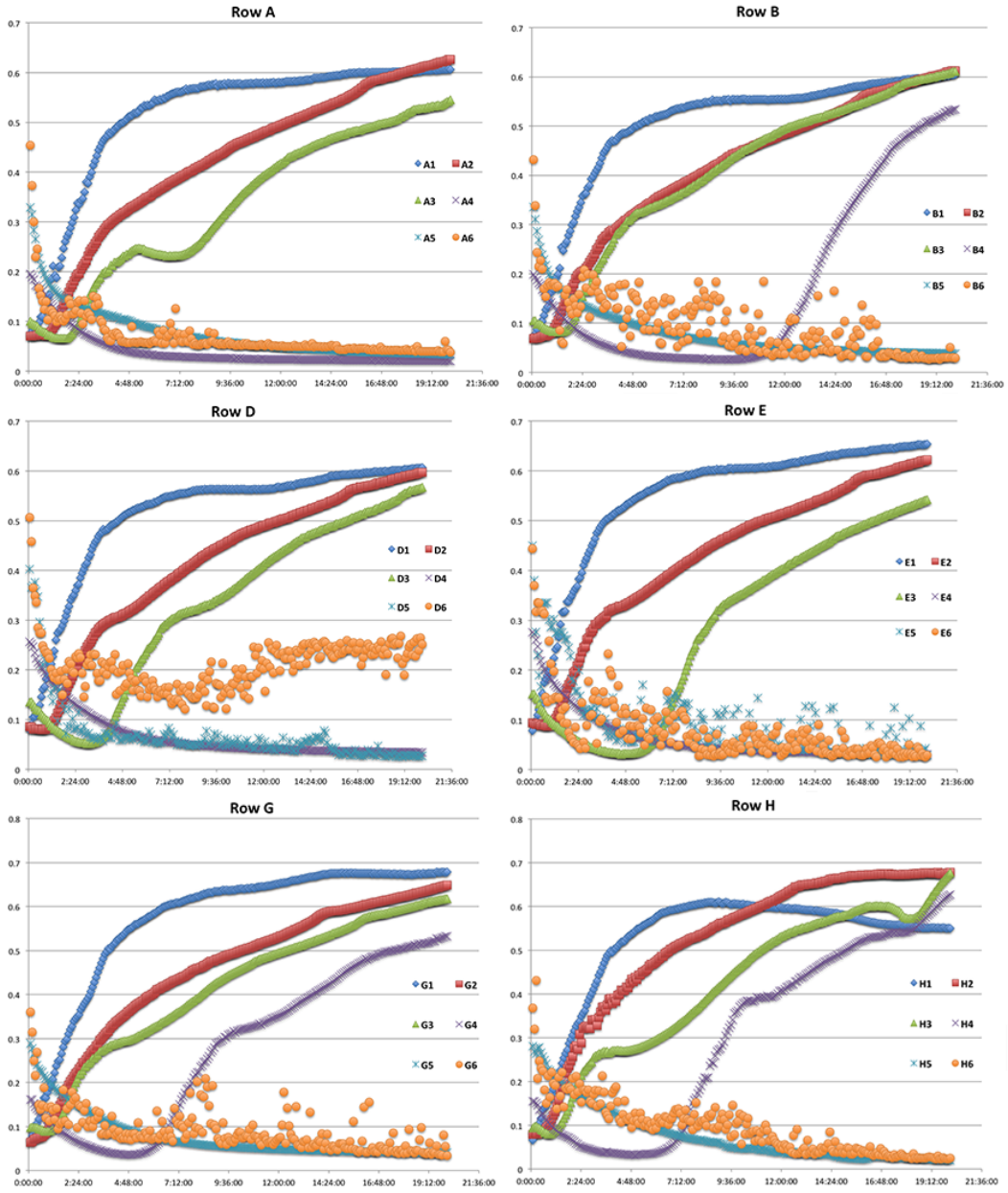

Figure 4.57. Absorbance measurement (at 600 nm) of all samples for each row (rows A-H) of the microplate.

The initial OD_{600} values for the samples with higher melittin concentration are higher compared to the control sets or the samples with lower melittin concentration, showing that melittin already increases the OD of the sample itself. The control sets

(wells A1, B1, D1, E1, G1 and H1) have an increasing OD trend from the start of the experiment until they reach the stationary phase (around 7-8 hours). On the other hand, in the cultures treated with sub MIC concentrations of melittin (wells A2-3, B2-3, D2-3, E2-3, G2-4, H2-4), the OD_{600} decreases to some extent (for 2-7 hours), but then they start increasing logarithmically and converge to the control OD curves. At MIC or supra MIC concentrations (wells A4-6, B5-6, D4-6, E4-6, G5-6, H5-6), the OD_{600} values start decreasing immediately and at around 6-7 hours they converge to their minimum value and these OD_{600} values are conserved until the end of the experiment.

Another independent experiment with different melittin concentrations (Figure 4.58) was carried out using the same experimental procedure and samples from the microplate were used to determine the number of CFUs after melittin treatment. After 20 hours of incubation time, there was no visible growth in columns 3 and 4 (Figure 4.58). The MIC for melittin on *E. coli* K12 pUC18 cells at high inoculation cell density was again determined as 25 μM.

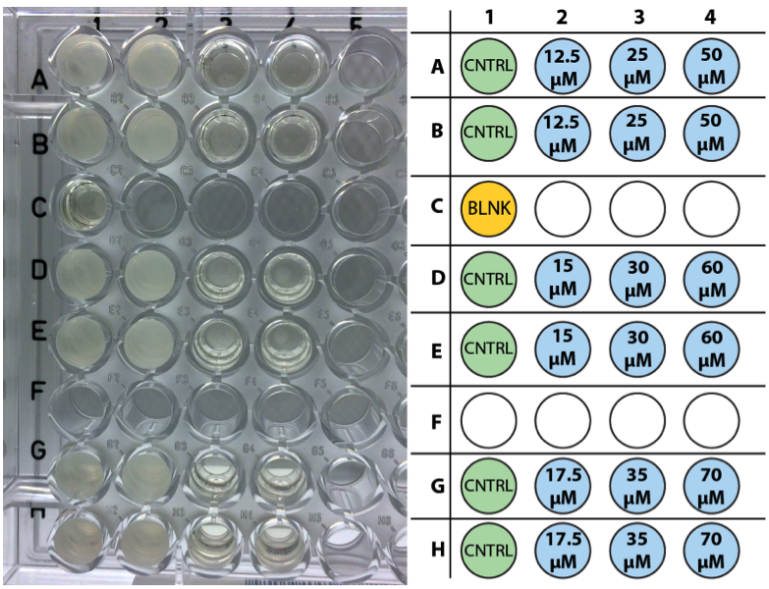

Figure 4.58. The photograph of the plate after incubation of 20 hours (left) and the plate setup used in the experiment (right).

The OD_{600} of each sample was monitored for 20 hours (Figure 4.59). The initial OD_{600} values for the samples with higher melittin concentration are higher compared

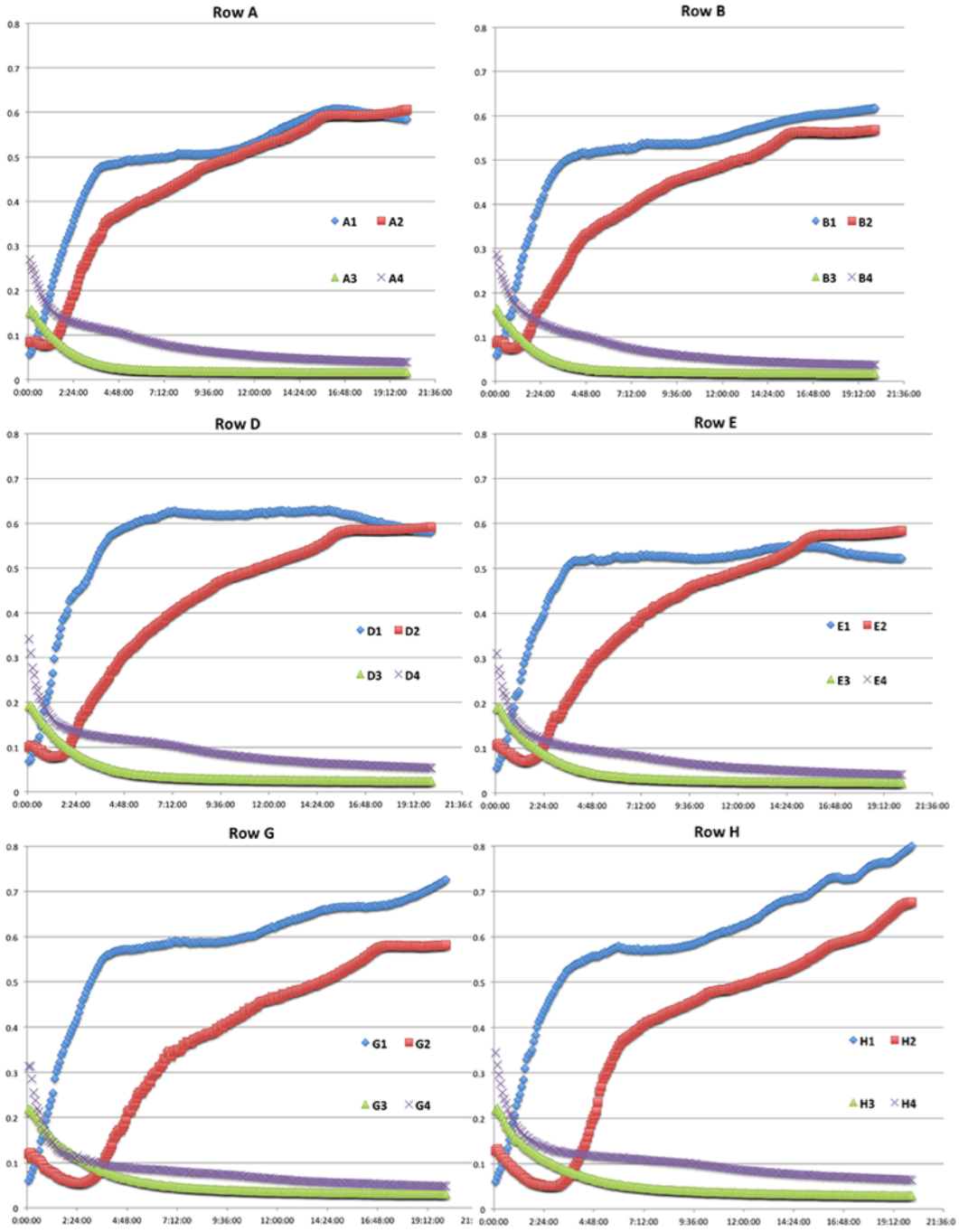

Figure 4.59. Absorbance measurement (at 600 nm) of all samples for each row (rows A-H) of the microplate.

to the control sets or the samples with lower melittin concentration, showing that melittin already increases the OD of the sample itself. The control sets (wells A1, B1, D1, E1, G1 and H1) have an increasing OD trend from the start of the experiment

until they reach the stationary phase (around 4-6 hours). On the other hand, in the cultures treated with sub MIC concentrations of melittin (wells in column 2), the OD_{600} decreases to some extent (for 2-3 hours), but then they start increasing logarithmically and converge to the control OD curves. At MIC or supra-MIC concentrations (wells columns 3 and 4), the OD_{600} values start decreasing immediately and at around 8-9 hours they converge to their minimum value and these OD_{600} values are conserved until the end of the experiment.

In order to determine the MIC of melittin at lower inoculum doses, different melittin concentration were added to the wells inoculated with the 1:10 dilution of the culture at $OD_{600} = 0.2$ and to the wells inoculated with the 1:100 dilution of the culture at $OD_{600} = 0.2$. After incubation at 37 °C and 180 rpm for 20 hours, no visible growth was observed in the samples treated with melittin concentration of 12.5 μM or higher. The growth curves (OD_{600} vs. time) for 20 hours of incubation for each melittin concentration is given in Figure 4.60. For simplicity, the control curves are plotted as the average of each set with the standard error of the mean.

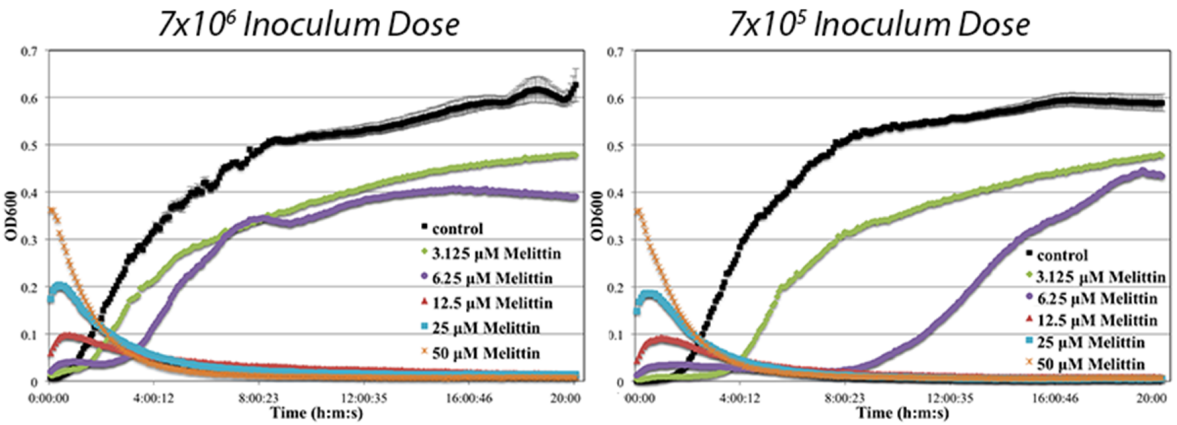

Figure 4.60. Growth curve of *E. coli* K12 pUC18 cultures treated with different melittin concentrations for 20 hours. Control curves are the average of each set and plotted with the standard error of the mean.

In order to determine and compare the effect of the antimicrobial peptide melittin on both wild-type *E. coli* K12 and antibiotic resistant *E. coli* K12 pUC18 cells, cultures at standard and high inoculation cell density were treated with different melittin

concentrations in the 1.56 μM - 100 μM range. For these experiments, a new melittin stock solution was prepared, therefore previous MIC determination experiments with melittin and *E. coli* K12 pUC18 cells had to be repeated. Since melittin stock solution was prepared in water, control samples were treated with water as well, for comparison.

After 20 hours of incubation of the melittin treated and control cultures, visible growth was observed in control cultures at both standard and high inoculation density of *E. coli* K12 and *E. coli* K12 pUC18 cells. At standard inoculation cell density, visible growth was not observed in the *E. coli* K12 cultures treated with 3.125 μM or higher concentrations of melittin, and visible growth was not observed in the *E. coli* K12 pUC18 cultures treated with 6.25 μM or higher melittin concentrations. At high inoculation density of both *E. coli* K12 and *E. coli* K12 pUC18 cells, visible growth was not observed in the cultures treated 50 μM or higher melittin concentrations. The determined MIC value for *E. coli* K12 pUC18 at high inoculum was different than the MIC value (25 μM) determined with the first melittin stock. Since two melittin stock solutions were prepared from two different delivered melittin powders with different purity values, melittin solutions were not identical to each other. These two different melittin stock solutions caused a discrepancy in the antimicrobial action and the determined MIC values of melittin.

Growth curves of each melittin treated culture and control cultures are given in (Figure 4.61). Even though the MIC for melittin was determined as 50 μM at high inoculation density of both *E. coli* strains and 3.125 μM and 6.25 μM at standard inoculation density of *E. coli* K12 and *E. coli* K12 pUC18 cells, respectively, it was observed that all of the tested concentrations inhibit the growth of cells, effective immediately with the addition of melittin (Figure 4.61). The results suggest that the antimicrobial action of melittin is similar for wild-type *E. coli* K12 and antibiotic resistant *E. coli* K12 pUC18 cells at their high inoculation cell density. At standard inoculation density, *E. coli* K12 pUC18 cells can tolerate 2-folds higher melittin concentration when compared to that of *E. coli* K12 cells. Moreover, the absorbance measurements showed that 6.25 μM and higher melittin concentrations increase the initial absorbance values significantly when compared to the control samples (Figure 4.61).

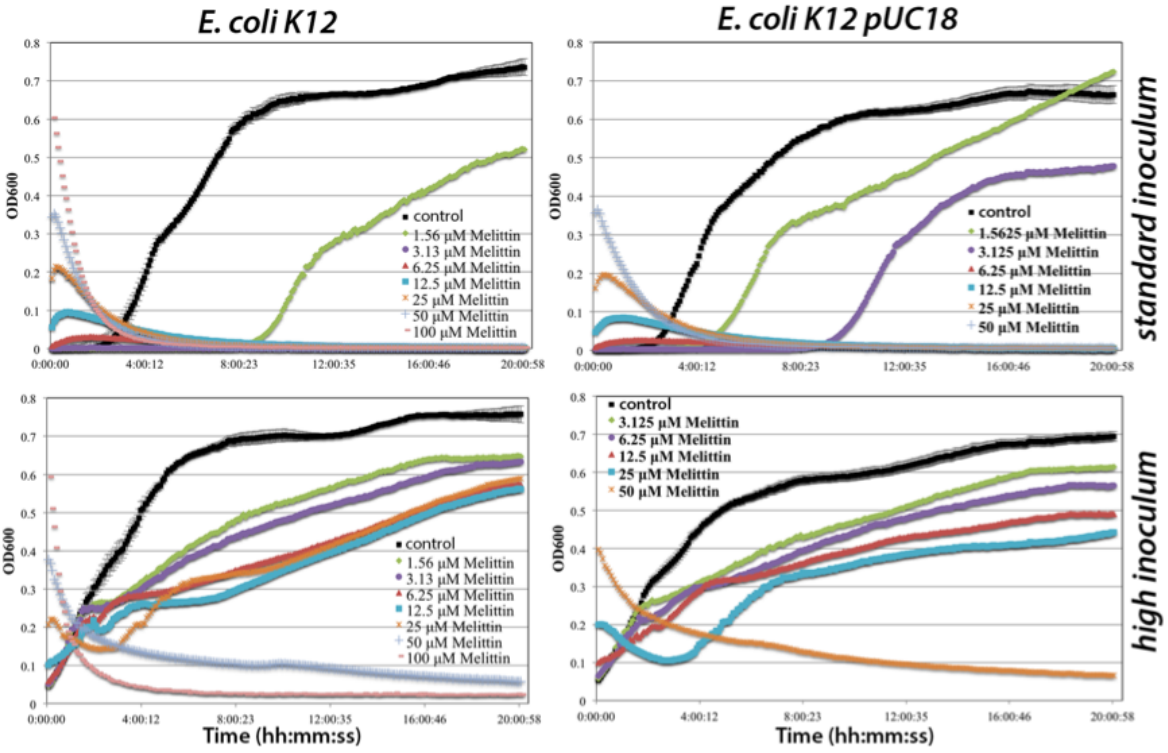

Figure 4.61. Growth curves of *E. coli* K12 (left) and *E. coli* K12 pUC18 (right) cultures for 20 hours of incubation. Bacteria at standard inoculum (top) and high inoculum (bottom) dose were treated with different melittin concentrations.

The samples from the cultures at high inoculation cell density that were incubated with sub-MIC (MIC/2) and MIC of melittin for 2 hours were used for measurement of CFUs. The control samples of both *E. coli* K12 and *E. coli* K12 pUC18 cultures had CFU counts on the order of 10^8 to 10^9 (Figure 4.62). When the cells were incubated with sub-MIC (25 μM) of melittin for 2 hours, the number of CFUs decreased around 35-folds and 300-folds for *E. coli* K12 pUC18 and *E. coli* K12 cells, respectively (Figure 4.62). The number of CFUs in the cultures treated with MIC (50 μM) of melittin could not be detected at the lowest possible dilution (10^1), indicating that the number of CFUs in both cultures was in the 0-10 range (Figure 4.62).

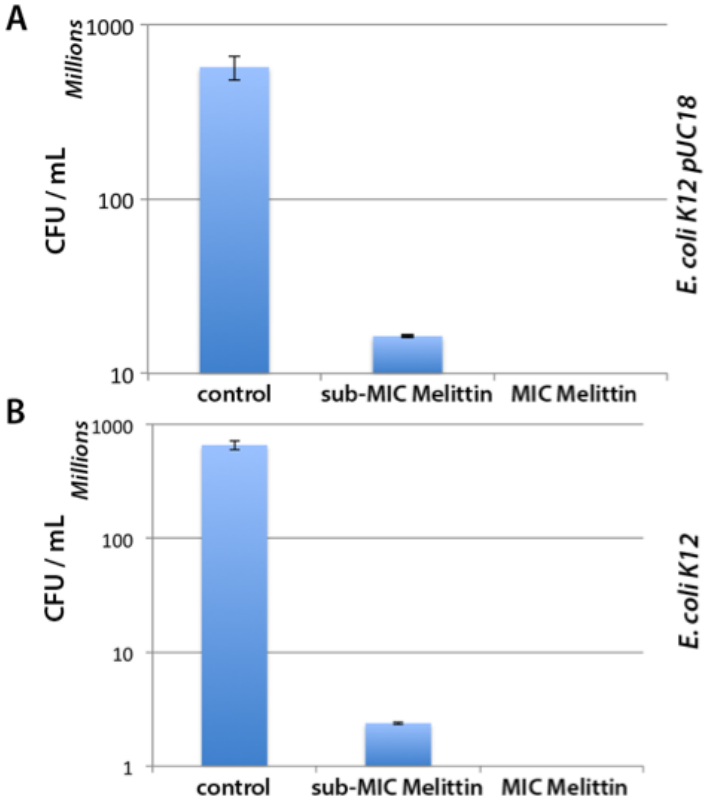

Figure 4.62. Number of colony forming units (A) in antibiotic resistant *E. coli* K12 pUC18 and (B) in wild-type *E. coli* K12 cultures after 2 hours of incubation with sub-MIC and MIC of melittin compared with the control samples.

4.3.3. Effect of Ampicillin on Bacterial Growth

In order to determine the effect of the beta-lactam antibiotic ampicillin on wild-type *E. coli* K12 and antibiotic resistant *E. coli* K12 pUC18 cells, cultures at standard and high inoculation cell density were treated with different ampicillin concentrations in the 0.191 - 12.2 μg/mL range for *E. coli* K12 cells, and in the 1.56 - 200 mg/mL range for *E. coli* K12 pUC18 cells. Since ampicillin stock solution was prepared in water, control samples were treated with water as well, for comparison.

After 20 hours of incubation of the ampicillin treated and control cultures, visible growth was observed in control cultures at both standard and high inoculation density of *E. coli* K12 and *E. coli* K12 pUC18 cells. At standard inoculation cell density,

visible growth was not observed in the *E. coli* K12 cultures treated with 3.05 μg/mL or higher concentrations of ampicillin, and visible growth was not observed in the *E. coli* K12 pUC18 cultures treated with 12.5 mg/mL or higher ampicillin concentrations. At high inoculation density, visible growth was not observed in the *E. coli* K12 cultures treated with 6.1 μg/mL or higher concentrations, and visible growth was not observed in the *E. coli* K12 pUC18 cultures treated with 200 mg/mL ampicillin, which was the highest concentration tested.

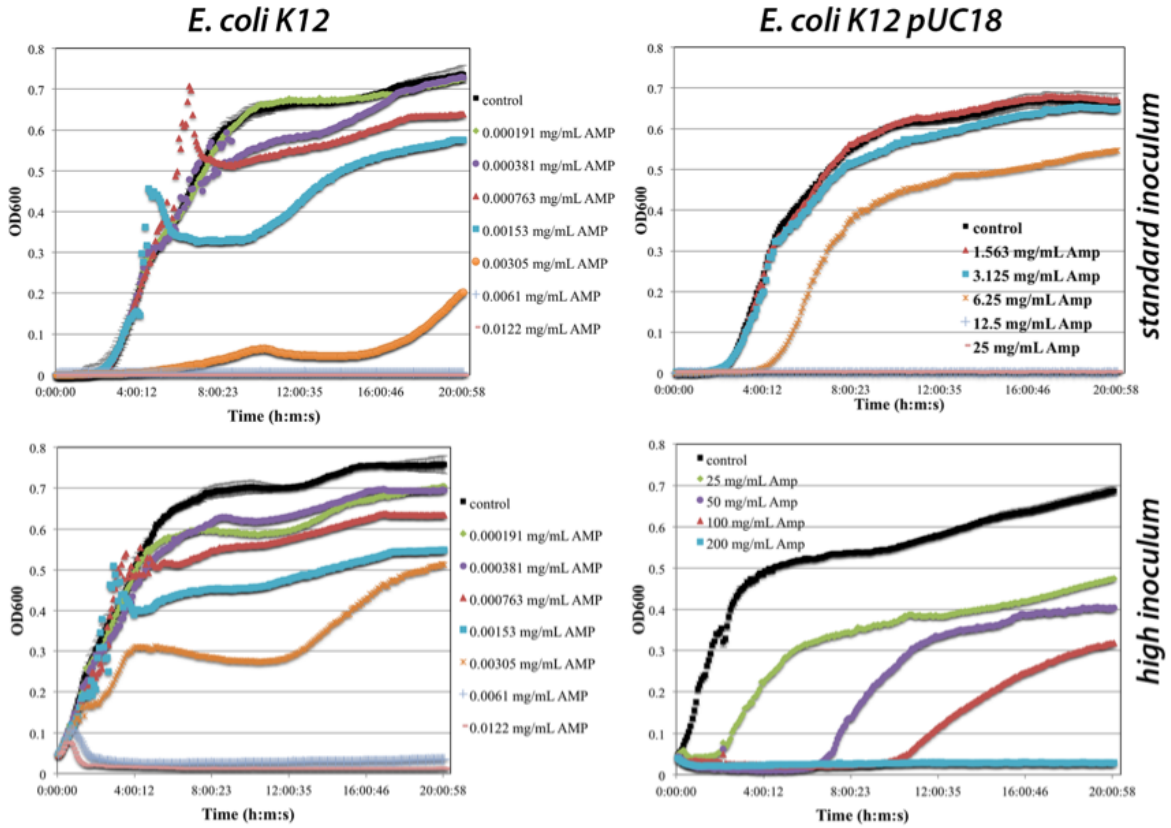

Figure 4.63. Growth curves of *E. coli* K12 (left) and *E. coli* K12 pUC18 (right) cultures for 20 hours of incubation. Bacteria at standard inoculum (top) and high inoculum (bottom) dose were treated with different ampicillin concentrations.

Growth curves of each ampicillin treated culture and control cultures are given in (Figure 4.63). The results suggest that at high inoculation cell density antibiotic resistant *E. coli* K12 pUC18 cells can tolerate up to 200 mg/mL ampicillin, which is over 32,000-folds when compared to the ampicillin concentration that *E. coli* K12 cells could tolerate. Similarly, at standard inoculation cell density, *E. coli* K12 pUC18 cells

are resistant to ampicillin at 12.5 mg/mL, which is over 4000-folds when compared to the ampicillin concentration that *E. coli* K12 cells could tolerate.

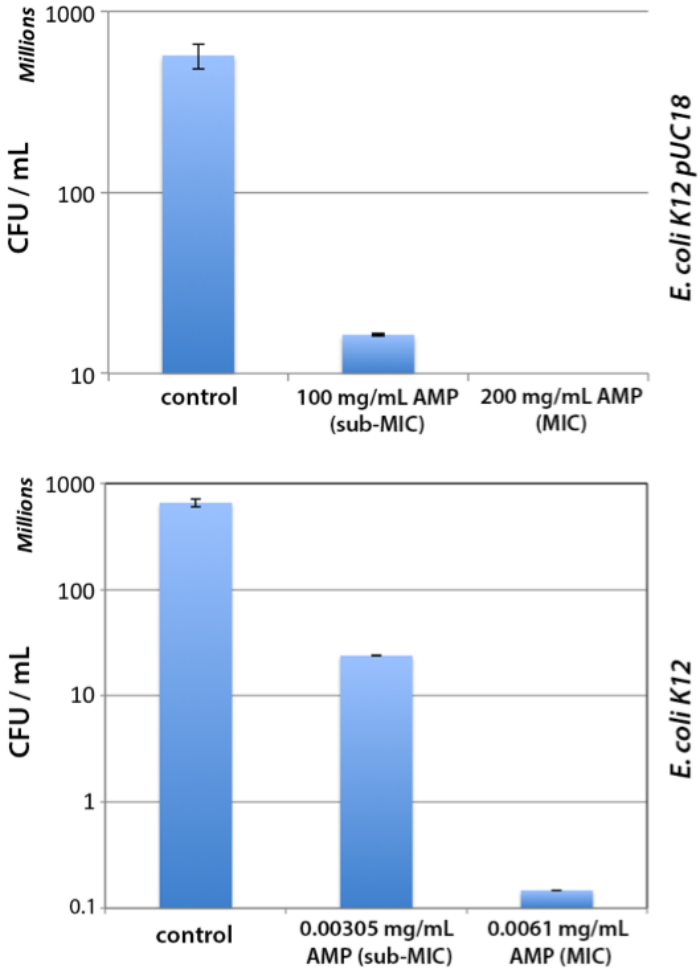

Figure 4.64. Number of colony forming units (top) in antibiotic resistant *E. coli* K12 pUC18 and (bottom) in wild-type *E. coli* K12 cultures after 2 hours of incubation with sub-MIC and MIC of ampicillin compared with the control samples.

For CFU measurements, culture samples at high inoculation cell density were incubated with sub-MIC (MIC/2) and MIC of ampicillin for 2 hours. The control samples of both *E. coli* K12 and *E. coli* K12 pUC18 cultures had CFU counts on the order of 10^8 to 10^9 (Figure 4.64). When *E. coli* K12 pUC18 cells were incubated with sub-MIC (100 mg/mL) of ampicillin for 2 hours, the number of CFUs decreased around 200-folds when compared to the control samples. When *E. coli* K12 pUC18 cells were incubated with MIC (200 mg/mL) of ampicillin for 2 hours, the number of CFUs could

not be detected at the lowest possible dilution (10^1), indicating that the number of CFUs was in the 0-10 range (Figure 4.64). When *E. coli* K12 cells were incubated with sub-MIC (3.05 μg/mL) of ampicillin for 2 hours, the number of CFUs decreased around 30-folds when compared to the control samples (Figure 4.64). Similarly, when *E. coli* K12 cells were treated with MIC (6.1 μg/mL) of ampicillin for 2 hours, the number of CFUs decreased around 4500-folds when compared to the control samples (Figure 4.64).

4.3.4. Effect of Potassium Clavulanate on Bacterial Growth

In order to determine the effect of the beta-lactamase inhibitor potassium clavulanate (PC) on wild-type *E. coli* K12 and antibiotic resistant *E. coli* K12 pUC18 cells, cultures at standard and high inoculation cell density were treated with different potassium clavulanate (PC) concentrations in the 7.81 μM - 500 μM range. Since potassium clavulanate (PC) stock solution was prepared in water, control samples were treated with water as well, for comparison.

After 20 hours of incubation of the PC treated and control cultures, visible growth was observed in control cultures at both standard and high inoculation density of *E. coli* K12 and *E. coli* K12 pUC18 cells. At standard inoculation cell density, visible growth was not observed in the *E. coli* K12 cultures treated with 125 μM or higher concentrations of PC, and visible growth was not observed in the *E. coli* K12 pUC18 cultures treated with 31.25 μM or higher PC concentrations. At high inoculation density of both *E. coli* K12 and *E. coli* K12 pUC18 cells, visible growth was not observed in the cultures treated with 250 μM or higher PC concentrations.

Growth curves of each PC treated culture and control cultures are given in (Figure 4.65). Even though the MIC for PC was determined as 250 μM at high inoculation density of both *E. coli* strains and 31.25 μM and 125 μM at standard inoculation density of *E. coli* K12 pUC18 and *E. coli* K12 cells, respectively, it was observed that all of the tested concentrations inhibit the growth of cells, effective immediately with the addition of PC (Figure 4.65). The results suggest that the antimicrobial action of

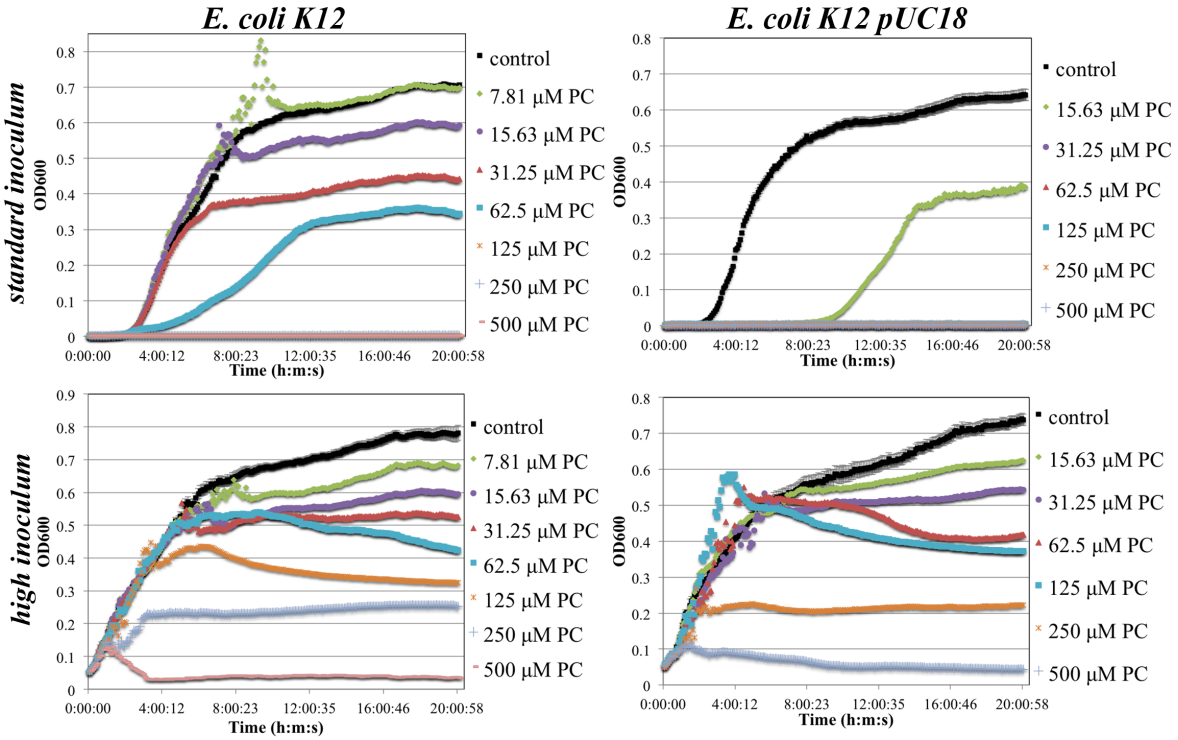

Figure 4.65. Growth curves of *E. coli* K12 (left) and *E. coli* K12 pUC18 (right) cultures for 20 hours of incubation. Bacteria at standard inoculum (top) and high inoculum (bottom) dose were treated with different PC concentrations.

PC is similar for wild-type *E. coli* K12 and antibiotic resistant *E. coli* K12 pUC18 cells at their high inoculation cell density. At standard inoculation density, *E. coli* K12 cells can tolerate 4-folds higher PC concentration when compared to that of *E. coli* K12 pUC18 cells (Figure 4.65).

For CFU measurements, culture samples at high inoculation cell density were incubated with sub-MIC (MIC/2) and MIC of PC for 2 hours. The control samples of both *E. coli* K12 and *E. coli* K12 pUC18 cultures had CFU counts on the order of 10^8 to 10^9 (Figure 4.66). When *E. coli* K12 pUC18 cells or *E. coli* K12 cells were incubated with sub-MIC (125 μM) of PC for 2 hours, the decrease in the number of CFUs was around 2-folds when compared to the control samples (Figure 4.66). Similarly, when the cultures were incubated with MIC (250 μM) of PC for 2 hours, the decrease in the number of CFUs was around 5-folds when compared to the control samples.

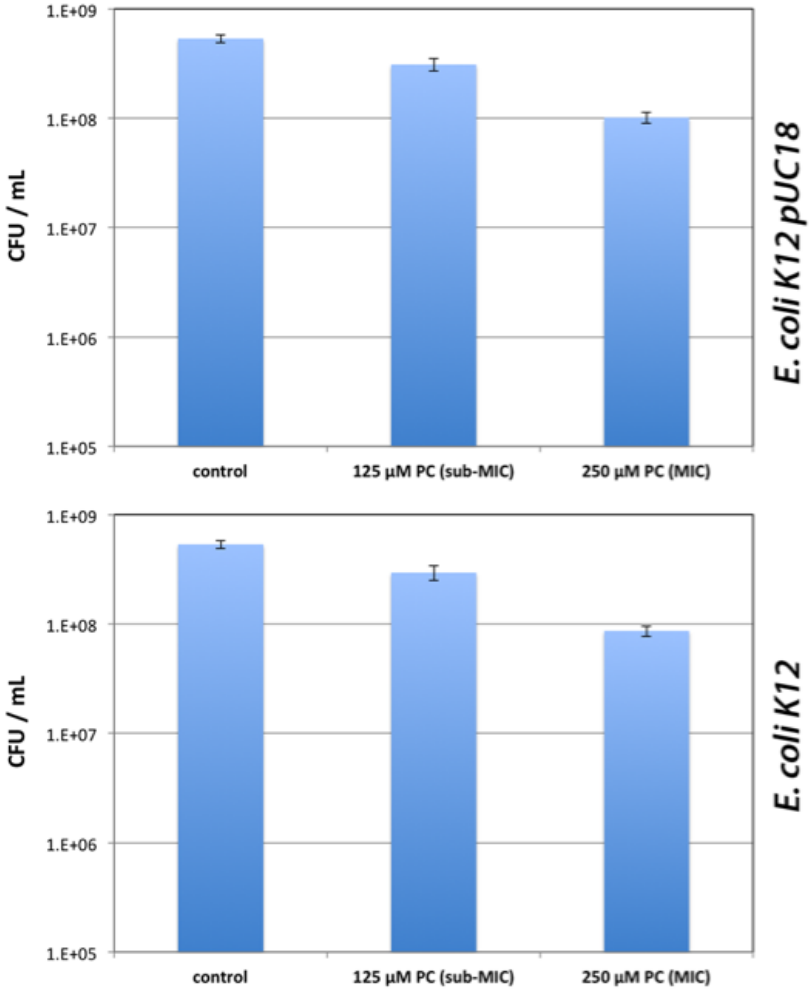

Figure 4.66. Number of colony forming units (top) in antibiotic resistant *E. coli* K12 pUC18 and (bottom) in wild-type *E. coli* K12 cultures after 2 hours of incubation with sub-MIC and MIC of (PC) compared with the control samples.

Even though PC is a beta-lactamase inhibitor, the results suggest that the antimicrobial action of PC is not specific to the beta-lactamase expressing *E. coli* K12 pUC18 cells. In terms of the determined MIC values and measured CFU counts of the treated cultures, the antimicrobial action of PC was similar for both *E. coli* K12 pUC18 and *E. coli* K12 cells, suggesting that the antimicrobial action may not be directly related to the beta-lactamase inhibition, but may be related to some other mechanism as well.

4.3.5. Effect of pVEC and del5 pVEC Peptides on Bacterial Growth

In order to determine the effect of the cell-penetrating peptide pVEC (from VE-cadherin protein) and del5 pVEC on wild-type *E. coli* K12 cells, cultures at standard and high inoculation cell density were treated with different pVEC and del5 pVEC concentrations in the 7.813 μM - 250 μM range. Since pVEC and del5 pVEC stock solutions were prepared in DMSO-water mixture, control samples were treated with the same concentration of this mixture, for comparison.

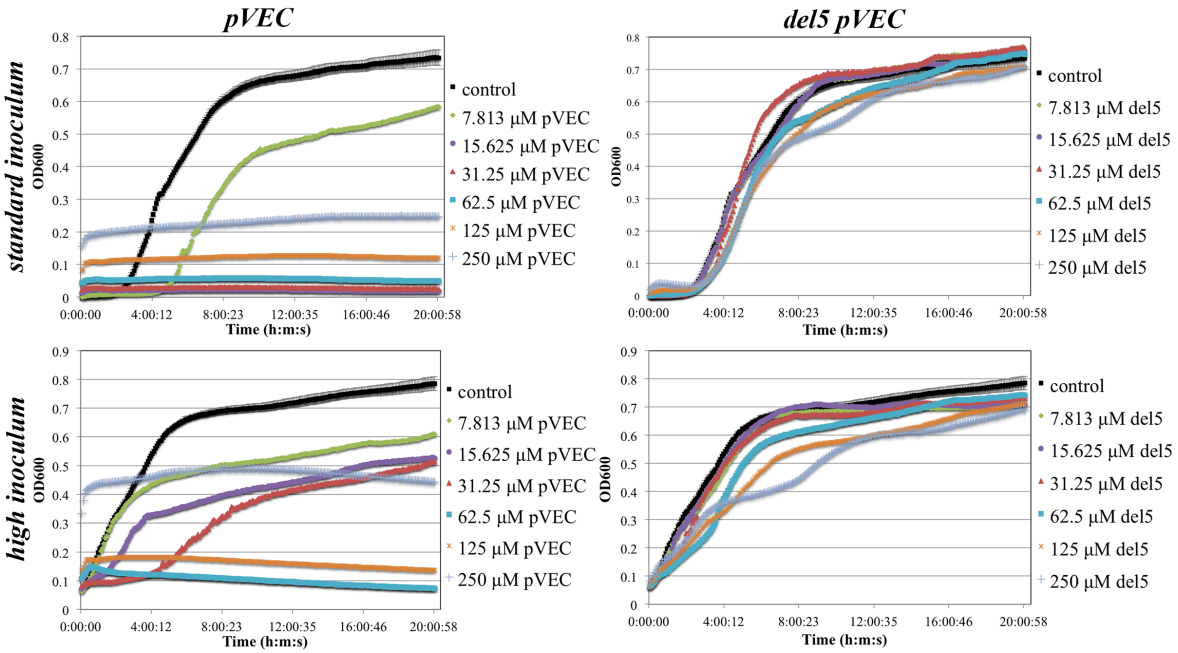

Figure 4.67. Growth curves of *E. coli* K12 (left) and *E. coli* K12 pUC18 (right) cultures for 20 hours of incubation. Bacteria at standard inoculum (top) and high inoculum (bottom) dose were treated with different peptide concentrations.

After 20 hours of incubation, visible growth was observed in control cultures and del5 pVEC treated cultures at both standard and high inoculation density of *E. coli* K12 cells (Figure 4.67). Visible growth was not observed in the cultures treated with 15.625 μM or higher concentrations of pVEC, and visible growth was not observed in the cultures treated with 62.5 μM or higher concentrations of pVEC, at standard and high inoculation cell densities, respectively. Even though 125 and 250 μM del5 pVEC concentrations had inhibitory effect on the growth curve of the cells, the MIC value

could not be detected at the highest concentration (250 μM) tested.

The experiment was repeated to test different peptide concentration ranges. *E. coli* K12 cultures at standard and high inoculation cell density were treated with pVEC peptide in the 6.25 μM - 100 μM concentration range, and treated with del5 pVEC peptide in the 31.25 μM - 500 μM range concentration range. After 20 hours of incubation, visible growth was observed in control cultures and del5 pVEC treated cultures at both standard and high inoculation density of *E. coli* K12 cells (Figure 4.68). Visible growth was not observed in the cultures treated with 12.5 μM or higher concentrations of pVEC, and visible growth was not observed in the cultures treated with 100 μM or higher concentrations of pVEC, at standard and high inoculation cell densities, respectively. Even though the tested del5 pVEC concentrations had inhibitory effect on the growth curve of the cells, the MIC value could not be detected at the highest concentration (500 μM) tested.

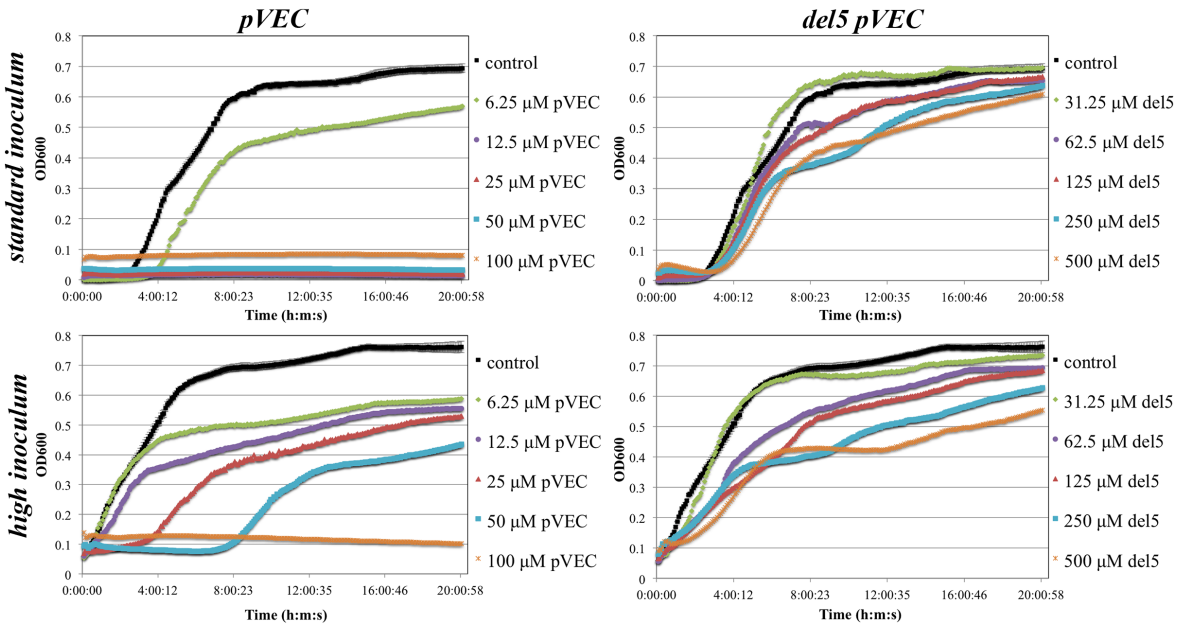

Figure 4.68. Growth curves of *E. coli* K12 (left) and *E. coli* K12 pUC18 (right) cultures for 20 hours of incubation. Bacteria at standard inoculum (top) and high inoculum (bottom) dose were treated with different peptide concentrations.

For CFU measurements, culture samples at high inoculation cell density were incubated with sub-MIC (MIC/2) or MIC of pVEC, and 500 μM of del5 pVEC for 2 hours. The control samples had CFU counts on the order of 10^8 to 10^9 (Figure 4.69). When *E. coli* K12 cells were incubated with sub-MIC of pVEC for 2 hours, the decrease in the number of CFUs was around 10-folds when compared to the control samples (Figure 4.69). Similarly, when the cultures were incubated with MIC of pVEC for 2 hours, the number of CFUs decreased to 10^2 (Figure 4.69). When *E. coli* K12 cells were incubated with 500 μM of del5 pVEC for 2 hours, around 5-folds decrease was determined in the number of CFUs (Figure 4.69).

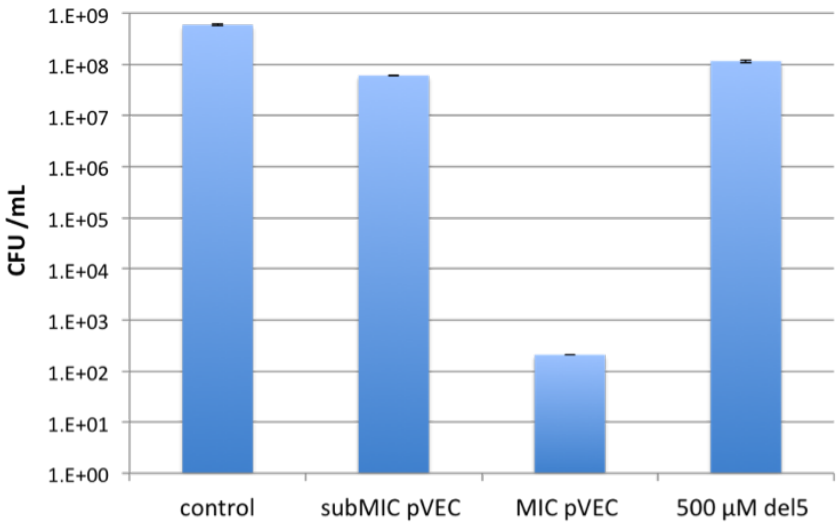

Figure 4.69. Number of colony forming units in wild-type *E. coli* K12 cultures after 2 hours of incubation with sub-MIC and MIC of pVEC, and 500 μM del5 pVEC compared with the control samples.

4.3.6. Effect of P1 and P2 Peptides on Bacterial Growth

The results given in this section can also be found in the paper published in the Journal of Peptide Science entitled 'A Novel Chimeric Peptide with Antimicrobial Activity' by Begum Alaybeyoglu, Berna Sariyar Akbulut and Elif Ozkirimli.

In order to determine the effect of the beta-lactamase inhibitory peptides P1 and P2 on wild-type *E. coli* K12 and antibiotic resistant *E. coli* K12 pUC18 cells, cultures

in early logarithmic growth phase (OD_{600} = 0.2) were treated with peptides P1 or P2 at a final concentration of 100 μM. All of the experiments were repeated three times and the average of duplicate plate counts at each time point for three repetitions of each experiment were plotted with standard error.

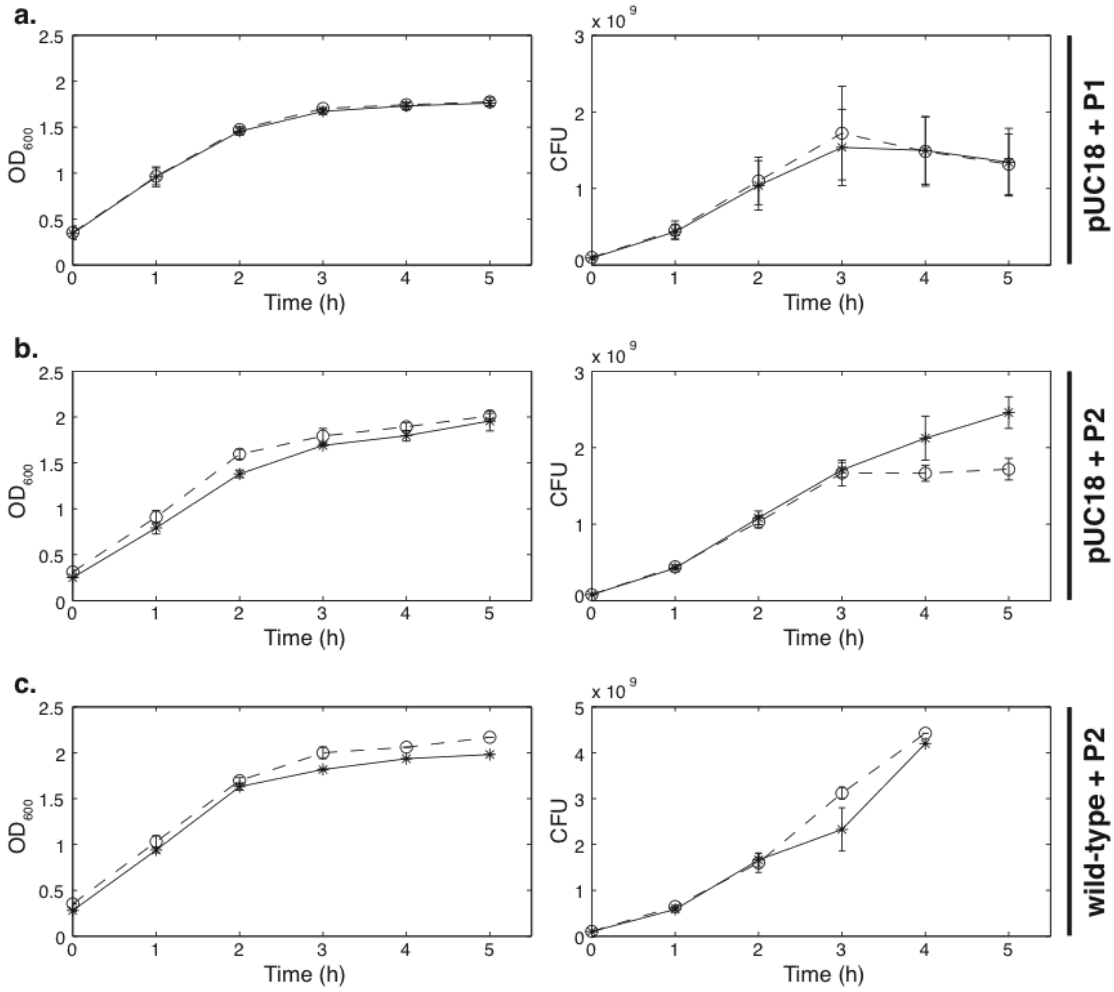

Figure 4.70. Growth profiles (left) and colony forming units (right) in the presence of 100 μM peptide (circles) or in the absence of peptide (stars) for *E. coli* K12 pUC18 or *E. coli* K12 cells treated with P1 or P2. 0 hour indicates the time of peptide addition.

Growth curves of P1 or P2 treated samples showed that incubation of P1 or P2 had no effect on the growth of cells (Figure 4.70). The growth curves of control sets of both peptides were similar (Figure 4.70), showing that the effect of DMSO and/or buffer is negligible. Incubation with P1 had no effect on the number of viable cells (Figure 4.70), either suggesting that P1 had no antimicrobial activity or it was unable

to disrupt or penetrate the cell wall to reach and inhibit beta-lactamase. Interestingly, the number of viable cells decreased by 30% upon incubation with P2. In order to ascertain that retardation in cell growth is due to uptake of the peptide and inhibition of intracellular beta-lactamase, wild type *E. coli* K12 cells with no beta-lactamase production were also treated with P2. If disruption of the cell wall/membrane is the reason for cell death, then these cells would die upon treatment with P2. On the other hand, if the antimicrobial action of P2 is due to inhibition of beta-lactamase, then these wild type cells would be unaffected. Consistent with the second hypothesis, P2 did not have any effect on wild-type *E. coli* K12 cells (Figure 4.70). These results showed that P2 acts as a beta-lactamase inhibitor while P1 has no effect on bacterial cells suggesting that addition of the N terminus hydrophobic tail facilitates delivery into the cell to access an intracellular enzyme.

4.3.7. Effect of P2r Peptide on Bacterial Growth

In order to determine the effect of the P2r peptide on antibiotic resistant *E. coli* K12 pUC18 cells at high inoculation density, 25, 50, 100, 200 and 400 μM peptide concentrations were tested. Since the 1 mM stock peptide solution contains 3.69% DMSO, control samples were prepared for each sample that was incubated with peptide with the same DMSO concentration (Figure 4.71).

The growth curves (OD_{600} vs. time) for 2, 4, and 20 hours of incubation for each well of the microplate are given in Figure 4.72. Samples from rows A-D were used to count CFUs at the 2nd and 4th hours of incubation, rows E and F were incubated either with or without the peptide for 20 hours at 37 °C.

Visible growth was observed in each well of the microplate (in rows E and F) after 20 hours of incubation, suggesting that the MIC value of this peptide is larger than 400 μM for *E. coli* K12 pUC18 cells. It was observed that the peptide inhibits the growth even at 25 μM concentration and higher peptide concentrations (100 μM or more) increases the initial OD_{600} values at the beginning of the experiment. The numbers of colony forming units (CFU) were counted for the samples that were withdrawn after 2

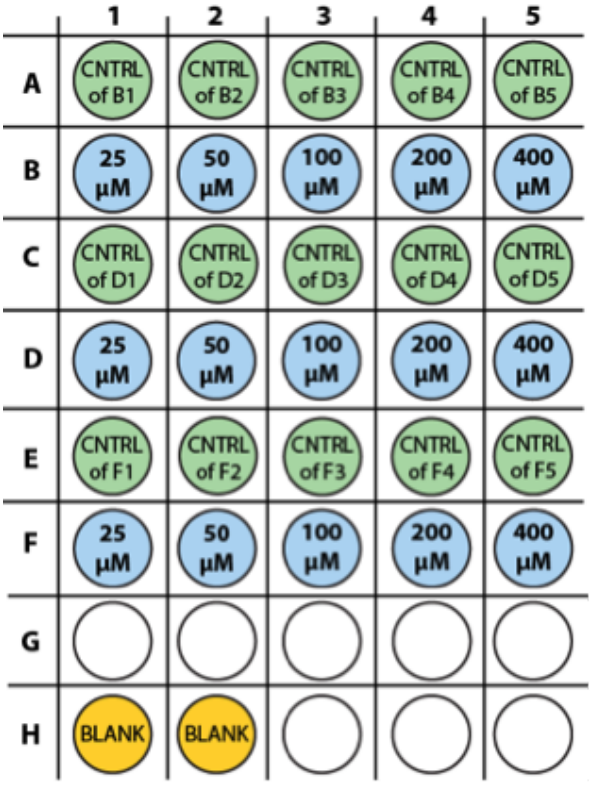

Figure 4.71. The microplate setup used in the experiment.

hours (from wells A3, A4, B3 and B4) or 4 hours (from wells C3, C4, D3 and D4) of incubation in the microplate (Figure 4.73).

The results show that the peptide inhibits the growth even at the lowest tested concentration (25 μM), which was effective immediately at the beginning of the experiment (Figure 4.72). Moreover, incubation of the cultures with 100 μM or 200 μM peptide caused a decrease in the CFU counts (Figure 4.73) around 10 times (1 log) or approximately 100 times (2 log) respectively, after incubation with the peptide for 2 hours. Similarly, after incubation of bacteria with 100 μM or 200 μM peptide, the CFU counts decreased to half or by approximately 100 times (2 log) respectively.

In order to determine the MIC of P2r peptide at lower inoculum doses of *E. coli* K12 pUC18 cells, different P2r peptide concentration were added to the wells inoculated with the 1:10 dilution of the culture at $OD_{600} = 0.2$, and to the wells inoculated with

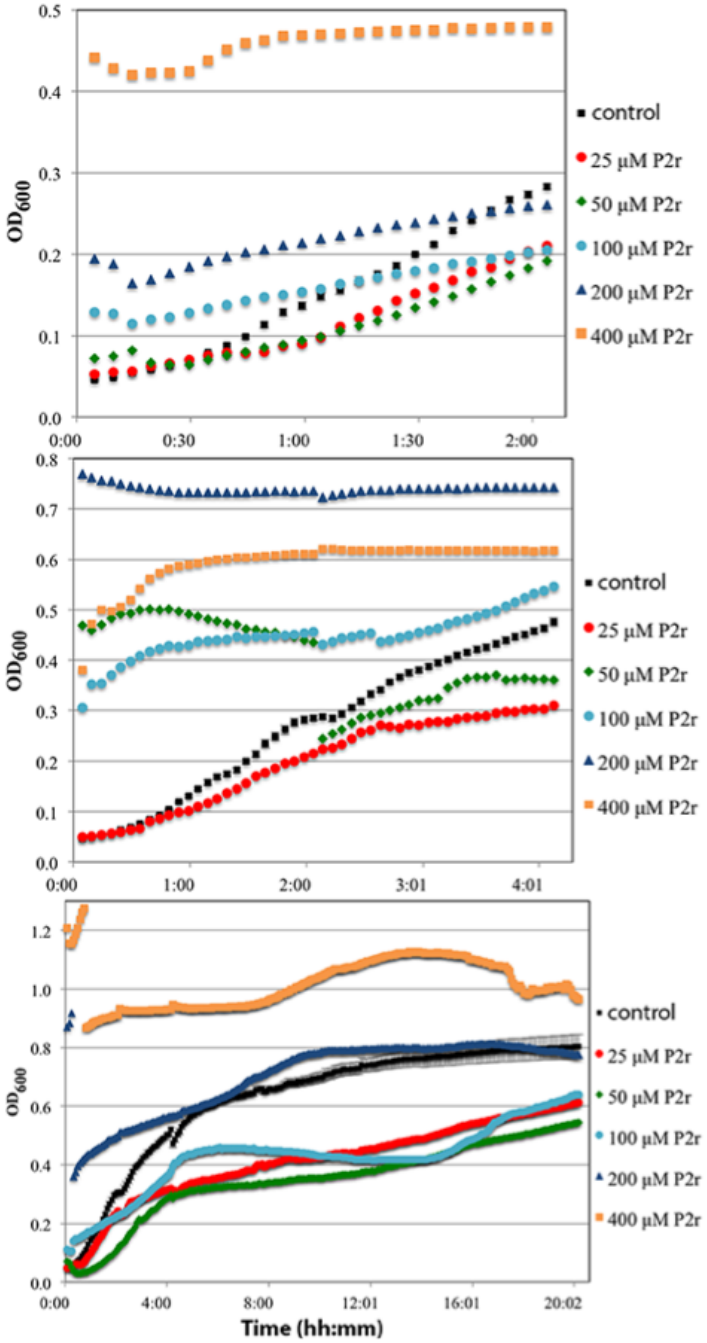

Figure 4.72. Growth curves of the P2r peptide treated cultures and control samples for the first 2 hours of incubation (top), for 4 hours of incubation (middle), and for 20 hours of incubation (bottom).

the 1:100 dilution of the culture at OD_{600} = 0.2. After incubation at 37 °C and 180 rpm for 20 hours, visible growth was observed in all samples treated with different concentrations of P2r, and MIC of P2r peptide could not be detected. The growth

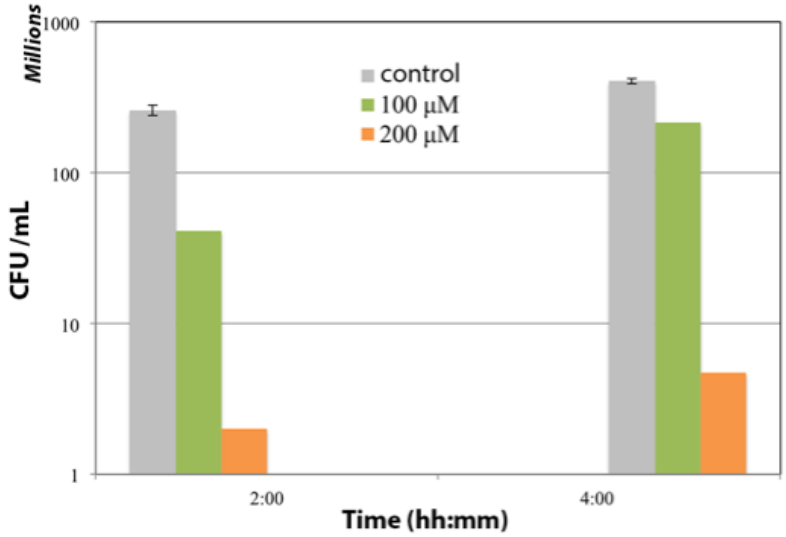

Figure 4.73. Comparison of CFU counts for the P2r treated and control samples in *E. coli* K12 pUC18 cultures after incubation for 2 or 4 hours. The average counts are shown for the control sample CFUs.

curves (OD_{600} vs. time) for 20 hours of incubation for each P2r treatment is given in Figure 4.74. For simplicity, the control curves are plotted as the average of each set with the standard error of the mean.

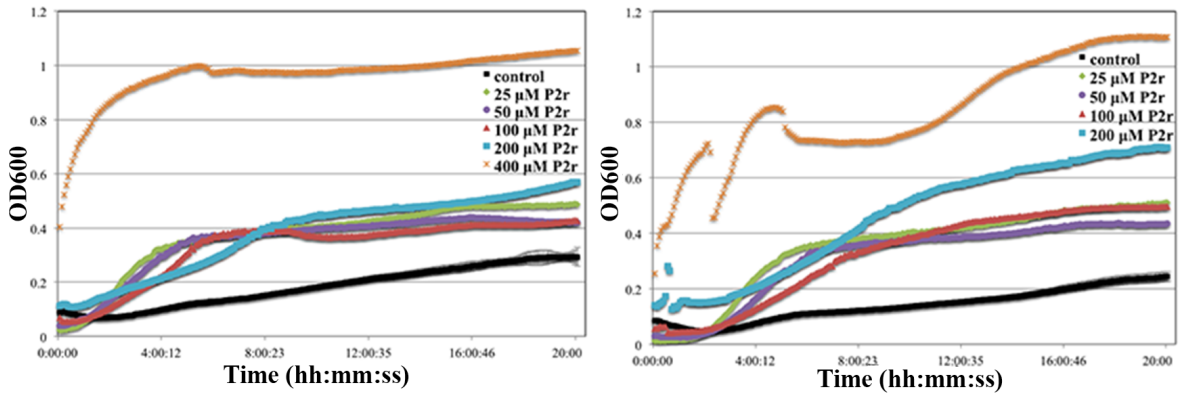

Figure 4.74. Growth curves of bacteria at $7x10^6$ CFU/mL cell density (left) and at $7x10^5$ CFU/mL cell density (right) treated with different P2r peptide concentrations.

In order to determine the effect of the P2r peptide on wild-type *E. coli* K12 cells, a similar experiment was carried out with 25, 50, 100, 200 and 400 μM peptide

concentrations with high inoculation density of *E. coli* K12 cells. Visible growth was observed in each well of the microplate after 20 hours of incubation, suggesting that the MIC value of this peptide is larger than 400 μM for *E. coli* K12 cells. 2-hour incubation of the cultures with 100 μM or 200 μM peptide caused a decrease in the CFU counts around 2-fold or approximately 4-fold respectively (Figure 4.75). Similarly, after 4-hour incubation of bacteria with 100 μM or 200 μM peptide, a 2-fold decrease in the CFU counts was observed (Figure 4.75).

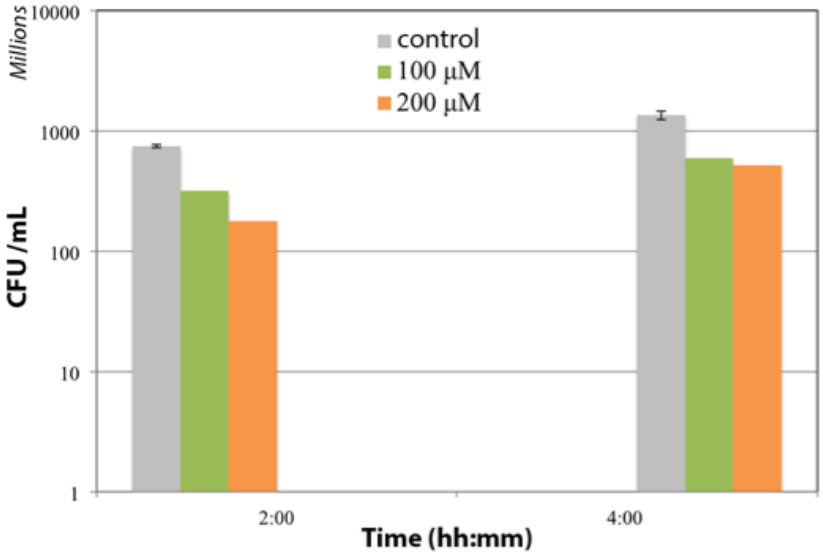

Figure 4.75. Comparison of CFU counts for the P2r treated and control samples in *E. coli* K12 cultures after incubation for 2 or 4 hours. The average counts are shown for the control sample CFUs.

When the effect of Pr2 peptide on antibiotic resistant *E. coli* K12 pUC18 and wild-type *E. coli* K12 cells was compared, it was observed that the peptide has a stronger antimicrobial effect on antibiotic resistant cells in the presence of ampicillin. On the other hand, the weak antimicrobial activity of P2r peptide on wild-type bacteria suggests that the antimicrobial action of this peptide is not directly or only related to the beta-lactamase inhibition. It is possible that the peptide or the LLIIL/LLIILRRR region alone has membrane disruptive activity, which may be contributing to this peptide's cellular uptake.

4.3.8. Effect of P3A Peptide on Bacterial Growth

In order to determine the effect of the P3A peptide on antibiotic resistant *E. coli* K12 pUC18 cells at high inoculation density, 25, 50, 100, 200 and 400 μM peptide concentrations were tested. Since the 1 mM stock peptide solution contains 2.303% DMSO, control samples were prepared for each sample that was incubated with peptide with the same DMSO concentration (Figure 4.76).



Figure 4.76. The microplate setup used in the experiment.

The growth curves (OD_{600} vs. time) for 2, 4 and 20 hours of incubation for each well of the microplate are given in Figure 4.77. The average curves for the control samples are shown with the standard error of the mean. It was observed that the peptide does not have any inhibitory effect on the growth of cells after incubation for 2 hours, 4 hours or even for 20 hours.

The number of colony forming units (CFUs) was counted for each sample that was withdrawn after 2 hours (wells A2, A4, B2, B3 and B4) or 4 hours (wells C2, C4, D2, D3 and D4) of incubation and plotted in Figure 4.78 with logarithmic scale. The

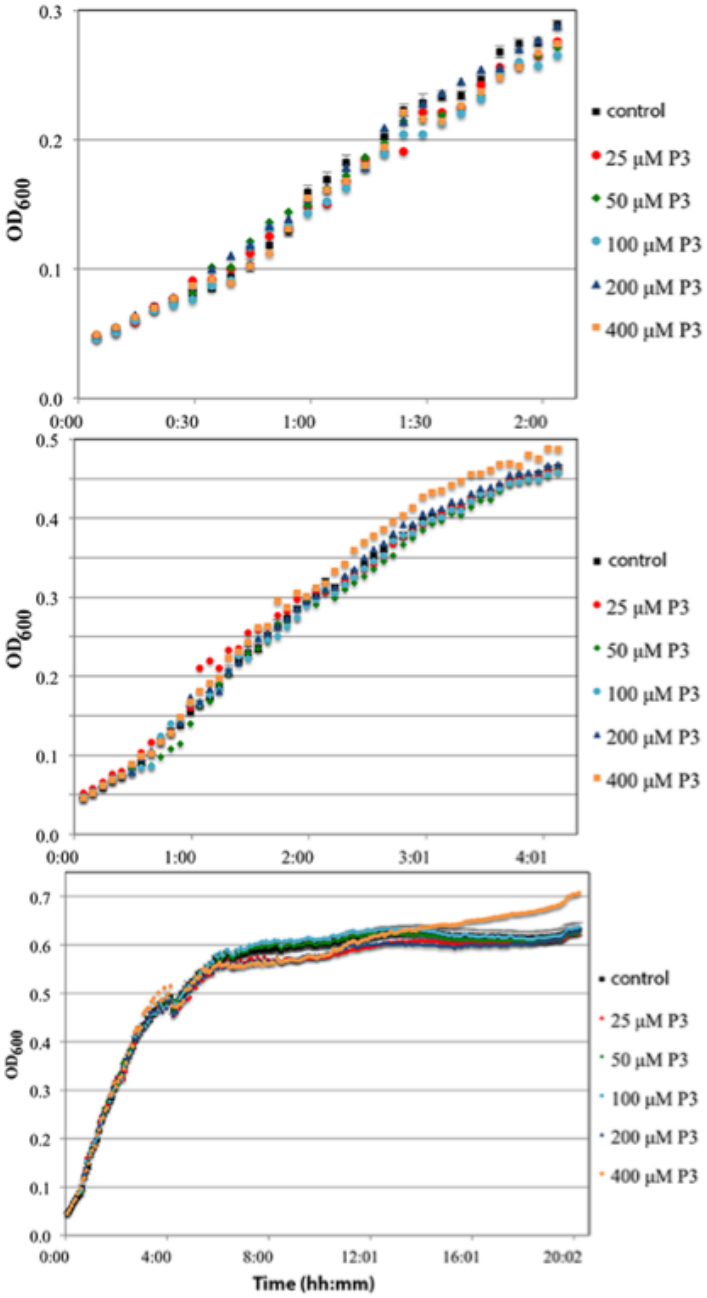

Figure 4.77. Growth curves of the P3A peptide treated cultures and control samples for the first 2 hours of incubation (top), for 4 hours of incubation (middle), and for 20 hours of incubation (bottom).

results show that incubation of the cultures with 50 μM, 100 μM or 200 μM peptide caused a slight increase in the CFU counts (Figure 4.78) after incubation for 2 or 4 hours.

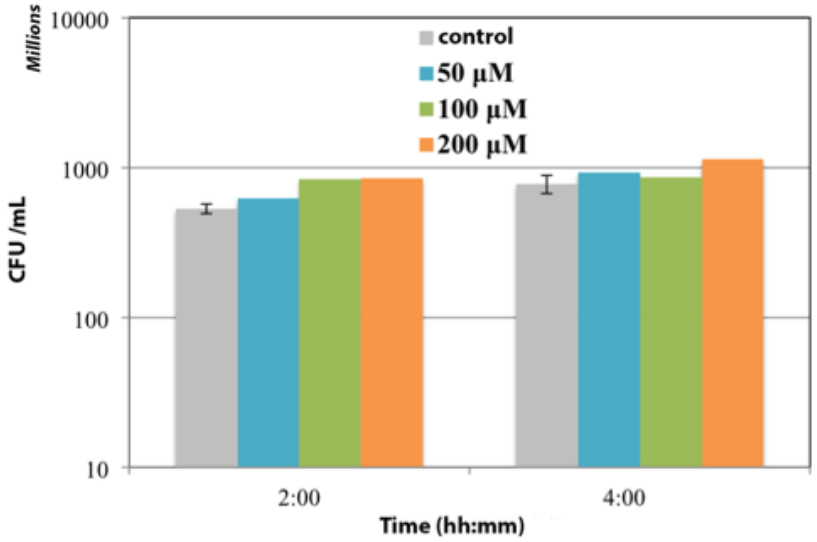

Figure 4.78. Comparison of CFU counts for the P3A treated and control samples in *E. coli* K12 pUC18 cultures after incubation for 2 or 4 hours. The average counts are shown for the control sample CFUs.

4.3.9. Effect of P3 Peptide on Bacterial Growth

In order to determine the effect of the beta-lactamase inhibitory peptide P3 (RRGHYY) on wild-type *E. coli* K12 and antibiotic resistant *E. coli* K12 pUC18 cells, cultures at standard inoculation cell density were treated with different P3 concentrations in the 31.25 μM - 500 μMM range and cultures at high inoculation cell density were treated with different P3 concentrations in the 62.5 μM - 2500 μM range. Since P3 stock solution was prepared in water, control samples were treated with water as well, for comparison.

After 20 hours of incubation of the P3 peptide treated and control cultures, visible growth was observed in control cultures at both standard and high inoculation density of *E. coli* K12 and *E. coli* K12 pUC18 cells. At standard inoculation cell density, visible growth was observed in all *E. coli* K12 and *E. coli* K12 pUC18 samples treated with up to 500 μM P3. Similarly, at high inoculation cell density, visible growth was observed in all *E. coli* K12 and *E. coli* K12 pUC18 samples treated with up to 2500 μM P3.

Under these experimental conditions, the MIC value for P3 could not be determined.

Growth curves of each P3 treated culture and control cultures are given in (Figure 4.79). At standard inoculation cell density, the growth curves of P3 treated cultures were very similar to that of the control samples. Similarly, at high inoculation density, the growth profiles of P3 treated cultures were similar to those of the control samples. Only a minor decrease in the growth of cells that were incubated with 1250 μM or 2500 μM P3 was observed. The results suggest that P3 peptide does not have any inhibitory affect on the growth wild-type *E. coli* K12 and antibiotic resistant *E. coli* K12 pUC18 cells after 20 hours of incubation.

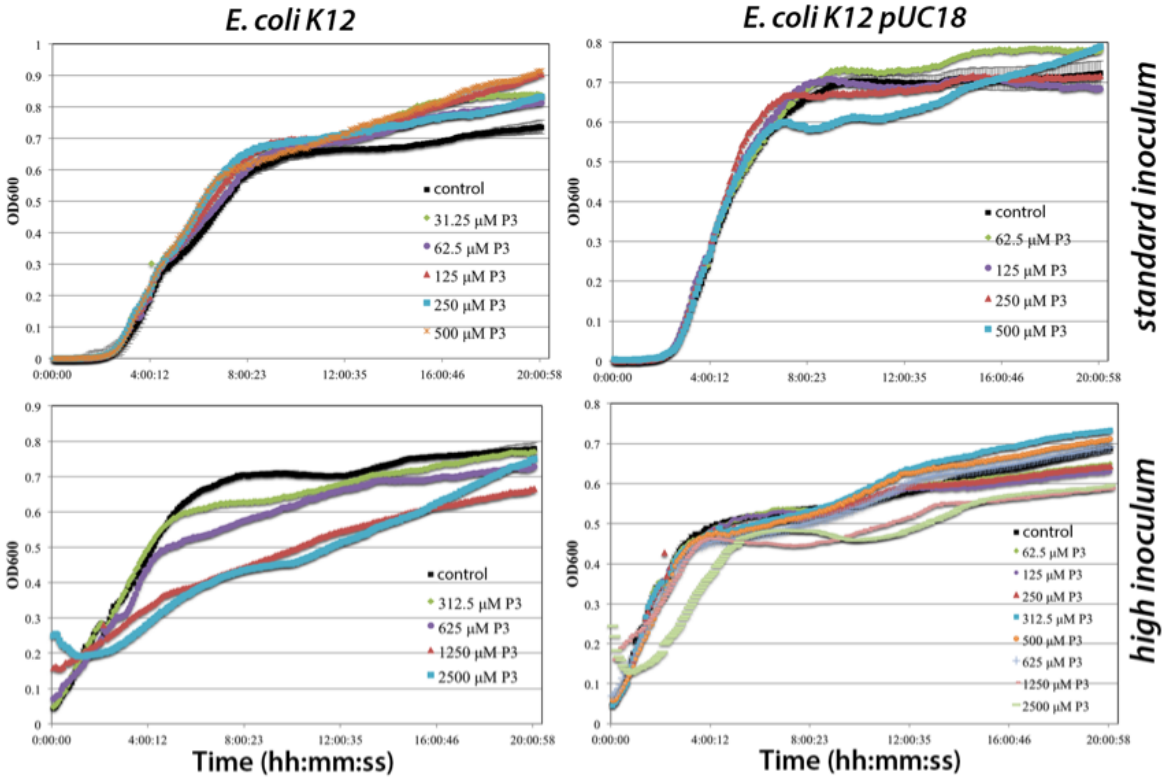

Figure 4.79. Growth curves of *E. coli* K12 (left) and *E. coli* K12 pUC18 (right) cultures for 20 hours of incubation. Bacteria at standard inoculum (top) and high inoculum (bottom) dose were treated with different P3 peptide concentrations.

For CFU measurements, culture samples at high inoculation cell density were incubated with 500 μM of P3 for 2 hours, as a test case. The control samples of both

E. coli K12 and *E. coli* K12 pUC18 cultures had CFU counts on the order of 10^8 to 10^9 (Figure 4.80). Upon incubation of *E. coli* K12 and *E. coli* K12 pUC18 cultures with 500 μM of P3 for 2 hours, a minor increase in the number of CFUs was observed (Figure 4.80).

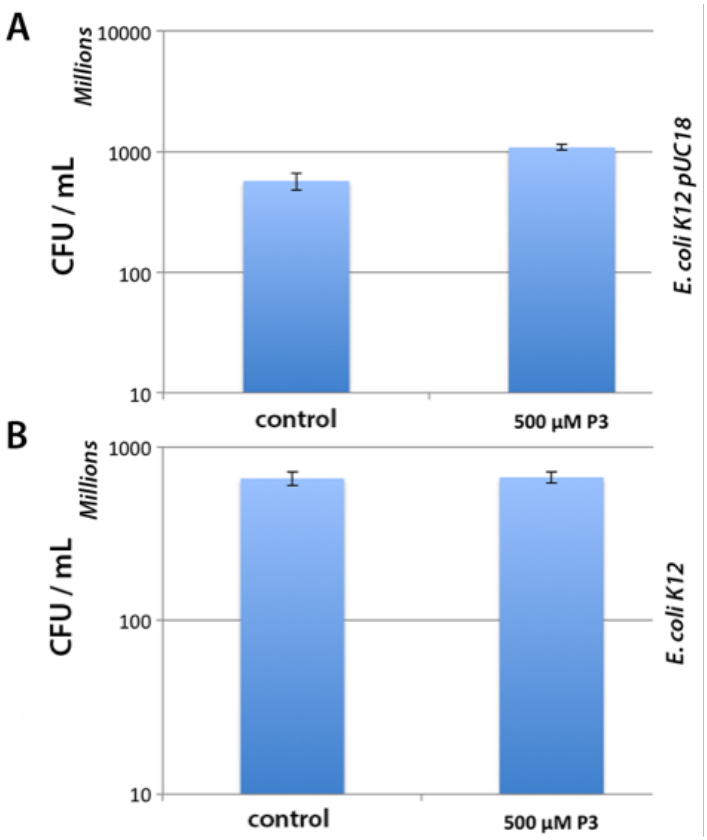

Figure 4.80. Number of colony forming units (top) in antibiotic resistant *E. coli* K12 pUC18 and (bottom) in wild-type *E. coli* K12 cultures after 2 hours of incubation with 500 μM of P3 peptide compared with the control samples.

The results suggest that beta-lactamase inhibitory peptide P3 does not have any antimicrobial effect on *E. coli* K12 or *E. coli* K12 pUC18 cells, either because the peptide does not have any membrane disruptive property or it cannot penetrate into the cells to reach beta-lactamase enzyme. In either case, it can be suggested that P3 is not a membrane active peptide.

4.3.10. Effect of P4 Peptide on Bacterial Growth

The initial experiments with P4 were carried out with antibiotic resistant *E. coli* K12 pUC18 cells at high inoculation density. In order to determine the effect of the modified beta-lactamase inhibitory peptide P4 (LLIILRRGHYY) on *E. coli* K12 pUC18 cells, 20, 40 and 80 μM peptide concentrations were tested. Since the 1 mM stock peptide solution contains 4.75% DMSO, control samples were prepared for each sample that was incubated with peptide with the same DMSO concentration (Figure 4.81).

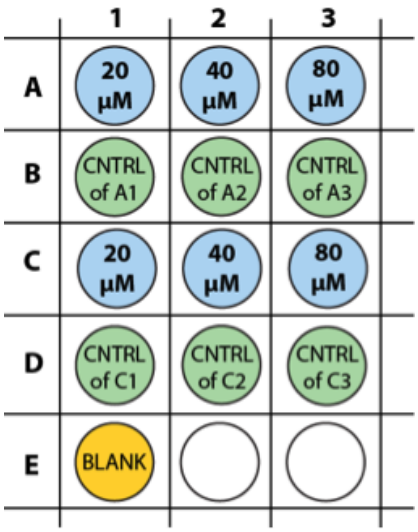

Figure 4.81. The microplate setup used in the experiment.

The growth curves (OD_{600} vs. time) for 2 and 4 hours of incubation for each well of the microplate are given in Figure 4.82. The average curves for the control samples are shown with the standard error of the mean. It was observed that the peptide inhibits the growth even at 20 μM concentration and higher peptide concentrations (80 μM) increases the initial OD_{600} values at the beginning of the experiment.

The number of colony forming units (CFUs) was counted for each sample that was withdrawn after 2 or 4 hours of incubation in the microplate (Figure 4.83). The results show that the peptide inhibits the growth even at the lowest tested concentration (20 μM), which was effective immediately at the beginning of the experiment. Moreover,

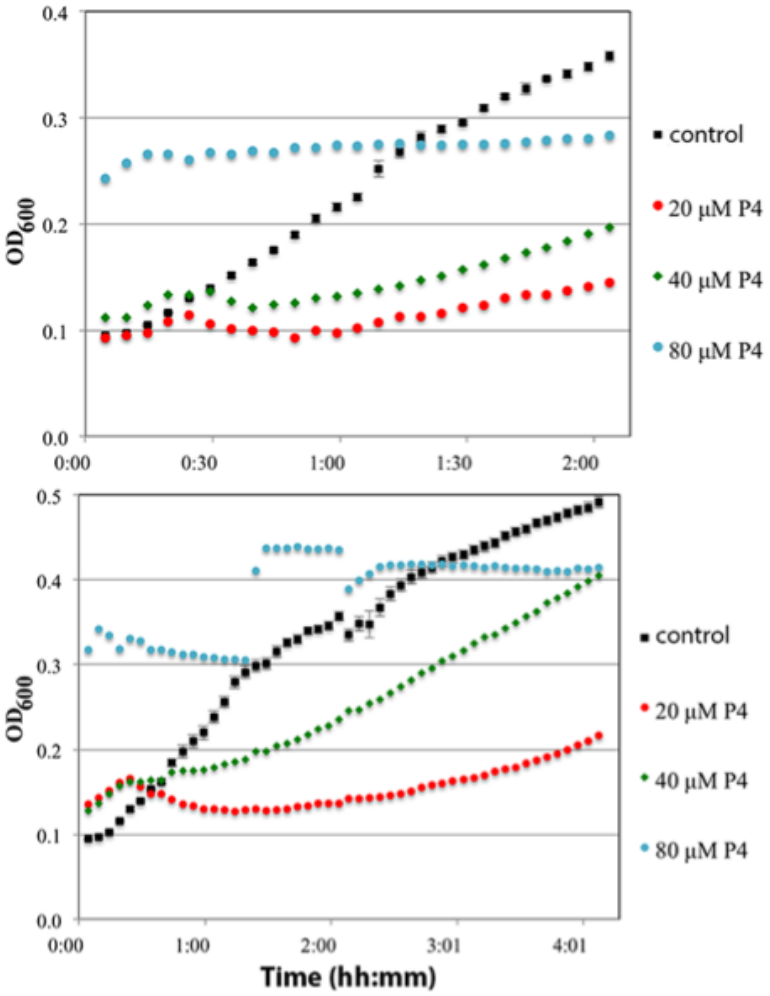

Figure 4.82. Growth curves of the P4 peptide treated and control samples for the first 2 hours of incubation (top), and for 4 hours of incubation (bottom).

incubation of the cultures with 40 μM peptide caused a decrease in the number of CFUs around 10 times (1 log), whereas approximately 100 times (2 log) decrease in the CFUs was determined upon incubation with 80 μM peptide (Figure 4.83).

In order to determine the MIC of P4 peptide at lower inoculum doses of *E. coli* K12 pUC18 cells, different P4 peptide concentration were added to the wells inoculated with the 1:10 dilution of the culture at $OD_{600} = 0.2$, and to the wells inoculated with the 1:100 dilution of the culture at $OD_{600} = 0.2$. After incubation at 37 °C and 180 rpm for 20 hours, no visible growth was observed in the samples treated with P4 concentration of 80 μM or higher (160 μM and 320 μM), suggestion that the MIC

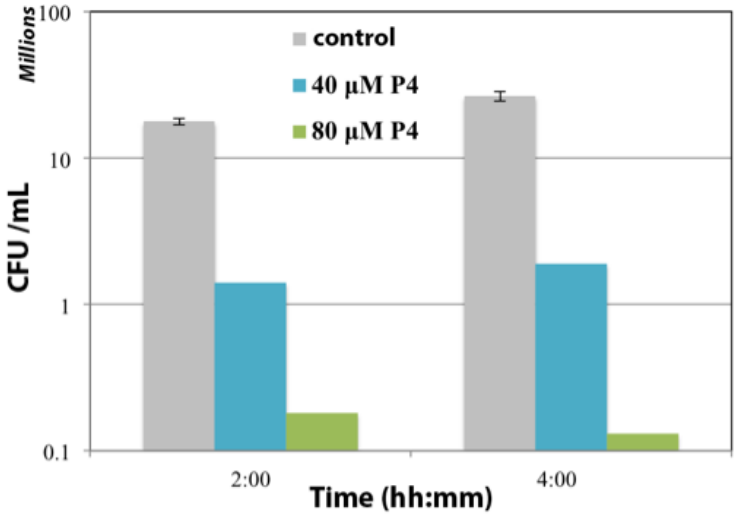

Figure 4.83. Comparison of CFU counts for the P4 treated and control samples in *E. coli* K12 pUC18 cultures after incubation for 2 or 4 hours. The average counts are shown for the control sample CFUs.

value of P4 peptide could be detected as 80 μM at low inoculum doses. The growth curves (OD_{600} vs. time) for 20 hours of incubation for each P4 treatment is given in Figure 4.84.

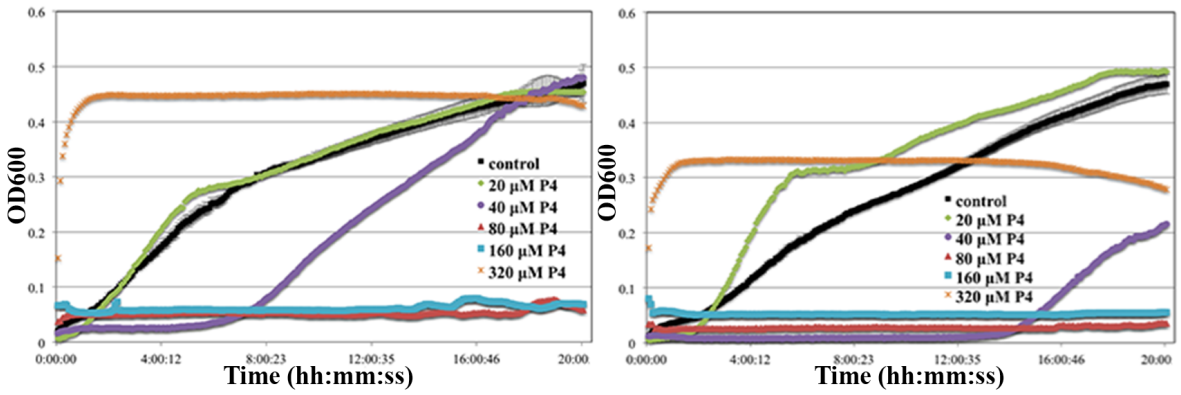

Figure 4.84. Growth curves of *E. coli* K12 pUC18 bacteria at $7x10^6$ CFU/mL cell density (left) and at $7x10^5$ CFU/mL cell density (right) treated with treated with different P4 peptide concentrations.

In order to determine the effect of the P4 peptide on wild-type *E. coli* K12 cells at high inoculation density, 20, 40, 80, and 160 μM peptide concentrations were tested

(Figure 4.85). Visible growth was observed in each well of the microplate (in rows E and F) after 20 hours of incubation, suggesting that the MIC value of this peptide is larger than 400 μM for *E. coli* K12 cells.

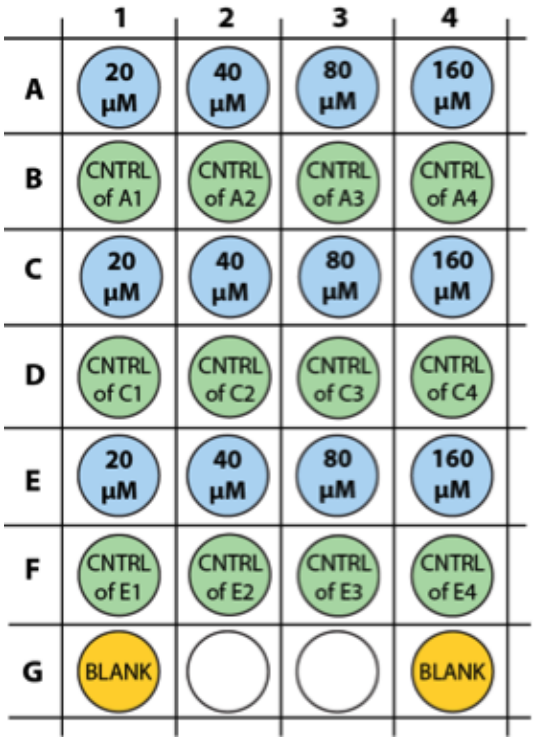

Figure 4.85. The microplate setup used in the experiment.

The number of colony forming units (CFUs) was counted for each sample that was withdrawn after 2, 4, and 20 hours of incubation (Figure 4.86). After 2 hours of incubation of the cultures with 20 μM, 40 μM or 80 μM peptide, a decrease in the CFU counts up to 10-fold (1 log), and a decrease up to 100 times (2 log) upon incubation with 160 μM peptide was observed. For 4 hours of incubation, the CFU counts of the cultures treated with peptide were 10-fold (1 log) less than those of the control samples. Interestingly, after 20 hours of incubation, the cultures treated with different peptide concentrations gave similar results in terms of CFU counts with their control samples.

When the effect of P4 peptide on antibiotic resistant *E. coli* K12 pUC18 and wild-type *E. coli* K12 cells, it was observed that the peptide has a stronger antimicrobial

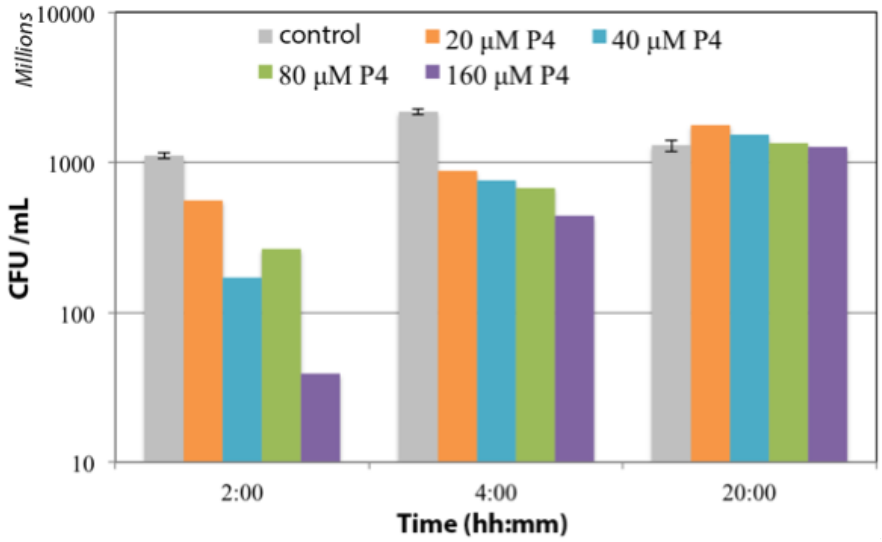

Figure 4.86. Comparison of CFU counts for the P4 treated and control *E. coli* K12 cultures after incubation for 2, 4, and 20 hours. The average counts are shown for the control sample CFUs.

effect on antibiotic resistant cells in the presence of ampicillin. On the other hand, the weak antimicrobial activity of P2r peptide on wild-type bacteria suggests that the antimicrobial action of this peptide is not directly or only related to the beta-lactamase inhibition. It is possible that the peptide or the LLIIL region alone has membrane disruptive activity, which may be contributing to this peptide's cellular uptake.

For repetitive experiments to determine and compare the effect of P4 peptide on wild-type and antibiotic resistant bacteria, a new P4 peptide stock solution was prepared, therefore previous experiments with P4 had to be repeated. The determined MIC values for P4 peptide may differ depending on the stock solution, since two peptide stock solutions are prepared from two different delivered peptide powders with possibly different purity values, making the peptide stock solutions non-identical to each other.

In order to determine the effect of P4 peptide on wild-type *E. coli* K12 and antibiotic resistant *E. coli* K12 pUC18 cells, cultures at standard inoculation cell density were treated with different P4 concentrations in the 18.75 μM - 125 μM range and at high inoculation cell density were treated with different P4 concentrations in the 25

μM - 300 μM range. Since P4 stock was prepared in DMSO-water solution (5 mM stock with 4% DMSO), control samples were treated with DMSO-water to include the same DMSO concentration in the P4 treated cultures accordingly.

After 20 hours of incubation of the P4 peptide treated and control cultures, visible growth was observed in control cultures at both standard and high inoculation density of *E. coli* K12 and *E. coli* K12 pUC18 cells. At standard inoculation cell density, visible growth was not observed in the *E. coli* K12 cultures treated with 100 μM or higher concentrations of P4 peptide, and visible growth was not observed in the *E. coli* K12 pUC18 cultures treated with 80 μM or higher P4 peptide concentrations. At high inoculation density of both *E. coli* K12 and *E. coli* K12 pUC18 cells, visible growth was not observed in the cultures treated with 250 μM or higher P4 peptide concentrations.

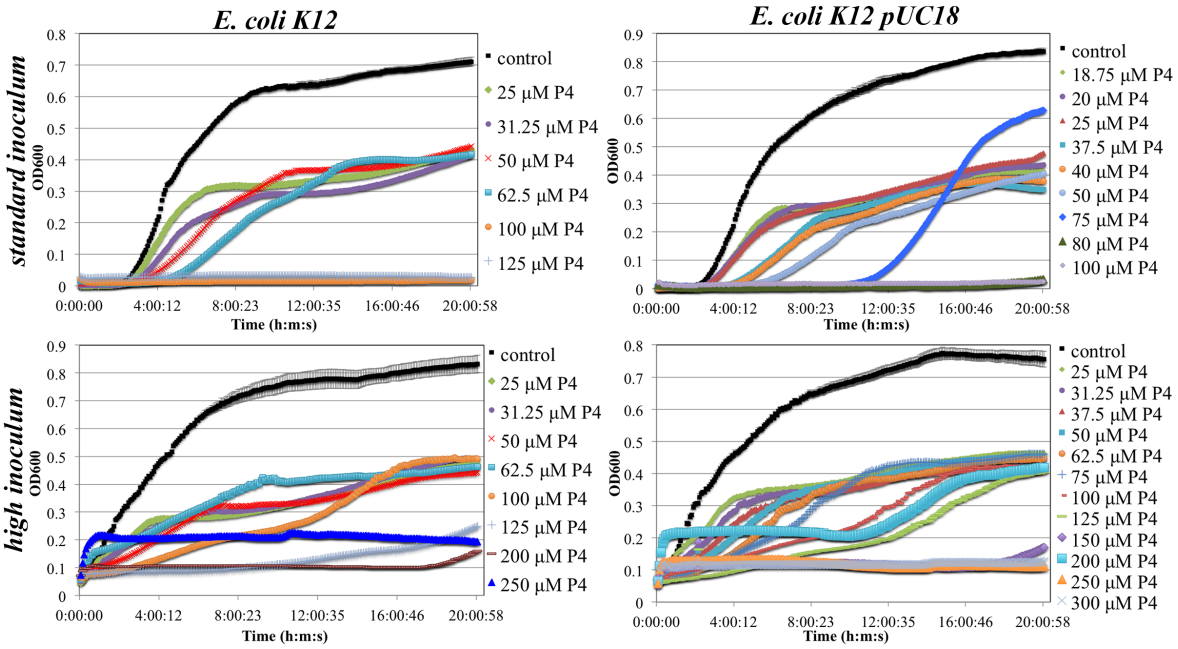

Figure 4.87. Growth curves of *E. coli* K12 (left) and *E. coli* K12 pUC18 (right) cultures for 20 hours of incubation. Bacteria at standard inoculum (top) and high inoculum (bottom) dose were treated with different P4 peptide concentrations.

Growth curves of each P4 peptide treated culture and control cultures are given in (Figure 4.87). Even though the MIC for P4 was determined as 250 μM at high inoculation density of both *E. coli* strains and 80 μM and 100 μM at standard inoculation

density of *E. coli* K12 pUC18 and *E. coli* K12 cells, respectively, it was observed that all of the tested concentrations inhibit the growth of cells (Figure 4.87). The results suggest that the antimicrobial action of P4 is similar for wild-type *E. coli* K12 and antibiotic resistant *E. coli* K12 pUC18 cells at their standard and high inoculation cell density.

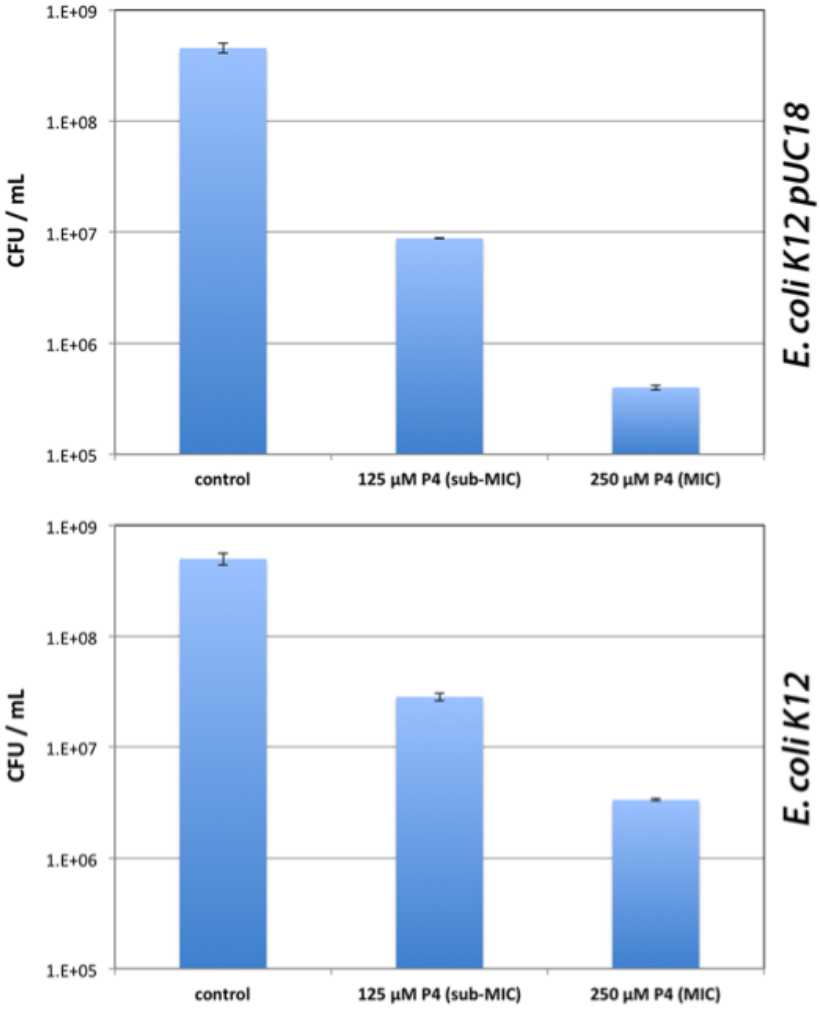

Figure 4.88. Number of colony forming units (top) in antibiotic resistant *E. coli* K12 pUC18 and (bottom) in wild-type *E. coli* K12 cultures after 2 hours of incubation with sub-MIC and MIC of P4 peptide compared with the control samples.

For CFU measurements, culture samples at high inoculation cell density were incubated with sub-MIC (MIC/2) and MIC of P4 for 2 hours. The control samples of both *E. coli* K12 and *E. coli* K12 pUC18 cultures had CFU counts on the order of 10^8

to 10^9 (Figure 4.88). When *E. coli* K12 pUC18 cells were incubated with sub-MIC (125 μM) of P4 for 2 hours, the decrease in the number of CFUs was around 50-folds when compared to the control samples (Figure 4.88). Upon increasing the concentration to MIC (250 μM) of P4, the number of CFUs in *E. coli* K12 pUC18 cultures decreased around 1200-folds, when compared to the control samples (Figure 4.88). Similarly, for the wild-type *E. coli* K12 cells incubated with sub-MIC (125 μM) of P4, the number of CFUs decreased around 18-folds and for the wild-type *E. coli* K12 cells incubated with MIC (250 μM) of P4, the number of CFUs decreased around 150-folds (Figure 4.88).

The results show that P4 is antimicrobial for both antibiotic resistant *E. coli* K12 pUC18 and wild-type *E. coli* K12 cells, suggesting that the peptide has membrane disruptive properties. Moreover, P4 has either selectively stronger antimicrobial activity for *E. coli* K12 pUC18 cells, or the antimicrobial action is faster in *E. coli* K12 pUC18 cultures when compared to *E. coli* K12 cultures.

4.3.11. Comparison of the Antibacterial Activity of Drugs

The determined MIC value of each drug for antibiotic resistant *E. coli* K12 pUC18 and wild-type *E. coli* K12 cells under standard (low) and high inoculum doses are given in Table 4.2.

Minimal inhibitory concentration value is highly dependent on the initial cell density. For DMSO, the MIC values were determined as 2-folds higher at high inoculation cell density when compared to the ones determined at standard inoculation density of both *E. coli* K12 pUC18 and *E. coli* K12 cells (Table 4.2). The MIC values determined for DMSO were the same for both strains.

At standard inoculation cell density, the determined MIC value of melittin is in the range of MIC values reported in literature [33, 35, 38, 43]. At high inoculation cell density, the MIC value of melittin was determined 8-folds higher for *E. coli* K12 pUC18 cells and 16-folds higher for *E. coli* K12 cells when compared to the values determined at

standard inoculation cell density (Table 4.2). The MIC values determined for melittin were similar for both strains.

Table 4.2. Minimal inhibitory concentration of each drug against antibiotic resistant *E. coli* K12 pUC18 and wild-type *E. coli* K12 bacteria at standard and high inoculum doses.

	***E. coli* K12 pUC18**		***E. coli* K12**	
	Standard Inoculum Dose	**High Inoculum Dose**	**Standard Inoculum Dose**	**High Inoculum Dose**
DMSO	12.5%	25%	12.5%	25%
Melittin	6.25 μM	50 μM	3.125 μM	50 μM
Ampicillin	12.5 mg/mL	200 mg/mL	3.05 μg/mL	6.1 μg/mL
Potassium Clavulanate	31.25 μM	250 μM	125 μM	250 μM
pVEC	-	-	12.5 μM	62.5 μM
del5 pVEC	-	-	$>$ 500 μM	$>$ 500 μM
P2r	-	$>$ 400 μM	-	$>$ 400 μM
P3A	-	$>$ 400 μM	-	-
P3	$>$ 500 μM	$>$ 2500 μM	$>$ 500 μM	$>$ 2500 μM
P4	80 μM	250 μM	100 μM	250 μM

The MIC values were determined as 3.05 μg/mL and 12.5 mg/mL at standard inoculation density of wild-type *E. coli* K12 and antibiotic resistant *E. coli* K12 pUC18 cells, respectively, suggesting that the *E. coli* K12 pUC18 strain is resistant to ampicillin over 4000-folds when compared to the *E. coli* K12 strain (Table 4.2). Similarly, at high inoculation cell density, the MIC values were determined as 6.1 μg/mL and 200 mg/mL for wild-type *E. coli* K12 and antibiotic resistant *E. coli* K12 pUC18 cells, respectively, suggesting that the *E. coli* K12 pUC18 strain is resistant to ampicillin over 32,000-folds when compared to the *E. coli* K12 strain (Table 4.2).

The MIC values for the beta-lactamase inhibitor potassium clavulanate (PC) were determined as 125 μM and 31.25 μM at standard inoculation density of wild-type *E. coli* K12 and antibiotic resistant *E. coli* K12 pUC18 cells, respectively (Table 4.2). At high inoculation density of *E. coli* K12 and *E. coli* K12 pUC18 cells, the values were determined as 250 μM, suggesting that the antimicrobial action of PC is similar for both strains (Table 4.2). The results suggest that the antimicrobial action of PC may not be limited to the inhibition of the beta-lactamase enzyme, but may be related to some other mechanism as well.

The MIC values for the cell-penetrating peptide pVEC was determined as 12.5 μM and 62.5 μM for the standard and high inoculum doses of wild-type bacteria, respectively. Even though the tested del5 pVEC concentrations had inhibitory effect on the growth curve of the cells, the MIC value of del5 pVEC could not be detected at the highest concentration (500 μM) tested. The results show that pVEC loses its antimicrobial effect to a great extent upon deletion of the LLIIL residues (Table 4.2).

For the beta-lactamase inhibitory peptide P2r, no MIC value could be determined at high inoculation cell density of wild-type and antibiotic resistant cells, with the highest tested peptide concentration of 400 μM (Table 4.2). The weaker antimicrobial activity of P2r peptide on wild-type bacteria (compared to that on antibiotic resistant bacteria) suggests that the antimicrobial action of this peptide is not directly or only related to the beta-lactamase inhibition. It is possible that the peptide or the LLIIL/LLIILRRR region alone has membrane disruptive activity.

For the beta-lactamase inhibitory peptide P3A, no MIC value could be determined at high inoculation cell density of antibiotic resistant bacteria, with the highest tested peptide concentration of 400 μM (Table 4.2). Since the focus of the study was on P3 and P4, experiments were not repeated with this peptide for wild-type cells or at different inoculum doses.

For the beta-lactamase inhibitory peptide P3, no MIC value could be determined at standard or high inoculation cell density, with the highest tested peptide concentra-

tions of 500 μM and 2500 μM, respectively (Table 4.2). Considering that the growth curves and the number of CFUs of the P3 treated cultures and the control samples were very similar, it can be suggested that P3 peptide does not have any antimicrobial effect on wild-type *E. coli* K12 and antibiotic resistant *E. coli* K12 pUC18 cells.

The MIC values for the modified beta-lactamase inhibitory peptide P4 were determined as 100 μM and 80 μM at standard inoculation density of wild-type *E. coli* K12 and antibiotic resistant *E. coli* K12 pUC18 cells, respectively (Table 4.2). At high inoculation density of *E. coli* K12 and *E. coli* K12 pUC18 cells, the values were determined as 250 μM, suggesting that the antimicrobial action of P4 is similar for both strains (Table 4.2). Similar to our observations for potassium clavulanate (PC), the results suggest that the antimicrobial action of the P4 peptide may be related to some mechanism other than inhibition of the beta-lactamase enzyme.

4.3.12. Drug Synergy Tests

The main goal of our study is to design a beta-lactamase inhibitory peptide that is able to penetrate into bacteria to reach and inhibit its target protein. If beta-lactamase is inhibited, cells will act like beta-lactamase-free or wild-type cells that can be killed by the addition of antibiotics. This proposed mechanism necessitates the investigation of effects of drug combinations, in our case, the combination of drugs with the beta-lactam antibiotic ampicillin. If a drug synergy occurs between any drug pair, then, the antimicrobial action of the combination should be different, stronger or weaker, compared to the antimicrobial effect of each drug alone.

In order to investigate if drug synergy occurs, we tested the effect of melittin & ampicillin, potassium clavulanate & ampicillin, P3 peptide & ampicillin, and P4 peptide & ampicillin combinations on antibiotic resistant *E. coli* K12 pUC18 cells. Cultures were incubated for 20 hours with decreasing concentrations of combinations, starting from the combination at each drugs sub-MIC (MIC/2) value. The MIC values of each drug at standard and high inoculation cell density were previously given in Table 4.2.

At standard inoculation cell density, visible growth was not observed in the cultures treated with 3.125 μM melittin & 12.5 mg/mL ampicillin or higher concentrations (Figure 4.89), suggesting that the MIC of ampicillin (12.5 mg/mL) is still required even when it is combined with melittin. At high inoculation cell density, visible growth was observed in all treated cultures with the highest concentration of the combination as 25 μM melittin & 100 mg/mL ampicillin, which is the addition of sub-MIC of both drugs (Figure 4.89). It was observed that the combination of sub-MIC values of the two drugs is not enough to abolish cell growth. These results suggest that melittin and ampicillin are not synergetic since the combined effect is similar to that of each drug alone.

For the potassium clavulanate (PC) & ampicillin combination, at standard inoculation cell density, visible growth was not observed in any of the cultures treated with this combination, with the lowest tested concentration as 7.81 μM potassium clavulanate & 0.78 mg/mL ampicillin (Figure 4.89), which is 4-fold lower than the MIC of potassium clavulanate alone and 16-fold lower than the MIC of ampicillin alone. At high inoculation cell density, visible growth was not observed in the cultures treated with 15.63 μM potassium clavulanate & 1.56 mg/mL ampicillin or higher concentrations (Figure 4.89), which is around 16-fold lower than the MIC of potassium clavulanate and over 120-folds lower than the MIC of ampicillin alone. The results suggest that the inhibitory effect of potassium clavulanate with ampicillin addition was enhanced and cell growth was inhibited effectively for all tested concentrations between 3.91 μM potassium clavulanate & 0.39 mg/mL ampicillin and 250 μM potassium clavulanate & 25 mg/mL ampicillin concentration. The antimicrobial action of potassium clavulanate against antibiotic resistant bacteria was stronger in the presence of ampicillin indicating that their antimicrobial mechanism is correlated.

For the P3 peptide & ampicillin combination, at standard inoculation cell density, visible growth was not observed in the cultures treated with 62.5 μM P3 & 25 mg/mL ampicillin or higher concentrations (Figure 4.89), suggesting that the MIC value of ampicillin is still 12.5 mg/mL even when it is combined with P3. At high inoculation cell density, visible growth was observed in all treated cultures with the highest con-

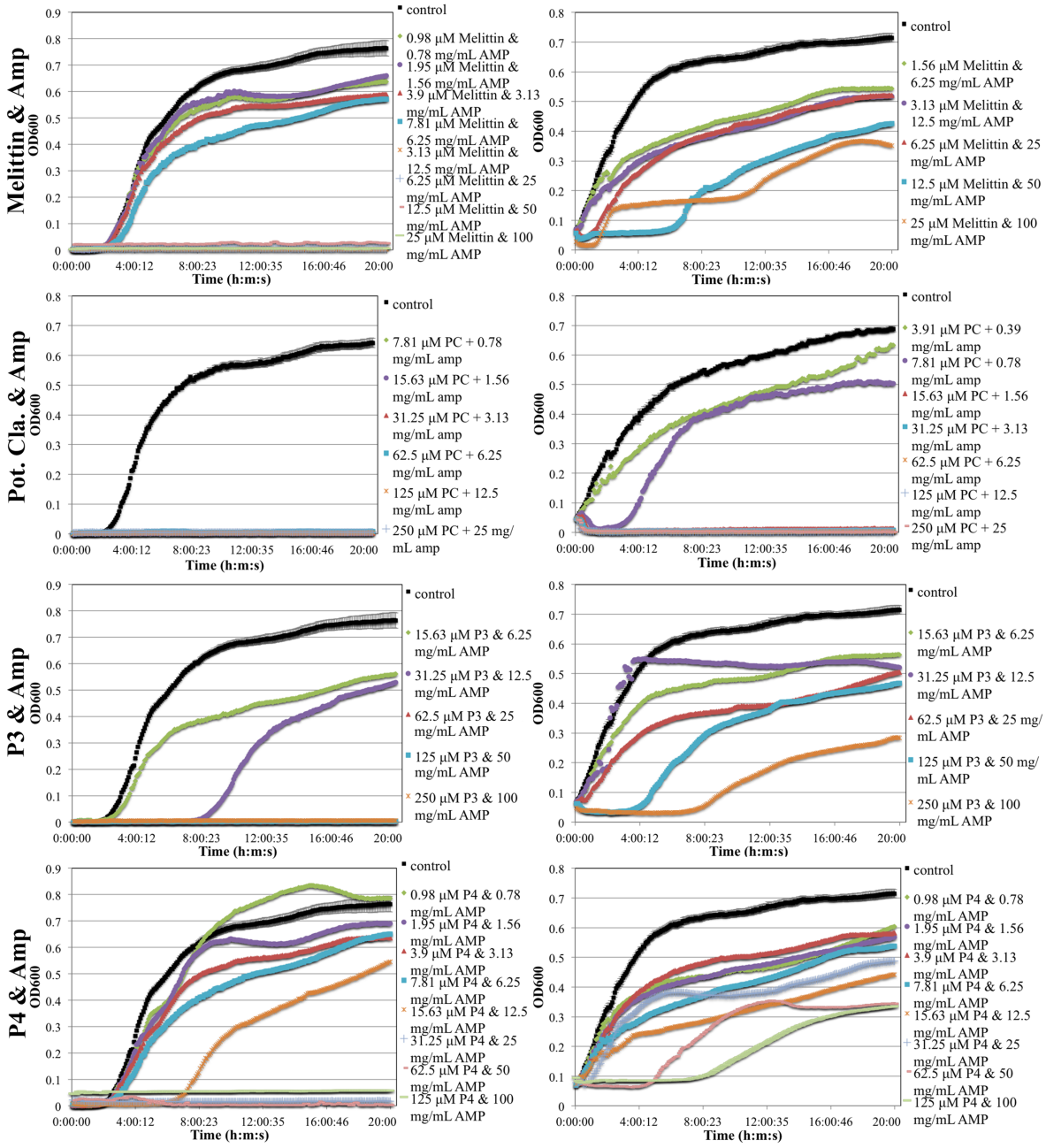

Figure 4.89. Growth curves of *E. coli* K12 pUC18 cultures for 20 hours of incubation. Bacteria at standard inoculation cell density (left) and high inoculation cell density (right) were treated with different concentrations of drug combinations.

centration of the combination as 250 μM P3 & 100 mg/mL ampicillin, which is the addition of sub-MIC of ampicillin and half of the test case concentration (500 μM) of P3 peptide (Figure 4.89). It was observed that the tested concentrations of the com-

bination were not enough to abolish cell growth. These results suggest that P3 and ampicillin are not synergetic since the combination effect is similar to that of each drug alone.

For the P4 peptide & ampicillin combination, at standard inoculation cell density, visible growth was not observed in the cultures treated with 31.25 μM P4 & 25 mg/mL ampicillin or higher concentrations (Figure 4.89), suggesting that the MIC value of ampicillin (12.5 mg/mL) is still required even when it is combined with P4. At high inoculation cell density, visible growth was observed in all treated cultures with the highest concentration of the combination as 125 μM P4 & 100 mg/mL ampicillin, which is the addition of sub-MIC of both drugs (Figure 4.89). It was observed that the combination of sub-MIC values of two drugs is not enough to abolish the cell growth completely. These results suggest that P4 and ampicillin are not synergetic since the combination effect is similar to that of each drug alone.

4.4. Visualization of Drug Effects on Bacteria

4.4.1. Visualization of Membrane Permeability and Bacterial Viability

4.4.1.1. Visualization of P1 Effects on Cells Using Time-Lapse Microscopy. Effect of P1 peptide on cell growth was observed using time-lapse microscopy. The first experiment was carried out under confocal microscopy with untreated cells pipetted on agarose pads and even after 5-6 hours no cell growth was observed. Later, inverted microscope was set up for time-lapse imaging and a chamber of microscopy glasses stuck together with Vaseline at the edges was prepared. Using this setup, movies were recorded using untreated cells, cells incubated with antibiotic or P1. In all movies, cell growth was observed similarly in terms of number of division cycles and duration of each cell division cycle. 40X magnification was found appropriate for stable focus and single cell observation. Figure 4.90 shows snapshots taken at different time points of the time-lapse video of cells incubated with P1. The time-lapse images of live cells incubated with P1 showed that the peptide does not effect growth of cells, as it was already determined by the growth curves and the change in number of CFUs.

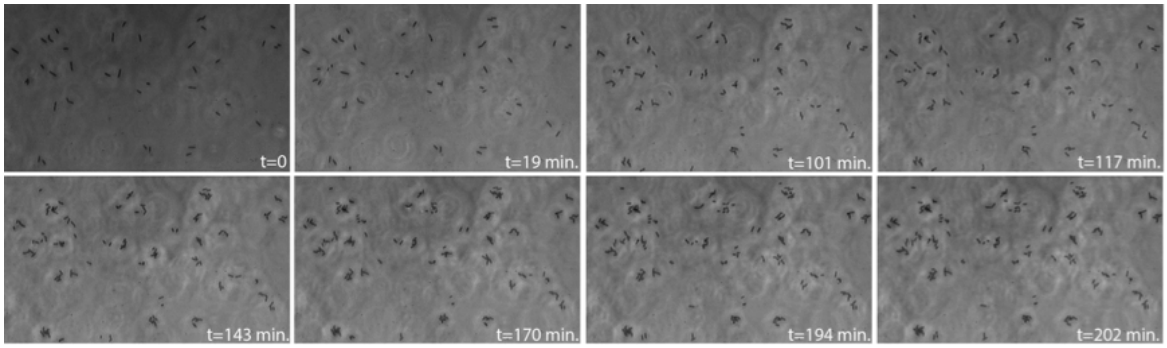

Figure 4.90. Time-lapse imaging of cells incubated with P1. Within a recording time of approximately 3.5 hours, 4-5 cell cycles were observed.

4.4.1.2. Bacterial Viability Tests with wild-type and Antibiotic Resistant Cells. In order to test the bacterial viability kit, antibiotic resistant *E. coli* K12 pUC18 and wild-type *E. coli* K12 cultures were prepared. Precultures from bacterial stocks were incubated overnight at 37 °C and 180 rpm. The next morning, fresh LB medium (supplemented with 0.1 mg/mL ampicillin for the resistant cell culture) were inoculated with preculture and left to grow at 37 °C and 180 rpm. After 3 hours, ampicillin was also added to the culture of wild-type cells (at the same concentration of ampicillin in the resistant cell culture, 0.1 mg/mL) to determine the effect of antibiotics on growth of wild-type cells. After 1 hour of incubation with ampicillin, samples were withdrawn from both resistant and wild-type cultures and were incubated with the bacterial viability kit dyes after centrifugation and washing steps.

The snapshots taken for each sample are shown in Figure 4.91 and Figure 4.92. It was observed that both samples contained live and dead cells indicated by green and red fluorescence respectively. The quantitative analysis was carried out using Fiji (ImageJ) software to count the cells with green or red fluorescence. The ratio of the number of dead to live cells can provide information about the effect of ampicillin addition.

For the sample from the antibiotic resistant culture, 1210 cells were live while 194 cells had membrane damage (Figure 4.91). The ratio of dead/live cells and dead/all

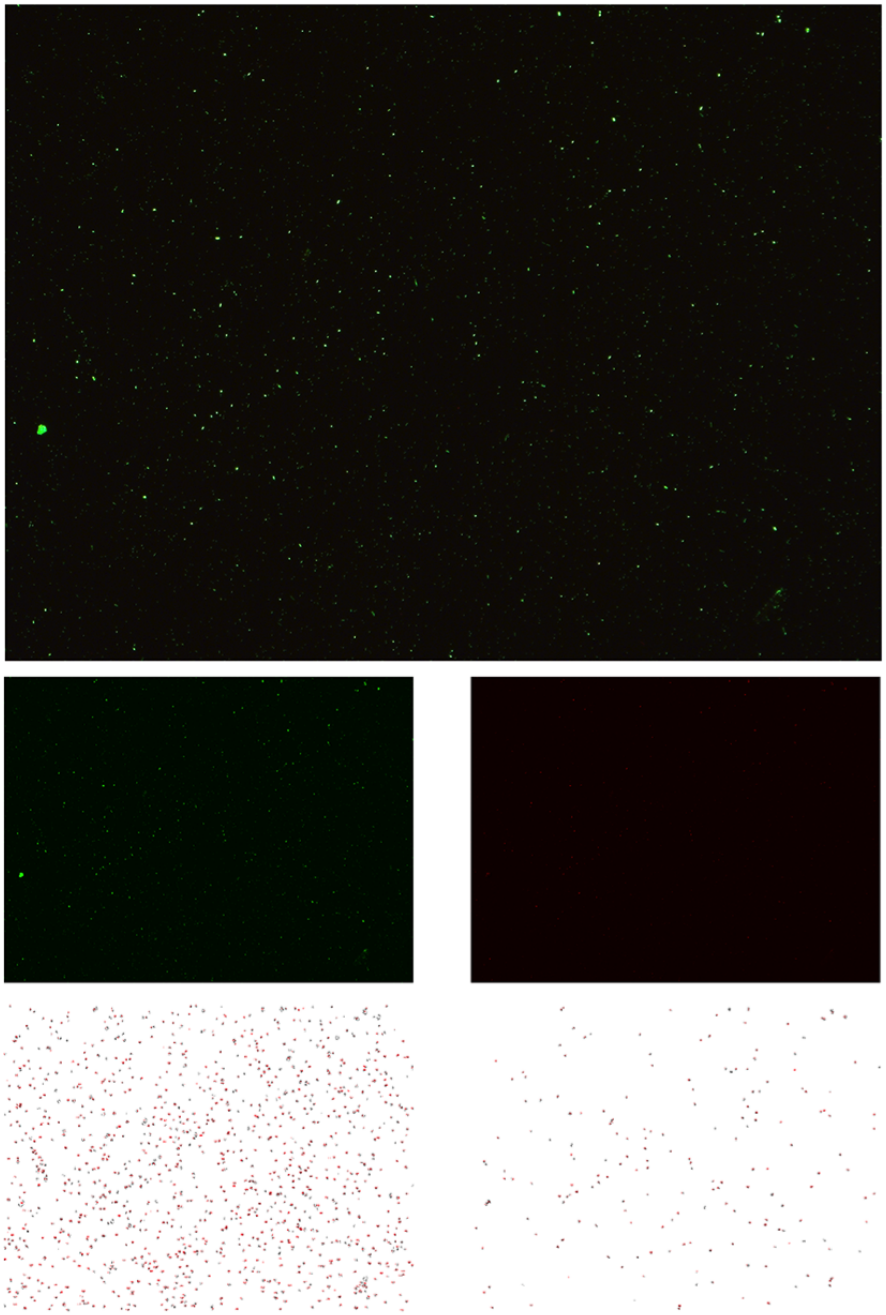

Figure 4.91. Snapshots of antibiotic resistant cells, green and red fluorescence overlaid (top), green fluorescence (middle-left), red fluorescence (middle-right), and their counts (bottom).

cells were calculated to be 16% and 14% respectively. The sample of wild-type cells incubated with ampicillin for 1 hour (Figure 4.92) showed that 459 cells were live while 122 cells had damaged membranes. The ratio of dead/live cells and dead/all cells

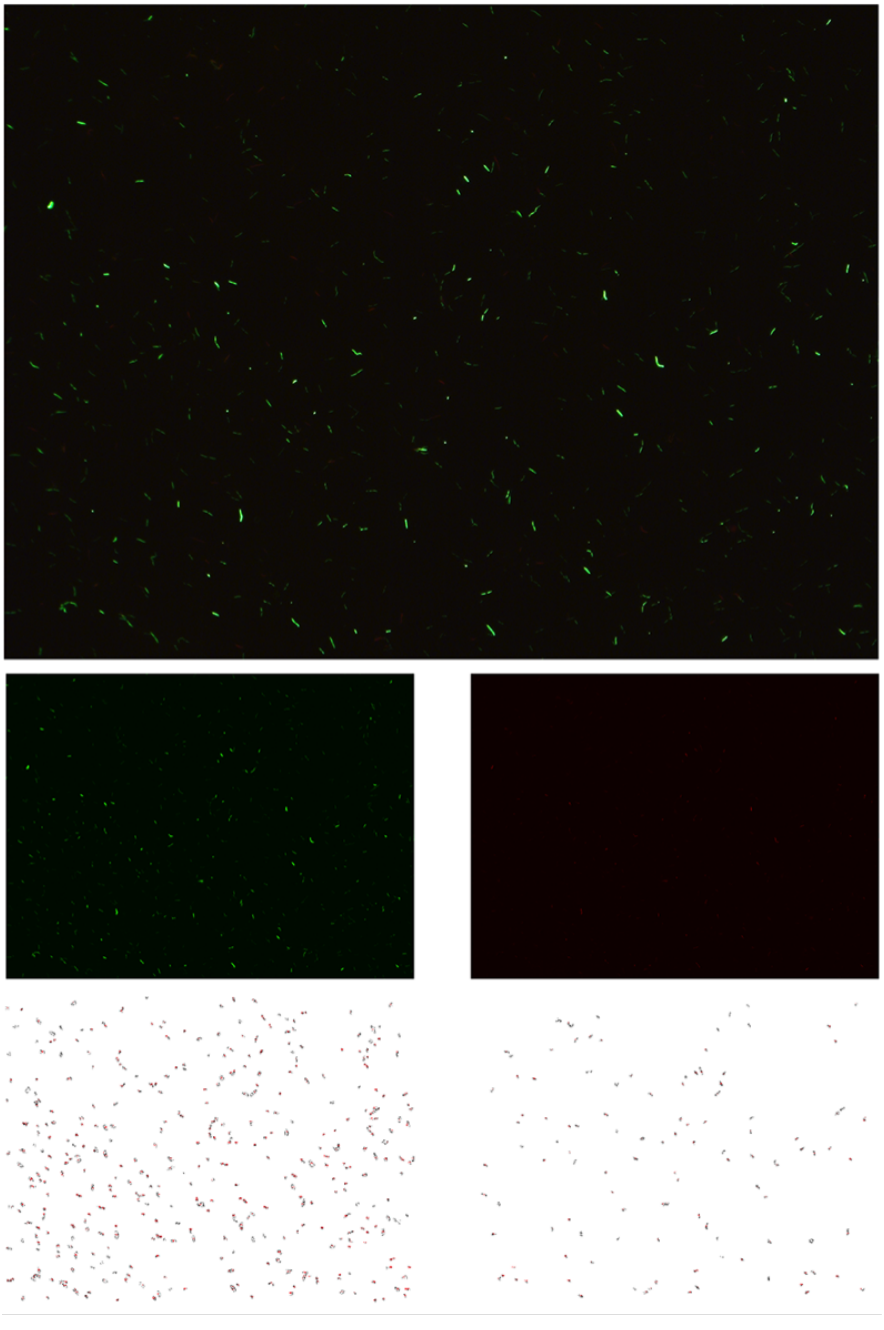

Figure 4.92. Snapshots of wild-type bacteria incubated with ampicillin for 1 hour. Green and red fluorescence overlaid (top), green fluorescence (middle-left), red fluorescence (middle-right), and their counts (bottom).

were calculated to be 27% and 21% respectively. Furthermore, although the initial cell concentrations and the amount of samples used for visualization were the same for resistant and wild-type cells, it was observed that the total number of cells was

much higher for resistant cells indicating that antibiotic addition inhibited the growth of wild-type cells. This was also proved by the OD_{600} values at the time of sample withdrawal, which were measured as 0.46 and 0.35 for resistant and wild-type cells respectively.

The morphology of the cells was different. The wild-type cells had a better-defined rod-shape, whereas the resistant cells were shorter and observed as dots under low magnification.

4.4.1.3. Effect of Melittin on Bacterial Viability. In order to visualize the effect of melittin on *E. coli* K12 and *E. coli* K12 pUC18 cells, samples either incubated with water only (control), with 25 μM Melittin (sub-MIC), or with 50 μM of Melittin (MIC) for 2 hours were used for bacterial viability experiments. The second stock solution of melittin was used in these experiments and determined MIC values were reported previously.

Cells treated with water (control) were intact and almost all of them were live (green) (Figure 4.93). Upon incubation of *E. coli* K12 and *E. coli* K12 pUC18 cells with 25 μM Melittin (sub-MIC), the live/dead (green/red) cell ratio decreased, most of the cells were dead and the cell density in the images was low (Figure 4.93). Moreover, minor increase in cell size and abnormal shapes were observed. Upon increasing the concentration to 50 μM (MIC), the number of cells decreased considerably in each image and live cells were hardly observed (Figure 4.93).

Although the fluorescence microscopy images do not provide quantitative results, images suggest that the antimicrobial action of melittin causes membrane damage for both wild-type *E. coli* K12 and antibiotic resistant *E. coli* K12 pUC18 cells.

4.4.1.4. Effect of Ampicillin on Bacterial Viability. In order to visualize the effect of ampicillin on *E. coli* K12 and *E. coli* K12 pUC18 cells, samples either incubated with water only (control), with sub-MIC of ampicillin (0.00305 mg/mL for *E. coli* K12 and

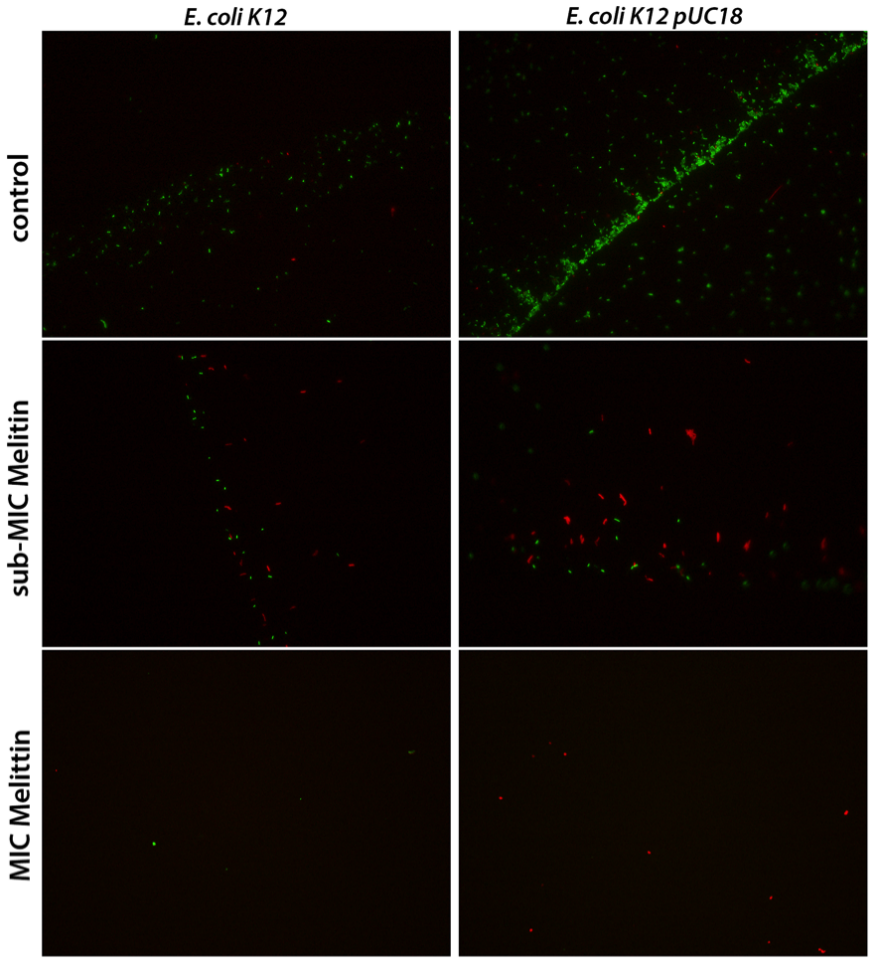

Figure 4.93. Fluorescence microscopy images of *E. coli* K12 (left) and *E. coli* K12 pUC18 (right) cells treated with sub-MIC and MIC of melittin, compared with the control samples (top).

100 mg/mL for *E. coli* K12 pUC18 cells), or with MIC of ampicillin (0.0061 mg/mL for *E. coli* K12 and 200 mg/mL for *E. coli* K12 pUC18 cells) for 2 hours were used for bacterial viability experiments.

The fluorescence microscopy images of *E. coli* K12 cells treated with water (top), and ampicillin followed by double staining with SYTO9 and PI nucleic acid dyes are given in Figure 4.94. Cells treated with water (control) were intact and most of them were live (green) (Figure 4.94). Upon incubation of *E. coli* K12 cells with 0.00305 mg/mL ampicillin (sub-MIC), the live/dead (green/red) cell ratio and the cell density

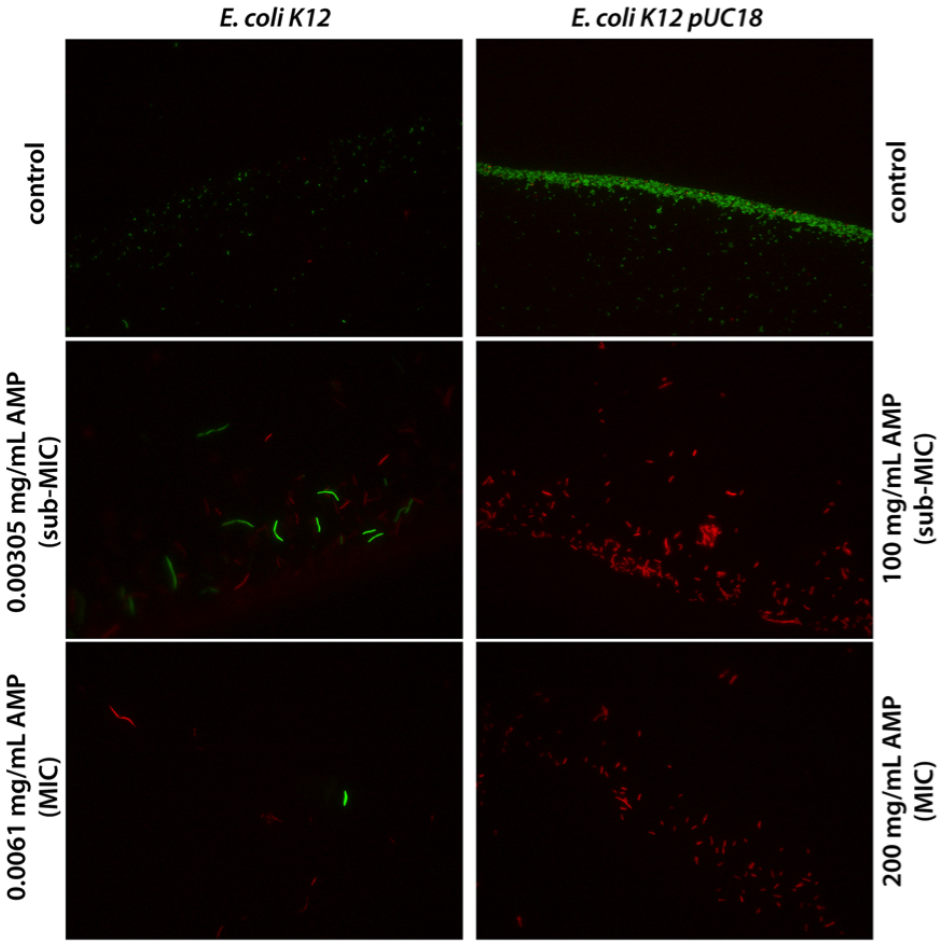

Figure 4.94. Fluorescence microscopy images of *E. coli* K12 (left) and *E. coli* K12 pUC18 (right) cells treated with sub-MIC and MIC of ampicillin, compared with the control samples (top).

in the images decreased. Changes in the shape of the cells resembling filaments were observed, suggesting that cell division may be hindered. Upon increasing the ampicillin concentration to 0.0061 mg/mL (MIC), the number of cells decreased considerably in each image and live cells were hardly observed (Figure 4.94).

Although the MIC and sub-MIC values of ampicillin that was determined against antibiotic resistant *E. coli* K12 pUC18 cells were much higher when compared to those of wild-type *E. coli* K12 cells, the effect of ampicillin on bacterial viability was similar. Upon incubation of *E. coli* K12 pUC18 cells with 100 mg/mL ampicillin (sub-MIC), the live/dead (green/red) cell ratio decreased considerably and almost all of the cells

were dead. The cell shape changed to resemble filaments, suggesting that cell division may be hindered. Upon increasing the ampicillin concentration to 200 mg/mL (MIC), the number of cells decreased and all of the cells observed were dead (Figure 4.94).

4.4.1.5. Effect of Potassium Clavulanate on Bacterial Viability. In order to visualize the effect of potassium clavulanate on *E. coli* K12 and *E. coli* K12 pUC18 cells, samples either incubated with water only (control), with 125 μM potassium clavulanate (sub-MIC), or with 250 μM of potassium clavulanate (MIC) for 2 hours were used for bacterial viability experiments.

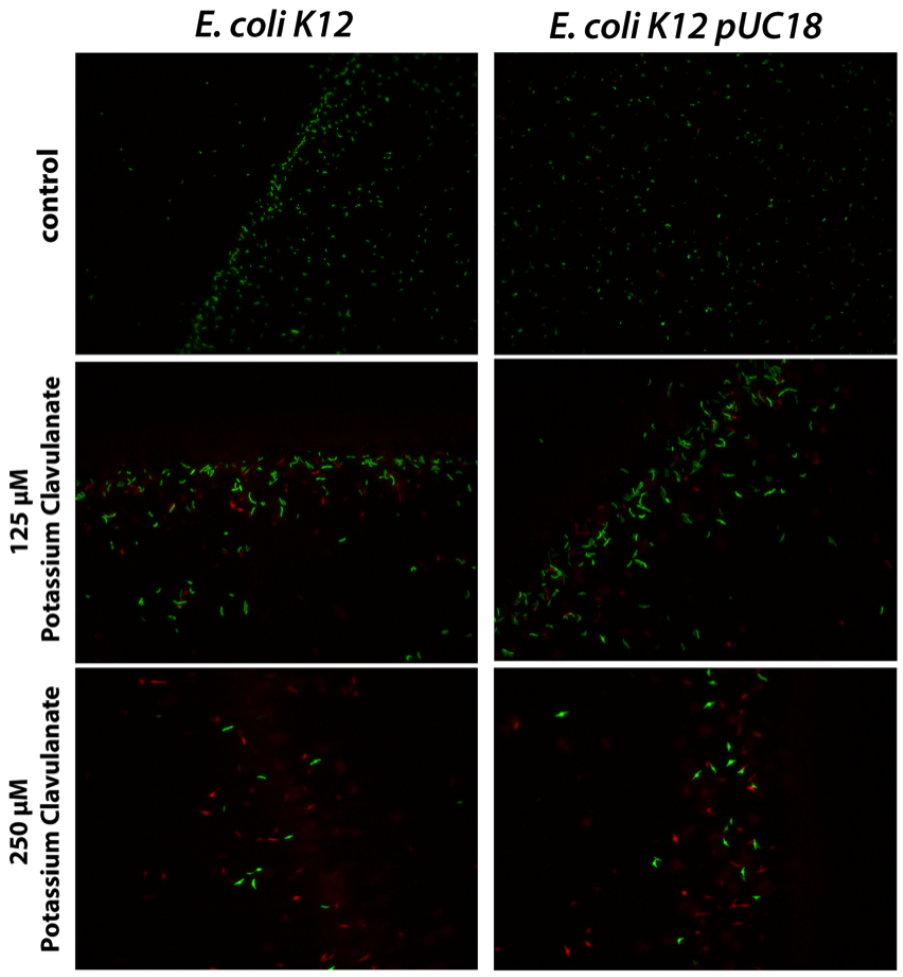

Figure 4.95. Fluorescence microscopy images of *E. coli* K12 (left) and *E. coli* K12 pUC18 (right) cells treated with sub-MIC and MIC of potassium clavulanate, compared with the control samples (top).

Cells treated with water (control) were intact and most of them were live (green) (Figure 4.95). Upon incubation of *E. coli* K12 and *E. coli* K12 pUC18 cells with 125 μM potassium clavulanate (sub-MIC), the live/dead (green/red) cell ratio decreased, and the cell morphology changed (Figure 4.95). A major increase in the cell size and 'bubbly' structures accumulated in the midsection of the cells were observed (Figure 4.95). When the potassium clavulanate concentration was increased to 250 μM (MIC), the bubbles were observed in almost all the cells. Cells were not long and intact anymore; instead their shapes resembled a 'boomerang' with a 'bubble' in the midsection (Figure 4.95).

4.4.1.6. Effect of Potassium Clavulanate & Ampicillin on Bacterial Viability. In order to visualize the effect of potassium clavulanate (PC) & ampicillin combination on antibiotic resistant *E. coli* K12 pUC18 cells, samples either incubated with water only (control), with 3.91 μM PC & 0.39 mg/mL ampicillin (sub-MIC/2), or with 7.81 μM PC & 0.78 mg/mL ampicillin (sub-MIC) for 2 hours were used for bacterial viability experiments.

Upon incubation with 3.91 μM PC & 0.39 mg/mL ampicillin, the number of dead cells increased (when compared to the control sample) and the cells were like 'filaments', suggesting that cell division may also be hindered (Figure 4.96). Upon increasing the concentration to 7.81 μM PC & 0.78 mg/mL ampicillin, almost all the cells were 'dead' and the cell density in the images were low, since PC & ampicillin already inhibited the cell growth (Figure 4.96).

The florescence microscopy studies also suggested that, morphology of cells incubated with the PC-ampicillin combination was different from the cells treated with PC alone. Upon treatment with PC, both wild-type and antibiotic resistant bacteria resembled 'boomerang' with a 'bulge' in the midsection (Figure 4.96). On the other hand, the PC-ampicillin combination treatment of antibiotic resistant bacteria resulted in cell morphology (Figure 4.96) very similar to the ones observed upon treatment of wild-type bacteria with ampicillin (Figure 4.94). Instead of the 'boomerang' shapes

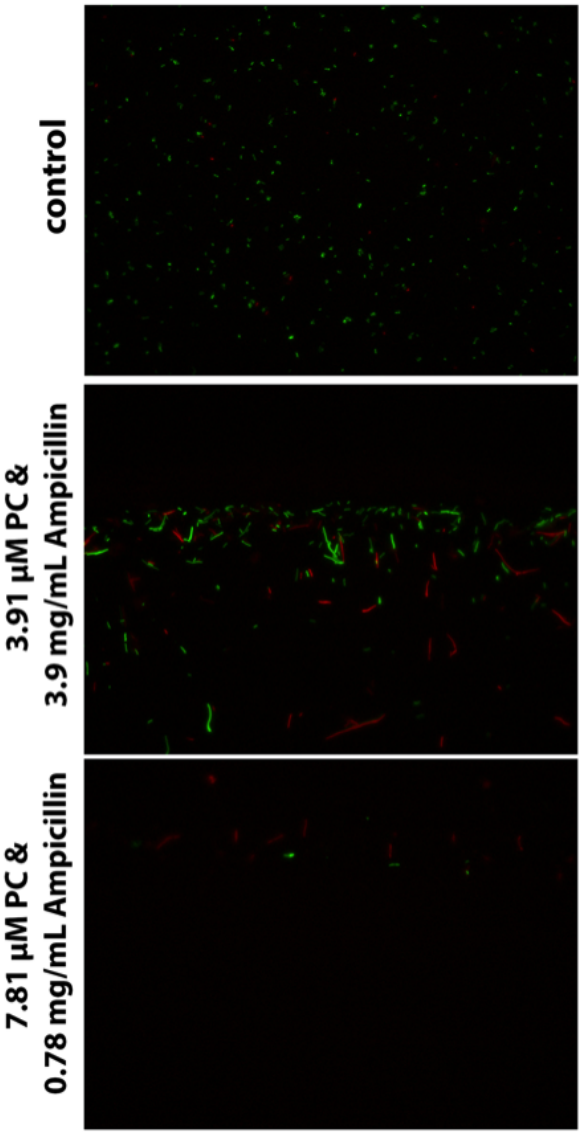

Figure 4.96. Fluorescence microscopy images of *E. coli* K12 pUC18 cells treated with sub-MIC/2 and sub-MIC of potassium clavulanate (PC) & ampicillin combination, compared with the control sample (top).

with a 'bulge' in the midsection, cells were like 'filaments, suggesting that cell division may be hindered (Figure 4.96).

4.4.1.7. Effect of pVEC and del5 pVEC peptides on Bacterial Bacterial Viability. In order to visualize the effect of pVEC and del5 pVEC on *E. coli* K12 cells, samples incubated with 31.25 μM pVEC (sub-MIC), with 62.5 μM of pVEC (MIC), or with

500 μM of del5 pVEC for 2 hours were used and compared with control samples.

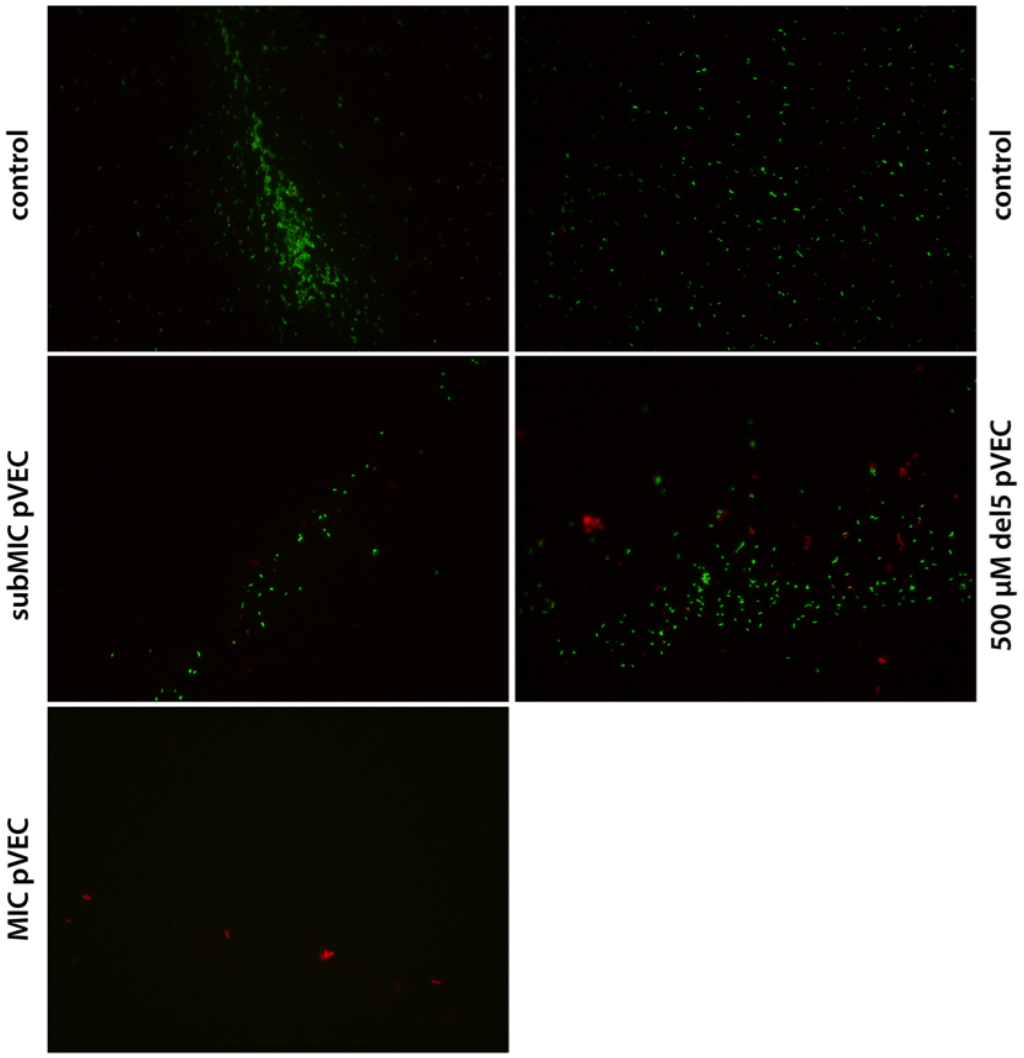

Figure 4.97. Fluorescence microscopy images of control samples and *E. coli* K12 cells treated with pVEC or del5 pVEC peptides. Cells were incubated with SYTO9 and PI nucleic acid dyes before imaging.

Cells treated with DMSO-water mixture (control) were intact and almost all of them were live (green) (Figure 4.97). Upon incubation of *E. coli* K12 cells with 31.25 μM pVEC (sub-MIC), the number of cells in the images was low and the live/dead (green/red) cell ratio decreased (Figure 4.97). Moreover, minor increase in cell size was observed. Upon increasing the concentration to 62.5 μM (MIC), the number of cells decreased considerably in each image and live cells were hardly observed (Figure

4.97). Upon incubation of *E. coli* K12 cells with 500 μM del5 pVEC, the live/dead (green/red) cell ratio decreased (Figure 4.97), even though this ratio was higher than that in the sub-MIC pVEC treated samples.

Fluorescence microscopy images suggest that the antimicrobial action of pVEC causes membrane damage and permeability at sub-MIC and MIC concentrations. Although the MIC of del5 pVEC could not be determined, at 500 μM, we have observed membrane damage and permeability on *E. coli* K12 cells. At this concentration, the number of live cells was higher than that in the sub-MIC pVEC treated samples, suggesting that the growth inhibitory action of del5 pVEC is weaker than pVEC.

4.4.1.8. Effect of P2 Peptide on Bacterial Viability. In order to visualize the viability of the cultures upon incubation with different P2 concentrations (50 and 100 μM), samples (75-100 μM) were withdrawn from the selected wells of the microplate and stained with the bacterial viability kit.

The viability experiments with P2 peptide were carried out by visualizing the 2.5 μL sample cultures (incubated with bacterial viability kit) both by pipetting directly in between the microscopy glasses and onto the agar gel support (Figure 4.98). The average live/dead cell ratio decreased upon incubation of the cells by 100 μM P2 peptide. When the culture samples were visualized with the agar gel support (Figure 4.98) the image quality was better due to the decreased mobility of the bacteria. Moreover, the number of cells visualized was found to be higher, which enables a more accurate analysis of bacterial viability.

4.4.1.9. Effect of P2r Peptide on Bacterial Viability. In order to visualize the viability of the cultures upon incubation with different P2r concentrations (100 and 200 μM), samples (75-100 μL) were withdrawn from the selected wells of the microplate and stained with the bacterial viability kit. The imaging of bacteria was carried out on the agar gel supports that improve image quality and increase the number of cells in each image.

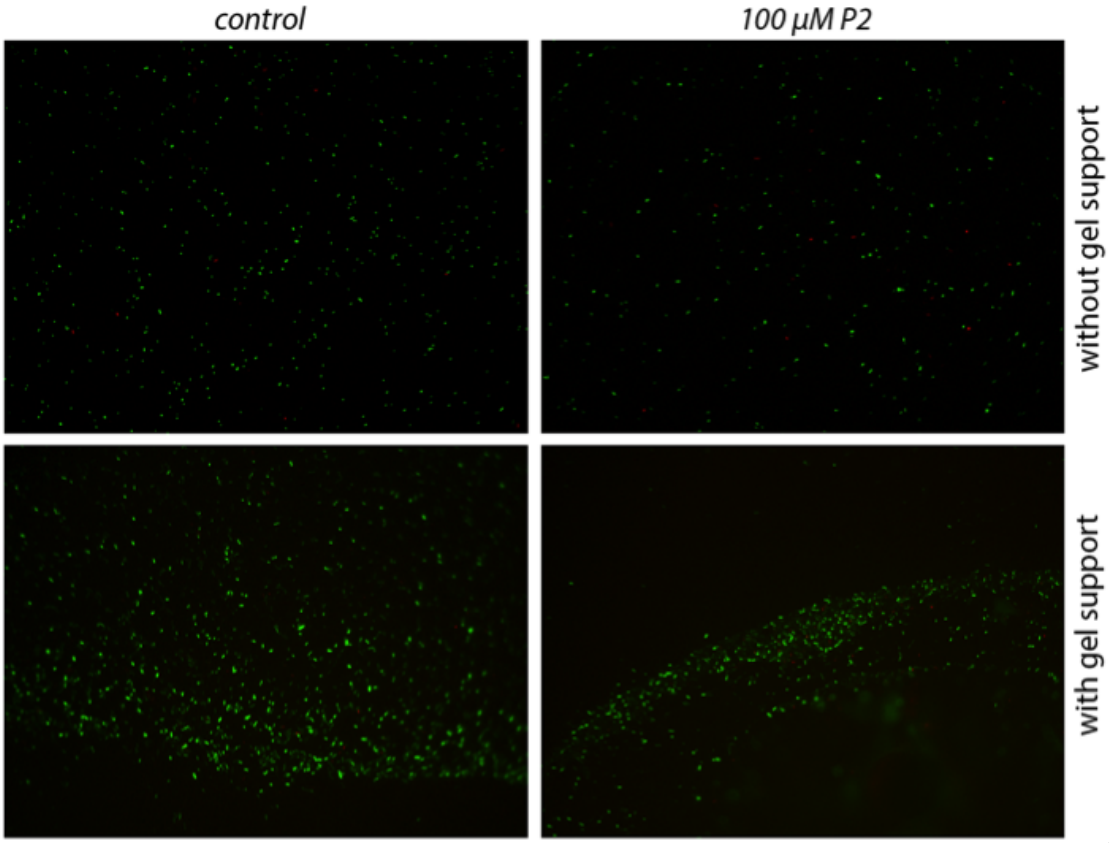

Figure 4.98. Microscopy images of *E. coli* K12 pUC18 cells that were either incubated with buffer solution (left) or 100 μM P2 peptide (right) for four hours. Images captured using green and red microscopy filters were overlaid.

The microscopy images were analyzed using ImageJ software and the number of live or dead cells in each snapshot was counted. The average live/dead cell ratio is lower at increasing peptide concentrations. Moreover, the live/dead cell ratio is lower for the samples treated with peptide compared to that of the control samples. Interestingly, the dead cell clusters observed in snapshots of 200 μM P2r peptide treated cell samples (Figure 4.99) consisted mostly of the bacteria 'filaments' that seem to be growing in length without encountering cell division. On the other hand, the 100 μM P2r peptide treated cells (Figure 4.99) were observed to be consisting of not only the 'filament' like bacteria, but also bacteria that are shorter as well. Overall, the peptide is observed to have destructive effect on the viability and the morphology of the bacteria.

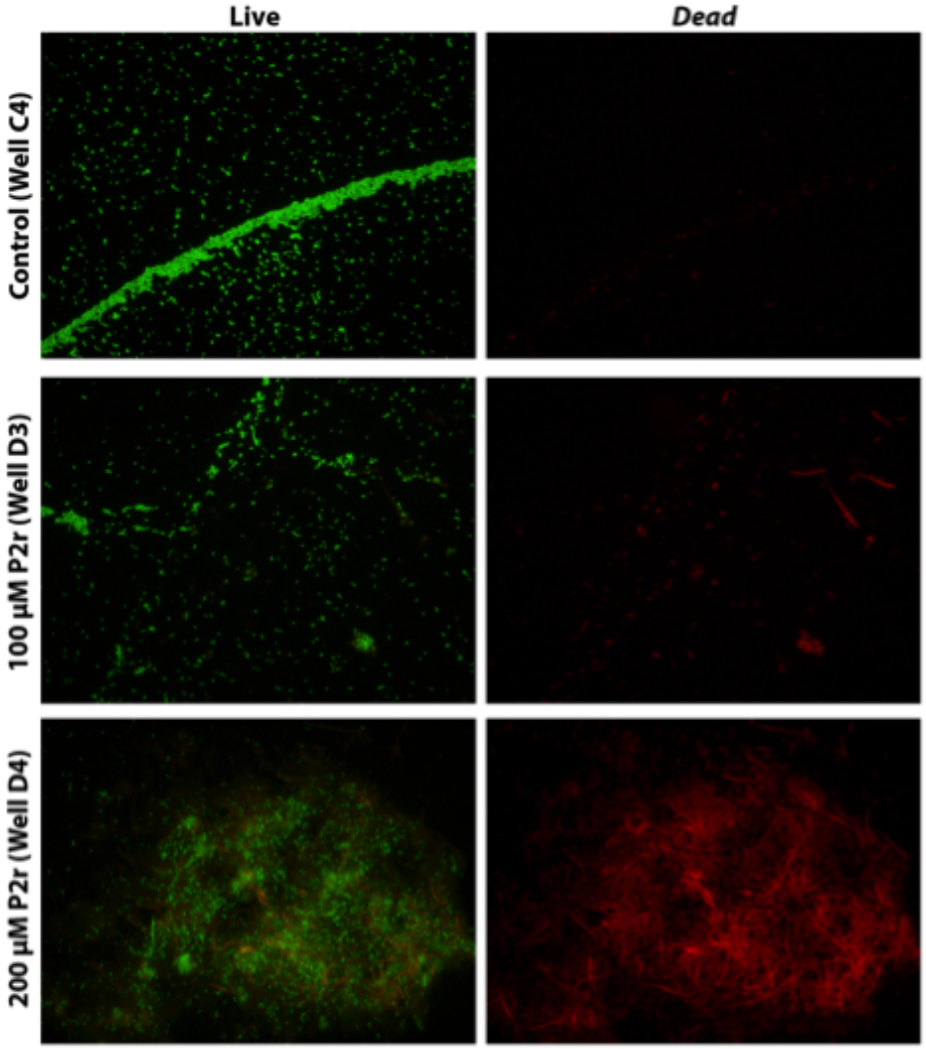

Figure 4.99. Microscopy images of antibiotic resistant *E. coli* K12 pUC18 cultures that were either incubated with buffer solution (top) or with 100 μM P2r peptide (center) or with 200 μM P2r peptide (bottom) for four hours.

In order to compare the effect of P2r peptide on the viability of antibiotic resistant (*E. coli* K12 pUC18) and wild-type (*E. coli* K12) bacteria, the viability experiment was repeated with wild-type bacteria. Figure 4.100 shows the comparison of effect of different concentrations of P2r on viability of the cells. It was observed that the peptide has antibacterial effect on both types of bacteria, but relatively a stronger effect on antibiotic resistant cells.

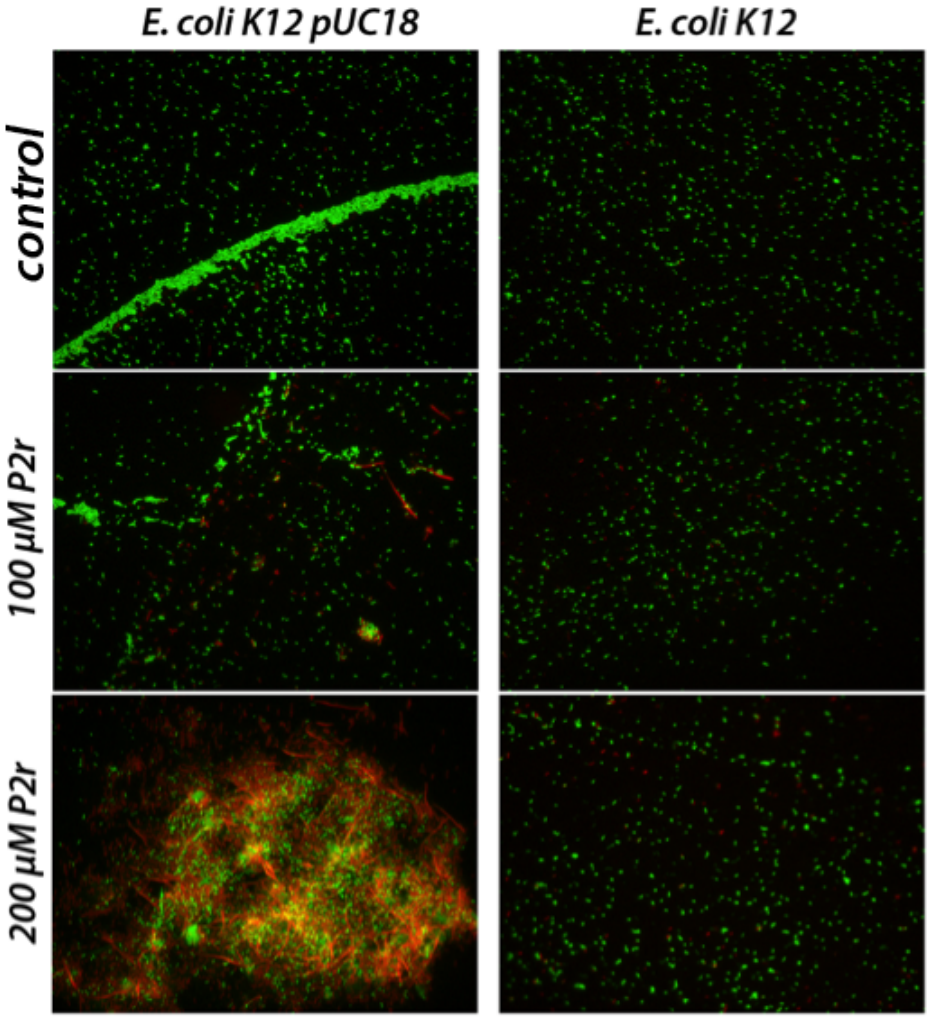

Figure 4.100. Microscopy images of antibiotic resistant (left) and wild-type (right) cultures that were either incubated with buffer solution (top) or with 100 μM P2r peptide (center) or with 200 μM P2r peptide (bottom) for four hours.

4.4.1.10. Effect of P3A Peptide on Bacterial Viability. In order to visualize the viability of the antibiotic resistant *E. coli* K12 pUC18 cultures upon incubation with 100 μM P3A peptide for two or four hours, samples (75-100 μL) were withdrawn from the selected wells of the microplate and stained with the viability kit. The imaging of bacteria was carried out on the agar gel supports. At the end of 2 and 4 hours of incubation, it was observed that the average live/dead cell ratio is similar for the peptide treated and control samples (Figure 4.101). Similar to our results reported on the effect of P3A peptide on bacterial growth, the viability tests show that the P3A

peptide does not have any damaging effect on the membrane integrity of the antibiotic resistant *E. coli* K12 pUC18 cells.

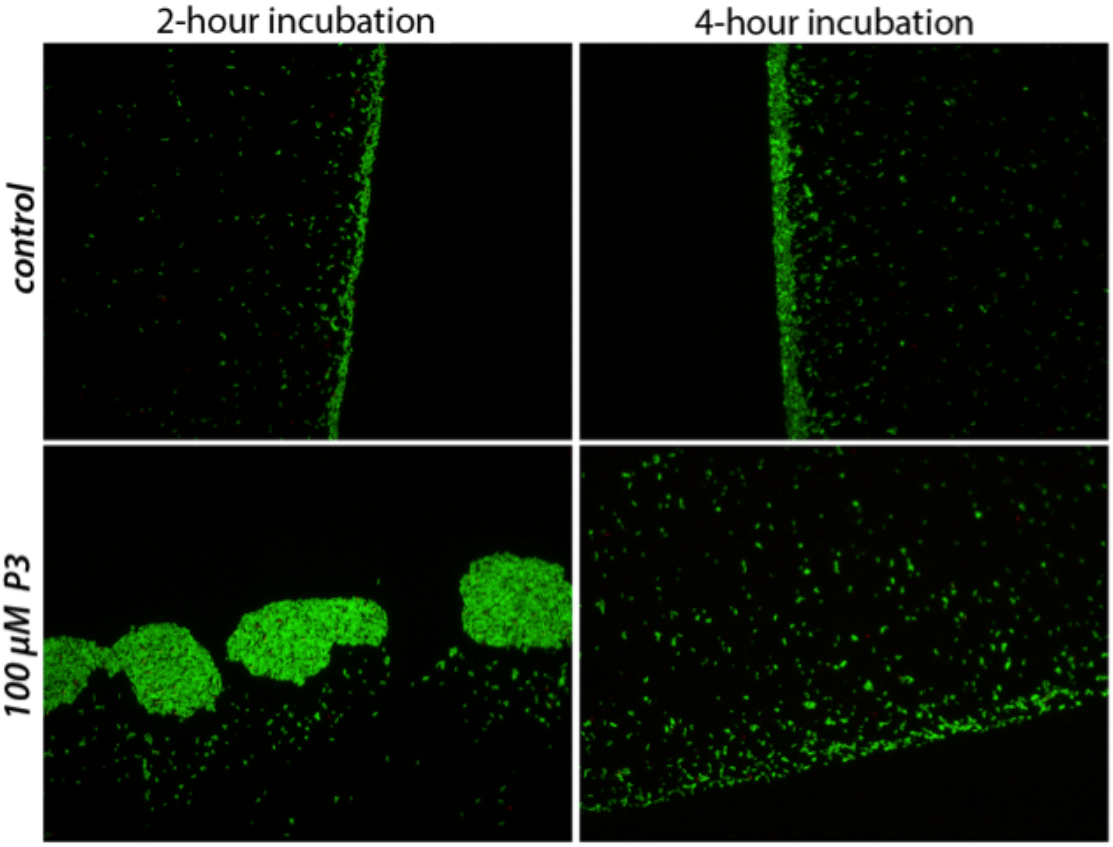

Figure 4.101. Microscopy images of antibiotic resistant *E. coli* K12 pUC18 cultures that were either incubated with buffer solution (top) or with 100 μM P3A peptide (bottom) for two (left) or four (right) hours.

4.4.1.11. Effect of P3 Peptide on Bacterial Viability. In order to visualize the effect of P3 peptide on *E. coli* K12 and *E. coli* K12 pUC18 cells, samples either incubated with water only (control), with 500 μM (test case concentration) P3 for 2 hours were used for bacterial viability experiments.

Cells treated with water (control) were intact and almost all of them were live (green) (Figure 4.102). Upon incubation of *E. coli* K12 and *E. coli* K12 pUC18 cells with 500 μM P3, the live/dead (green/red) cell ratio did not change and almost all of the cells were live (Figure 4.102), suggesting that P3 does not damage the membrane.

Moreover, the number of cells was also similar in the control and P3 treated samples (Figure 4.102). Similar to our MIC and CFU measurement results, the fluorescence microscopy studies also suggested that P3 peptide does not have any antimicrobial or membrane permeabilizer activity on antibiotic resistant *E. coli* K12 pUC18 and wild-type *E. coli* K12 cells.

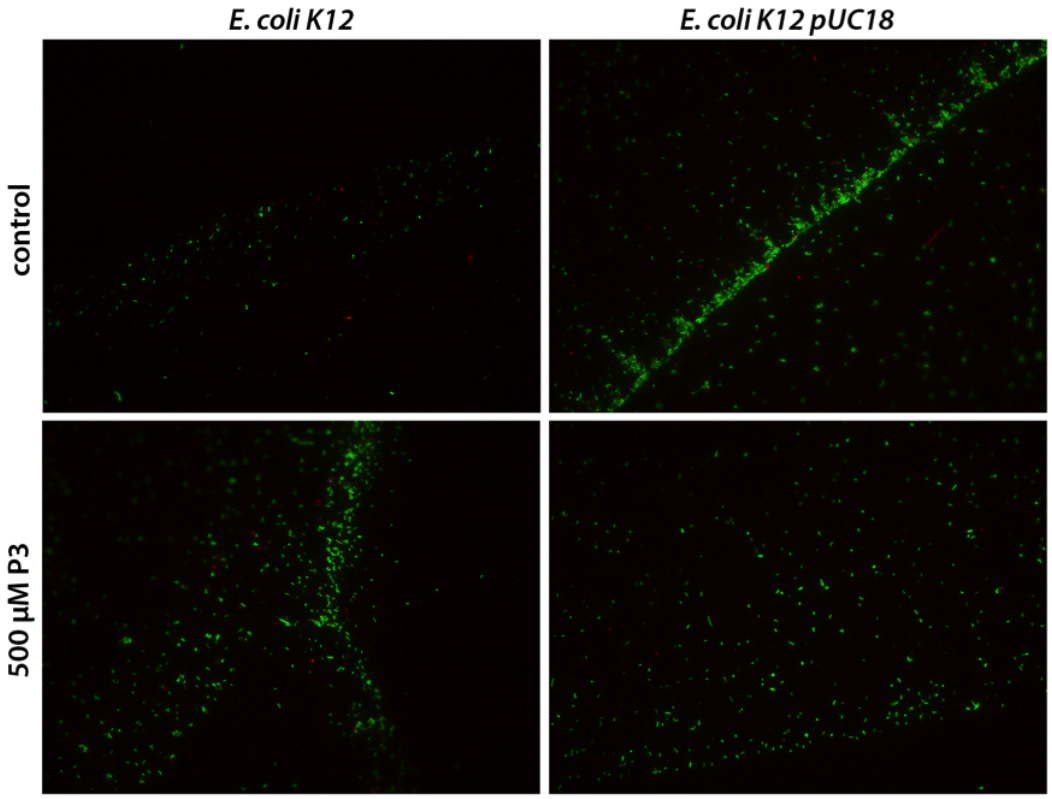

Figure 4.102. Fluorescence microscopy images of *E. coli* K12 (left) and *E. coli* K12 pUC18 (right) cells treated with 500 μM of P3 peptide, compared with the control samples (top).

4.4.1.12. Effect of P4 Peptide on Bacterial Viability. In order to visualize the effect of P4 peptide on *E. coli* K12 pUC18 viability, initial experiments with the first stock solution of P4 was used to incubate the cells for 4 hours at final concentrations of 20, 40 and 80 μM.

The first round of viability experiments with P4 peptide was carried out by visualizing the 2.5 μL sample cultures (incubated with bacterial viability kit) that

were pipetted directly in between the microscopy glasses. The microscopy images were analyzed using ImageJ software and the number of live or dead cells in each image was counted (Figure 4.103). It was observed that the average live/dead cell ratio decreases with increasing peptide concentration.

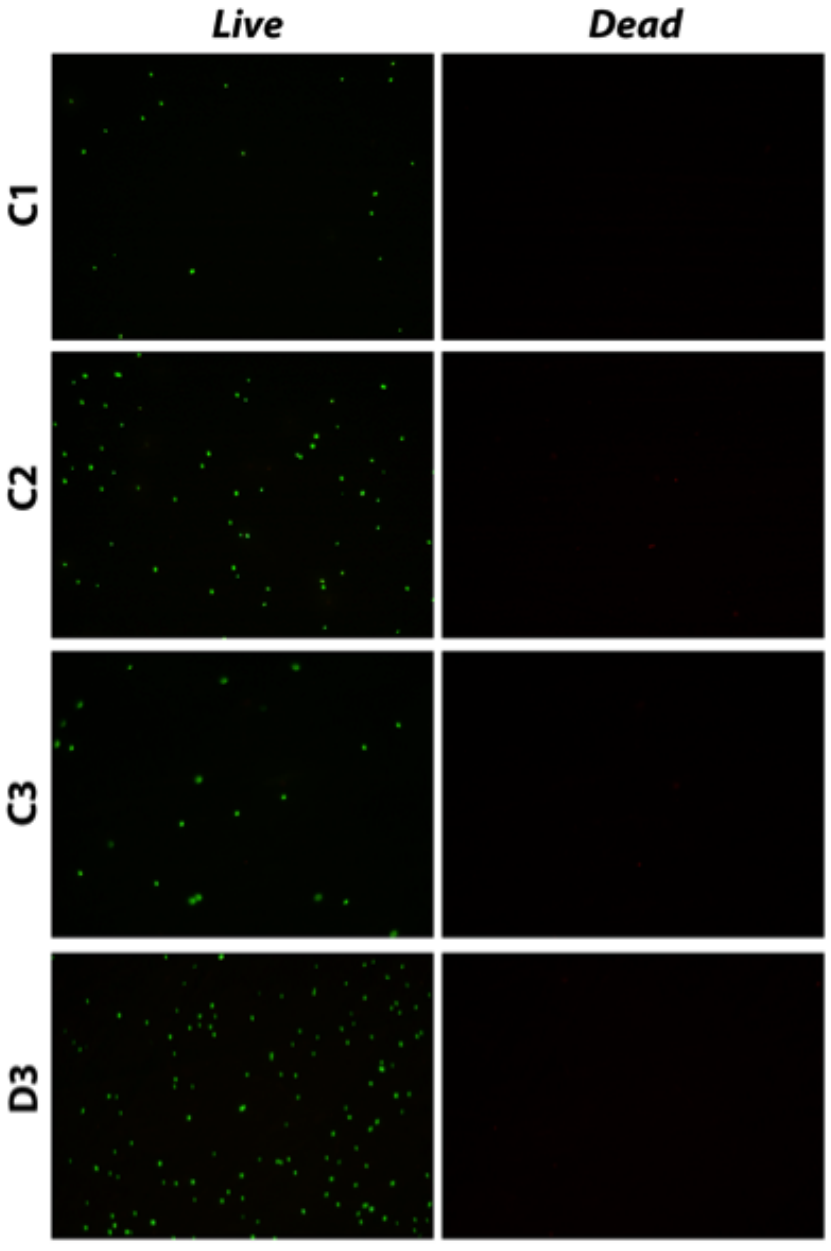

Figure 4.103. Microscopy images of antibiotic resistant *E. coli* K12 pUC18 cultures that were either incubated with buffer solution (D3) or with 20 μM (C1), 40 μM (C2), 80 μM (C3) P4 peptide for four hours.

In the second round of viability experiments with P4 peptide, agar gel supports were used. It was observed that, when the culture samples were visualized with the agar gel support (Figure 4.104) the image quality was better due to the decreased mobility of the bacteria.

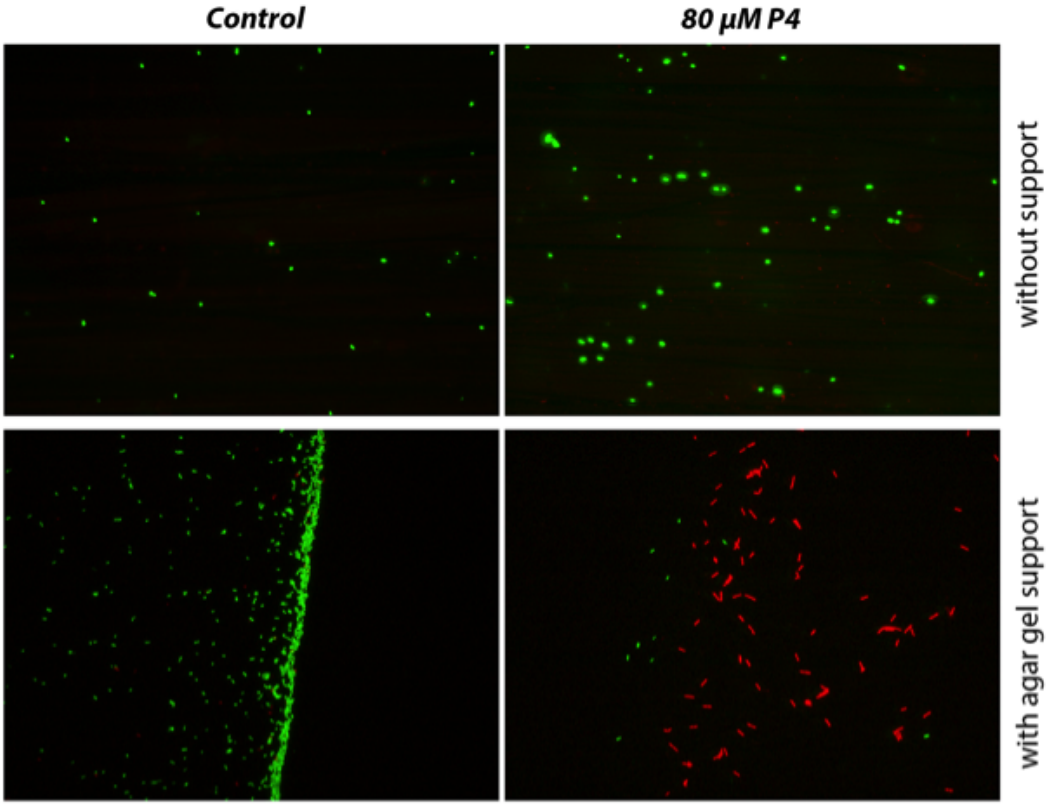

Figure 4.104. Microscopy images of *E. coli* K12 pUC18 cells, either incubated with buffer solution (left) or with 80 μM P4 peptide (right) for two hours, either without agar supports (top), or with agar gel supports (bottom).

The results of the viability experiments repeated with P4 concentrations of 80 and 160 μM are given in Figure 4.105. It was observed that the live/dead cell ratio decreases with increasing peptide concentration and incubation with 160 μM of P4 for two or four hours resulted in membrane damage for almost all of the bacteria.

Since the MIC experiments were repeated with the second stock solution of P4 peptide and the determined MIC values changed, the viability experiments were repeated accordingly. In order to visualize the effect of P4 peptide on *E. coli* K12 and

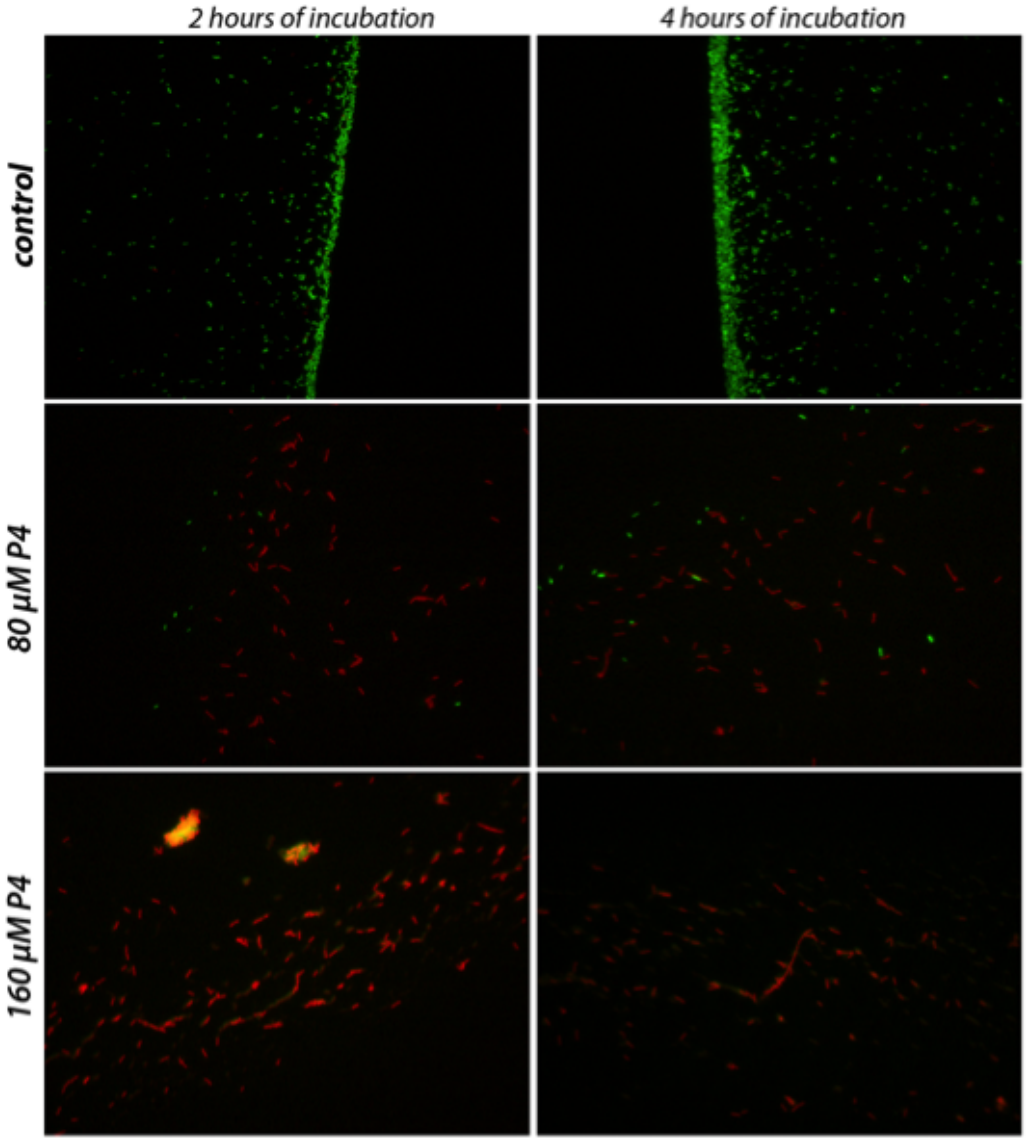

Figure 4.105. Microscopy images of antibiotic resistant cells that were either incubated with buffer solution (top) or with 80 μM P4 peptide (center) or with 160 μM P4 peptide (bottom) for two (left) or four (right) hours.

E. coli K12 pUC18 cells, samples either incubated with water only (control), with 125 μM P4 (sub-MIC), or with 250 μM of P4 (MIC) for 2 hours were used for bacterial viability experiments.

Cells treated with water (control) were intact and almost all of them were live (Figure 4.106). Upon incubation of *E. coli* K12 and *E. coli* K12 pUC18 cells with 125

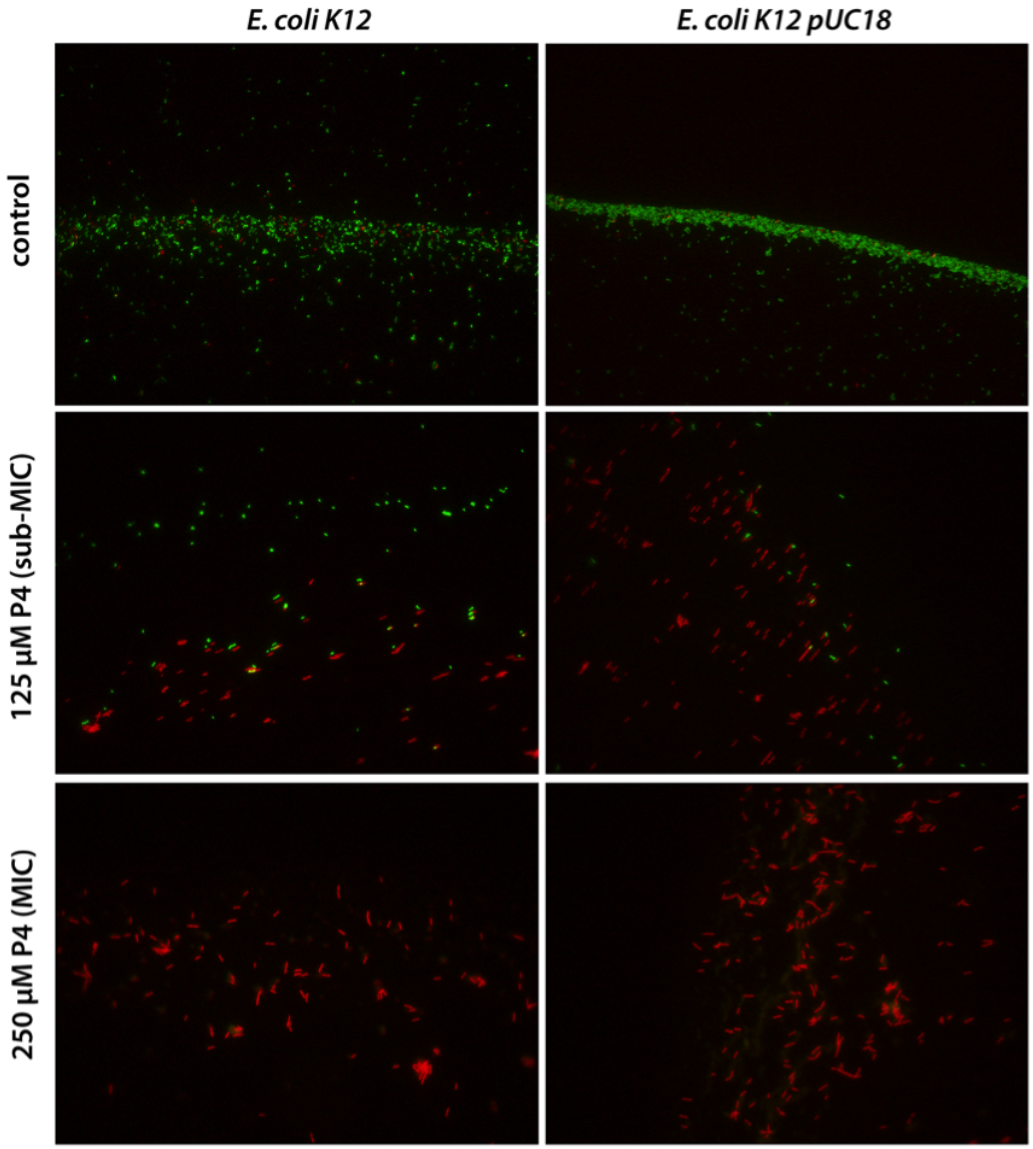

Figure 4.106. Fluorescence microscopy images of *E. coli* K12 (left) and *E. coli* K12 pUC18 (right) cells treated with sub-MIC and MIC of P4 peptide, compared with the control samples (top).

μM P4 (sub-MIC), the live/dead (green/red) ratio decreased, and the cell morphology changed (Figure 4.106). Dead cells were larger and longer when compared to the live cells. Moreover, the live/dead cell ratio was smaller in the *E. coli* K12 pUC18 samples, suggesting that the antimicrobial action of P4 is either stronger or faster for these cells, when compared to *E. coli* K12 cells. Upon increasing the P4 concentration to 250 μM (MIC), all of the *E. coli* K12 and *E. coli* K12 pUC18 cells observed were dead (Figure

4.106). Dead cells were larger and longer when compared to the cells in the control samples (Figure 4.106). These results suggest that P4 effect on morphology is similar for *E. coli* K12 and *E. coli* K12 pUC18 cells. At sub-MIC concentrations of P4, the antimicrobial action may either be faster or stronger against antibiotic resistant *E. coli* K12 pUC18 cells.

4.4.2. Visualization of Drug Effects on Bacteria Using Scanning Electron Microscopy

Membrane perturbation and permeabilization is the first step action of many antimicrobial drugs [22–24]. For this aim, the observation of changes in membrane integrity by electron microscopy (EM) may help to clarify the detailed mechanisms of antimicrobial activity. Scanning electron microscopy (SEM) may be preferred due to its ability to provide high-resolution images to visualize 'protuberances' or 'blebs' related to local disruptions on the bacterial cell envelope by antibacterials [47,101–103].

4.4.2.1. Visualization of Bacteria Using Scanning Electron Microscopy. Before investigation of the drug effects on the cell morphology and membrane structure, as a trial run and a control set, *E. coli* K12 pUC18 cells were visualized under SEM without any peptide incubation.

Figure 4.107 shows some SEM images captured under different magnifications and of different areas on the filter. It was observed that the shape and size of the bacteria were well proportioned (with an average length of 2 μm) and membrane surface of the bacteria were smooth.

The image quality and the possibility of observing the membrane surface were found to be satisfactory; therefore the applied experimental procedure was considered appropriate for SEM imaging.

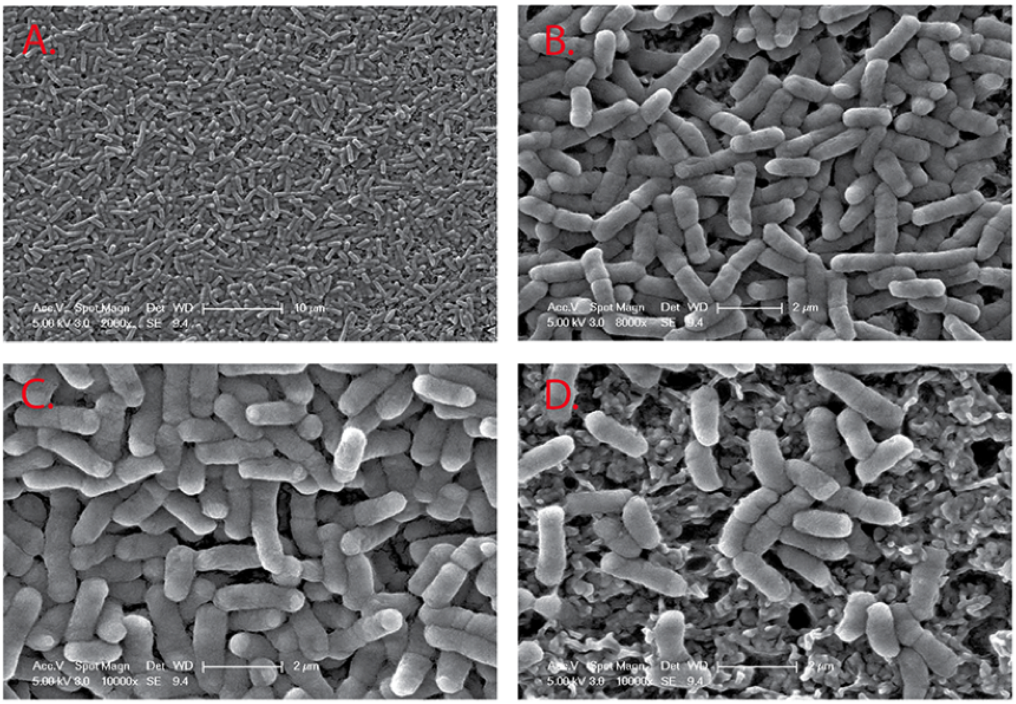

Figure 4.107. SEM images of *E. coli* K12 pUC18 cells. (A) Cells captured at 2000X, and (B) 8000X magnification. (C) At 10000X magnification cell surface can be observed, (D) a less crowded area captured at 10000X magnification.

4.4.2.2. Visualization of DMSO Effects on Cell Surface. *E. coli* K12 pUC18 and *E. coli* K12 samples incubated either with water (control), or 3.125% DMSO (sub-MIC), or 6.25% DMSO (sub-MIC) for 2 hours were used to visualize the effect of DMSO.

E. coli K12 pUC18 and *E. coli* K12 cells alone in water (control) were observed to maintain their integrity with a smooth cell surface (Figure 4.108). When the cells were incubated with 3.125% DMSO for 2 hours, no significant change was observed in the cell surface roughness or the cell size for neither *E. coli* K12 pUC18 nor *E. coli* K12 cells (Figure 4.108). After increasing the DMSO concentration to 6.25%, *E. coli* K12 pUC18 cells were observed to have 'dimples' and 'holes' on the surface (Figure 4.108). The damage caused on *E. coli* K12 pUC18 cells was not observed when *E. coli* K12 cells were treated with 6.25% DMSO (Figure 4.108). Cells were smooth and their average length remained unaltered in general, suggesting that *E. coli* K12 cells can tolerate higher concentrations of DMSO.

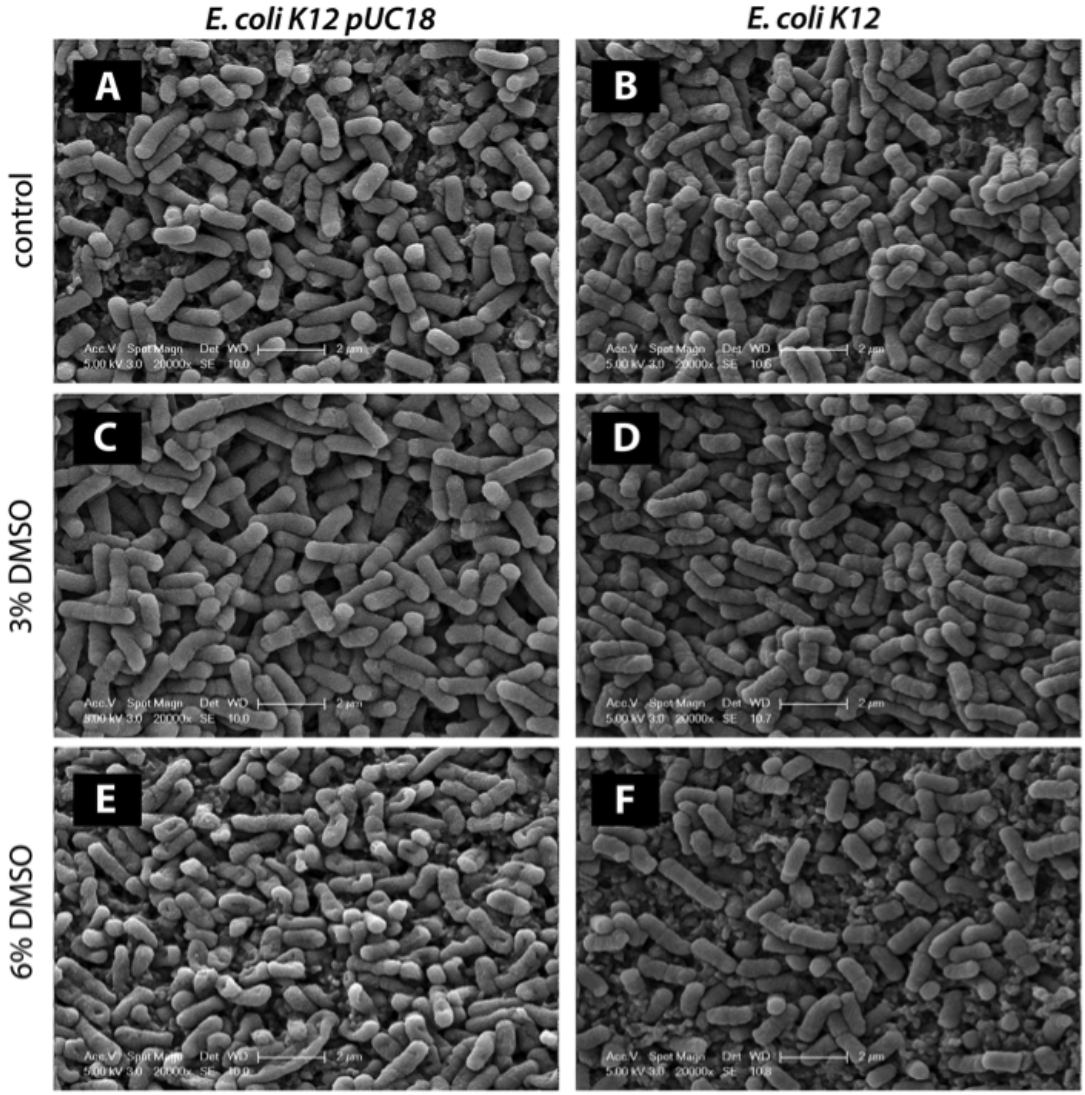

Figure 4.108. SEM images of control samples treated with water (A, B), and DMSO treated *E. coli* K12 pUC18 (C, E) and *E. coli* K12 (D, F) cells.

4.4.2.3. Visualization of Melittin Effects on Cell Surface. The effects of melittin on cell surface was investigated using the first stock solution of melittin with which the MIC was previously determined as 25 μM for both wild-type and antibiotic resistant cells at their high inoculation density.

As the control set, *E. coli* K12 pUC18 cells alone in DMSO-PBS buffer mixture (0.375% DMSO) were observed to maintain their integrity with a smooth cell surface (Figure 4.109).

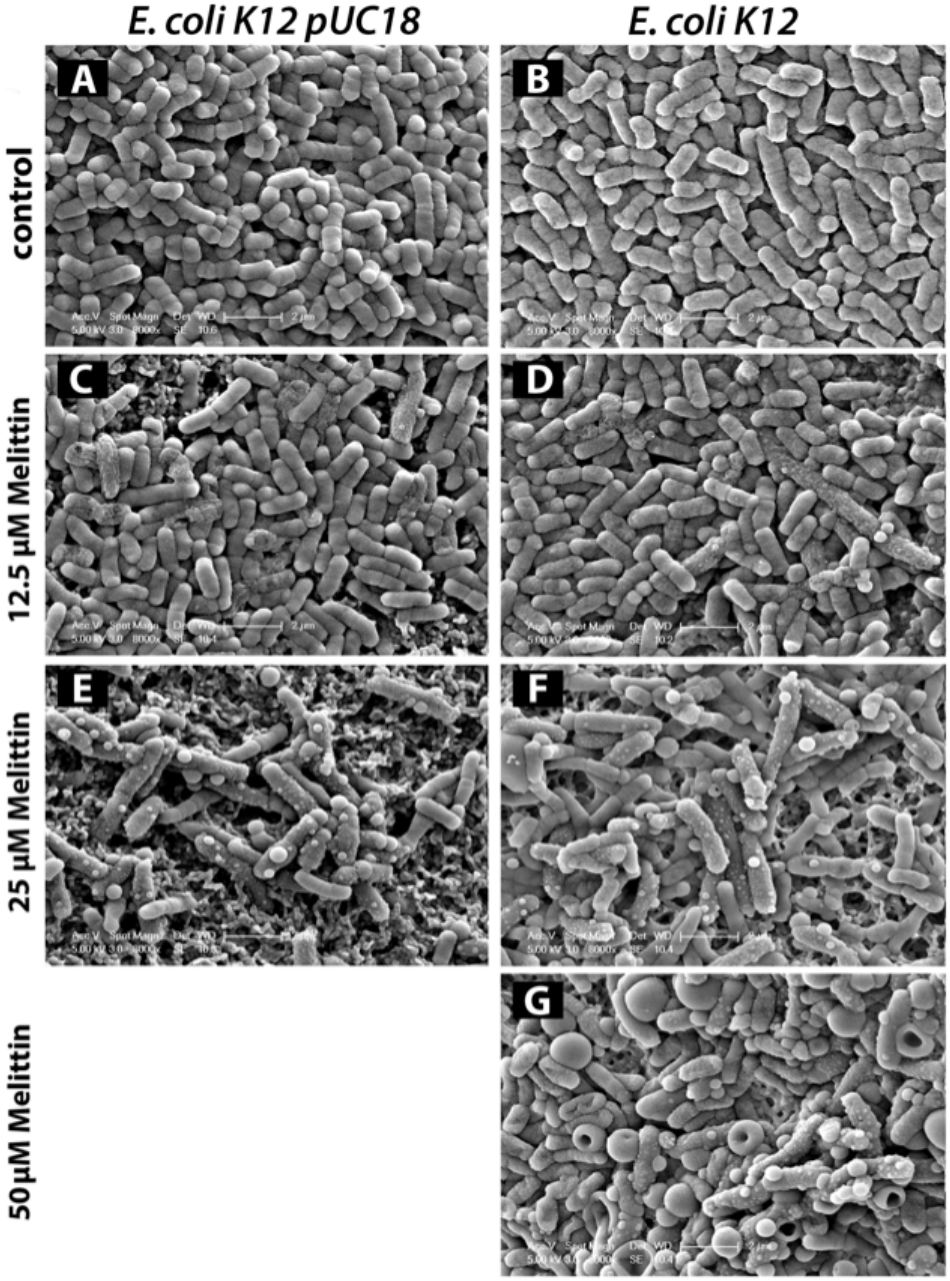

Figure 4.109. SEM images of *E. coli* K12 pUC18 (C and E) or *E. coli* K12 (D, F, and G) cells treated with different concentrations of melittin in comparison with the control samples (A and B). Images are captured with 8000X magnification.

E. coli K12 pUC18 cells treated with 12.5 μM (sub-MIC) of melittin were observed to have corrugated surfaces and new abnormal textures like 'membrane blebs' over the cell surface were observed (Figure 4.109). Incubation of the cells with 25 μM (MIC) of melittin resulted in significant increase in the size and number of 'blebs' forming over

the cell surface, indicating that almost all the cells have damaged membrane (Figure 4.109).

E. coli K12 cells alone in DMSO-PBS buffer mixture (0.375% DMSO) were observed to long and intact with an almost smooth cell surface (Figure 4.109). Upon treatment of the *E. coli* K12 cells with 12.5 μM (sub-MIC) of melittin, some of the cells were observed have corrugated surfaces and 'membrane blebs' over the cell surface (Figure 4.109). After increasing the melittin concentration to 25 μM (MIC), most of the cells were observed to have corrugated surfaces and 'membrane blebs' all over the cell surface (Figure 4.109). Incubation of the cells with 50 μM (supra-MIC) of melittin resulted in abrupt increase in the size of circular 'blebs' agglomerating over the cell surface and the cells were observed to have abnormal shape, unlike the untreated long and rod-shaped *E. coli* (Figure 4.109).

4.4.2.4. Visualization of Ampicillin Effects on Cell Surface. In order to visualize the effect of ampicillin (Amp) on bacteria, cells incubated with water (control), *E. coli* K12 pUC18 cells incubated with 100 mg/mL (sub-MIC) or 200 mg/mL (MIC) ampicillin, *E. coli* K12 cells incubated with 3.05 μg/mL (sub-MIC) or 6.1 μg/mL (MIC) ampicillin for 2 hours were used.

E. coli K12 pUC18 and *E. coli* K12 cells in water (control) maintained their integrity with a smooth cell surface (Figure 4.110). When *E. coli* K12 pUC18 cells were incubated with 100 mg/mL ampicillin (sub-MIC) for 2 hours, cell were mostly elongated (Figure 4.110), suggesting that ampicillin treatment may have an inhibitory effect on bacterial cell division. Moreover, corrugated surface structure, and dimples on the cell surface was observed (Figure 4.110). Upon increasing the ampicillin concentration to 200 mg/mL (MIC), cell elongation was observed and corrugation on the cell surface increased (Figure 4.110).

When *E. coli* K12 cells were incubated with 3.05 μg/mL ampicillin (sub-MIC) for 2 hours, the cell elongation observed in the ampicillin treated *E. coli* K12 pUC18

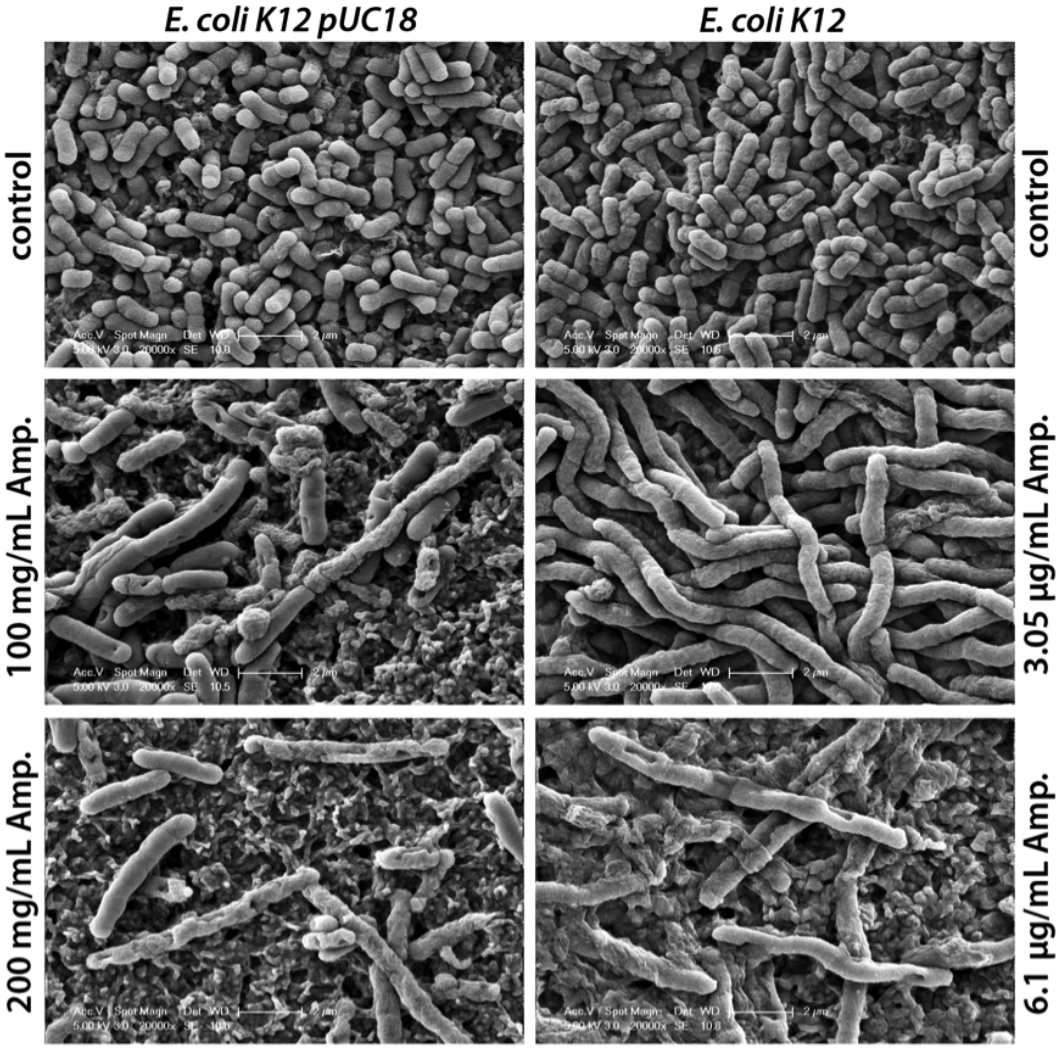

Figure 4.110. SEM images of control samples (top row) and ampicillin treated *E. coli* K12 pUC18 (left column) and *E. coli* K12 (right column) cells.

sample was observed for *E. coli* K12 cells as well (Figure 4.110). Moreover, some of the cells had corrugated surface, indicating the initiation of the antimicrobial action. After increasing the ampicillin concentration to 6.1 μg/mL (MIC), most of the cells have lost their integrity, large membrane ruptures on the cell surface and cell residuals could be observed (Figure 4.110). Similar to the 3.05 μg/mL ampicillin treated samples; cell elongation was observed for all the cells.

Although the MIC and sub-MIC values of ampicillin determined against antibiotic resistant *E. coli* cells were much higher when compared to those of wild type *E.*

coli cells, the effect of ampicillin on cell morphology and surface structure was similar. The common effect of ampicillin treatment in all tested concentrations with antibiotic resistant *E. coli* K12 pUC18 and wild-type *E. coli* K12 cells was cell elongation, suggesting that ampicillin has an inhibitory effect on bacterial cell division.

4.4.2.5. Visualization of Potassium Clavulanate Effects on Cell Surface. *E. coli* K12 pUC18 and *E. coli* K12 samples incubated either with water (control), or 125 μM (sub-MIC), or 250 μM (MIC) potassium clavulanate (PC) for 2 hours were used to visualize the effect of potassium clavulanate.

E. coli K12 pUC18 and *E. coli* K12 cells in water (control) maintained their integrity with a smooth cell surface (Figure 4.111). When *E. coli* K12 pUC18 and *E. coli* K12 cells were incubated with 125 μM PC (sub-MIC) for 2 hours, the cells had corrugated surfaces (Figure 4.111). Moreover, the cell shape became 'curved' like a 'boomerang' instead of the conventional rod-shape of the control samples, which suggests either the disruption of the cell integrity or accumulation of the cell content around the division plane (Z ring) of a mother cell. The cells were much larger when compared to the cells in the control samples.

When the PC concentration was increased to 250 μM (MIC), the cells had corrugated surfaces and cell shape was distorted (Figure 4.111). More cell material accumulated in the middle of the cells when compared with the cells that were treated with 125 μM PC. The increase in the size of each cell was larger, forming a 'croissant-like' cell shape, suggesting that cell material keeps increasing in each cell, without undergoing a cell division. The cells will likely keep getting 'fatter' and the cell surface will keep stretching until the cells burst.

The common effect of PC treatment in all tested concentrations was the increase in the size of the cells and accumulation of the cell material in the middle of the cells. The effect of PC was similar for both *E. coli* K12 pUC18 and *E. coli* K12 cells, suggesting that the drug does not have any cell specificity.

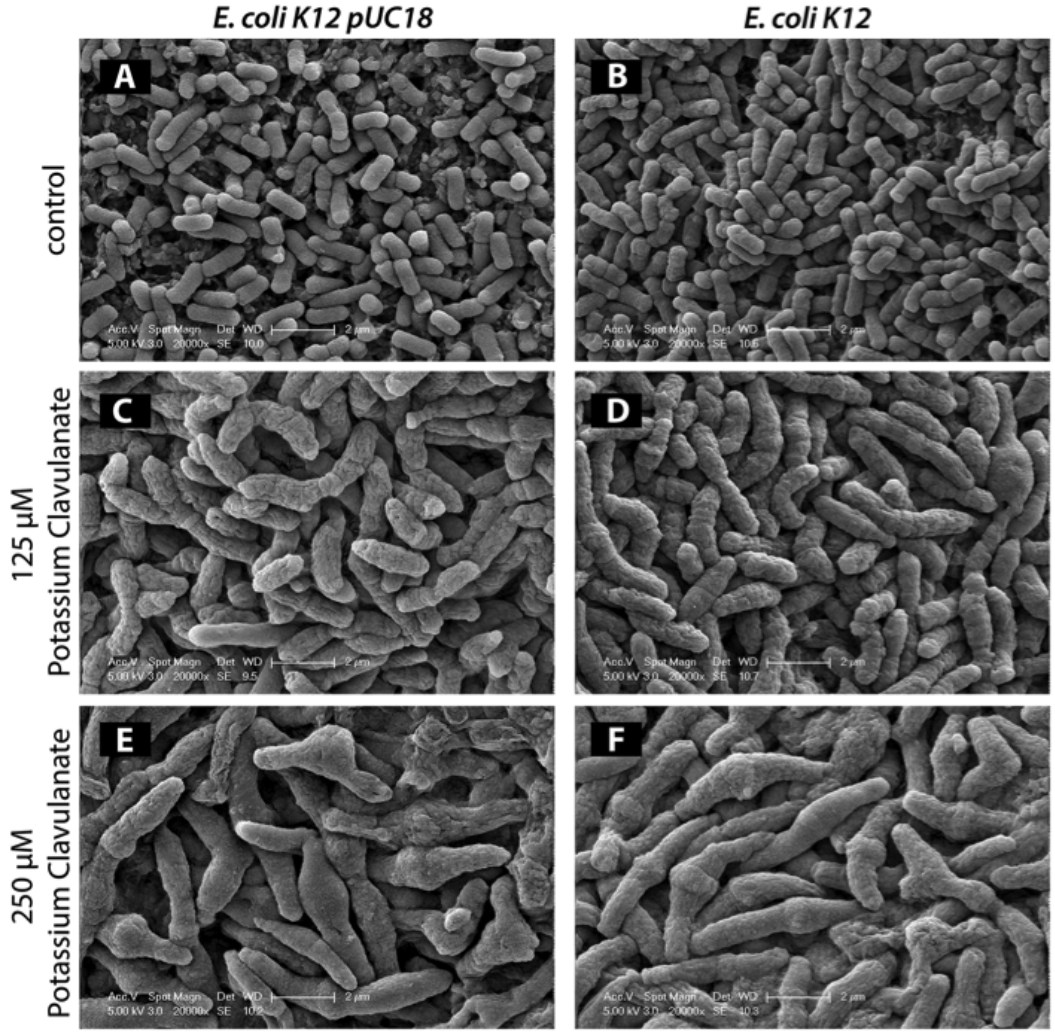

Figure 4.111. SEM images of control samples (A, B) and potassium clavulanate treated *E. coli* K12 pUC18 (C, E) and *E. coli* K12 (D, F) cells.

4.4.2.6. Visualization of Potassium Clavulanate & Ampicillin Effects on Cell Surface.
In order to visualize the effect of the combination of potassium clavulanate (PC) and ampicillin (Amp), *E. coli* K12 pUC18 cells incubated with 3.9 μM PC & 0.39 mg/mL Amp (sub-MIC/2) or 7.81 μM PC & 0.78 mg/mL Amp (sub-MIC) were visualized and compared to the control samples (Figure 4.112).

E. coli K12 pUC18 cells treated with 3.9 μM PC & 0.39 mg/mL Amp had 'dimples' on the surface (Figure 4.112). After increasing the concentration to 7.81 μM PC & 0.78 mg/mL Amp, the cells had deeper 'dimples' and 'holes' on the surface.

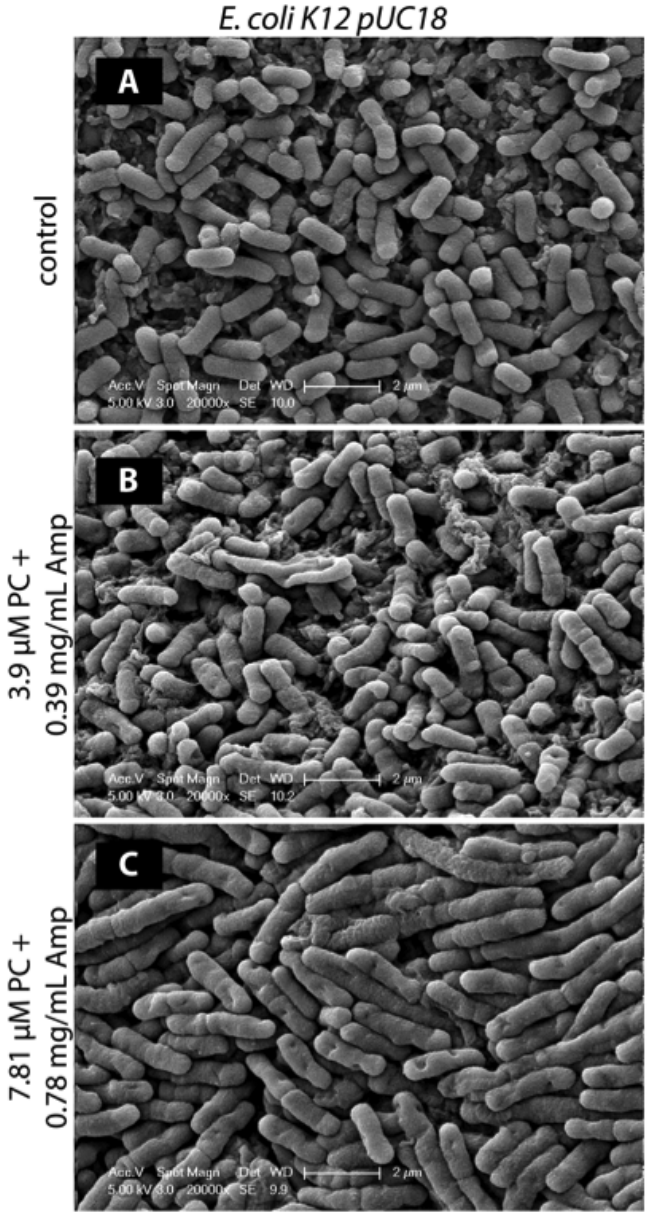

Figure 4.112. SEM images of control sample (A) and *E. coli* K12 pUC18 cells treated with different concentrations of the potassium clavulanate (PC) and ampicillin (Amp) combination (B, C).

Moreover, cell elongation observed in the ampicillin treated samples was observed once again (Figure 4.112).

Although ampicillin alone (0.78 mg/mL or lower concentrations) or PC alone (7.81 μM or lower concentrations) does not have any inhibitory effect on growth of *E.*

coli K12 pUC18 cells (Figure 4.112), their combination results in growth inhibition and deformation on the cell surface. The defects observed upon treatment of the cells with the PC and ampicillin combination resemble the defects observed after the ampicillin treatment of the wild-type *E. coli* K12 cells. These observations may suggest that PC and ampicillin take action in an interrelated mechanism. If PC alone could inhibit the intracellular beta-lactamase, then the cells would behave like beta-lactamase-free cells and they could be inhibited by the addition of ampicillin.

4.4.2.7. Visualization of pVEC and del5 pVEC Peptide Effects on Cell Surface. In order to visualize the effect of pVEC and del5 pVEC peptides on bacteria, *E. coli* K12 samples incubated with DMSO-water mixture (control), with 31.25 μM (sub-MIC) of pVEC, with 62.5 μM (MIC) of pVEC, with 250 μM of del5 pVEC, or with 500 μM of del5 pVEC for 2 hours were used.

E. coli K12 cells alone in DMSO-water mixture (control) were observed to maintain their integrity with a smooth cell surface (Figure 4.113). Upon incubation of the *E. coli* K12 cells with 31.25 μM pVEC (sub-MIC) for 2 hours, the cells had corrugated surfaces (Figure 4.113). The size of the cells was larger when compared to the cells in the control samples. Dimples and holes over the cell surface were observed for all the cells. After increasing the pVEC concentration to 62.5 μM (MIC), the corrugation on the surface of cells increased (Figure 4.113). The increase in the size of the cells was larger, and membrane ruptures over the surface were observed.

Upon incubation of the cells with 250 μM del5 pVEC for 2 hours, no major change in the shape of the cells was observed when compared to that in the control samples (Figure 4.113). A minor increase in the cell size, and little membrane blebs over the surface of some cells were observed in the del5 pVEC treated samples (Figure 4.113). After increasing the del5 pVEC concentration to 500 μM (MIC), corrugation on the surface of cells was observed (Figure 4.113). Some of the cells were 'curved', and the size and number of membrane blebs increased.

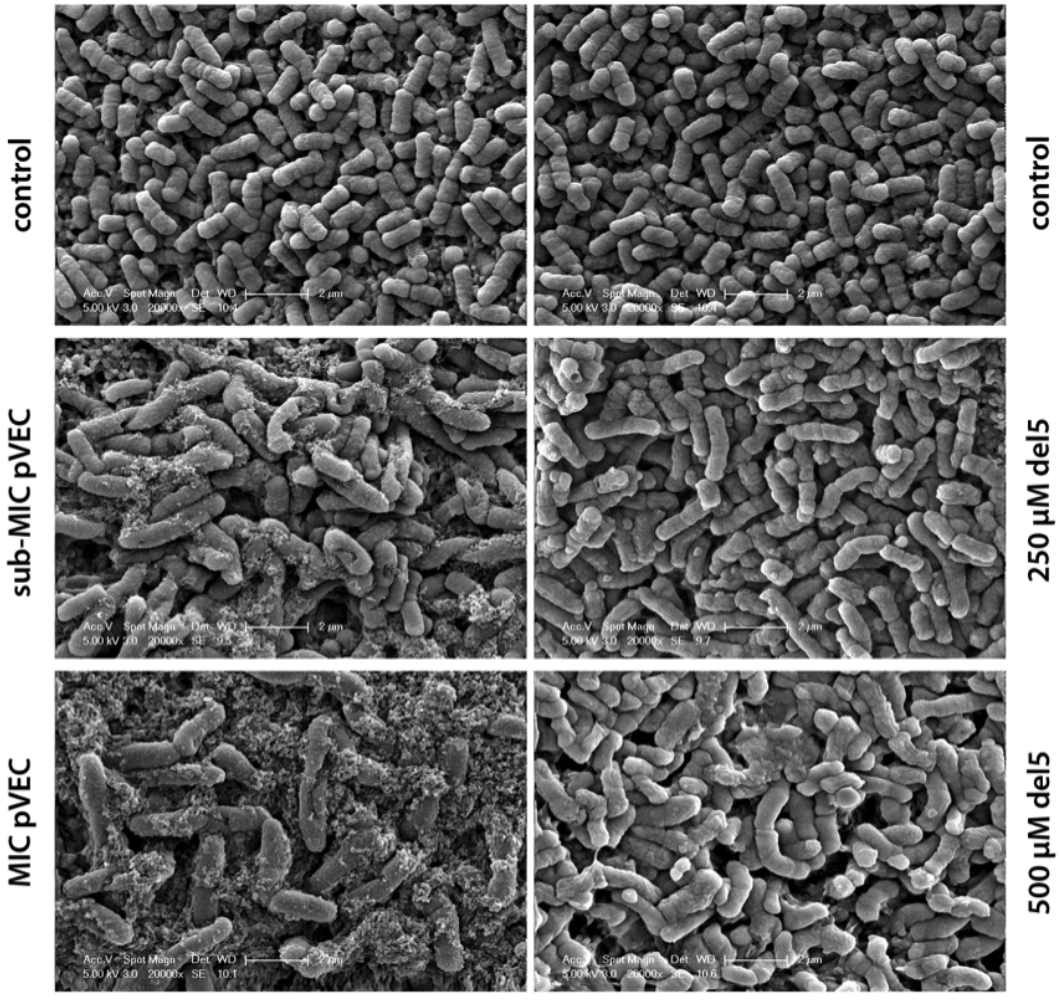

Figure 4.113. SEM images of control samples (top row) and *E. coli* K12 cells treated with pVEC (left column) or del5 pVEC (right column) peptides.

Microscopy experiments showed that while both peptides cause membrane permeability, the action of pVEC and del5 pVEC are different in terms of effect on the cell surface. While pVEC causes increase in the cell size, surface corrugation and membrane ruptures, treatment with del5 pVEC results in the formation of membrane blebs. The results suggest that even though the deletion of the first 5 residues (LLIIL) diminishes the antimicrobial action of the pVEC peptide, del5 pVEC may also possess minor antimicrobial effects on *E. coli* K12 cells.

4.4.2.8. Visualization of P2r Peptide Effects on Cell Surface. In order to visualize the effect of P2r peptide on bacteria, *E. coli* K12 or *E. coli* K12 pUC18 cells were incubated either with DMSO-water mixture (control) or with 100 μM of P2r for 2 hours.

The damage caused by incubation with 100 μM P2r on *E. coli* K12 pUC18 cells (Figure 4.114) is similar to the one observed upon treatment with P4 peptide. Most of the cells have 'cracks' and 'holes' on the surface, some of which are large enough to cause membrane rupture. Moreover, most of the cells treated with P2r were observed to be shorter in size when compared to the control sample (Figure 4.114) and they were often found in clumps, suggesting that the peptide may have an effect on the growth and division of the cells.

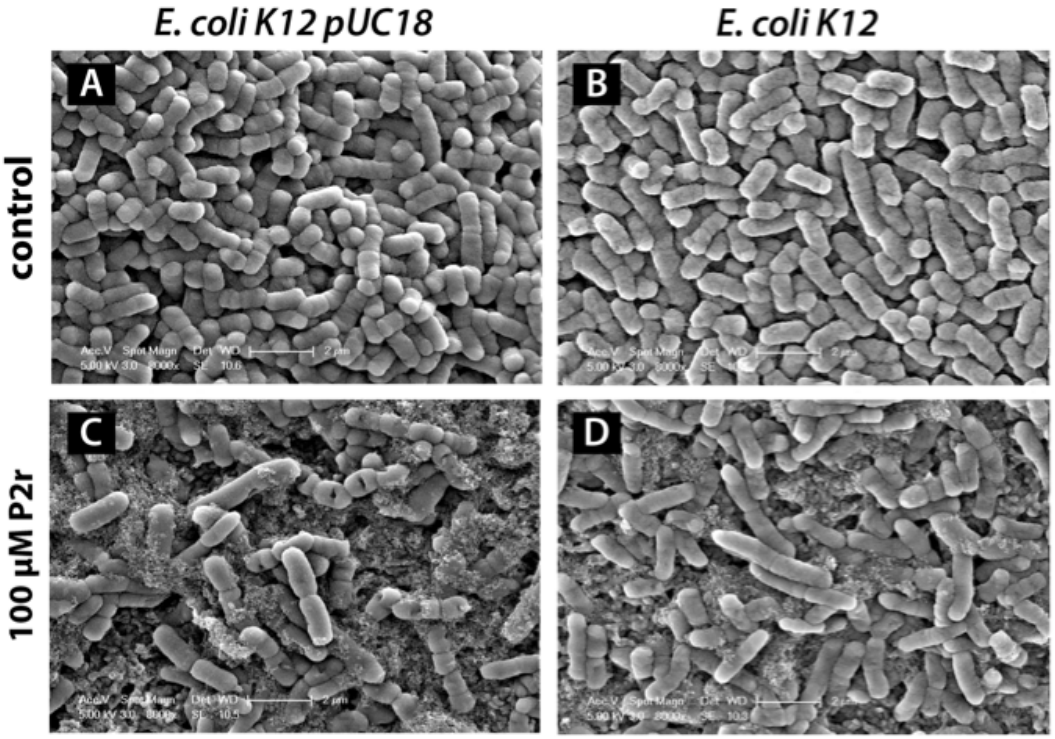

Figure 4.114. SEM images of *E. coli* K12 pUC18 (C) or *E. coli* K12 (D) cells treated with 100 μM P2r peptide in comparison with the untreated cells (A and B). Images are captured with 8000X magnification.

E. coli K12 cells incubated with 100 μM P2r (Figure 4.114) were observed to be slightly damaged on the surface and the cells were mostly observed to be long and

intact when compared to the control sample (Figure 4.114). Only some of the cells were observed to have small 'cracks' on the surface, suggesting that the membrane disruptive effect of P2r is selective to antibiotic resistant *E. coli*.

It is also important to note that, nanoparticles of peptide precipitates were observed in the samples treated with P2r (Figure 4.114), suggesting the low peptide solubility and low amount of effective peptide in the medium. P2r precipitates were well distributed, although they were observed to fill the pores of the membrane filter.

4.4.2.9. Visualization of P4 Peptide Effects on Cell Surface. In order to visualize the effect of P4 peptide on bacteria, *E. coli* K12 or *E. coli* K12 pUC18 cells were incubated either with DMSO-water mixture (control) or with 80 μM of P4 peptide (first stock solution) for 2 hours.

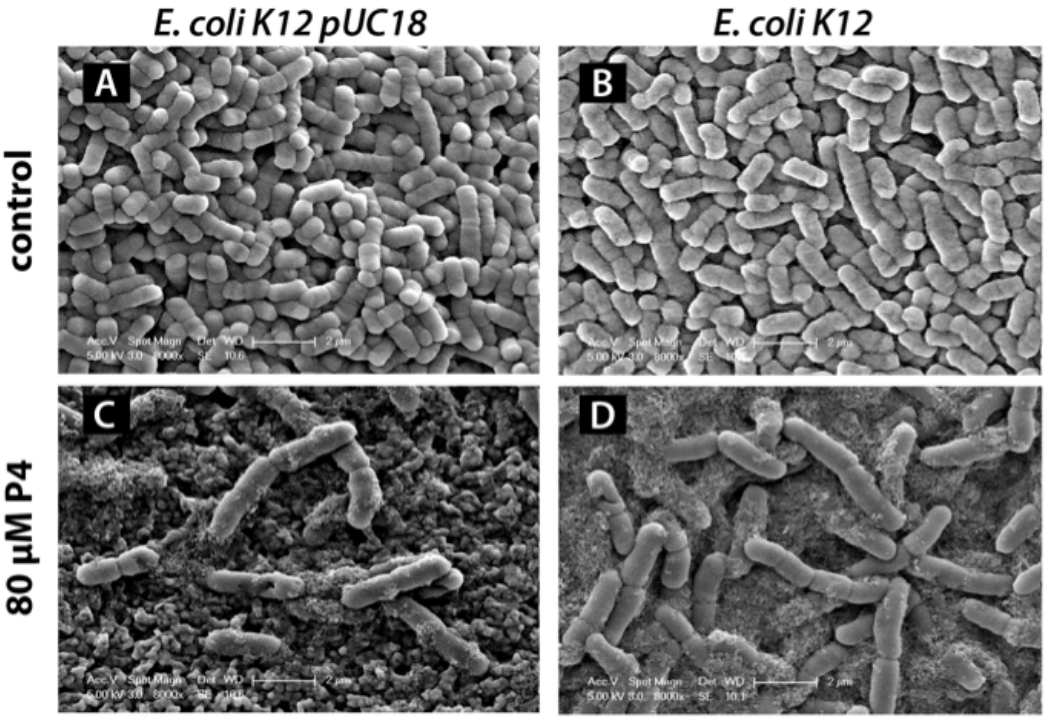

Figure 4.115. SEM images of *E. coli* K12 pUC18 (C) or *E. coli* K12 (D) cells treated with 80 μM P4 peptide in comparison with the untreated cells (A and B). Images are captured with 8000X magnification.

E. coli K12 pUC18 cells incubated with 80 μM P4 (Figure 4.115) had damaged cell surface. Although the surface of the cells was smooth and average cell length remained unaltered when compared to the control sample (Figure 4.115), most of the cells had 'dimples' on the surface, most of the time deep enough to resemble 'holes' in the middle of the cells.

E. coli K12 cells treated with 80 μM P4 (Figure 4.115) had smooth cell surface and the average cell length remained unaltered when compared to the control sample (Figure 4.115). Similar to our previous observations on the effect of this peptide on *E. coli* K12 pUC18 cells, some of the cells had 'dimples' on the surface, but the damage seemed scarcer for the wild-type *E. coli*.

Similar to our previous observations with the P2r peptide, peptide precipitates were observed in the samples treated with P4 (Figure 4.115) as well. While the P2r precipitates were well distributed in the SEM images, the P4 precipitates were observed to be mostly 'stuck' on the cell surface suggesting once again that the low peptide solubility and the low effective amount of peptide in the medium.

The SEM experiments with P4 were repeated since two different stock solutions were used in the MIC determination experiments. For the second round of SEM experiments with the second stock solution of P4 peptide, antibiotic resistant *E. coli* K12 pUC18 and wild-type *E. coli* K12 cells incubated with DMSO-water mixture (control), with 125 μM (sub-MIC) or 250 μM (MIC) of P4 peptide for 2 hours were used.

E. coli K12 cells in water (control) maintained their integrity with a smooth cell surface (Figure 4.116). Upon incubation of resistant and wild type *E. coli* cells with 125 μM (sub-MIC) P4 for 2 hours, an increase in the cell size was observed (Figure 4.116). Moreover, the conventional rod shape was distorted and some of the cells had 'dimples' on the surface. After increasing the P4 concentration to 250 μM (MIC), the 'dimples' and 'holes' on the surface were deeper and larger (Figure 4.116). It should be noted that, nanoparticles of peptide precipitates were observed during SEM imaging for the samples treated with P4 indicating the low solubility of this peptide, which

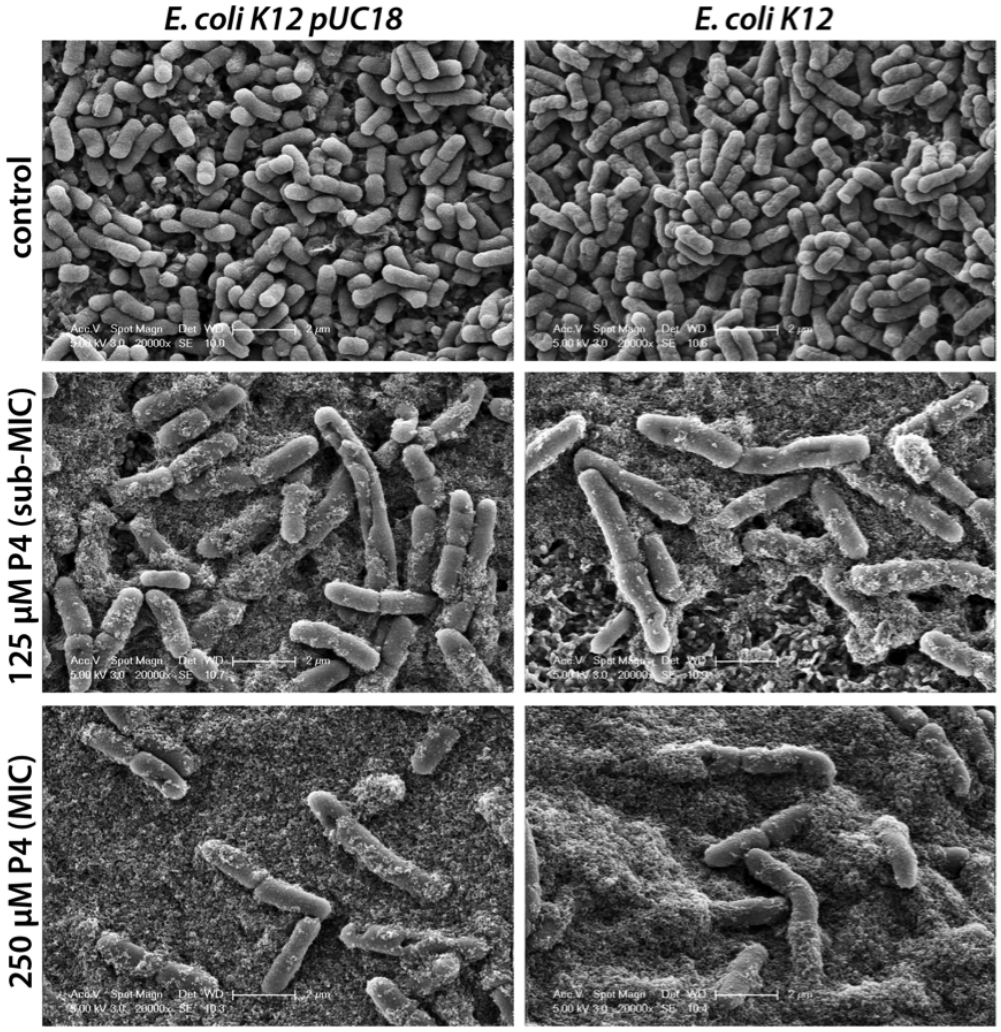

Figure 4.116. SEM images of control samples (top row) and P4 peptide treated *E. coli* K12 pUC18 (left column) and *E. coli* K12 (right column) cells.

could have resulted in a decreased concentration of the active peptide in medium. The results suggest that the effect of P4 peptide on cell surface and membrane damage is similar for antibiotic resistant and wild-type bacteria.

4.4.3. Visualization of Peptide Uptake

The main goal of the study was to design chimeric peptides that can penetrate into bacteria to reach and inhibit the periplasmic beta-lactamase enzyme. With this aim, beta-lactamase inhibitory peptides were modified to enhance their bacterial uptake. All

peptides were tested on wild-type and antibiotic resistant *E. coli* strains to investigate if they have antimicrobial properties. Here, the peptides were tested to see if they can penetrate into bacteria. By attaching fluorophore molecules to peptides P1, P2, pVEC, and P4 fluorescent peptides were obtained. These fluorescent peptides were used to incubate bacteria and culture samples were visualized under fluorescence microscopy to investigate the bacterial uptake of the peptides.

4.4.3.1. Visualization of P1 and P2 Uptake Using Confocal Microscopy. In order to visualize the bacterial uptake of P1 and P2 peptides, *E. coli* K12 pUC18 cells were incubated with fluorescein labeled P1 and fluorescein labeled P2 at a final concentration of 100 μM and samples were withdrawn after 4 hours of incubation.

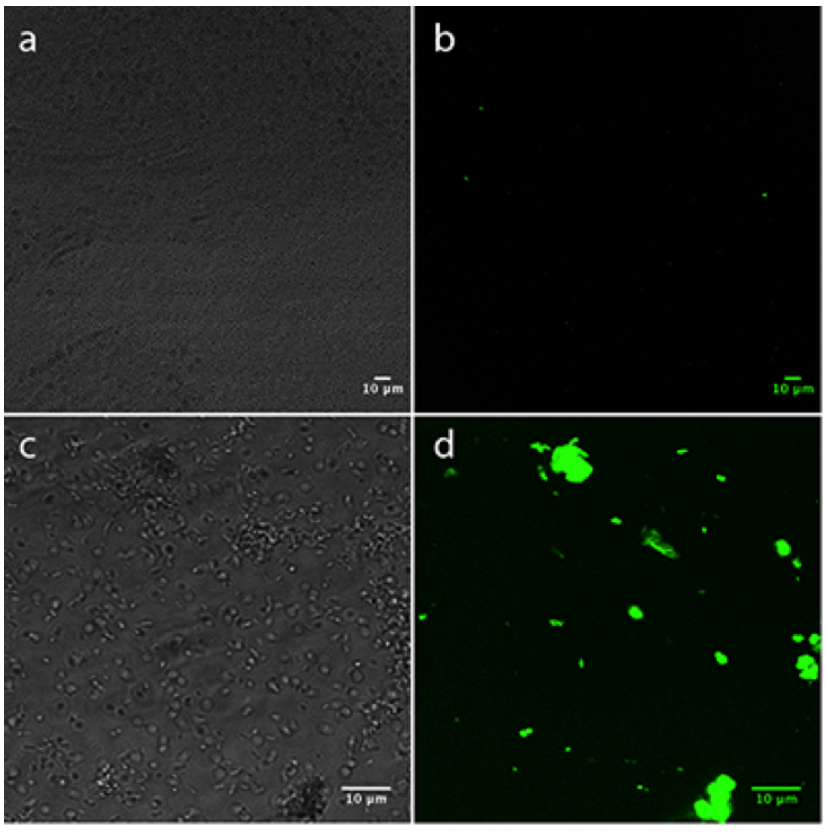

Figure 4.117. Captures of cells 4 hours after incubation with (a, b) P1 or (c, d) P2. (a) and (c) are the phase microscopy, (b) and (d) are the fluorescence microscopy images.

Figure 4.117 shows the confocal microscopy captures of cells 4 hours after incubation with P1 or P2. It was observed that P1 treated cells showed almost no intensity under fluorescence microscopy (Figure 4.117b), suggesting that the cells did not take up the peptide. On the contrary, the P2 treated cells showed high intensity (Figure 4.117d) either due to the uptake of the peptide or the accumulation of peptide precipitates that were not dissolved in the solution centrifuged with the cell pellet.

4.4.3.2. Visualization of pVEC Uptake. The cell-penetrating peptide pVEC is known to be able to internalize in mammalian cells and carry cargo into the cells [57,72]. Most of the experiments with pVEC were carried out in mammalian cell culture, but later it was reported that pVEC has antimicrobial properties and it is able to internalize in bacteria as well [71]. Here, fluorescein labeled pVEC was used to incubate bacteria to serve as a positive control set of the peptide uptake experiments.

In order to visualize the bacterial uptake of pVEC peptide, *E. coli* K12 cells were incubated with fluorescein labeled pVEC; pVEC (H-LLIILRRRIRKQAHAHSKK (HF488) - NH_2) at a final concentration of 250 μM, and samples were withdrawn after 30 minutes, 90 minutes, and 180 minutes of incubation.

Even after 30 minutes of incubation, fluorescence intensity in the cells was observed (Figure 4.118) indicating that pVEC was internalized by the bacteria. Images captured from the cultures that were incubated with pVEC for longer (Figure 4.118, 90 min and 180 min) showed that fluorescence intensity in the cells increased.

In all captured images background fluorescence was observed (Figure 4.118). The peptide precipitates observed in brightfield images were the reason of the background fluorescence. Since culture samples were prepared using serial centrifugation and washing, the peptide precipitates that were not dissolved in the solution were recovered with the cells.

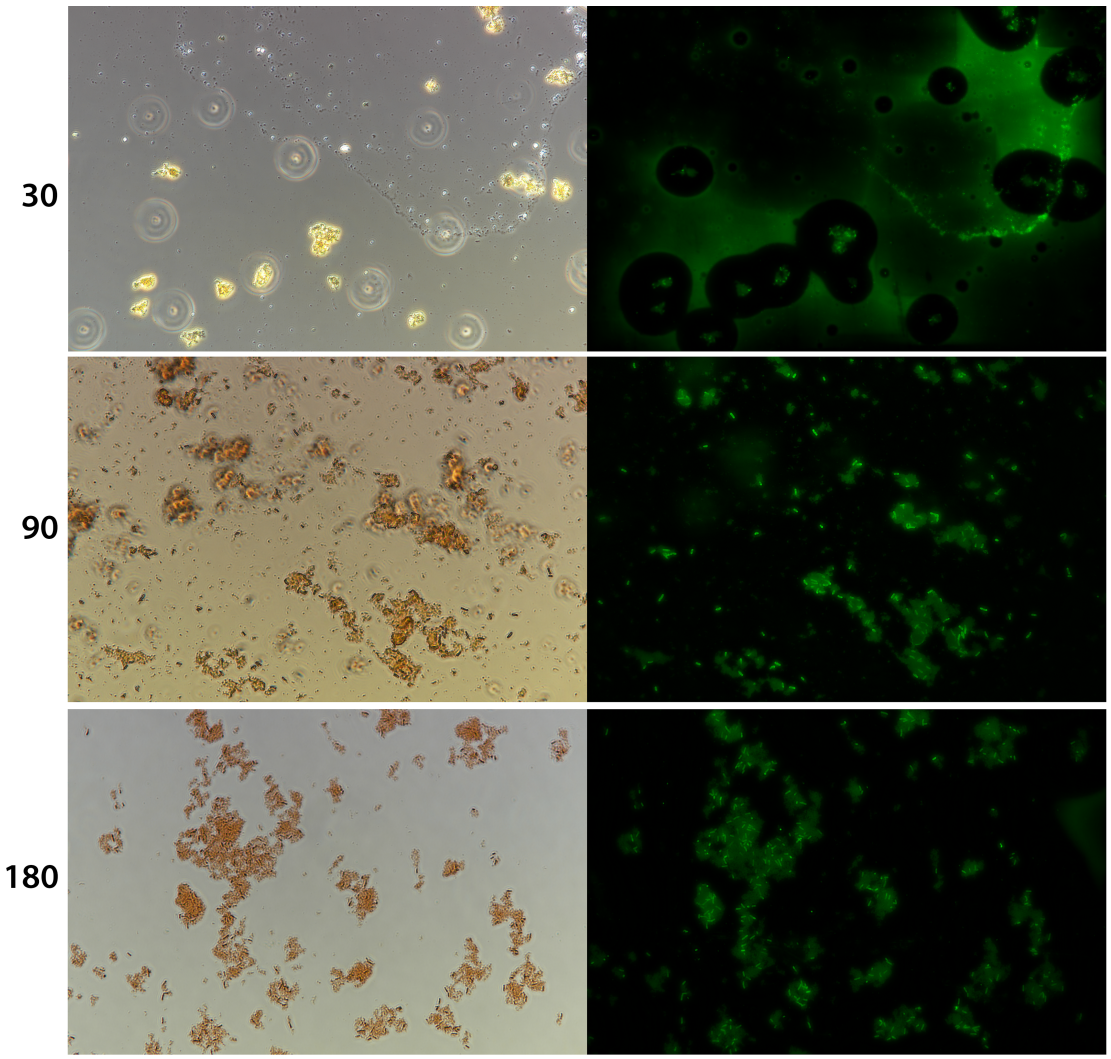

Figure 4.118. Visualization of pVEC uptake after 30 minutes (top row), 90 minutes (middle row), and 180 minutes (bottom row) of incubation time, under brightfield (left) and UV with FITC filter (right).

4.4.3.3. Visualization of P4 Uptake. In order to visualize the bacterial uptake of P4 peptide, *E. coli* K12 cells were incubated with fluorescein labeled P4; P4 (H-LLIILRRG HYYK (HF488) - NH_2) at a final concentration of 250 μM, and samples were withdrawn after 30 minutes, 90 minutes, and 180 minutes of incubation.

Even after 30 minutes of incubation, fluorescence intensity in the cells was observed (Figure 4.119) indicating that the bacteria internalized P4 peptide. Images captured from the cultures that were incubated with P4 for longer (Figure 4.119, 90

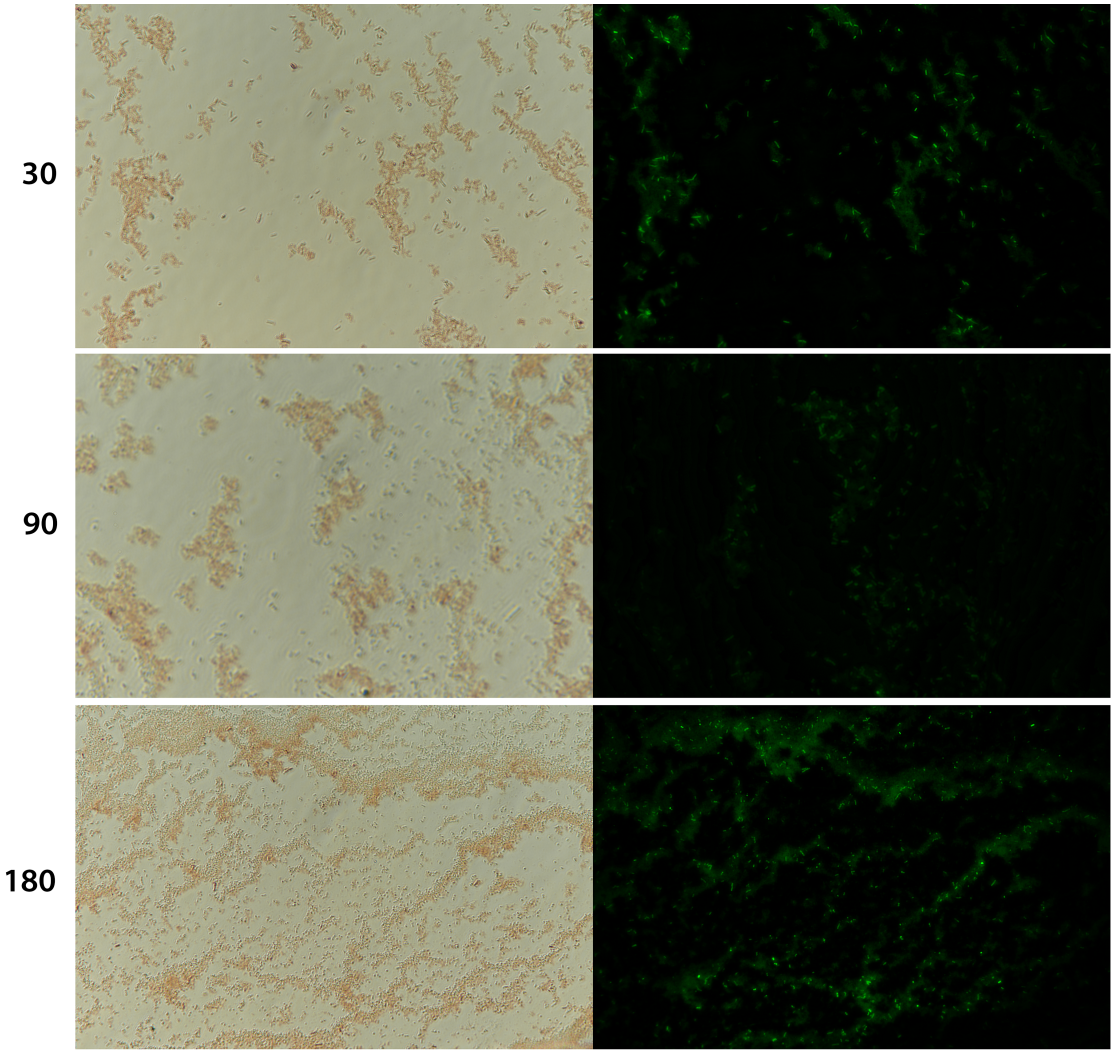

Figure 4.119. Visualization of P4 uptake after 30 minutes (top row), 90 minutes (middle row), and 180 minutes (bottom row) of incubation time, under brightfield (left) and under UV with FITC filter (right).

min and 180 min) showed that fluorescence intensity in the cells increased. The highest fluorescence intensity in cells was observed in the culture that was incubated with P4 peptide for 180 minutes (Figure 4.119). In all captured images background fluorescence was observed (Figure 4.119). Similar to the observations with the pVEC peptide, the P4 peptide precipitates that were observable even in the brightfield images were the reason of the background fluorescence. Since culture samples were prepared using serial centrifugation and washing, the peptide precipitates that were not dissolved in the solution were recovered with the cells.

4.4.4. Live Cell Imaging with Microfluidic Systems

The aim in using microfluidic chips was to conduct a live cell imaging study on the uptake of cell-penetrating and antimicrobial peptides into bacteria. For this purpose, Zeonor reaction chamber chips of 10 μL volume and 500 μm depth were used in all experiments. In order to test the microfluidic system, bead test, bacterial growth, fluorescein amine and bacterial viability dye uptake experiments were carried out before moving on to the peptide uptake experiments.

4.4.4.1. Reaction Chip Test Using Beads. In order to develop an experimental procedure for live imaging of bacteria in the microfluidic chips, loading and imaging of beads was tried in order to test the suitability of the chips for our purpose, and to adjust the fluid connectors and flow rates for the system to avoid sweeping and bubbling in the chamber. Beads with a diameter of 2 μm to closely match the size of the *E. coli* bacteria, was selected for this experiment.

After perfusion of the beads into the chamber, the chamber was washed and continuously monitored for 5 hours (Figure 4.120). In the first hour of washing, some beads escaped (Figure 4.120), but after 1 hour of washing, most of the beads were retained in the chamber (Figure 4.120), suggesting that the size of the chip and selected flow rates were suitable for experiments with bacteria.

4.4.4.2. Bacterial Growth in the Reaction Chip. After testing the chips with beads, the chips were tested for bacterial growth. The chamber was perfused with LB medium and then bacterial culture was fed to the channel. After bacteria settled down in the chamber, the flow of plain LB medium was turned on and the chamber was monitored continuously to capture images from the same spot every 15 minutes starting from the time point when the cells were loaded in the chamber (Figure 4.121).

The experiment was carried out for 2.5 hours, and a really fast bacterial growth indicated by the number of cells in the chamber was observed, especially after 1 hour of

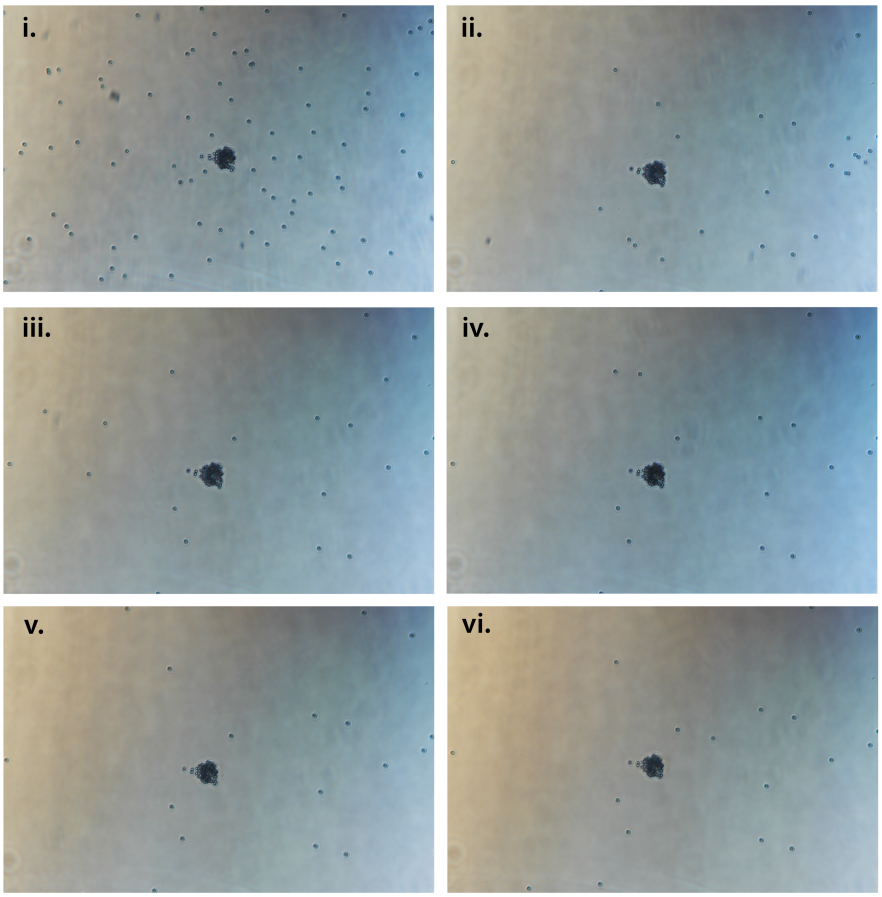

Figure 4.120. Microscopy images of the chip test with beads. After bead loading (i), distilled water was pumped. Images were captured from the same spot after (ii) 1 hour, (iii) 2 hours, (iv) 3 hours, (v) 4 hours, and (vi) after 5 hours.

reintroducing LB medium (Figure 4.121). Even though the reaction chips were found suitable for bacterial growth, most of the bacteria was mobile during the experiments, which may hinder the visualization of peptide effects on single-cells.

At the end of the experiment, the chamber was filled with bacteria (Figure 4.122). Moreover, some of the perfused bacteria were found in the outlet well, which were clearly swept away during the reintroduction of LB medium (Figure 4.122). The cell density was found to be high for such a short duration experiment, and the perfusion of a lower inoculation cell density was suggested for the following experiments.

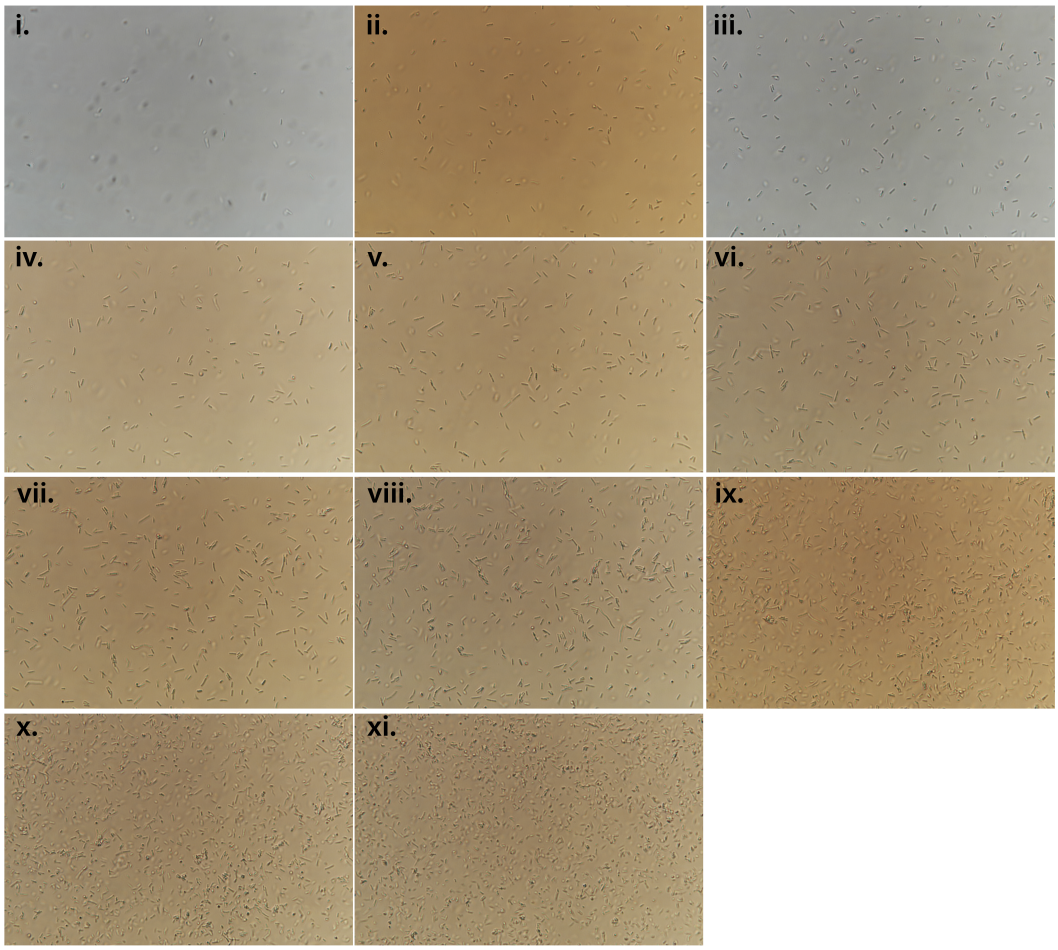

Figure 4.121. Microscopy images of bacterial growth captured at 60X zoom. After cell loading (i), only LB medium was pumped. Images were captured from the same spot every 15 minutes (ii-xi) in total experiment duration of 2.5 hours.

4.4.4.3. Bacterial Uptake of Fluorescein Amine. After testing the chips with beads and bacteria, the chips were tested for their suitability for visualization of fluorescent dyes in bacterial culture.

After the cells were loaded into the chamber and washed with LB medium, fluorescein amine pump was turned on (Figure 4.123i), and it was pumped for 1 hour at a rate of 0.1 μL/min to the channel. After 1.5 hours (Figure 4.123vii), the fluorescein amine syringe pump was turned off and then only LB medium was pumped at a rate of 0.1 μL/min to the channel. Images were captured from the same spot every 15 minutes (vi-xii) in total experiment duration of 3 hours.

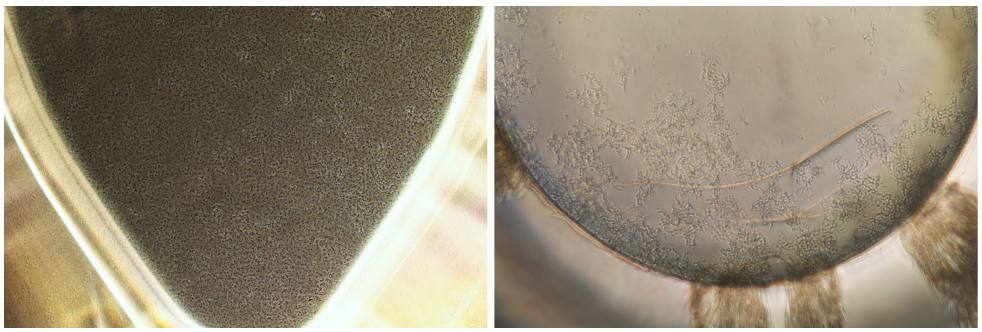

Figure 4.122. Microscopy images of the chip at the end of the experiment. At the end of 2.5 hours (left) the chamber was filled with bacteria, and (right) the outlet well had a much lower concentration of bacteria swept away by the flow.

The experiment was carried out for 3 hours, and bacterial growth was observed in the chamber, especially after 1 hour of perfusion with fluorescein amine (Figure 4.123v) indicated by the increase in the number of cells in the chamber. Bacterial growth was fast and the chamber was filled with bacteria at the end of 3 hours, similar to the observations in the previous bacterial growth experiment. Even though inhibitory effect of fluorescein amine on cell growth was not observed, its uptake into bacteria was not observed either. This result was expected since fluorescein amine is not able to penetrate into bacteria spontaneously, but it can be carried through the membrane as a cargo. On the other hand, increasing fluorescence intensity in the background was observed, especially in the last 1 hour of the experiment, indicating the delayed accumulation of fluorescein amine in the chamber.

4.4.4.4. Bacterial Uptake of the Bacterial Viability Kit. In the previous experiments, the chips were tested with beads and wild-type *E. coli* K12 strain, and live cell imaging of fluorescein amine uptake were performed. Since fluorescein amine is known to not penetrate into bacterial cells spontaneously, the bacterial viability kit was used to monitor the uptake of two different dyes into bacterial cells.

The chamber was first perfused with water without bacteria, and then with cultured bacteria (at OD_{600} of around 0.1). The culture pump was later switched off and

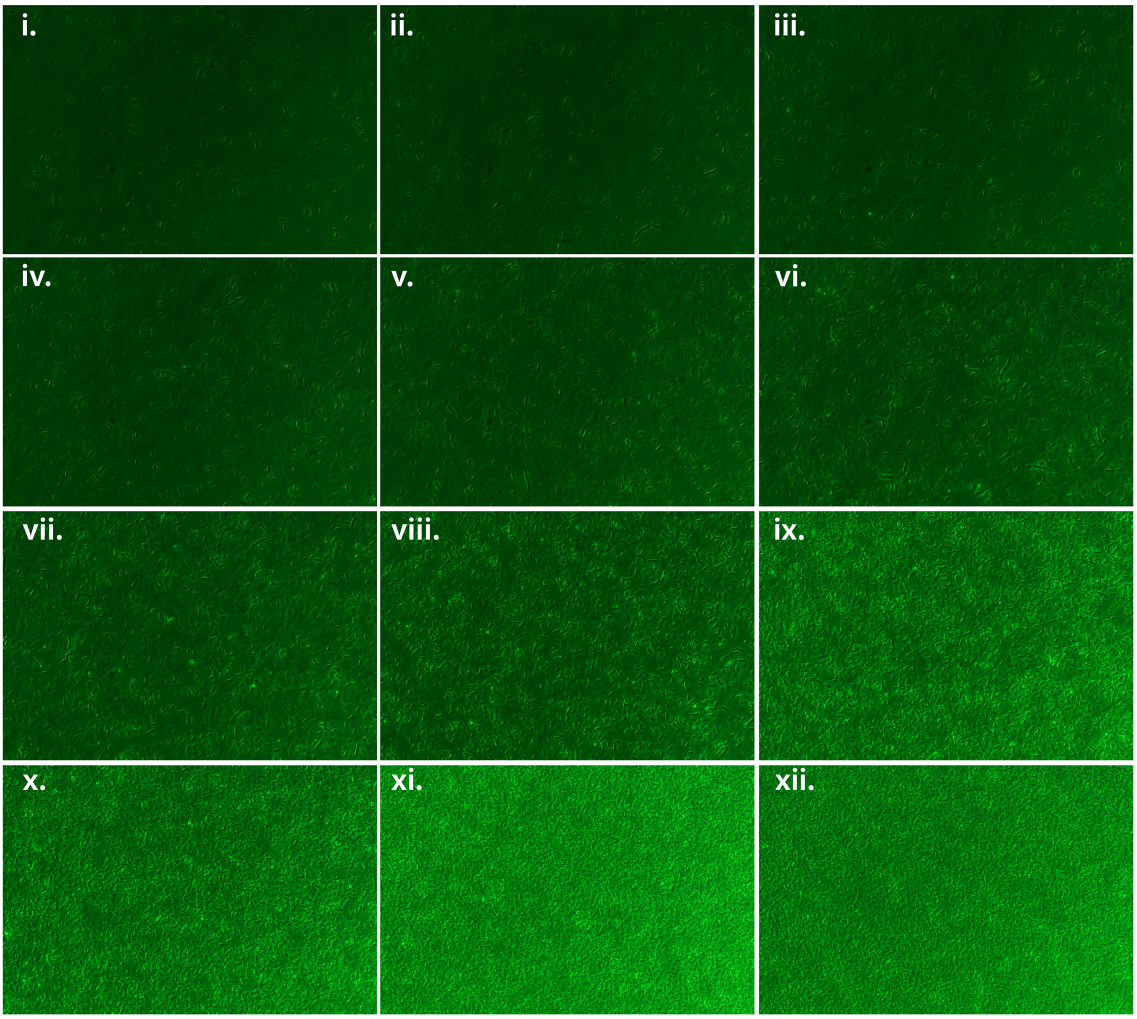

Figure 4.123. Microscopy images of bacterial uptake of fluorescein amine. After cell loading, fluorescein amine was perfused (i) for 1 hour. Images were captured from the same spot every 15 min (ii-iv). After 1.5 hours (vii), only LB medium was pumped.

the dye solution pump was switched on. The experiment was carried out for 3 hours, and even though sterile water was as perfusion liquid, bacterial growth in the chamber was observed, especially after 2 hours of perfusion with viability dye solution (Figure 4.124v and Figure 4.124vi). Bacterial growth was fast, and at the end of 3 hours the chamber was filled with bacteria (Figure 4.124vi), similar to the observations in the previous experiments of bacterial growth and bacterial uptake of fluorescein amine.

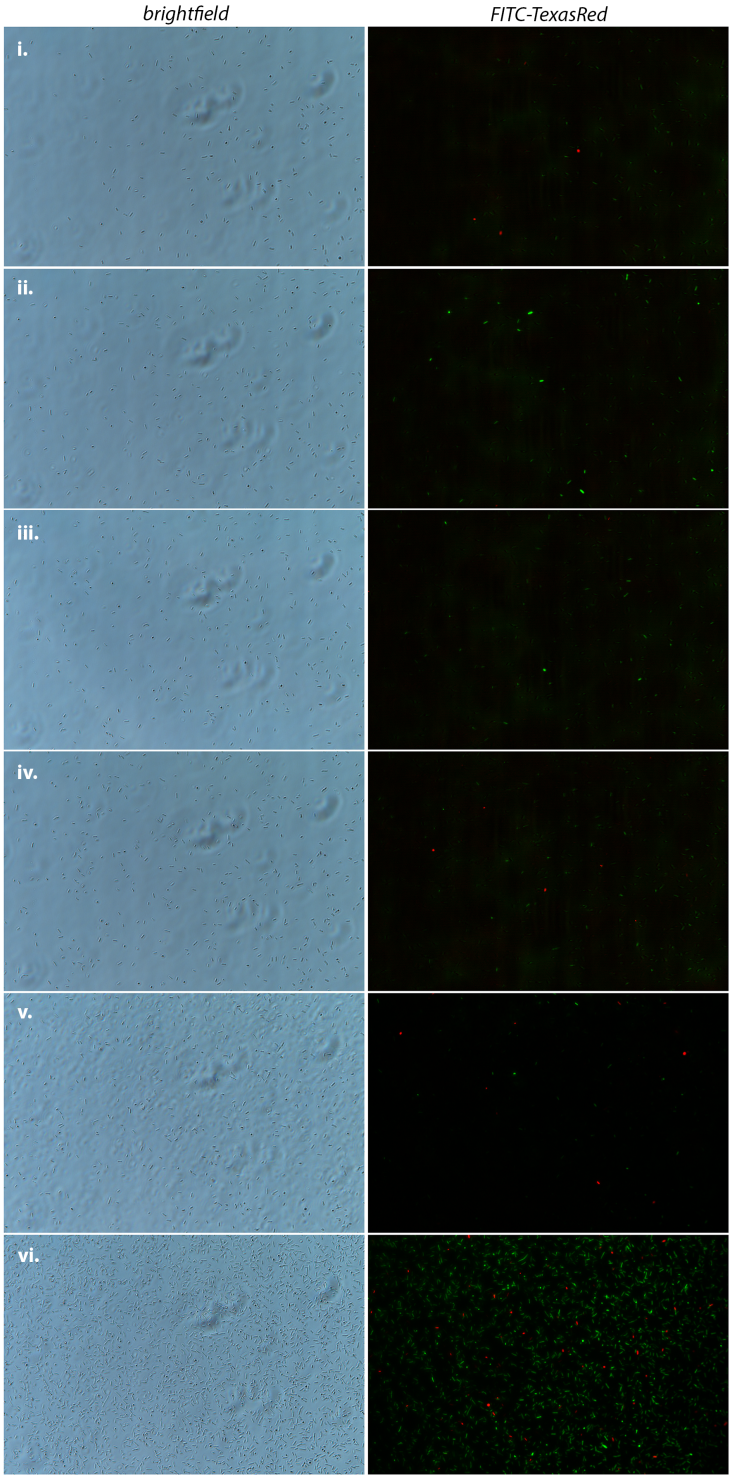

Figure 4.124. Microscopy images of bacterial viability dye uptake. After cell loading, viability dye was perfused. After 30 minutes of incubation time (i), images were captured from the same spot every 30 minutes.

After 30 minutes of feeding the viability dye solution (Figure 4.124i), some fluorescence intensity in the cells was observed, but background fluorescence was comparatively higher. This observation was valid for about 2 hours (Figure 4.124i - Figure 4.124iv) and the images corresponding to these time points were processed using the ImageJ software's 'subtract background' command. After 2 hours of feeding the viability dye solution, a decrease in the background fluorescence was observed and the images corresponding to these time points (Figure 4.124v and Figure 4.124vi) did not need to be processed to subtract the background fluorescence. A gradual increase in the fluorescence in the cells was observed, suggesting a threshold concentration is needed for imaging of the dye uptake into the cells. Furthermore, in the last 1 hour of the experiment, the room was dimmed, which may have also contributed to decreasing the background fluorescence. At the end of the 3rd hour, a great amount of fluorescence in the cells was observed with almost no background fluorescence (Figure 4.124vi). Even though water was used as the perfusion liquid, almost all of the cells were viable after 3 hours of growth in the chip (Figure 4.124vi). Possibly due to the lack of growth medium in the chip, it was easier to focus on the cells at each time point because their mobility was lower compared to the previous experiments. Moreover, the flagella of bacteria may have been damaged during the centrifugation and washing steps of the cells, which may have resulted in restricted movement capability of bacteria.

4.4.4.5. Bacterial Uptake of pVEC Peptide. In the previous experiments, the chips were tested with beads, tested for growth of wild-type *E. coli* K12 strain, and bacterial uptake of fluorescein amine and bacterial viability kit were monitored. For live cell imaging of bacterial uptake of pVEC peptide, the chamber was first perfused with water without bacteria, and then with cultured bacteria (at OD_{600} of around 0.1). The culture pump was later switched off and the pVEC solution (250 μM in DMSO-water mixture) pump was switched on. After 30 minutes of incubation images were captured from the same spot in the chamber every 30 minutes (Figure 4.125).

The imaging was carried out for 2 hours and after the initial incubation time with the peptide (Figure 4.125, 0 min) bacterial uptake of pVEC was observed indi-

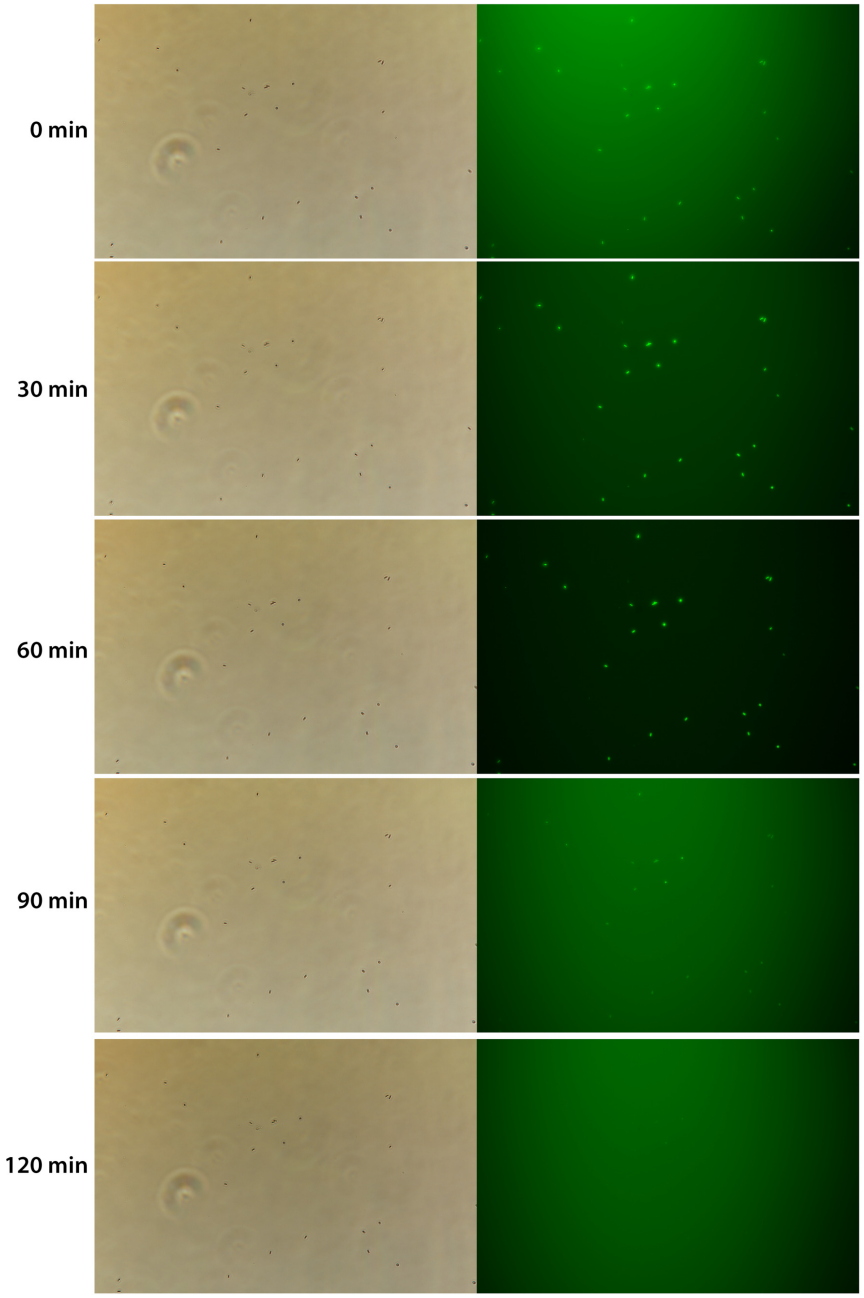

Figure 4.125. Microscopy images of pVEC uptake. After cell loading, pVEC was perfused. After 30 minutes of incubation time, images were captured from the same spot every 30 minutes.

cated by the fluorescence intensity in the cells. Upon continuous feeding of pVEC, the background fluorescence decreased and intensity in the cells increased (Figure 4.125, 30 min and 60 min). The washing of the channel with sterile water was carried out with the aim to decrease the background fluorescence by sweeping the access peptide

in solution, which is not taken up by the cells. On the contrary, the images captured after the washing was started showed that the background fluorescence did not decrease (Figure 4.125, 90 min and 120 min). Especially at the end of the 2nd hour, the cells were hardly observable because of the high background fluorescence (Figure 4.125, 120 min). Similar to the observations in the previous experiments with the pVEC peptide, peptide precipitations accumulated in the bottom of channel may be the reason for the increasing background fluorescence. Therefore, the washing step is impractical since it is not possible to wash off the precipitates from the channel at such small flow rates.

pVEC uptake was observed in almost all the cells starting from the end of the (30 minutes) incubation time. Moreover, the antibacterial effect of this cell-penetrating peptide was observed since the cell growth was hindered and the number of cells stayed almost the same throughout the experiment.

4.4.4.6. Bacterial Uptake of P4 Peptide. In the previous experiments, the chips were tested with beads, tested for growth of wild-type *E. coli* K12 strain, and bacterial uptake of fluorescein amine, bacterial viability kit, and pVEC peptide were monitored. For live cell imaging of bacterial uptake of P4 peptide, the chamber was first perfused with water without bacteria, and then with cultured bacteria (at OD_{600} of around 0.1). The culture pump was later switched off and the P4 solution (250 μM in DMSO-water mixture) pump was switched on. While feeding the P4 peptide solution, images were captured from the same spot in the chamber every 30 minutes (Figure 4.126).

The imaging was carried out for 1.5 hours and the first images were captured as the P4 pump was switched on (Figure 4.126, 0 min). At this time point, almost no fluorescence intensity was observed in the cells or in the background. Upon continuous feeding of P4, the fluorescence intensity in the cells increased (Figure 4.126, 30 min and 60 min). The images captured at the last 30 minutes of the experiment showed that the background fluorescence increased as well (Figure 4.126, 90 min). The cells were hardly observable because of the high background fluorescence. Similar to the experiment carried out with pVEC, P4 peptide precipitations accumulated in the bottom of channel

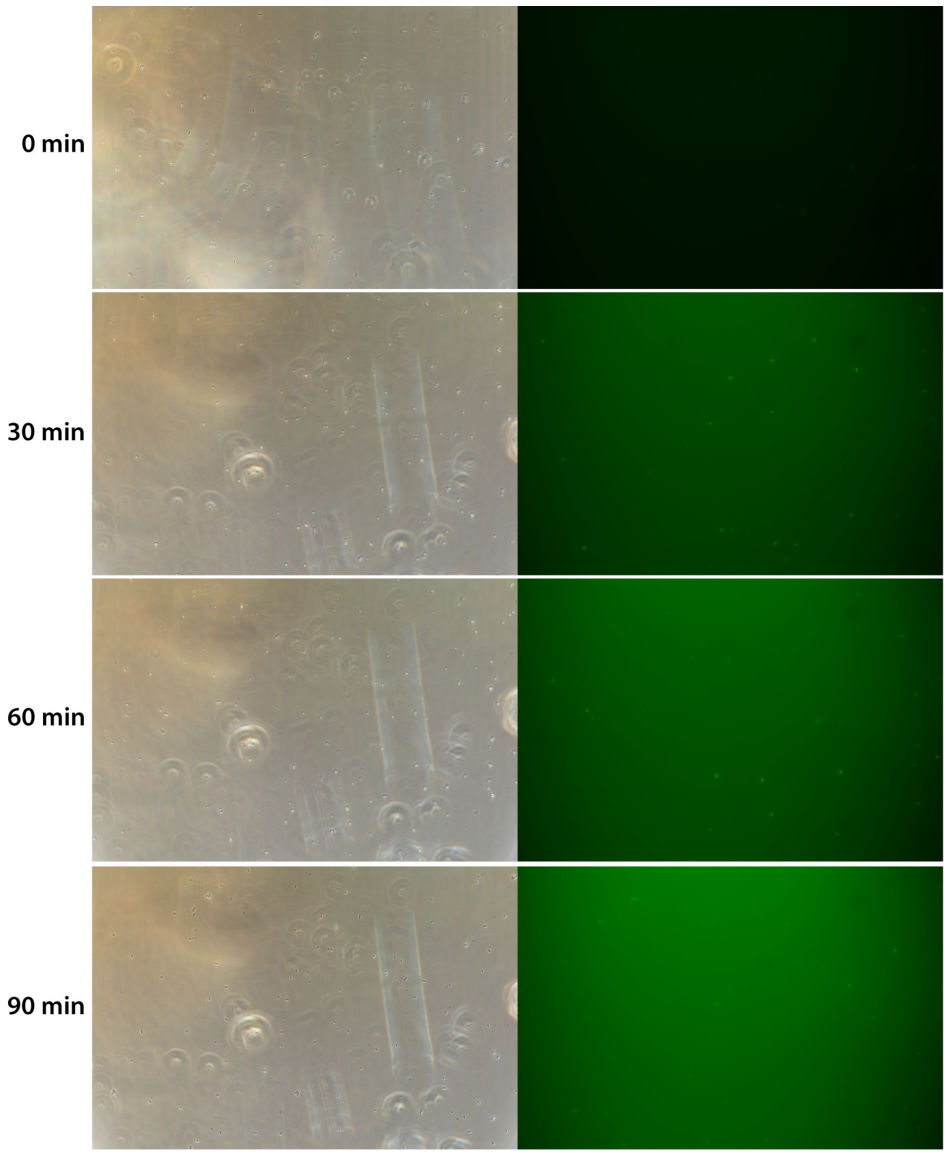

Figure 4.126. Microscopy images of P4 uptake. After cell loading, P4 solution pump was switched on, and images were captured from the same spot every 30 minutes under brightfield (left column) and UV with FITC filter (right column).

may be the reason for the increasing background fluorescence.

P4 uptake was observed in almost all the cells starting from the end of the 30th minute of incubation. Moreover, the antibacterial effect of this beta-lactamase inhibitory peptide was observed since the cell growth was hindered and the number of cells stayed almost the same throughout the experiment.

4.5. Drugs Effects in Mammalian Cell Culture

In this part of the study, the effect of ampicillin, P1 peptide, melittin, potassium clavulanate, pVEC peptide, and P4 peptide on mammalian cells were tested. The minimal inhibitory concentration (MIC) values for each drug (except P1 peptide) was previously determined at standard inoculum doses ($1x10^5$ CFU/mL) of *E. coli* K12 pUC18 cells incubated with drugs for 20 hours. MIC or multiple MIC values were used in cytotoxicity experiments to determine if these drugs are toxic to mammalian cells.

4.5.1. Effect of P1 on HeLa Cells

In order to determine the effect of antibiotic ampicillin and P1 peptide on mammalian HeLa cells, cells were incubated with PBS only (as a control set), with ampicillin and P1 peptide for 6 days. Microscopy images were taken of the same spot on each plate on the first, third and sixth days and can be seen in Figure 4.127, Figure 4.128 and Figure 4.129.

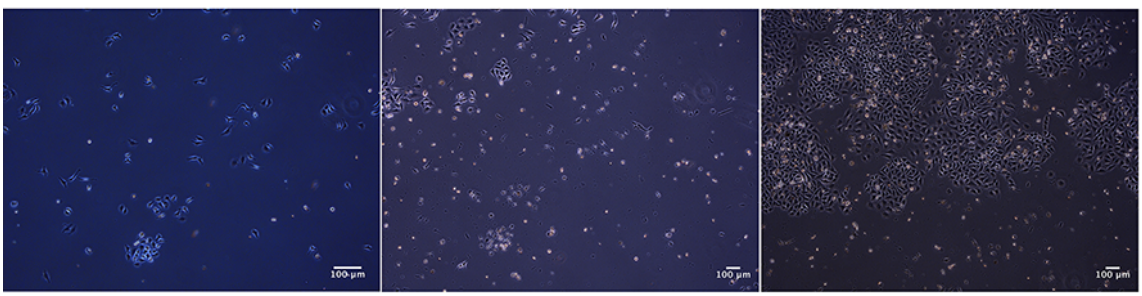

Figure 4.127. Snapshots of cells in PBS added medium on days 1 (left), 3 (middle) and 6 (right).

The initial count was calculated as $2.6x10^4$ cells in each treated culture. On the sixth day, the number of cells was calculated as $6.8x10^5$ for PBS added medium, $7.6x10^5$ for amp & PBS added medium and $5.3x10^5$ for the P1 & amp added medium respectively. It was concluded that neither ampicillin nor P1 addition caused a decrease in the viability of HeLa cells when compared to the control set that included PBS addition only.

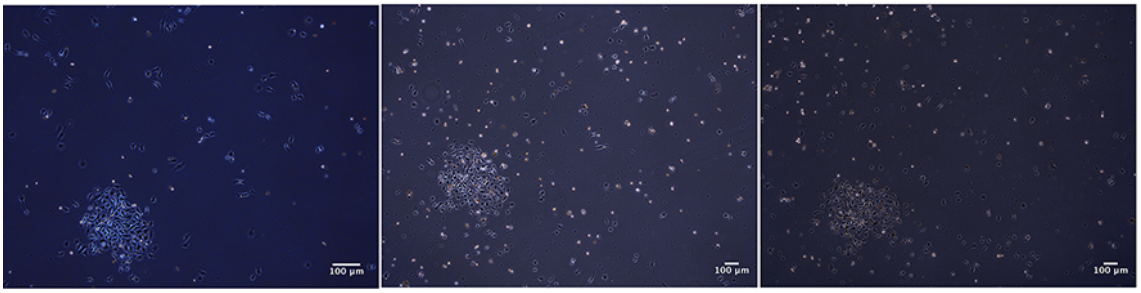

Figure 4.128. Snapshots of cells in amp and PBS added medium on days 1 (left), 3 (middle) and 6 (right).

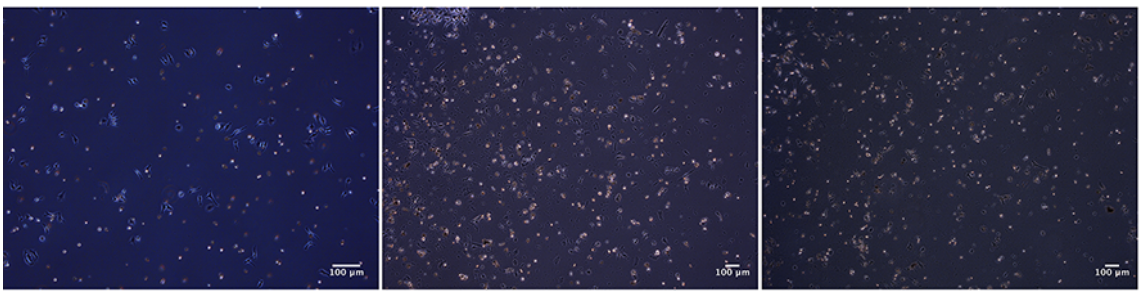

Figure 4.129. Snapshots of cells in P1 and amp added medium on days 1 (left), 3 (middle) and 6 (right).

4.5.2. Measurement of Drug Cytotoxicity Using XTT Assay

In order to test the cytotoxicity of melittin, potassium clavulanate and ampicillin, MIC, 2.5XMIC and 5XMIC of melittin (1 mM stock in water) or potassium clavulanate (5 mM stock in water), and MIC and 2XMIC of ampicillin (450 mg/mL stock in water) were used to incubate HK-2 cells. The minimal inhibitory concentration (MIC) values for each drug was previously determined at standard inoculum doses ($1x10^5$ CFU/mL) of *E. coli* K12 pUC18 cells incubated with drugs for 20 hours.

All of the samples were prepared as triplicates (Figure 4.130). Control samples have the same amount of water/buffer corresponding to their drug treated sample. After the cells were treated with these drugs for 20-22 hours, the XTT assay was added to all wells. After 3 hours of incubation with the XTT reagents (Figure 4.130),

absorbance for each well at 490 and 650 nm wavelengths were measured.

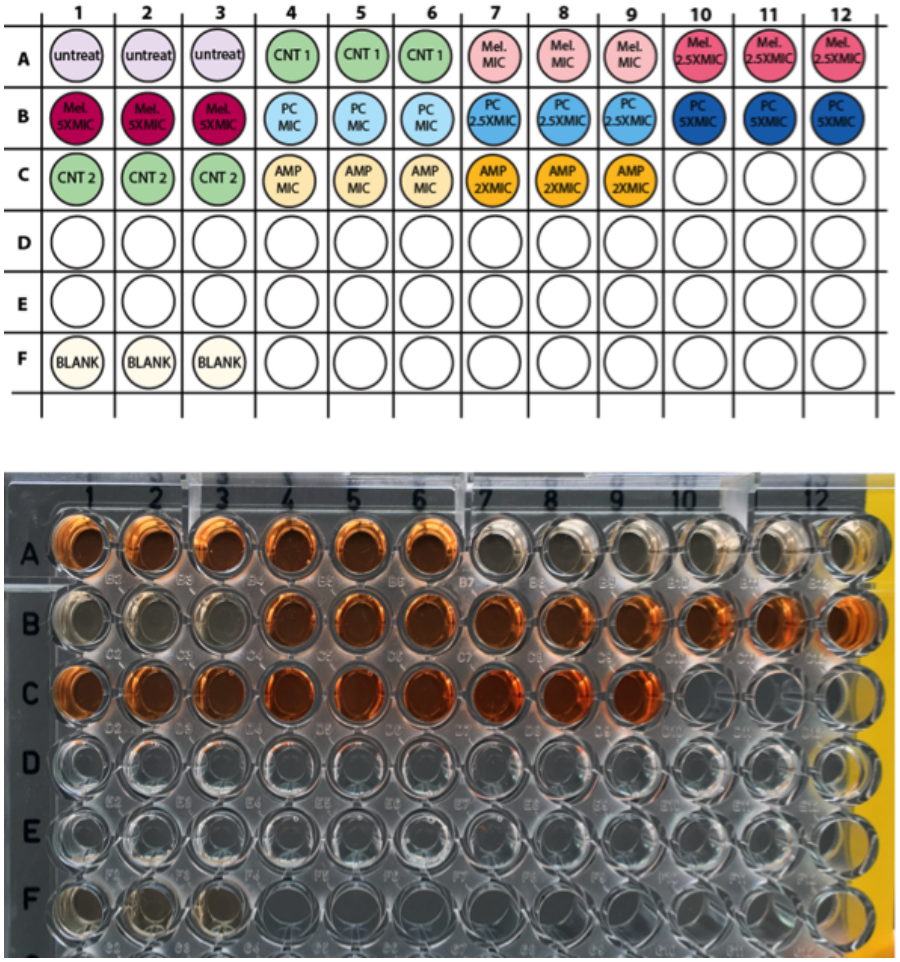

Figure 4.130. Plate layout used in the cytotoxicity experiment (top). Plate photograph after 3 hours of incubation with the cell proliferation assay (bottom).

Viability measurements of drug treated and control cultures are given in Figure 1.107 as the average of triplicate samples with the standard error of the mean. The results suggest that melittin; even at the lowest tested concentration (at MIC) is highly toxic to HK-2 cultures (Figure 4.131). Control 1 and Control 2 samples were 99% and 95% viable, respectively (Figure 4.131). These results are expected since melittin (from honey bee venom) is an antimicrobial peptide that is also toxic to mammalian cells [35,39–41]. Since the control samples have additional amount of water in medium, the medium is diluted and the viability could decrease upon dilution of nutrients. OD measurements of melittin treated cultures were calculated to be negative (after OD_{490}

- OD_{650} and subtraction of the blank samples) and therefore assumed to be not viable.

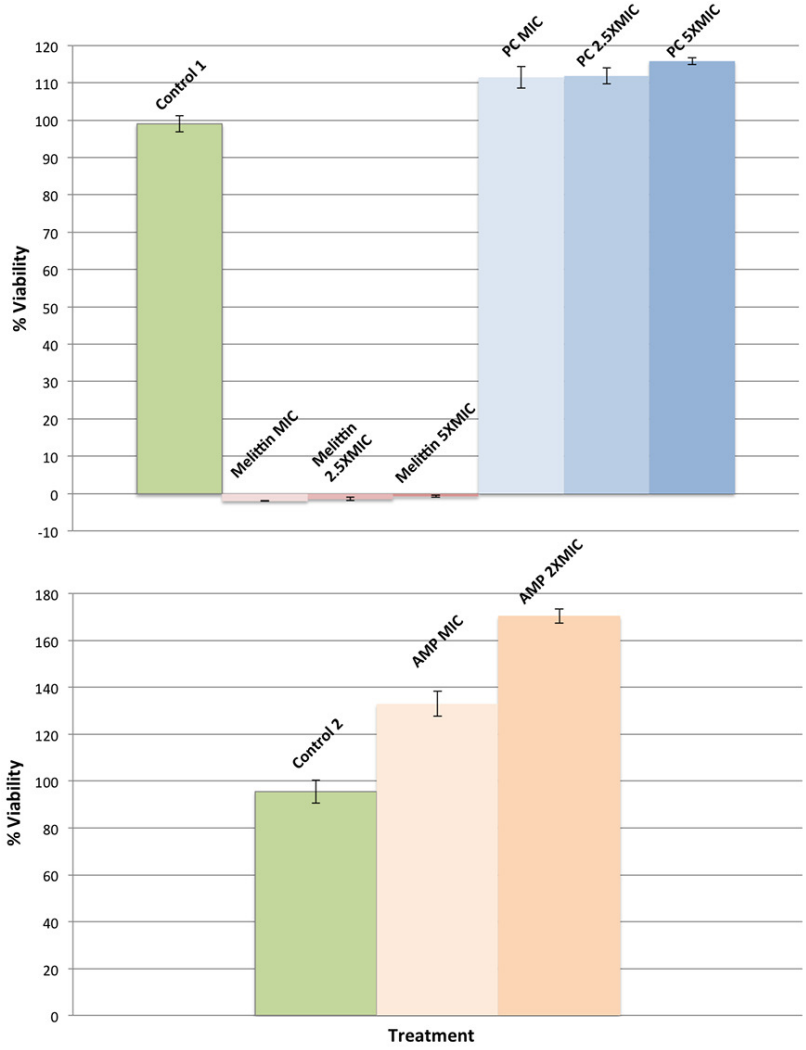

Figure 4.131. Percent viability of HK-2 cultures treated with (top) melittin or potassium clavulanate, and (bottom) treated with ampicillin with respect to the nontreated cultures. Nontreated cultures are assumed to be 100% viable.

The viability of cells treated with potassium clavulanate and ampicillin was higher when compared to the nontreated cultures (Figure 4.131). This could either be because of the increase in the number of cells, or the increase in the metabolic activity of the cells. When the samples were observed under microscopy, the number of cells was found to be higher in the potassium clavulanate and ampicillin treated cultures. Under these conditions, potassium clavulanate and ampicillin were found to be nontoxic to HK-2.

In order to test the cytotoxicity of pVEC and P4 peptides, MIC, 2.5XMIC and 5XMIC of pVEC (1 mM stock in water) or P4 (5 mM stock in water), were used to incubate HK-2 cells. In order to be able to compare the results with the previous experiment, MIC and 2.5XMIC of ampicillin (450 mg/mL stock in water) were used to incubate HK-2 cells as well. The minimal inhibitory concentration (MIC) values for each drug was previously determined at standard inoculum doses ($1x10^5$ CFU/mL) of *E. coli* K12 pUC18 cells incubated with drugs for 20 hours.

All of the samples were prepared as triplicates. Control samples have the same amount of water/buffer (or DMSO-water mixture) corresponding to their drug treated sample. Since pVEC and P4 peptide stock solutions were prepared in DMSO-water mixture, 3 different control sets were prepared for 3 different drug concentrations tested. After the cells were treated with these drugs for 20-22 hours, the XTT assay was added to all wells. After 3 hours of incubation with the XTT reagents, absorbance for each well at 490 and 650 nm wavelengths were measured.

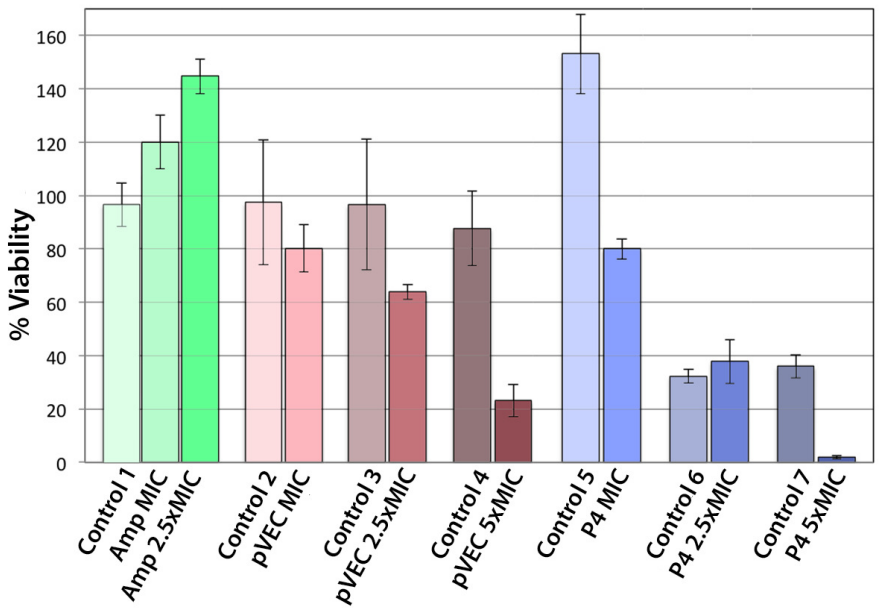

Figure 4.132. Percent viability of HK-2 cultures treated with different concentrations of ampicillin, pVEC peptide or P4 peptide with respect to the nontreated cultures. Nontreated cultures are assumed to be 100% viable.

Viability measurements of drug treated and control cultures are given in Figure 4.132 as the average of triplicate samples with the standard error of the mean. The results suggest that the viability of control samples of the ampicillin treatment was around 96%. Since the control samples have additional amount of water in medium, the medium is diluted and the viability could decrease upon dilution of nutrients. The viability of the cultures treated with MIC and 2.5XMIC of ampicillin were 120% and 145%, respectively (Figure 4.132). These results were similar to the results obtained in the first set of cytotoxicity experiments with XTT assay.

The viability of cells treated with MIC of pVEC was around 80% and the corresponding control set was 97% viable (Figure 4.132). Upon increasing the concentration of pVEC to 2.5XMIC and 5XMIC, the viability decreased to 64% and 23%, respectively. Since the viability of the control samples of pVEC were similar, the increasing amount of DMSO in the peptide solution may not be the reason of the decreasing viability with increasing peptide concentration. Even though pVEC is a cell-penetrating peptide and supposedly harmless to mammalian cells, it was found to be toxic at high concentrations (at 2.5XMIC = 31.25 μM and higher).

The viability of cells treated with MIC of P4 was around 80% and the corresponding control set was 150% viable (Figure 4.132). Upon increasing the concentration of P4 to 2.5XMIC and 5XMIC, the viability decreased to 38% and 2%, respectively (Figure 4.132). Similarly, the viability of the control samples of P4 decreased to 32% and 36%, respectively, with increasing amount of DMSO (Figure 4.132). The results suggest that the amount of DMSO in P4 solution is already toxic to HK-2 cells, so the cytotoxicity of P4 is debatable. At its MIC value, the cytotoxicity of P4 peptide is similar to that of pVEC at its MIC value.

4.5.3. Measurement of Drug Cytotoxicity Using Cell Counter and Trypan Blue

The cytotoxicity induced by three antibacterial drugs; melittin, potassium clavulanate and ampicillin were tested previously using XTT proliferation assay. The results

suggested that melittin, even at the lowest tested concentration (at MIC value determined for *E. coli* K12 pUC18 cells) is highly toxic to HK-2 cultures, where as ampicillin and potassium clavulanate were found to be nontoxic to HK-2 cells. Since XTT assay measures metabolic activity of the treated culture, the results could indicate either the change in the number of cells or the change in the metabolic activity of the cells. Considering this, the number of viable cells upon treatment with drugs was also measured by using a cell counter and trypan blue dye.

In order to test the cytotoxicity of melittin, ampicillin, potassium clavulanate, pVEC, and P4 peptide, MIC of each drug was used to incubate HK-2 cells. The minimal inhibitory concentration (MIC) values for each drug was previously determined at standard inoculum doses ($1x10^5$ CFU/mL) of *E. coli* K12 pUC18 cells (*E. coli* K12 cells for pVEC peptide only) incubated with drugs for 20 hours. The MIC was determined as 6.25 μM for melittin, 12.5 mg/mL for ampicillin, 31.25 μM for potassium clavulanate, 12.5 μM for pVEC peptide, and 80 μM for P4 peptide, respectively.

The microscopy images of cells treated with drugs for 24 hours are shown in Figure 4.133. The cells in the nontreated sample are well spread and adherent to the well surface. On the other hand, cells treated with drugs are 'fixated' upon drug treatment and the cells are not spread out on the well surface. Treated cells are 'shriveled' and the cell volume is smaller compared to the cells in the nontreated sample (Figure 4.133).

The number of viable cells in each sample was determined using the trypan blue viability dye and the cell counter. The cells in the nontreated sample were almost 100% viable (Figure 4.134). Upon treatment with MIC of melittin, the viability decreased to 3% (Figure 4.134), suggesting melittin is highly toxic to HK-2 cells at this concentration. The cells in the blank sample of melittin (cells incubated with the same amount of water in the melittin treated sample) were around 87% viable (Figure 4.134). These results were expected since Melittin is known to be an antimicrobial peptide, which is toxic to mammalian cells. Since the control (blank) sample has additional amount of water in the medium, the medium is diluted and the viability could decrease upon dilution of nutrients.

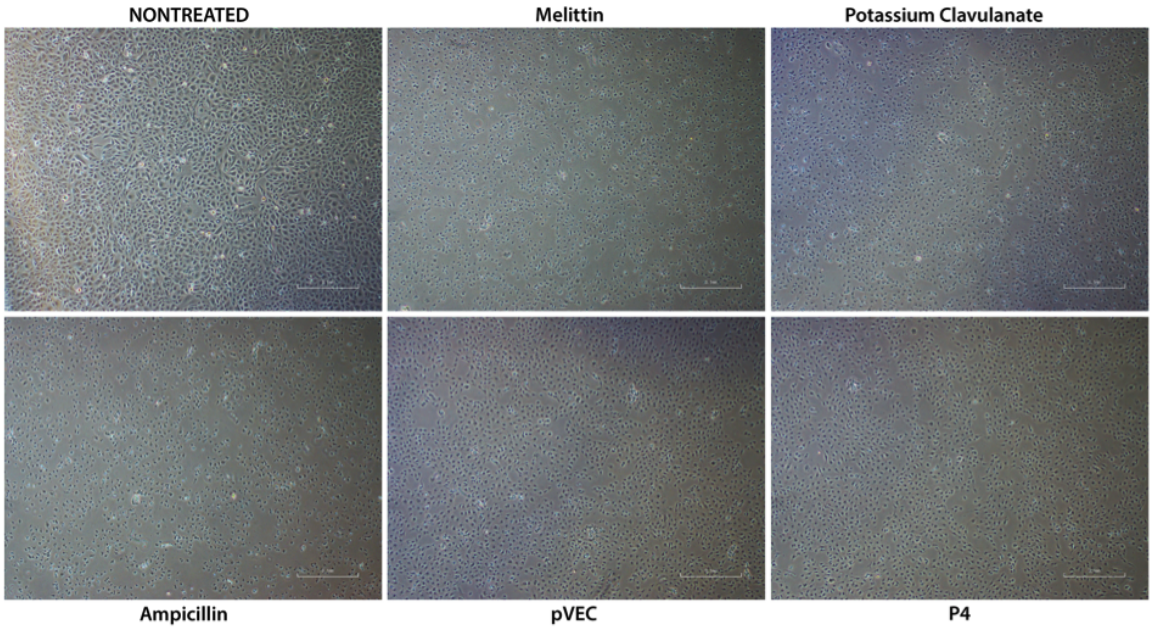

Figure 4.133. Microscopy images of HK-2 cells upon 24 hour treatment with melittin, potassium clavulanate, ampicillin, pVEC, and P4 peptide in comparison with the nontreated cells.

Upon treatment with MIC of ampicillin, there were almost no viable cells left in the culture (Figure 4.134), suggesting ampicillin is highly toxic to HK-2 cells at this concentration. Moreover, the cells in the blank sample of ampicillin (cells incubated with the same amount of water in the ampicillin treated sample) were around 37% viable. These results are inconsistent with our previous XTT assay results, in which the treatment with ampicillin led to a major increase in the number of viable cells.

Upon treatment with MIC of potassium clavulanate, the viability decreased to 80% (Figure 4.134), suggesting potassium clavulanate may be toxic to HK-2 cells at this concentration. Moreover, the cells in the blank sample of potassium clavulanate (cells incubated with the same amount of water in the potassium clavulanate treated sample) were around 87% viable. These results are inconsistent with our previous XTT assay results, in which the treatment with potassium clavulanate led to a major increase in the number of viable cells.

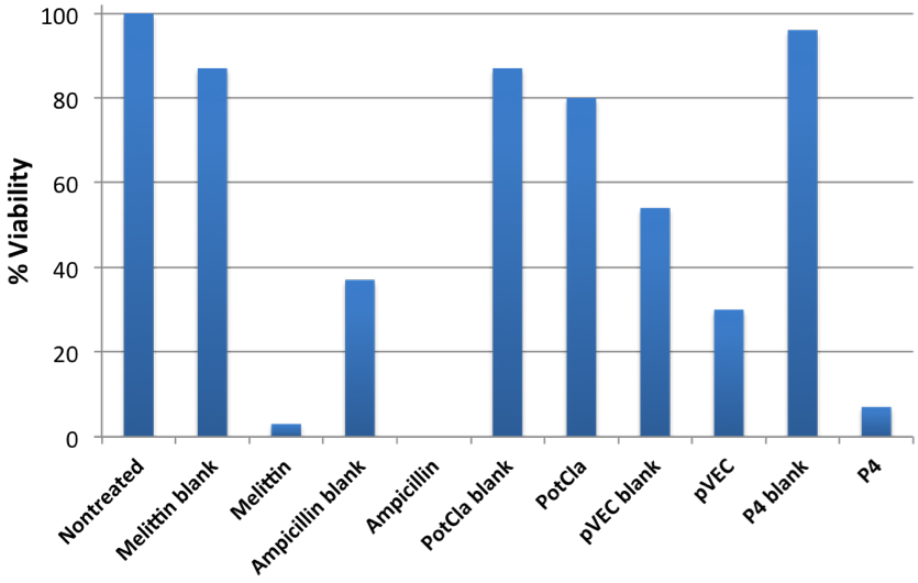

Figure 4.134. Percent viability of HK-2 cultures treated with MIC of melittin, ampicillin, potassium clavulanate, pVEC, and P4 peptide with respect to the nontreated cultures.

Upon treatment with MIC of pVEC peptide, the viability decreased to 30% (Figure 4.134), suggesting pVEC is highly toxic to HK-2 cells at this concentration. The cells in the blank sample of pVEC (cells incubated with the same amount of DMSO-water mixture in the pVEC treated sample) were around 54% viable (Figure 4.134). These results were not expected since pVEC is known to be a cell-penetrating peptide, which is not toxic to mammalian cells. On the other hand, since the control (blank) sample has additional amount of DMSO-water mixture in media, the media is diluted and the viability could decrease upon dilution of nutrients.

Upon treatment with MIC of P4 peptide, the viability decreased to 7% (Figure 4.134), suggesting P4 peptide is highly toxic to HK-2 cells at this concentration. The cells in the blank sample of P4 (cells incubated with the same amount of DMSO-water mixture in the P4 treated sample) were around 96% viable (Figure 4.134). Since the control (blank) sample has additional amount of DMSO-water mixture in media, the media is diluted and the viability could decrease upon dilution of nutrients. On the

other hand, out results suggest that the novel antimicrobial peptide P4 may be toxic to mammalian cells.

5. CONCLUSIONS AND RECOMMENDATIONS

In the first part of the study, molecular dynamics simulations of the cell-penetrating peptide pVEC and its variants, and two beta-lactamase inhibitory peptides were carried out in order to gain insights about their membrane translocation mechanisms. Steered molecular dynamics simulations of two beta-lactamase inhibitory peptide P1 and P2 shoed that the initial penetration into the upper P-heads is an important energy barrier in the uptake of these peptides. Moreover, P2 created slightly higher disorder especially near the lipid head groups suggesting that the higher hydrophobicity of P2 results in increased interactions with the membrane lipids. Steered molecular dynamics simulations of pVEC and mutants with either improved (pVEC-1, pVEC-9, pVEC-11) of decreased (pVEC-2) activity showed that the interaction energy and force profiles of pVEC-2 peptide resembled a shallow dip, which may suggest a decreased uptake of this peptide. Moreover, the results suggested that formation of a larger water pore and strong electrostatic interactions may be related to an increase in the uptake potential of these peptides. In order to investigate the contribution of the hydrophobic N-terminus of pVEC to its uptake mechanism, SMD simulations followed by replica exchange umbrella sampling simulations were carried out for pVEC and del5 pVEC peptides. The potential of mean force calculated for each peptide suggested that del5 pVEC reaches to the membrane core at a lower energetic cost, when compared to pVEC. The results suggested that equilibrium PMF profiles are difficult to achieve and single peptide dynamics may be different than community action. When different molecular dynamics trajectories were analyzed using dimensionality reduction algorithms PCA and ISOMAP, it was observed that the variation of SMD data using ISOMAP was higher in the first dimension when compared to PCA. The first dimension of the ISOMAP projection gave information about the main motion of the system, which was translocation in the z-direction.

In the second part of the study, the aim was to discover novel peptide antimicrobials that are not only periplasmic beta- lactamase inhibitors, but can also penetrate into bacteria. Melittin, a well-established antimicrobial peptide was found to be the

strongest antibacterial drug among the ones tested in this study. While the antibiotic resistant strain could tolerate around 4000-folds of ampicillin concentration when compared to the wild-type strain, the effect of potassium clavulanate was similar for both strains. Ampicillin treated bacteria were elongated, while potassium clavulanate cause an increase in the cell size with a disruption in the rod shape. The deletion of LLIIL residues from the pVEC sequence abolished this peptide's antimicrobial activity, as expected. The beta-lactamase inhibitory peptides P3 and P3A showed no signs of antibacterial effect, but P3 gained antimicrobial properties upon combination with LLIIL. P4 peptide showed similar antimicrobial activity for wild-type and antibiotic resistant strains, and upon treatment of bacteria with P4 membrane damage and permeabilization was observed. Moreover, P4 caused an increase in the cell size, 'dimples' and 'holes' on the surface of bacteria upon treatment with this peptide. The drug synergy tests showed that 1:4 MIC concentration of potassium clavulanate was enough to reduce the MIC of ampicillin over 16-folds. On the other hand, melittin, P3, and P4 did not exhibit any synergetic effect with ampicillin.

Live-cell imaging studies showed that, while the microfluidic chips are suitable for bacterial growth and visualization of peptide uptake, many control experiments should be carried out. We have successfully observed the internalization of the cell-penetrating peptide pVEC, and the novel chimeric peptide P4 using reaction chamber chips.

For future studies, the free energy calculations of pVEC and del5 pVEC peptide should be carried out either using a different enhanced sampling approach, or by extending the REUS simulations until a converged PMF profile is achieved. It would also be interesting to investigate multiple peptide systems, since many membrane active peptides take advantage of higher concentrations for internalization, and multiple peptide systems may actually have a lower free energy profile than single peptides. Live-cell imaging studies have a great potential since the cells are in their natural environment and are not subjected to any fixation during the imaging. For the peptide uptake studies, a trypsin washing step should be introduced to the live imaging protocol to remove any access amount of labeled peptide in solution or bound on the outer surface of the cells. This step may be vital since bacteria are really small organisms,

and it is really challenging to visually detect if the peptides are internalized by the cells or they are spread on the cell surface. In the context of the design of chimeric peptides, it is still not clear if the modified beta-lactamase inhibitory peptides reach their target protein. Since this is a challenging concept to prove, this approach may be tested for another target protein involved in a simpler biological mechanism. Another test case could be the design of a chimeric peptide by the addition of LLIIL residues to a non-drug peptide. By treating the cells with this chimera, we could have an idea about whether the LLIIL stretch is the source of the antimicrobial action rather than the cargo carrier of this sequence.

REFERENCES

1. Nitschke, N., K. Atkovska and J. S. Hub, "Accelerating potential of mean force calculations for lipid membrane permeation: System size, reaction coordinate, solute-solute distance, and cutoffs", *The Journal of chemical physics*, Vol. 145, No. 12, p. 125101, 2016.

2. Heitz, F., M. C. Morris and G. Divita, "Twenty years of cell-penetrating peptides: from molecular mechanism to therapeutics", *British Journal of Pharmacology*, Vol. 157, pp. 195–206, 2009.

3. Magzoub, M. and A. Graslund, "Cell-penetrating peptides: small from inception to application", *Quarterly Reviews of Biophysics*, Vol. 37, pp. 147–195, 2004.

4. Takeuchi, T. and S. Futaki, "Current Understanding of Direct Translocation of Arginine-Rich Cell-Penetrating Peptides and Its Internalization Mechanisms.", *Chemical & pharmaceutical bulletin*, Vol. 64, No. 10, pp. 1431–1437, 2016.

5. Copolovici, D. M., K. Langel, E. Eriste and U. Langel, "Cell-penetrating peptides: design, synthesis, and applications", *ACS nano*, Vol. 8, No. 3, pp. 1972–1994, 2014.

6. Spellberg, B., "Antibiotic resistance and antibiotic development", *The Lancet Infectious Diseases*, Vol. 8, No. 4, pp. 211–212, 2008.

7. Wilke, M. S., A. L. Lovering and N. C. Strynadka, "Beta-lactam antibiotic resistance: a current structural perspective", *Current opinion in microbiology*, Vol. 8, No. 5, pp. 525–533, 2005.

8. Babic, M., A. M. Hujer and R. A. Bonomo, "What's new in antibiotic resistance? Focus on beta-lactamases", *Drug Resistance Updates*, Vol. 9, No. 3, pp. 142–156, 2006.

9. Lee, J. H., I. K. Bae and S. Hee Lee, "New definitions of extended-spectrum beta-lactamase conferring worldwide emerging antibiotic resistance", *Medicinal research reviews*, Vol. 32, No. 1, pp. 216–232, 2012.

10. Williams, J. D., "Beta-lactamases and beta-lactamase inhibitors.", *International journal of antimicrobial agents*, Vol. 12 Suppl 1, pp. S3–7– discussion S26–7, 1999.

11. Rudgers, G. W., W. Huang and T. Palzkill, "Binding properties of a peptide derived from beta-lactamase inhibitory protein", *Antimicrobial agents and chemotherapy*, Vol. 45, No. 12, pp. 3279–3286, 2001.

12. Reichmann, D., M. Cohen, R. Abramovich, O. Dym, D. Lim, N. C. Strynadka and G. Schreiber, "Binding hot spots in the TEM1-BLIP interface in light of its modular architecture", *Journal of molecular biology*, Vol. 365, No. 3, pp. 663–679, 2007.

13. Gennis, R. B., *Biomembranes: molecular structure and function*, Springer Science & Business Media, 2013.

14. Dorairaj, S. and T. W. Allen, "On the thermodynamic stability of a charged arginine side chain in a transmembrane helix.", *Proceedings of the National Academy of Sciences of the United States of America*, Vol. 104, No. 12, pp. 4943–4948, 2007.

15. Yeung, N., M. S. Cline, A. Kuchinsky, M. E. Smoot and G. D. Bader, "Exploring biological networks with Cytoscape software", *Current Protocols in Bioinformatics*, pp. 8–13, 2008.

16. Wimley, W. C., "Describing the Mechanism of Antimicrobial Peptide Action with the Interfacial Activity Model", *ACS Chemical Biology*, Vol. 5, No. 10, pp. 905–917, 2010.

17. Zasloff, M., "Antimicrobial peptides of multicellular organisms.", *Nature*, Vol.

415, No. 6870, pp. 389–395, 2002.

18. Koczulla, A. R. and R. Bals, "Antimicrobial peptides: current status and therapeutic potential.", *Drugs*, Vol. 63, No. 4, pp. 389–406, 2003.

19. Brogden, K. A., "Antimicrobial peptides: pore formers or metabolic inhibitors in bacteria?", *Nature reviews. Microbiology*, Vol. 3, No. 3, pp. 238–250, 2005.

20. Phoenix, D. A., S. R. Dennison and F. Harris, *Antimicrobial Peptides*, Wiley-VCH Verlag GmbH & Co. KGaA., 2013.

21. Splith, K. and I. Neundorf, "Antimicrobial peptides with cell-penetrating peptide properties and vice versa", *European biophysics journal*, Vol. 40, No. 4, pp. 387–397, 2011.

22. Mihajlovic, M. and T. Lazaridis, "Antimicrobial peptides in toroidal and cylindrical pores", *Biochimica et Biophysica Acta (BBA) - Biomembranes*, Vol. 1798, No. 8, pp. 1485–1493, 2010.

23. Sengupta, D., H. Leontiadou, A. E. Mark and S.-J. Marrink, "Toroidal pores formed by antimicrobial peptides show significant disorder", *Biochimica et Biophysica Acta (BBA) - Biomembranes*, Vol. 1778, No. 10, pp. 2308–2317, 2008.

24. Bobone, S., Y. Gerelli, M. De Zotti, G. Bocchinfuso, A. Farrotti, B. Orioni, F. Sebastiani, E. Latter, J. Penfold, R. Senesi, F. Formaggio, A. Palleschi, C. Toniolo, G. Fragneto and L. Stella, "Membrane thickness and the mechanism of action of the short peptaibol trichogin GA IV", *Biochimica et Biophysica Acta (BBA) - Biomembranes*, Vol. 1828, No. 3, pp. 1013–1024, 2013.

25. Huang, H. W., "Action of Antimicrobial Peptides: Two-State Model", *Biochemistry*, Vol. 39, No. 29, pp. 8347–8352, 2000.

26. Huang, H. W., "Molecular mechanism of antimicrobial peptides: The origin of

cooperativity", *Biochimica et Biophysica Acta (BBA) - Biomembranes*, Vol. 1758, No. 9, pp. 1292–1302, 2006.

27. Oren, Z. and Y. Shai, "Mode of action of linear amphipathic α-helical antimicrobial peptides", *Peptide Science*, Vol. 47, No. 6, pp. 451–463, 1998.

28. Salomone, F., F. Cardarelli, M. Di Luca, C. Boccardi, R. Nifosì, G. Bardi, L. Di Bari, M. Serresi and F. Beltram, "A novel chimeric cell-penetrating peptide with membrane-disruptive properties for efficient endosomal escape", *Journal of controlled release*, Vol. 163, No. 3, pp. 293–303, 2012.

29. Cantini, L., C. C. Attaway, B. Butler, L. M. Andino, M. L. Sokolosky and A. Jakymiw, "Fusogenic-Oligoarginine Peptide-Mediated Delivery of siRNAs Targeting the CIP2A Oncogene into Oral Cancer Cells", *PLoS One*, Vol. 8, No. 9, p. e73348, 2013.

30. Québatte, G., E. Kitas and J. Seelig, "riDOM, a cell-penetrating peptide. Interaction with DNA and heparan sulfate", *The Journal of Physical Chemistry B*, Vol. 117, No. 37, pp. 10807–10817, 2013.

31. Myrberg, H., L. Zhang, M. Mäe and Ü. Langel, "Design of a tumor-homing cell-penetrating peptide", *Bioconjugate chemistry*, Vol. 19, No. 1, pp. 70–75, 2007.

32. Habermann, E. and J. Jentsch, "Sequence analysis of melittin from tryptic and peptic degradation products", *Hoppe-Seyler's Zeitschrift fur Physiologische Chemie*, Vol. 348, No. 1, pp. 37–50, 1967.

33. Fennell, J. F., W. H. Shipman and L. J. Cole, "Antibacterial action of melittin, a polypeptide from bee venom", *Proceedings of the Society for Experimental Biology and Medicine*, Vol. 127, No. 3, pp. 707–710, 1968.

34. Habermann, E., "Bee and Wasp Venoms", *Science*, Vol. 177, No. 4046, pp. 314–322, 1972.

35. Jamasbi, E., S. Batinovic, R. A. Sharples, M.-A. Sani, R. M. Robins-Browne, J. D. Wade, F. Separovic and M. A. Hossain, "Melittin peptides exhibit different activity on different cells and model membranes.", *Amino acids*, Vol. 46, No. 12, pp. 2759–2766, 2014.

36. Raghuraman, H. and A. Chattopadhyay, "Melittin: a membrane-active peptide with diverse functions.", *Bioscience Reports*, Vol. 27, No. 4-5, pp. 189–223, 2007.

37. Lee, M.-T., T.-L. Sun, W.-C. Hung and H. W. Huang, "Process of inducing pores in membranes by melittin", *Proceedings of the National Academy of Sciences*, Vol. 110, No. 35, pp. 14243–14248, 2013.

38. Zhu, W. L., Y. H. Nan, K.-S. Hahm and S. Y. Shin, "Cell selectivity of an antimicrobial peptide melittin diastereomer with D-amino acid in the leucine zipper sequence.", *Journal of biochemistry and molecular biology*, Vol. 40, No. 6, pp. 1090–1094, 2007.

39. Asthana, N., S. P. Yadav and J. K. Ghosh, "Dissection of antibacterial and toxic activity of melittin: a leucine zipper motif plays a crucial role in determining its hemolytic activity but not antibacterial activity.", *The Journal of biological chemistry*, Vol. 279, No. 53, pp. 55042–55050, 2004.

40. Cho, H.-J., J.-H. Kang, K.-K. Park, J.-Y. Choe, Y.-Y. Park, Y.-S. Moon, I.-K. Chung, H.-W. Chang, C.-H. Kim, Y. H. Choi, W.-J. Kim, S.-K. Moon and Y.-C. Chang, "Comparative proteome analysis of Tumor necrosis factor α-stimulated human Vascular Smooth Muscle Cells in response to melittin.", *Proteome science*, Vol. 11, No. 1, p. 20, 2013.

41. Khatun, U. L. and C. Mukhopadhyay, "Interaction of bee venom toxin melittin with ganglioside GM1 bicelle.", *Biophysical chemistry*, Vol. 180-181, pp. 66–75, 2013.

42. Gajski, G. and V. Garaj-Vrhovac, "Melittin: a lytic peptide with anticancer prop-

erties.", *Environmental Toxicology and Pharmacology*, Vol. 36, No. 2, pp. 697–705, 2013.

43. Oren, Z. and Y. Shai, "Selective lysis of bacteria but not mammalian cells by diastereomers of melittin: structure-function study.", *Biochemistry*, Vol. 36, No. 7, pp. 1826–1835, 1997.

44. Terwilliger, T. C. and D. Eisenberg, "The structure of melittin. II. Interpretation of the structure.", *The Journal of biological chemistry*, Vol. 257, No. 11, pp. 6016–6022, 1982.

45. Dempsey, C. E., "The actions of melittin on membranes.", *Biochimica Et Biophysica Acta-Biomembranes*, Vol. 1031, No. 2, pp. 143–161, May 1990.

46. Ladokhin, A. S. and S. H. White, "Folding of amphipathic alpha-helices on membranes: energetics of helix formation by melittin.", *Journal of molecular biology*, Vol. 285, No. 4, pp. 1363–1369, 1999.

47. Henk, W. G., W. J. Todd, F. M. Enright and P. S. Mitchell, "The morphological effects of two antimicrobial peptides, hecate-1 and melittin, on Escherichia coli.", *Scanning microscopy*, Vol. 9, No. 2, pp. 501–507, 1995.

48. Gee, M. L., M. Burton, A. Grevis-James, M. A. Hossain, S. McArthur, E. A. Palombo, J. D. Wade and A. H. Clayton, "Imaging the action of antimicrobial peptides on living bacterial cells", *Scientific reports*, Vol. 3, p. 1557, 2013.

49. Henriques, S. T., M. N. Melo and M. A. R. B. Castanho, "Cell-penetrating peptides and antimicrobial peptides: how different are they?", *The Biochemical journal*, Vol. 399, No. 1, pp. 1–7, 2006.

50. Vivès, E., P. Brodin and B. Lebleu, "A Truncated HIV-1 Tat Protein Basic Domain Rapidly Translocates through the Plasma Membrane and Accumulates in the Cell Nucleus", *The Journal of biological chemistry*, Vol. 272, No. 25, pp.

16010–16017, 1997.

51. Derossi, D., A. H. Joliot, G. Chassaing and A. Prochiantz, "The third helix of the Antennapedia homeodomain translocates through biological membranes.", *The Journal of biological chemistry*, Vol. 269, No. 14, pp. 10444–10450, 1994.

52. Herce, H. D. and A. E. Garcia, "Molecular dynamics simulations suggest a mechanism for translocation of the HIV-1 TAT peptide across lipid membranes", *Proceedings of the National Academy of Sciences of the United States of America*, Vol. 104, No. 52, pp. 20805–20810, 2007.

53. Yesylevskyy, S., S.-J. Marrink and A. E. Mark, "Alternative mechanisms for the interaction of the cell-penetrating peptides penetratin and the TAT peptide with lipid bilayers", *Biophysical journal*, Vol. 97, No. 1, pp. 40–49, 2009.

54. Madani, F. L. S. L. Ü. F. S. and G. A, "Mechanism of Cellular Uptake of Cell-Penetrating Peptides", *Journal of Biophysics*, Vol. 2011, 2011.

55. Pooga, M., M. Hallbrink, M. Zorko and U. Langel, "Cell penetration by transportan.", *FASEB journal: official publication of the Federation of American Societies for Experimental Biology*, Vol. 12, No. 1, pp. 67–77, 1998.

56. Soomets, U., M. Lindgren, X. Gallet, M. Hallbrink, A. Elmquist, L. Balaspiri, M. Zorko, M. Pooga, R. Brasseur and U. Langel, "Deletion analogues of transportan", *Biochimica Et Biophysica Acta-Biomembranes*, Vol. 1467, No. 1, pp. 165–176, 2000.

57. Elmquist, A., M. Lindgren, T. Bartfai and U. Langel, "VE-cadherin-derived cell-penetrating peptide, pVEC, with carrier functions.", *Experimental cell research*, Vol. 269, No. 2, pp. 237–244, 2001.

58. Xia, H., Q. Mao and B. L. Davidson, "The HIV Tat protein transduction domain improves the biodistribution of beta-glucuronidase expressed from recombinant

viral vectors", *Nature biotechnology*, Vol. 19, No. 7, pp. 640–644, 2001.

59. Gratton, J.-P., J. Yu, J. W. Griffith, R. W. Babbitt, R. S. Scotland, R. Hickey, F. J. Giordano and W. C. Sessa, "Cell-permeable peptides improve cellular uptake and therapeutic gene delivery of replication-deficient viruses in cells and in vivo.", *Nature medicine*, Vol. 9, No. 3, pp. 357–362, 2003.

60. Eiriksdottir, E., K. Konate, U. Langel, G. Divita and S. Deshayes, "Secondary structure of cell-penetrating peptides controls membrane interaction and insertion", *Biochimica Et Biophysica Acta-Biomembranes*, Vol. 1798, No. 6, pp. 1119–1128, 2010.

61. Zorko, M. and U. Langel, "Cell-penetrating peptides: mechanism and kinetics of cargo delivery.", *Advanced drug delivery reviews*, Vol. 57, No. 4, pp. 529–545, 2005.

62. El Andaloussi, S., T. Holm and U. Langel, "Cell-Penetrating Peptides: Mechanisms and Applications", *Current Pharmaceutical Design*, Vol. 11, No. 28, pp. 3597–3611, 2005.

63. Morris, M. C., S. Deshayes, F. Heitz and G. Divita, "Cell-penetrating peptides: from molecular mechanisms to therapeutics", *Biology of the Cell*, Vol. 100, No. 4, pp. 201–217, 2008.

64. Mäger, I., E. Eiríksdóttir, K. Langel, S. El Andaloussi and U. Langel, "Assessing the uptake kinetics and internalization mechanisms of cell-penetrating peptides using a quenched fluorescence assay.", *Biochimica Et Biophysica Acta-Biomembranes*, Vol. 1798, No. 3, pp. 338–343, 2010.

65. Richard, J. P., K. Melikov, E. Vives, C. Ramos, B. Verbeure, M. J. Gait, L. V. Chernomordik and B. Lebleu, "Cell-penetrating peptides. A reevaluation of the mechanism of cellular uptake.", *The Journal of biological chemistry*, Vol. 278, No. 1, pp. 585–590, 2003.

66. Lundberg, M., S. Wikström and M. Johansson, "Cell surface adherence and endocytosis of protein transduction domains.", *Molecular therapy : the journal of the American Society of Gene Therapy*, Vol. 8, No. 1, pp. 143–150, 2003.

67. Guterstam, P., F. Madani, H. Hirose, T. Takeuchi, S. Futaki, S. El Andaloussi, A. Graslund and U. Langel, "Elucidating cell-penetrating peptide mechanisms of action for membrane interaction, cellular uptake, and translocation utilizing the hydrophobic counter-anion pyrenebutyrate", *Biochimica Et Biophysica Acta-Biomembranes*, Vol. 1788, No. 12, pp. 2509–2517, 2009.

68. Lindgren, M., X. Gallet, U. Soomets, M. Hällbrink, E. Bråkenhielm, M. Pooga, R. Brasseur and Ü. Langel, "Translocation properties of novel cell penetrating transportan and penetratin analogues", *Bioconjugate chemistry*, Vol. 11, No. 5, pp. 619–626, 2000.

69. Nekhotiaeva, N., A. Elmquist, G. K. Rajarao, M. Hällbrink, U. Langel and L. Good, "Cell entry and antimicrobial properties of eukaryotic cell-penetrating peptides", *FASEB journal: official publication of the Federation of American Societies for Experimental Biology*, Vol. 18, No. 2, pp. 394–396, 2004.

70. Eriksson, O. S., M. Geörg, H. Sjölinder, R. Sillard, S. Lindberg, U. Langel and A.-B. Jonsson, "Identification of cell-penetrating peptides that are bactericidal to Neisseria meningitidis and prevent inflammatory responses upon infection.", *Antimicrobial agents and chemotherapy*, Vol. 57, No. 8, pp. 3704–3712, 2013.

71. Palm, C., S. Netzereab and M. Hällbrink, "Quantitatively determined uptake of cell-penetrating peptides in non-mammalian cells with an evaluation of degradation and antimicrobial effects.", *Peptides*, Vol. 27, No. 7, pp. 1710–1716, 2006.

72. Elmquist, A., M. Hansen and U. Langel, "Structure-activity relationship study of the cell-penetrating peptide pVEC.", *Biochimica Et Biophysica Acta-Biomembranes*, Vol. 1758, No. 6, pp. 721–729, 2006.

73. Dejana, E., G. Bazzoni and M. G. Lampugnani, "Vascular endothelial (VE)-cadherin: only an intercellular glue?", *Experimental cell research*, Vol. 252, No. 1, pp. 13–19, 1999.

74. Alaybeyoglu, B., B. Sariyar Akbulut and E. Ozkirimli, "Insights into membrane translocation of the cell-penetrating peptide pVEC from molecular dynamics calculations", *Journal of Biomolecular Structure and Dynamics*, Vol. 34, No. 11, pp. 2387–2398, 2016.

75. Nan, Y. H., I.-S. Park, K.-S. Hahm and S. Y. Shin, "Antimicrobial activity, bactericidal mechanism and LPS-neutralizing activity of the cell-penetrating peptide pVEC and its analogs.", *Journal of peptide science : an official publication of the European Peptide Society*, Vol. 17, No. 12, pp. 812–817, 2011.

76. Dunkin, C. M., A. Pokorny, P. F. Almeida and H.-S. Lee, "Molecular dynamics studies of transportan 10 (Tp10) interacting with a POPC lipid bilayer", *The Journal of Physical Chemistry B*, Vol. 115, No. 5, pp. 1188–1198, 2010.

77. Herce, H. D., A. E. Garcia and M. C. Cardoso, "Fundamental molecular mechanism for the cellular uptake of guanidinium-rich molecules.", *Journal of the American Chemical Society*, Vol. 136, No. 50, pp. 17459–17467, 2014.

78. Deshayes, S., M. C. Morris, G. Divita and F. Heitz, "Cell-penetrating peptides: tools for intracellular delivery of therapeutics.", *Cellular and molecular life sciences : CMLS*, Vol. 62, No. 16, pp. 1839–1849, 2005.

79. Beck, D. A. C., G. W. N. White and V. Daggett, "Exploring the energy landscape of protein folding using replica-exchange and conventional molecular dynamics simulations", *Journal of structural biology*, Vol. 157, No. 3, pp. 514–523, 2007.

80. Nguyen, T. H. T., N. Z. Rao, W. M. Schroeder and P. B. Moore, "Coarse-grained molecular dynamics of tetrameric transmembrane peptide bundles within a lipid bilayer.", *Chemistry and physics of lipids*, Vol. 163, No. 6, pp. 530–537, 2010.

81. Nymeyer, H., T. B. Woolf and A. E. Garcia, "Folding is not required for bilayer insertion: replica exchange simulations of an alpha-helical peptide with an explicit lipid bilayer.", *Proteins*, Vol. 59, No. 4, pp. 783–790, 2005.

82. Polyansky, A. A., P. E. Volynsky, A. S. Arseniev and R. G. Efremov, "Adaptation of a Membrane-active Peptide to Heterogeneous Environment. I. Structural Plasticity of the Peptide", *The journal of physical chemistry B*, Vol. 113, No. 4, pp. 1107–1119, 2009.

83. Akdag, I. O. and E. Ozkirimli, "The Uptake Mechanism of the Cell-Penetrating pVEC Peptide", *Journal of Chemistry*, 2013.

84. Alaybeyoglu, B., B. Sariyar Akbulut and E. Ozkirimli, "A novel chimeric peptide with antimicrobial activity", *Journal of peptide science : an official publication of the European Peptide Society*, Vol. 21, No. 4, pp. 294–301, 2015.

85. MacCallum, J. L., W. F. D. Bennett and D. P. Tieleman, "Distribution of amino acids in a lipid bilayer from computer simulations.", *Biophysical journal*, Vol. 94, No. 9, pp. 3393–3404, May 2008.

86. Tsai, C. W., N. Y. Hsu, C. H. Wang, C. Y. Lu, Y. Chang, H. H. G. Tsai and R. C. Ruaan, "Coupling Molecular Dynamics Simulations with Experiments for the Rational Design of Indolicidin-Analogous Antimicrobial Peptides", *Journal of molecular biology*, Vol. 392, No. 3, pp. 837–854, 2009.

87. Epand, R. M. and H. J. Vogel, "Diversity of antimicrobial peptides and their mechanisms of action.", *Biochimica Et Biophysica Acta-Biomembranes*, Vol. 1462, No. 1-2, pp. 11–28, 1999.

88. Duchardt, F., M. Fotin-Mleczek, H. Schwarz, R. Fischer and R. Brock, "A comprehensive model for the cellular uptake of cationic cell-penetrating peptides", *Traffic*, Vol. 8, No. 7, pp. 848–866, 2007.

89. Ciobanasu, C., J. P. Siebrasse and U. Kubitscheck, "Cell-penetrating HIV1 TAT peptides can generate pores in model membranes", *Biophysical journal*, Vol. 99, No. 1, pp. 153–162, 2010.

90. MacCallum, J. L., W. D. Bennett and D. P. Tieleman, "Transfer of arginine into lipid bilayers is nonadditive", *Biophysical journal*, Vol. 101, No. 1, pp. 110–117, 2011.

91. Mitchell, D. J., D. T. Kim, L. Steinman, C. G. Fathman and J. B. Rothbard, "Polyarginine enters cells more efficiently than other polycationic homopolymers.", *The journal of peptide research : official journal of the American Peptide Society*, Vol. 56, No. 5, pp. 318–325, 2000.

92. Rothbard, J. B., E. Kreider, C. L. VanDeusen, L. Wright, B. L. Wylie and P. A. Wender, "Arginine-rich molecular transporters for drug delivery: role of backbone spacing in cellular uptake", *Journal of medicinal chemistry*, Vol. 45, No. 17, pp. 3612–3618, 2002.

93. MacCallum, J. L., W. F. D. Bennett and D. P. Tieleman, "Partitioning of Amino Acid Side Chains into Lipid Bilayers: Results from Computer Simulations and Comparison to Experiment", *The Journal of general physiology*, Vol. 129, No. 5, pp. 371–377, May 2007.

94. Isralewitz, B., J. Baudry, J. Gullingsrud, D. Kosztin and K. Schulten, "Steered molecular dynamics investigations of protein function", *Journal of Molecular Graphics and Modelling*, Vol. 19, No. 1, pp. 13–25, 2001.

95. Lorenzo, A. C. and P. M. Bisch, "Analyzing different parameters of steered molecular dynamics for small membrane interacting molecules", *Journal of Molecular Graphics and Modelling*, Vol. 24, No. 1, pp. 59–71, 2005.

96. Das, P., M. Moll, H. Stamati, L. E. Kavraki and C. Clementi, "Low-dimensional, free-energy landscapes of protein-folding reactions by nonlinear dimensionality

reduction", *Proceedings of the National Academy of Sciences*, Vol. 103, No. 26, pp. 9885–9890, 2006.

97. Tenenbaum, J. B., V. de Silva and J. C. Langford, "A global geometric framework for nonlinear dimensionality reduction.", *Science*, Vol. 290, No. 5500, pp. 2319–2323, 2000.

98. Plaku, E., H. Stamati, C. Clementi and L. E. Kavraki, "Fast and reliable analysis of molecular motion using proximity relations and dimensionality reduction", *Proteins*, Vol. 67, No. 4, pp. 897–907, 2007.

99. Ferguson, A. L., A. Z. Panagiotopoulos, I. G. Kevrekidis and P. G. Debenedetti, "Nonlinear dimensionality reduction in molecular simulation: The diffusion map approach", *Chemical Physics Letters*, Vol. 509, No. 1-3, pp. 1–11, 2011.

100. Hartmann, M., M. Berditsch, J. Hawecker, M. F. Ardakani, D. Gerthsen and A. S. Ulrich, "Damage of the bacterial cell envelope by antimicrobial peptides gramicidin S and PGLa as revealed by transmission and scanning electron microscopy", *Antimicrobial agents and chemotherapy*, Vol. 54, No. 8, pp. 3132–3142, 2010.

101. Park, Y., D. G. Lee, S.-H. Jang, E.-R. Woo, H. G. Jeong, C.-H. Choi and K.-S. Hahm, "A Leu-Lys-rich antimicrobial peptide: activity and mechanism.", *Biochimica Et Biophysica Acta-Biomembranes*, Vol. 1645, No. 2, pp. 172–182, 2003.

102. Stenger, S., D. A. Hanson, R. Teitelbaum, P. Dewan, K. R. Niazi, C. J. Froelich, T. Ganz, S. Thoma-Uszynski, A. Melián, C. Bogdan, S. A. Porcelli, B. R. Bloom, A. M. Krensky and R. L. Modlin, "An antimicrobial activity of cytolytic T cells mediated by granulysin.", *Science*, Vol. 282, No. 5386, pp. 121–125, 1998.

103. Torrent, M., A. Sánchez-Chardi, M. Nogués and E. Boix, "Assessment of antimicrobial compounds by microscopy techniques", *Microscopy: Science, Technology, Applications and Education,(3), Series*, Vol. 3, No. 4, pp. 1115–1126, 2010.

104. Jensen, K. F., J. El-Ali and P. K. Sorger, *Cells on chips*, Nature, 2006.

105. Dittrich, P. S. and A. Manz, "Lab-on-a-chip: microfluidics in drug discovery", *Nature Reviews Drug Discovery*, Vol. 5, No. 3, pp. 210–218, 2006.

106. Boehm, D. A., P. A. Gottlieb and S. Z. Hua, "On-chip microfluidic biosensor for bacterial detection and identification", *Sensors and Actuators B: Chemical*, Vol. 126, No. 2, pp. 508–514, 2007.

107. Krüger, J., K. Singh, A. O'Neill, C. Jackson, A. Morrison and P. O'Brien, "Development of a microfluidic device for fluorescence activated cell sorting", *Journal of micromechanics and microengineering*, Vol. 12, No. 4, p. 486, 2002.

108. Groisman, A., C. Lobo, H. Cho, J. K. Campbell, Y. S. Dufour, A. M. Stevens and A. Levchenko, "A microfluidic chemostat for experiments with bacterial and yeast cells", *Nature methods*, Vol. 2, No. 9, pp. 685–689, 2005.

109. Mahalanabis, M., H. Al-Muayad, M. D. Kulinski, D. Altman and C. M. Klapperich, "Cell lysis and DNA extraction of gram-positive and gram-negative bacteria from whole blood in a disposable microfluidic chip", *Lab on a Chip*, Vol. 9, No. 19, pp. 2811–2817, 2009.

110. Kong, K.-F., L. Schneper and K. Mathee, "Beta-lactam antibiotics: from antibiosis to resistance and bacteriology.", *Acta Pathologica, Microbiologica et Immunologica Scandinavica*, Vol. 118, No. 1, pp. 1–36, 2010.

111. Majiduddin, F. K., I. C. Materon and T. G. Palzkill, "Molecular analysis of beta-lactamase structure and function", *International journal of medical microbiology*, Vol. 292, No. 2, pp. 127–137, 2002.

112. Ambler, R. P., "The structure of beta-lactamases", *Philosophical Transactions of the Royal Society B: Biological Sciences*, Vol. 289, No. 1036, pp. 321–331, May 1980.

113. Bush, K., G. A. Jacoby and A. A. Medeiros, "A functional classification scheme for beta-lactamases and its correlation with molecular structure", *Antimicrobial agents and chemotherapy*, Vol. 39, No. 6, pp. 1211–1233, 1995.

114. Öztürk, H., E. Ozkirimli and A. Özgür, "Classification of Beta-lactamases and penicillin binding proteins using ligand-centric network models", *PloS one*, Vol. 10, No. 2, p. e0117874, 2015.

115. Livermore, D. M., "Fourteen years in resistance", *International journal of antimicrobial agents*, Vol. 39, No. 4, pp. 283–294, 2012.

116. Page, M. G., "Beta-Lactamase inhibitors", *Drug Resistance Updates*, Vol. 3, No. 2, pp. 109–125, 2000.

117. Shlaes, D. M., "New beta-lactam-beta-lactamase inhibitor combinations in clinical development", *Annals of the New York Academy of Sciences*, Vol. 1277, No. 1, pp. 105–114, 2013.

118. Reading, C. and M. Cole, "Clavulanic acid: a beta-lactamase-inhibiting beta-lactam from Streptomyces clavuligerus", *Antimicrobial agents and chemotherapy*, Vol. 11, No. 5, pp. 852–857, 1977.

119. Rolinson, G. N., "A review of the microbiology of amoxycillin/clavulanic acid over the 15 year period 1978-1993", *Journal of chemotherapy*, Vol. 6, No. 5, pp. 283–318, 1994.

120. Finlay, J., L. Miller and J. A. Poupard, "A review of the antimicrobial activity of clavulanate", *Journal of Antimicrobial Chemotherapy*, Vol. 52, No. 1, pp. 18–23, 2003.

121. Severin, A., E. Severina and A. Tomasz, "Abnormal physiological properties and altered cell wall composition in Streptococcus pneumoniae grown in the presence of clavulanic acid.", *Antimicrobial agents and chemotherapy*, Vol. 41, No. 3, pp.

504–510, 1997.

122. Lim, D., H. U. Park, L. De Castro, S. G. Kang, H. S. Lee, S. Jensen, K. J. Lee and N. C. Strynadka, "Crystal structure and kinetic analysis of β-lactamase inhibitor protein-II in complex with TEM-1 β-lactamase", *Nature Structural & Molecular Biology*, Vol. 8, No. 10, pp. 848–852, 2001.

123. Yuan, J., W. Huang, D. C. Chow and T. Palzkill, "Fine mapping of the sequence requirements for binding of beta-lactamase inhibitory protein (BLIP) to TEM-1 beta-lactamase using a genetic screen for BLIP function", *Journal of molecular biology*, Vol. 389, No. 2, pp. 401–412, 2009.

124. Yuan, J., D. C. Chow, W. Huang and T. Palzkill, "Identification of a beta-lactamase inhibitory protein variant that is a potent inhibitor of Staphylococcus PC1 beta-lactamase", *Journal of molecular biology*, Vol. 406, No. 5, pp. 730–744, 2011.

125. Reynolds, K. A., M. S. Hanes, J. M. Thomson, A. J. Antczak, J. M. Berger, R. A. Bonomo, J. F. Kirsch and T. M. Handel, "Computational redesign of the SHV-1 beta-lactamase/beta-lactamase inhibitor protein interface", *Journal of molecular biology*, Vol. 382, No. 5, pp. 1265–1275, 2008.

126. Strynadka, N. C., H. Adachi, S. E. Jensen, K. Johns, A. Sielecki, C. Betzel, K. Sutoh and M. N. James, "Molecular structure of the acyl-enzyme intermediate in β-lactam hydrolysis at 1.7 Å resolution", *Nature*, Vol. 359, No. 6397, pp. 700–705, 1992.

127. Jelsch, C., L. Mourey, J.-M. Masson and J.-P. Samama, "Crystal structure of Escherichia coli TEM1 β-lactamase at 1.8 Å resolution", *Proteins: Structure, Function, and Bioinformatics*, Vol. 16, No. 4, pp. 364–383, 1993.

128. Doran, J. L., B. Leskiw, S. Aippersbach and S. E. Jensen, "Isolation and characterization of a beta-lactamase-inhibitory protein from Streptomyces clavuligerus

and cloning and analysis of the corresponding gene.", *Journal of bacteriology*, Vol. 172, No. 9, pp. 4909–4918, 1990.

129. Strynadka, N. C., S. E. Jensen, K. Johns, H. Blanchard, M. Page, A. Matagne, J. M. Frere and M. N. James, "Structural and kinetic characterization of a beta-lactamase-inhibitor protein.", *Nature*, Vol. 368, No. 6472, pp. 657–660, 1994.

130. Zhang, Z. and T. Palzkill, "Determinants of binding affinity and specificity for the interaction of TEM-1 and SME-1 beta-lactamase with beta-lactamase inhibitory protein.", *The Journal of biological chemistry*, Vol. 278, No. 46, pp. 45706–45712, 2003.

131. Huang, W., Z. Zhang and T. Palzkill, "Design of potent beta-lactamase inhibitors by phage display of beta-lactamase inhibitory protein.", *The Journal of biological chemistry*, Vol. 275, No. 20, pp. 14964–14968, May 2000.

132. Huang, W., Z. Beharry, Z. Zhang and T. Palzkill, "A broad-spectrum peptide inhibitor of β-lactamase identified using phage display and peptide arrays", *Protein engineering*, Vol. 16, No. 11, pp. 853–860, 2003.

133. Yribarren, A.-S., D. Thomas, A. Friboulet and B. Avalle, "Selection of peptides inhibiting a β-lactamase-like activity", *The FEBS Journal*, Vol. 270, No. 13, pp. 2789–2795, 2003.

134. Phichith, D., S. Bun, S. Padiolleau-Lefevre, A. Guellier, S. Banh, M. Galleni, J.-M. Frere, D. Thomas, A. Friboulet and B. Avalle, "Novel peptide inhibiting both TEM-1 β-lactamase and penicillin-binding proteins.", *The FEBS journal*, Vol. 277, No. 23, pp. 4965–4972, 2010.

135. Humphrey, W., A. Dalke and K. Schulten, "VMD: visual molecular dynamics.", *Journal of Molecular Graphics*, Vol. 14, No. 1, pp. 33–8– 27–8, 1996.

136. Kale, L., R. Skeel, M. Bhandarkar, R. Brunner, A. Gursoy, N. Krawetz, J. Phillips,

A. Shinozaki, K. Varadarajan and K. Schulten, "NAMD2: Greater scalability for parallel molecular dynamics", *Journal of Computational Physics*, Vol. 151, No. 1, pp. 283–312, May 1999.

137. Phillips, J. C., R. Braun, W. Wang, J. Gumbart, E. Tajkhorshid, E. Villa, C. Chipot, R. D. Skeel, L. Kale and K. Schulten, "Scalable molecular dynamics with NAMD", *Journal of Computational Chemistry*, Vol. 26, No. 16, pp. 1781–1802, 2005.

138. MacKerell Jr, A. D., D. Bashford, M. Bellott, R. L. Dunbrack Jr, J. D. Evanseck, M. J. Field, S. Fischer, J. Gao, H. Guo, S. Ha *et al.*, "All-atom empirical potential for molecular modeling and dynamics studies of proteins", *The journal of physical chemistry B*, Vol. 102, No. 18, pp. 3586–3616, 1998.

139. Vanommeslaeghe, K., E. Hatcher, C. Acharya, S. Kundu, S. Zhong, J. Shim, E. Darian, O. Guvench, P. Lopes, I. Vorobyov and A. D. MacKerell, "CHARMM general force field: A force field for drug-like molecules compatible with the CHARMM all-atom additive biological force fields.", *Journal of Computational Chemistry*, Vol. 31, No. 4, pp. 671–690, 2010.

140. Best, R. B., X. Zhu, J. Shim, P. E. M. Lopes, J. Mittal, M. Feig and A. D. Mackerell, "Optimization of the additive CHARMM all-atom protein force field targeting improved sampling of the backbone φ, ψ and side-chain $\chi(1)$ and $\chi(2)$ dihedral angles.", *Journal of chemical theory and computation*, Vol. 8, No. 9, pp. 3257–3273, 2012.

141. Joanne, P., C. Galanth, N. Goasdoue, P. Nicolas, S. Sagan, S. Lavielle, G. Chassaing, C. El Amri and I. D. Alves, "Lipid reorganization induced by membrane-active peptides probed using differential scanning calorimetry", *Biochimica Et Biophysica Acta-Biomembranes*, Vol. 1788, No. 9, pp. 1772–1781, 2009.

142. Murzyn, K., T. Róg and M. Pasenkiewicz-Gierula, "Phosphatidylethanolamine-phosphatidylglycerol bilayer as a model of the inner bacterial membrane", *Bio-*

physical journal, Vol. 88, No. 2, pp. 1091–1103, 2005.

143. Jo, S., J. B. Lim, J. B. Klauda and W. Im, "CHARMM-GUI Membrane Builder for mixed bilayers and its application to yeast membranes", *Biophysical journal*, Vol. 97, No. 1, pp. 50–58, 2009.

144. Wu, E. L., X. Cheng, S. Jo, H. Rui, K. C. Song, E. M. Dávila-Contreras, Y. Qi, J. Lee, V. Monje-Galvan, R. M. Venable, J. B. Klauda and W. Im, "CHARMM-GUI Membrane Builder toward realistic biological membrane simulations.", *Journal of Computational Chemistry*, Vol. 35, No. 27, pp. 1997–2004, 2014.

145. Lee, J., X. Cheng, J. M. Swails, M. S. Yeom, P. K. Eastman, J. A. Lemkul, S. Wei, J. Buckner, J. C. Jeong, Y. Qi, S. Jo, V. S. Pande, D. A. Case, C. L. Brooks, A. D. Mackerell, J. B. Klauda and W. Im, "CHARMM-GUI Input Generator for NAMD, GROMACS, AMBER, OpenMM, and CHARMM/OpenMM Simulations Using the CHARMM36 Additive Force Field.", *Journal of chemical theory and computation*, Vol. 12, No. 1, pp. 405–413, 2016.

146. Klauda, J. B., R. M. Venable, J. A. Freites, J. W. O Connor, D. J. Tobias, C. Mondragon-Ramirez, I. Vorobyov, A. D. MacKerell Jr and R. W. Pastor, "Update of the CHARMM all-atom additive force field for lipids: validation on six lipid types", *The journal of physical chemistry B*, Vol. 114, No. 23, pp. 7830–7843, 2010.

147. Fiorin, G., M. L. Klein and J. Hénin, "Using collective variables to drive molecular dynamics simulations", *Molecular Physics*, Vol. 111, No. 22-23, pp. 3345–3362, 2013.

148. Egberts, E., S.-J. Marrink and H. J. Berendsen, "Molecular dynamics simulation of a phospholipid membrane", *European biophysics journal*, Vol. 22, No. 6, pp. 423–436, 1994.

149. Torrie, G. M. and J. P. Valleau, "Nonphysical sampling distributions in Monte

Carlo free-energy estimation: Umbrella sampling", *Journal of Computational Physics*, 1977.

150. Sugita, Y. and Y. Okamoto, "Replica-exchange molecular dynamics method for protein folding", *Chemical Physics Letters*, Vol. 314, No. 1, pp. 141–151, 1999.

151. Sugita, Y., A. Kitao and Y. Okamoto, "Multidimensional replica-exchange method for free-energy calculations", *The Journal of Chemical Physics*, Vol. 113, No. 15, pp. 6042–6051, 2000.

152. Roux, B., "The calculation of the potential of mean force using computer simulations", *Computer Physics Communications*, Vol. 91, No. 1-3, pp. 275–282, 1995.

153. Kumar, S., J. M. Rosenberg, D. Bouzida, R. H. Swendsen and P. A. Kollman, "THE weighted histogram analysis method for free-energy calculations on biomolecules. I. The method", *Journal of Computational Chemistry*, Vol. 13, No. 8, pp. 1011–1021, 1992.

154. Kumar, S., J. M. Rosenberg, D. Bouzida, R. H. Swendsen and P. A. Kollman, "Multidimensional free-energy calculations using the weighted histogram analysis method", *Journal of Computational Chemistry*, Vol. 16, No. 11, pp. 1339–1350, 1995.

155. Souaille, M. and B. Roux, "Extension to the weighted histogram analysis method: combining umbrella sampling with free energy calculations", *Computer Physics Communications*, 2001.

156. Bebrone, C., C. Moali, F. Mahy, S. Rival, J. D. Docquier, G. M. Rossolini, J. Fastrez, R. F. Pratt, J. M. Frere and M. Galleni, "CENTA as a chromogenic substrate for studying beta-lactamases.", *Antimicrobial agents and chemotherapy*, Vol. 45, No. 6, pp. 1868–1871, 2001.

157. Amsterdam, D., "Susceptibility testing of antimicrobials in liquid media", *Antibi-*

otics in laboratory medicine, pp. 52–111, Lippincott Williams & Wilkins, Baltimore, MD, 1996.

158. Young, J. W., J. C. W. Locke, A. Altinok, N. Rosenfeld, T. Bacarian, P. S. Swain, E. Mjolsness and M. B. Elowitz, "Measuring single-cell gene expression dynamics in bacteria using fluorescence time-lapse microscopy", *Nature protocols*, Vol. 7, No. 1, pp. 80–88, 2012.

159. Boulos, L., M. Prevost, B. Barbeau, J. Coallier and R. Desjardins, "LIVE/DEAD® BacLight : application of a new rapid staining method for direct enumeration of viable and total bacteria in drinking water", *Journal of microbiological Methods*, Vol. 37, No. 1, pp. 77–86, 1999.

160. Altman, F. P., "Tetrazolium salts and formazans", *Progress in histochemistry and cytochemistry*, Vol. 9, No. 3, pp. III–51, 1976.

161. Berridge, M. V., P. M. Herst and A. S. Tan, "Tetrazolium dyes as tools in cell biology: new insights into their cellular reduction", *Biotechnology annual review*, Vol. 11, pp. 127–152, 2005.

162. Scudiero, D. A., R. H. Shoemaker, K. D. Paull, A. Monks, S. Tierney, T. H. Nofziger, M. J. Currens, D. Seniff and M. R. Boyd, "Evaluation of a soluble tetrazolium/formazan assay for cell growth and drug sensitivity in culture using human and other tumor cell lines", *Cancer research*, Vol. 48, No. 17, pp. 4827–4833, 1988.

163. Marshall, N. J., C. J. Goodwin and S. J. Holt, "A critical assessment of the use of microculture tetrazolium assays to measure cell growth and function.", *Growth regulation*, Vol. 5, No. 2, pp. 69–84, 1995.

164. Tennant, J. R., "Evaluation of the trypan blue technique for determination of cell viability.", *Transplantation*, Vol. 2, No. 6, pp. 685–694, 1964.

165. Altman, S. A., L. Randers and G. Rao, "Comparison of trypan blue dye exclusion and fluorometric assays for mammalian cell viability determinations", *Biotechnology Progress*, Vol. 9, No. 6, pp. 671–674, 1993.

166. Louis, K. S. and A. C. Siegel, "Cell Viability Analysis Using Trypan Blue: Manual and Automated Methods", *Mammalian Cell Viability*, pp. 7–12, Humana Press, Totowa, NJ, 2011.

167. Perly, B., I. C. Smith and H. C. Jarrell, "Acyl chain dynamics of phosphatidylethanolamines containing oleic acid and dihydrosterculic acid: 2H NMR relaxation studies", *Biochemistry*, Vol. 24, No. 17, pp. 4659–4665, 1985.

168. Huang, K. and A. E. García, "Free energy of translocating an arginine-rich cell-penetrating peptide across a lipid bilayer suggests pore formation", *Biophysical journal*, Vol. 104, No. 2, pp. 412–420, 2013.

169. Wright, A. J., "The penicillins", *Mayo Clinic Proceedings*, Vol. 74, pp. 290–307, Elsevier, 1999.